

The microstructural evolution and mechanical behavior of materials in the extreme environments  
of high-velocity impact and irradiation

By

Claire E. Griesbach

A dissertation submitted in partial fulfillment of  
the requirements for the degree of

Doctor of Philosophy

(Engineering Mechanics)

at the

UNIVERSITY OF WISCONSIN-MADISON

2023

Date of final oral examination: 5/5/2023

The dissertation is approved by the following members of the Final Oral Committee:

Ramathasan Thevamaran, Assistant Professor, Mechanical Engineering

Curt Bronkhorst, Professor, Mechanical Engineering

Wendy Crone, Professor, Mechanical Engineering

Paul Evans, Professor, Materials Science and Engineering

Yongfeng Zhang, Assistant Professor, Engineering Physics

## *Acknowledgements*

I would like to express the deepest gratitude to my advisor, Prof. Ramathasan Thevamaran. He is not only a phenomenal research mentor, but a life mentor—truly caring about me and my future career. He has provided me with countless opportunities to grow as a researcher and to advance my career. I would like to thank him for training me to be creative, yet detailed focused and motivating me to produce high-quality, impactful research. His energy and excitement for fundamental research is contagious.

I would like to thank my thesis defense committee members, Prof. Curt Bronkhorst, Prof. Wendy Crone, Prof. Paul Evans, and Prof. Yongfeng Zhang for their time and valuable advice. I would especially like to thank Prof. Bronkhorst, Prof. Zhang, and Dr. Tyler Gerczak for their continued support and mentorship during our collaborative research projects. I thank Dr. Jizhe Cai, Prof. Mauricio Ponga, and all other collaborators and co-workers for their expertise, insights, and support. I would also like to thank Dr. Julie Morasch, Mr. Richard Noll, and Dr. Casey McKinney for their assistance and advice with microscopy-related issues.

On a more personal note, I would like to thank my friends and family for their continued support and love. I thank Joseph for solving all my technology related issues, Marisa and Theresa for helping me through the daily ups and downs of research, and Louise and Maggie for exemplifying boundless energy and focus which I attempt to match. Most of all, I would like to thank my parents for providing me with all the opportunities, love, and support that got me here, and for teaching me that, above all else, I should strive to be a good person.

## ***Abstract***

Understanding the process-structure-property relations is imperative when designing materials for critical applications, especially when exposed to extreme environments. Clever design of materials containing structural heterogeneities or features spanning multiple length scales can provide synergistically improved properties well beyond the limits of their homogeneous components or provide predictable and acceptable failure modes. In this work, we investigate the process-structure-property relations and the potential for improved performance of materials exposed to the extreme environments of high-velocity impact and irradiation.

Similar to material processing techniques such as shot peening and cold spray which induce structural changes through high-velocity impact, we perform well-controlled single microprojectile impact tests of silver (Ag) single crystals which allows for clear correlation of the post-deformation microstructures to the impact-induced plasticity mechanisms. When comparing the impacted microsamples to their pristine single crystal counterparts, we find that the high-strain rates achieved during impact ( $\dot{\epsilon} \sim 10^8 \text{ s}^{-1}$ ) induce dramatic structural changes including extensive grain refinement, dislocation density gradients, and a martensitic phase transformation, while the quasi-statically ( $\dot{\epsilon} = 10^{-2} \text{ s}^{-1}$ ) compressed Ag microcubes remain single crystalline. The impacted samples show a synergistic improvement in strength and toughness, each on average over twice the respective properties of single crystal and bulk polycrystal Ag samples. Such synergistic improvements result from heterogeneous deformation induced stress and strain gradients. Progressive yielding of the gradient grain structure causes enhanced nucleation and pile-up of dislocations in the relatively softer domains to accommodate the elastic-plastic mismatch between grains. The observed dislocation accumulation—which is higher in larger grains—provides ultra-

high strain hardening. Additionally, enhanced toughness is achieved through intergranular plasticity mechanisms such as nanograin rotation and grain boundary migration, leading to grain coalescence. These complementary inter- and intragranular plasticity mechanisms elicit improved mechanical properties. We demonstrate the ability to tune the dominant plasticity mechanisms—and thus the resultant properties—through control over the crystal orientation and impact velocity. Our findings provide new understandings of impact-induced nanostructural evolution and mechanistic pathways to improve mechanical properties through heterogeneous deformation, which can be used to improve high strain rate metal processing techniques.

The second research thrust examines the effects of structural heterogeneity on the mechanical properties, performance, and failure of tristructural isotropic (TRISO) coated nuclear fuel particles. We examine the irradiation-induced densification and fracture behavior of the porous pyrocarbon buffer layer, which has pronounced effects on the overall particle's performance. Microstructural characterization of the initial as-fabricated buffer layer reveals a gradient of increasing porosity in the radial direction with the porosity reaching a maximum near the buffer-IPyC interface—which is commonly where circumferential tearing initiates in the buffer layer. Using the as-fabricated buffer structure as a basis to investigate the irradiation-induced structural changes, we study the influences of irradiation temperature and fluence on buffer layer response, by characterizing multiple TRISO particles from three different irradiation condition groups. The high temperatures, radiation damage, and mechanical stresses applied to the buffer layer during irradiation cause irradiation condition-dependent micro and nanostructural changes: localized densification near the kernel occurs in particles exposed to relatively lower temperatures, whereas significant changes in the entire pore microstructure occur in particles irradiated under high temperature and fluence. Intriguingly, a large proportion of the total buffer layer densification



is accommodated through graphitization of the pyrocarbon rather than the changes in the pore microstructure. Significant nanostructural changes—including an increase in crystallite size, decrease in interplanar spacing, and formation of onion-like graphitic structures—contribute to densification and are most pronounced in the samples exposed to the highest temperature and fluence. Our findings provide a new detailed understanding of the irradiation-induced densification and fracture behavior of the pyrocarbon buffer layer in TRISO nuclear fuel particles, which will enable better predictions of buffer failure, aid in improved future designs, and provide guidance on the acceptable usage of these particles given different reactor conditions.

# Table of Contents

<b>Chapter 1. Introduction.....</b>	<b>1</b>
1.1 Research objectives.....	1
1.1.1 Research Thrust I: Improving mechanical properties through impact-induced nanostructural evolution of initially single crystal metals .....	1
1.1.2 Research Thrust II: Investigating the fracture and densification behavior in the pyrocarbon buffer layer of TRISO nuclear fuel particles.....	2
1.2 Motivation for research.....	4
1.3 Organization and brief overview of thesis .....	5
<b>Chapter 2. Materials and Methods.....</b>	<b>7</b>
2.1 Materials .....	7
2.1.1 Single crystal silver microcubes and substrates .....	7
2.1.2 Tristructural Isotropic (TRISO) coated nuclear fuel particles .....	9
2.2 Sample preparation/fabrication .....	11
2.2.1 Preparation of Ag microcubes for testing and characterization .....	11
2.2.2 Mounting, grinding, and polishing TRISO particles .....	12
2.2.3 Fabrication of pillars with a focused ion beam (FIB) .....	13
2.2.4 Fabrication of electron transparent lamella with a FIB .....	16
2.3 Testing apparatus .....	17
2.3.1 High-velocity impact using a LIPIT apparatus .....	17
2.3.2 Nanoindentation.....	18
2.3.3 Quasi-static compression tests using an in-situ SEM nanoindenter.....	19
2.4 Characterization methods.....	25
2.4.1 Scanning Electron Microscopy (SEM).....	25
2.4.2 Transmission Electron Microscopy (TEM).....	26
2.4.3 Raman spectroscopy .....	26
2.4.4 Transmission Kikuchi Diffraction (TKD) .....	27
2.4.5 FIB-SEM tomography.....	35
2.5 Molecular statics (MS) and molecular dynamics (MD) simulations .....	42
2.5.1 Molecular statics (MS) simulations .....	43

2.5.2	<i>Molecular dynamics (MD) simulations</i> .....	45
2.6	Crystal plasticity simulations .....	47
2.6.1	<i>Single crystal constitutive model</i> .....	48
2.6.2	<i>Parameter determination and fitting</i> .....	51
2.6.3	<i>Synthetic microstructure generation</i> .....	54
2.6.4	<i>Incorporating dislocation density and grain size effects into the simulations</i> .....	60
2.6.5	<i>Building the models and running simulations</i> .....	64
<b>Chapter 3. Improving mechanical properties through impact-induced nanostructural evolution of initially single crystal metals</b> .....		<b>66</b>
3.1	Introduction .....	66
3.2	Quasi-static deformation of silver single crystals .....	70
3.2.1	<i>Quasi-static compression response of initially dislocation-free Ag microcubes</i> ....	72
3.2.2	<i>Effects of FIB-induced defects on the mechanical response of single crystals</i> .....	75
3.2.3	<i>Analysis of dislocation nucleation mechanisms through molecular statics simulations</i> .....	77
3.2.4	<i>Origins of sample size effects</i> .....	80
3.3	Impact-induced nanostructural evolution of single crystals .....	85
3.3.1	<i>High strain rate deformation of initially single crystal Ag microcubes</i> .....	86
3.3.2	<i>Impact-orientation dependent nanostructural evolution</i> .....	96
3.3.3	<i>Effect of loading conditions on dislocation nucleation and recrystallization</i> .....	105
3.4	Synergistic property improvement in impact-induced heterogeneous nanostructures ...	118
3.4.1	<i>Mechanical responses of impacted samples compared to single crystals</i> .....	118
3.4.2	<i>Heterogenous deformation induced strengthening</i> .....	131
3.4.3	<i>Synergistic property improvements</i> .....	137
3.5	Activation of complementary plasticity mechanisms provides synergistic property improvements .....	142
3.5.1	<i>Dominant plasticity mechanisms in [110]-impacted samples</i> .....	143
3.5.2	<i>Dominant plasticity mechanisms in [100]-impacted samples</i> .....	149
3.5.3	<i>Dominant plasticity mechanisms in [111]-impacted samples</i> .....	153
3.5.4	<i>Activation of complementary plasticity mechanisms through heterogeneous deformation</i> .....	157
3.6	Conclusion .....	158
<b>Chapter 4. Investigating the fracture and densification behavior in the pyrocarbon buffer layer of TRISO nuclear fuel particles</b> .....		<b>162</b>

4.1	Introduction.....	162
4.2	Implications of microstructural heterogeneity in the as-fabricated buffer layer of TRISO particles .....	167
4.2.1	<i>Experimental design.....</i>	167
4.2.2	<i>Porosity characterization across the radial direction of a single particle .....</i>	168
4.2.3	<i>Heterogeneity in porosity and mechanical properties.....</i>	180
4.2.4	<i>Potential implications to fracture and densification behavior .....</i>	188
4.3	Irradiation-induced changes in the porous buffer microstructure.....	193
4.3.1	<i>Experimental design.....</i>	193
4.3.2	<i>Porosity and fission product distribution across the buffer layer of particles irradiated at different temperatures and fluences .....</i>	197
4.3.3	<i>Implications of irradiation induced microstructural changes to the fracture and densification behavior .....</i>	205
4.4	Irradiation-induced nanostructural changes in pyrocarbon.....	211
4.4.1	<i>Experimental design.....</i>	211
4.4.2	<i>Crystallite size changes as a function of irradiation temperature and fluence ....</i>	214
4.4.3	<i>Changes in the interplanar spacing of graphene sheets due to irradiation .....</i>	221
4.4.4	<i>Nanostructural changes contributing to densification .....</i>	223
4.5	Conclusion .....	227
<b>Chapter 5.</b>	<b>Contributions and future work.....</b>	<b>230</b>
5.1	Summary of key findings.....	230
5.1.1	<i>Research Thrust I: Improving mechanical properties through impact-induced nanostructural evolution of initially single crystal metals .....</i>	230
5.1.2	<i>Research Thrust II: Investigating the fracture and densification behavior in the pyrocarbon buffer layer of TRISO nuclear fuel particles.....</i>	233
5.2	Additional contributions to the fields .....	236
5.3	Future work.....	237
<b>Appendix A</b>	<b>.....</b>	<b>239</b>
A.1	Schmid factor analysis of loading directions in an fcc structure.....	239
A.2	Elastic properties of silver.....	240
A.3	Estimates of key parameters of impact deformation [36] .....	242
A.4	Calculation of equilibrium vacancy concentration in silver.....	243
<b>Appendix B</b>	<b>.....</b>	<b>245</b>

B.1 Stochastic deformation response of quasi-statically compressed single crystal micro- and nano-cubes .....	245
B.2 Polytypes of Ag – SAD pattern indexing .....	254
B.3 Details for impacted samples.....	259
B.4 Porosity, fission product, and crack distribution plots from FIB-SEM tomography of irradiated buffer .....	261
<b>References .....</b>	<b>263</b>

## Figures

Figure 1-1: Investigating the process-structure-property relations of materials exposed to the extreme environments of high-velocity impact (left) and irradiation (right).....	3
Figure 2-1: Synthesized micro- and nanocubes .....	9
Figure 2-2: TRISO particle sample preparation.....	13
Figure 2-3: Micropillar fabrication process using a FIB .....	14
Figure 2-4: TEM lamella preparation with a FIB .....	17
Figure 2-5: High velocity impact testing .....	18
Figure 2-6: Hysitron PI85 SEM Picoindenter.....	20
Figure 2-7: Compliance correction applied to microcompression data .....	23
Figure 2-8: Peak deconvolution of the Raman spectrum with peaks identified .....	27
Figure 2-9: Reindexing Kikuchi patterns.....	29
Figure 2-10: Methods for estimating GND density .....	35
Figure 2-11: FIB-SEM tomography .....	37
Figure 2-12: Image processing and data analysis .....	41
Figure 2-13: Molecular statics simulation geometry .....	43
Figure 2-14: Data from literature used for parameter determination.....	51
Figure 2-15: Parameter fitting to bulk polycrystal silver stress-strain data at different temperatures, strain rates, and average grain size .....	53
Figure 2-16: Seed generation algorithm .....	59
Figure 2-17: Using experimentally defined GND density distributions in the simulations .....	61
Figure 2-18: Crystal plasticity simulations of [110]-impacted samples with analysis of different methods used to represent the grain size effect .....	63

Figure 3-1: Quasi-static compression response of an Ag microcube .....	72
Figure 3-2: Post-compression microstructure immediately after the massive strain-burst.....	73
Figure 3-3: Stochastic deformation nature.....	75
Figure 3-4: Effects of FIB milling on the mechanical response .....	76
Figure 3-5: Dislocation nucleation mechanisms revealed through molecular statics simulations	79
Figure 3-6: Size effect on yield strength:.....	81
Figure 3-7: Distinct deformed geometries depending on strain rate: .....	87
Figure 3-8: Phase transformation in [100]-impacted Ag microcube .....	89
Figure 3-9: Structural evolution of [100]-impacted cube found in MD simulations.....	92
Figure 3-10: Nanostructure of impacted microcubes.....	95
Figure 3-11: Nanostructural characterization of uncompressed pillars .....	98
Figure 3-12: No phase transformation in [110] impacted sample .....	101
Figure 3-13: Nanostructural evolution of [100] and [110] impacted nanocubes.....	104
Figure 3-14: LIPIT on single crystal Ag cubes and substrates .....	106
Figure 3-15: TKD scans beneath impact craters.....	108
Figure 3-16: Distributions of nanostructural features below impact craters.....	111
Figure 3-17: Impact-induced nanostructural evolution in single crystal microcubes and substrates .....	113
Figure 3-18: High-velocity impact of the [111] Ag substrate.....	117
Figure 3-19: Microcompression testing of single crystal and impacted samples .....	120
Figure 3-20: Engineering stress-strain curves from microcompression tests .....	123
Figure 3-21: Synthetic microstructures based on experimental data .....	127

Figure 3-22: Comparison of mechanical responses obtained through experiments and simulations .....	130
Figure 3-23: Heterogeneous deformation .....	132
Figure 3-24: Heterogeneous deformation induced strengthening .....	134
Figure 3-25: Multiaxial stress and strain states along the sample heights .....	137
Figure 3-26: Average mechanical properties of impacted samples compared to single crystal samples.....	139
Figure 3-27: Synergistic improvements in strength and toughness .....	141
Figure 3-28: Mechanical performance of samples selected for further nanostructural characterization .....	143
Figure 3-29: Nanostructural changes due to quasistatic compression of a [110]-impacted sample .....	145
Figure 3-30: Nanostructural changes in [110] samples tracked through CP simulations.....	148
Figure 3-31: Nanostructural changes due to quasistatic compression of a [100]-impacted sample .....	150
Figure 3-32: Nanostructural changes in [100] samples tracked through CP simulations.....	152
Figure 3-33: Nanostructural changes due to quasistatic compression of a [111]-impacted sample .....	154
Figure 3-34: Nanostructural changes in [111] samples tracked through CP simulations.....	156
Figure 3-35: Impact orientation-dependent plasticity mechanisms .....	158
Figure 4-1: FIB-SEM tomography on TRISO particles .....	167
Figure 4-2: Porosity distribution along buffer layer thickness .....	171
Figure 4-3: Pore size distribution.....	172



Figure 4-4: Pore size distribution across buffer thickness .....	174
Figure 4-5: Pore shape distribution.....	176
Figure 4-6: Pore orientation distribution.....	178
Figure 4-7: Porosity heterogeneity between particles.....	182
Figure 4-8: Pore shape and orientation .....	183
Figure 4-9: Super-elasticity of pyrocarbon buffer .....	185
Figure 4-10: Compression of buffer micropillars in the radial and tangential directions.....	188
Figure 4-11: Microstructural features dictating buffer response to irradiation.....	190
Figure 4-12: Irradiation conditions of the AGR-2 experiment's fuel compacts.....	194
Figure 4-13: FIB-SEM tomography of irradiated buffer layer .....	197
Figure 4-14: FIB-SEM tomography data from a Capsule 6 particle (low temperature and fluence) .....	200
Figure 4-15: FIB-SEM tomography data from a Capsule 5 particle (low temperature and high fluence) .....	202
Figure 4-16: FIB-SEM tomography data from a Capsule 2 particle (high temperature and fluence) .....	204
Figure 4-17: Porosity distribution in the buffer layers of a deconsolidated as-fabricated particle compared to a surrogate TRISO particle .....	206
Figure 4-18: Average and standard deviation in porosity separated by sample set.....	208
Figure 4-19: Radial fracture depending on irradiation conditions.....	209
Figure 4-20: Buffer densification accommodated through changes in microporosity .....	211
Figure 4-21: Sample preparation for Raman spectroscopy.....	213
Figure 4-22: ID/IG ratio analysis of an unirradiated buffer sample .....	216

Figure 4-23: ID/IG ratio analysis of a buffer cross-section from a Capsule 6 particle (low temperature and fluence).....	218
Figure 4-24: ID/IG ratio analysis of a buffer cross-section from a Capsule 5 particle (low temperature and high fluence) .....	219
Figure 4-25: ID/IG ratio analysis of a buffer cross-section from a Capsule 2 particle (high temperature and high fluence) .....	220
Figure 4-26: GFWHM measurements of an unirradiated sample.....	221
Figure 4-27: GFWHM measurements of a buffer sample from a Capsule 6 particle.....	222
Figure 4-28: GFWHM measurements of a buffer sample from a Capsule 5 particle.....	223
Figure 4-29: GFWHM measurements of a buffer sample from a Capsule 6 particle.....	223
Figure 4-30: Average crystallite size (a) and $G_{FWHM}$ (b) for each sample .....	224
Figure 4-31: Bright field TEM images of the buffer close to the kernel within a Capsule 6 particle .....	226
Figure 4-32: Dependence of micro and nanostructural changes on the irradiation conditions ..	229
Figure 5-1: Summary of key findings from Research Thrust I.....	233
Figure 5-2: Summary of key findings from Research Thrust II .....	235

## Tables

Table 2-1: Averages and standard deviations of layers in TRISO surrogate particles compared to uranium containing AGR-2 particles .....	10
Table 2-2: Optimized gains used for displacement-controlled tests .....	21
Table 2-3: Expressions used to define the variables in equations (2-26) and (2-27); variables given in these expressions are defined in Table 2-4 or in the equations above .....	50

Table 2-4: Material parameters for single crystal plasticity model .....	52
Table 3-1: Details for simulation samples .....	125
Table 4-1 Porosity characterization plan using FIB-SEM tomography.....	167
Table 4-2: Experiment matrix designed to investigate the irradiation-induced changes in the buffer layer's micro- and nanostructure .....	195

# *Chapter 1. Introduction*

## **1.1 Research objectives**

My research focuses on understanding the process-structure-property relations of materials exposed to the extreme environments of high-velocity impact and irradiation. Two main research thrusts are explored: *I) Improving mechanical properties through impact-induced nanostructural evolution of initially single crystal metals*, and *II) Investigating the fracture and densification behavior in the pyrocarbon buffer layer of TRISO nuclear fuel particles*. Several objectives are identified for each research thrust, which provide a fundamental understanding of the process-structure-property relations. An overview of the process-structure-property relations in each research study is presented in Figure 1-1.

### *1.1.1 Research Thrust I: Improving mechanical properties through impact-induced nanostructural evolution of initially single crystal metals*

In the first research thrust, single crystal silver samples are deformed through high-velocity microprojectile impact testing. The nanostructural evolutions that occur during impact and their subsequent effects on the mechanical properties are studied in detail. In order to achieve a fundamental understanding of the process-structure-property relations of these materials, four main research objectives are proposed:

- I-1. Determine the rate-dependence on the plasticity of silver single crystals through investigating the two distinct strain-rate regimes of quasi-static compression and high velocity impact.

- I-2. Determine the roles that the shock conditions, the free surfaces, and the crystallographic orientations play on the impact-induced nanostructural evolution.
- I-3. Investigate the effects of impact-induced nanostructural evolution on the resultant mechanical properties.
- I-4. Obtain a mechanistic understanding of heterogeneous deformation induced strengthening.

*1.1.2 Research Thrust II: Investigating the fracture and densification behavior in the pyrocarbon buffer layer of TRISO nuclear fuel particles*

In the second research thrust, we study the irradiation-induced fracture and densification behavior of the porous pyrocarbon buffer layer in TRISO nuclear fuel particles. Extensive micro and nanostructural characterization of unirradiated and irradiated particles provides key insights into the effects of structural heterogeneity and irradiation conditions on the fracture and densification behavior. To gain a fundamental understanding of the process-structure-property relations in this material, a few main objectives are proposed:

- II-1. Examine the heterogeneity in the synthesized buffer microstructure, and its potential effects on the fracture and densification behavior.
- II-2. Obtain a mechanistic understanding of the anisotropic mechanical behavior, including the effects of structural heterogeneity within the buffer layer.
- II-3. Investigate the irradiation-induced micro and nanostructural changes and their contribution to the densification and fracture behavior.
- II-4. Determine the effects of temperature and fast neutron fluence on the structural changes.

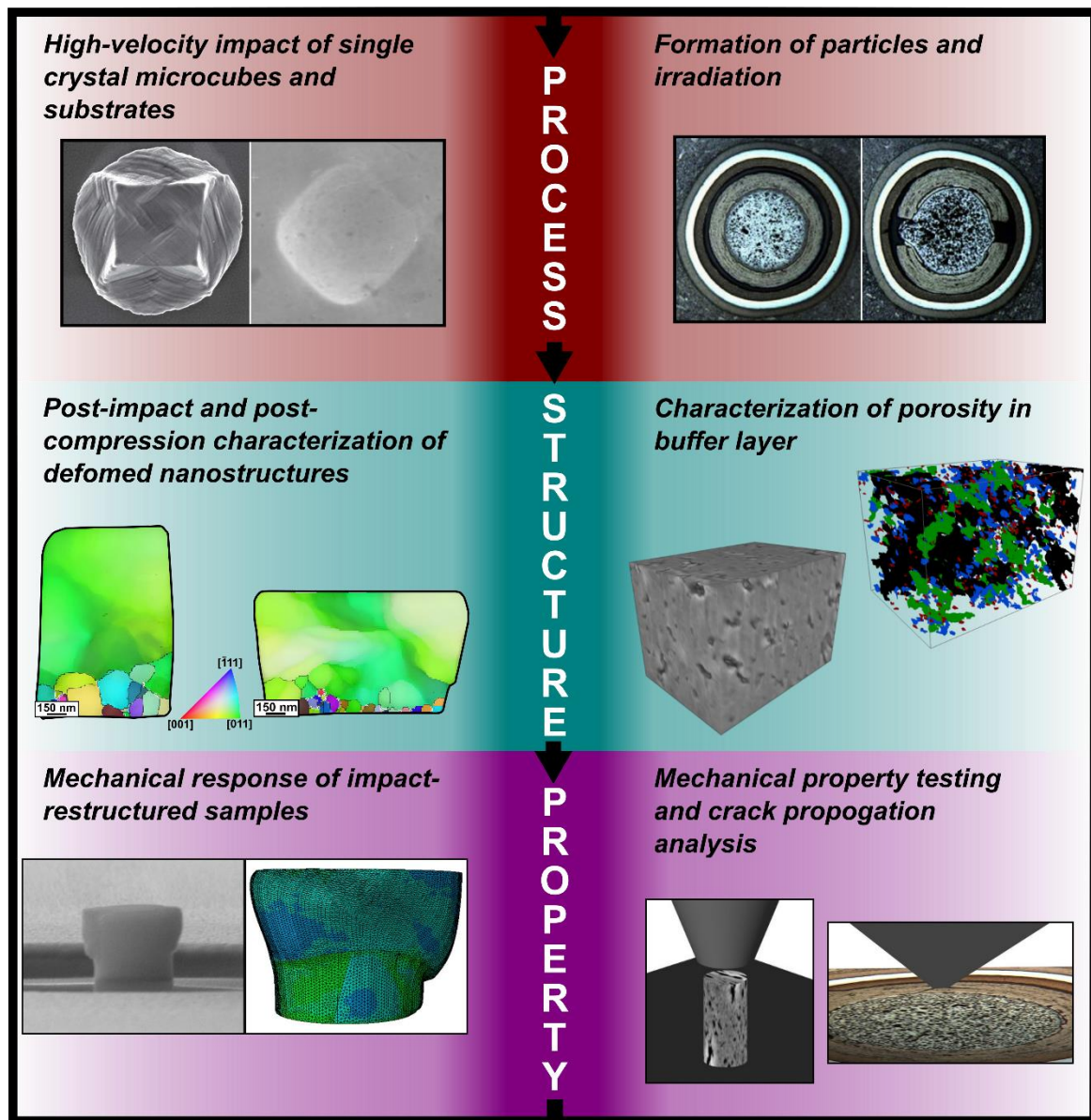


**Figure 1-1: Investigating the process-structure-property relations of materials exposed to the extreme environments of high-velocity impact (left) and irradiation (right)**

## 1.2 Motivation for research

The US Department of Energy and Department of Defense have frequently reiterated the need for research into materials that can withstand extreme environments such as high strain-rates, extreme temperatures, and chemical extremes—among others [1]. Extreme environments such as these can induce dramatic structural changes which affect the mechanical properties, which in turn determine how the material can sustain continued stress. In order to design materials to withstand such extreme conditions, we need to understand the process-structure-property relations of the material.

With the advent of many new nanofabrication, nanostructural characterization, and nanomechanical testing methods, we can study fundamental process-structure-property relations governed by nanoscale plasticity mechanisms. What happens at the nanoscale can significantly affect the macroscale material properties and mechanical response. Conversely, the micro-, meso-, and macro-scale structures can also influence the plasticity mechanisms active on the nanoscale. Materials incorporating different structural features on each length scale, which synergistically improve the material's overall mechanical performance, are prevalent in nature—one example is the size-dependent heterogeneity of bones [2]. Recently, researchers have designed synthetic materials inspired by naturally occurring materials which incorporate structural heterogeneities spanning multiple length-scales [3–5].

Structural heterogeneity itself can either be an asset or a detriment to the mechanical performance of a material. For example, a new class of metals, termed heterogeneous nanostructured materials have shown great promise in synergistically improving mechanical properties such as strength and toughness [6]. The presence of different structural components

elicits complementary deformation mechanisms which improve the material's overall mechanical performance, well beyond the limits of their homogeneous components. However, if not incorporated carefully, localized heterogeneities or defects can result in suboptimal performance and even catastrophic failure. The potential for dramatically improved properties, with the risk of suboptimal performance if poorly designed, necessitates a fundamental understanding of the process-structure-property relations.

These three themes of extreme environments, structural length scales, and structural heterogeneity are common to the two research thrusts of this work which are presented in Chapter 3 and Chapter 4. In Chapter 3, I demonstrate the ability to tune the mechanical properties of silver through impact-induced heterogeneous nanostructures. Structural heterogeneities formed through extreme strain rate deformation elicit uncharacteristic plasticity mechanisms which provide synergistic enhancements in strength and toughness. In Chapter 4, I study the fracture and densification behavior of a porous pyrocarbon material designed to withstand extreme temperatures, pressures, and radiation damage during nuclear fission. The influence of different irradiation conditions on the buffer behavior are investigated through extensive micro- and nanostructural characterization. Additional background information for each research thrust is given in Section 3.1 and Section 4.1.

### **1.3 Organization and brief overview of thesis**

This section outlines the remainder of this thesis with brief descriptions of the content of each chapter.

*Chapter 2* describes the materials and methods used in this research. Silver single crystals are the primary material studied in Chapter 3, while the pyrocarbon buffer layer of TRISO nuclear



fuel particles is the material of interest in Chapter 4. Many of the same sample preparation, testing, and characterization methods are used in the various studies. Details about the computational methods used—molecular dynamics and statics simulations and crystal plasticity simulations—are also discussed.

*Chapter 3* presents our findings into the process-structure-property relations of impact-restructured single crystal metals. The objectives summarized in Section 1.1.1 are addressed.

*Chapter 4* presents our findings into the process-structure-property relations of the pyrocarbon buffer layer in TRISO nuclear fuel particles. The objectives summarized in Section 1.1.2 are addressed.

*Chapter 5* provides summaries of the key findings, contributions, and future work.

# *Chapter 2. Materials and Methods*

## **2.1 Materials**

### *2.1.1 Single crystal silver microcubes and substrates*

We chose silver as the model material to study the fundamental process-structure-property relations of heterogeneous nanostructured metals with enhanced properties formed through impact-induced nanostructural evolution. To study what roles the crystallographic orientation and free surfaces have on impact-induced nanostructural evolution, we study both the deformation of single crystal silver *microcubes* impacted onto a rigid substrate and the deformation of single crystal silver *substrates* impacted with spherical microprojectiles. Beginning with a pristine single crystal structure allows for a controlled study of the nanostructural changes that occur during impact. Besides being advantageous to our fundamental study, silver is often used in superconductors to shield the superconducting material and to provide mechanical strength and strain relief [7]. Thus, it is beneficial to know the mechanical properties of silver on a small scale and the deformation responses to quasi-static and dynamic loading.

Silver is a face-centered-cubic metal (space group:  $Fm\bar{3}m$ , No. 225,  $a=4.09 \text{ \AA}$ ) with high thermal and electrical conductivities, diamagnetism, high reflectance and low emittance [7]. As a face-centered-cubic material, dislocation-mediated plasticity occurs readily through slip on the twelve primary slip systems—combinations of the four  $\{111\}$  close-packed planes and three  $\langle 110 \rangle$  directions. Silver also has a low stacking fault energy, with a high propensity for twinning [8,9]. Although silver naturally has a face-centered-cubic (fcc) structure, rare hexagonal polytypes

(space group: P63/mmc, No. 194) have been found in nature [10] or synthesized [11–20]. The 4H hexagonal polytype of silver ( $a=2.88 \text{ \AA}$ ,  $c=10 \text{ \AA}$ ) with an ABCBA stacking sequence has been synthesized in nanorods (diameter  $\sim 10\text{--}100 \text{ nm}$ ) [13–15,20], nanoribbons [16] and bulk films [17–19]. The 2H hexagonal polytype of silver ( $a=2.83 \text{ \AA}$ ,  $c=6.38 \text{ \AA}$ ) with ABA stacking sequence has also been synthesized [17,19] using electrochemical deposition, though it is extremely rare due to its highly metastable nature and as it can spontaneously transform to the fcc phase at room temperature [18]. The 4H phase is more stable than the 2H phase, but it also undergoes electron-beam-radiation-induced [15] and thermally-induced [18] phase transformations from 4H to 3C.

Single crystal Ag substrates were purchased from MTI corporation. Three substrates with surface normal directions of  $\langle 100 \rangle$ ,  $\langle 110 \rangle$ , and  $\langle 111 \rangle$  were selected to study the dependence of the crystallographic orientation on impact-induced recrystallization. The substrates are 99.999% pure silver, 0.5 mm thick, have a surface roughness of  $<30 \text{ \AA}$ , and the orientations are precise to  $\pm 2^\circ$  [21].

We synthesized Ag micro/nano-cubes using a bottom-up seed-growth process [22,23] that results in a large quantity of monodispersed single-crystals (Figure 2-1). The 100 nm cubes are initially synthesized with near-perfect cubic geometry [22], having slightly rounded or truncated vertices (Figure 2-1(c)). These nanocubes can be grown into larger cubes by performing additional synthesis steps [23]. The first seed growth step produces nanocubes with ~400-500 nm sides, and an additional seed growth step produces microcubes (1000-2000 nm, Figure 2-1(a)). The microcubes have much sharper edges and corners with radius of curvature to edge length ratios ( $r_e$ ) of  $0.023 \pm 0.003$ , compared to  $0.138 \pm 0.012$  for the ~100 nm sized nanocubes (Figure 2-1(b-c)). STEM analyses characterize the as-synthesized cube's internal structure. Selected area diffraction (SAD) reveals a perfect fcc single-crystal structure (Figure 2-1(d)). The high-resolution STEM images show a pristine fcc structure, free of any dislocations—as in the representative image shown in Figure 2-1(e). This synthesis process yields pristine single crystal Ag microcubes which are monodispersed and not substrate bound, allowing them to be used in microprojectile impact tests and study the resultant nanostructure and properties.

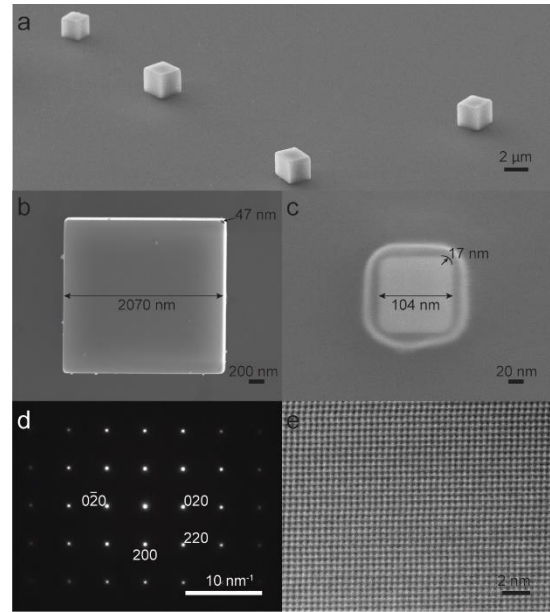


**Figure 2-1: Synthesized micro- and nanocubes** (a) dispersed ~2 μm cubes (b) ~2 μm cube with 47 nm edge radius of curvature, (c) ~100 nm cube with 17 nm edge radius of curvature, (d) SAD pattern showing single-crystal fcc structure, (e) HRTEM image showing defect-free structure.

### 2.1.2 Tristructural Isotropic (TRISO) coated nuclear fuel particles

As part of the DOE's Advanced Gas Reactor Fuel Development and Qualification Program, tristructural isotropic (TRISO) coated fuel particles have been developed as a high-

performance fuel for High Temperature Gas-cooled Reactors (HTGRs) [24]. The TRISO coating surrounds a spherical kernel containing uranium and is designed to retain the fissile by-products caused by irradiation. A fluidized bed chemical vapor deposition coating furnace is used to apply the layers of the coating [25]. Surrounding the kernel is a multilayered shell consisting of a porous pyrocarbon buffer layer, a dense inner pyrolytic carbon layer (IPyC), a silicon carbide layer (SiC), and dense outer pyrolytic carbon (OPyC) layer.

Surrogate TRISO fuel particles, with a zirconium core replacing the uranium-bearing kernel, are fabricated in a similar fashion to produce representative TRISO particles that can be studied outside of the confines of the national labs and safety protocols necessary for handling uranium containing particles. The surrogate particles have a nearly identical structure as the AGR-2 particles with a UCO kernel (Table 2-1). Microstructural characterization and mechanical testing were performed on surrogate particles (batch ZRX05-26T) at UW Madison.

**Table 2-1:** Averages and standard deviations of layers in TRISO surrogate particles compared to uranium containing AGR-2 particles

Property	ZrO <sub>2</sub> surrogate particles	AGR-2 fuel particles [26]
Kernel diameter (μm)	400.5 (14.1)	426.7 (8.8)
Average buffer thickness (SD) [μm]	104.5 (6.3)	98.9 (8.4)
Average IPyC thickness (SD) [μm]	39.3 (1.9)	40.4 (2.5)
Average SiC thickness (SD) [μm]	34.4 (0.9)	35.2 (1.2)
Average OPyC thickness (SD) [μm]	40.4 (2.5)	43.4 (2.9)

Microstructural characterization was also performed on irradiated TRISO particles with UCO kernels at Oak Ridge National Laboratory. These particles were irradiated for a total of 559.2 effective full power days in the Advanced Test Reactor at Idaho National Laboratory from June 2010 to October 2013 [26]. This was the second irradiation experiment carried out as part of the

Advanced Gas Reactor Fuel Development and Qualification Program and is referred to as the AGR-2 irradiation experiment. The TRISO layers are exposed to extreme temperatures and fast neutron fluences resulting from nuclear fission: the time average volume average (TAVA) temperature ranges from 1032°C – 1252 °C, the burnup ranges from 9.3% – 12.2% fissions per initial metal atom (FIMA), and the corresponding fast-neutron fluence ranges from 2.39 – 3.35  $\times 10^{25}$  n/m<sup>2</sup>. After completion of the experiment, the particles are deconsolidated from the graphitic compacts and mounts are prepared for post-irradiation examination (PIE) microscopy.

## **2.2 Sample preparation/fabrication**

### *2.2.1 Preparation of Ag microcubes for testing and characterization*

To prepare the Ag microcubes for imaging, fabrication, or testing, the cubes are dispersed on a substrate. A silicon substrate adhered to an SEM stub is used for quasi-static compression or FIB-fabrication, while the samples are dispersed on the specially designed launch pad (Section 2.3.1) for high-velocity impact testing. To ensure the cubes are monodispersed, the silver cube solution is diluted with ethanol in an approximately 1:10 ratio. The closed vial of diluted microcube solution is placed on a vortex mixer for ~2-4 min to ensure uniform dispersion of the particles. For the nanocubes, a sonicator is used instead for ~10 min to break up the cubes. There is also a thin (2-5 nm) polyvinylpyrrolidone (PVP) coating on the Ag cubes which helps to prevent agglomeration. Approximately 2-4  $\mu$ l of the well-mixed solution is pipetted onto the substrate and covered with an optical lens tissue to aid in dispersion until the ethanol evaporates.

### 2.2.2 *Mounting, grinding, and polishing TRISO particles*

Sample preparation methods were established based on [27,28], and sample preparation supplies purchased from Struers Inc. and Allied High Tech Products Inc. The sample preparation procedure is as follows: i) ~7-10 surrogate TRISO particles (~1 mm in diameter, shown in Figure 2-2(a)) are arranged in a hexagonal array on a small piece of double sided tape adhered to the bottom of a 1.25 in mounting cup, ii) Epofix epoxy is mixed according to package instructions and poured into the mounting cup, iii) epoxy is cured at room temperature until hard (~1 day) and puck removed from mounting cup, iv) particles are ground to approximately midplane using alcohol-based 6  $\mu\text{m}$  diamond suspension on a Struers MD-Allegro pad with Struers Blue DP-Lubricant (~400 rpm, ~30 min), v) particles are polished using alcohol-based 3  $\mu\text{m}$  diamond suspension on a Struers MD-Dac pad with lubricant (~300 rpm, ~4 min), vi) particles are polished using alcohol-based 1  $\mu\text{m}$  diamond suspension on a Struers MD-Plan pad with lubricant (~200 rpm, ~8 min), vii) particles are polished using 0.05  $\mu\text{m}$  colloidal silica solution on a Struers MD-Chem pad (~200 rpm, ~15 min), viii) particles are polished using 0.02  $\mu\text{m}$  colloidal silica solution on a Struers MD-Chem pad (~200 rpm, ~10 min), ix) puck is placed in deionized water, sonicated for ~1 min, rinsed in isopropanol alcohol, and dried. For all separate grinding/polishing steps, a different pad is used. The sample is rinsed between steps and progress is checked using an optical microscope. The puck is then prepared for electron microscopy by depositing a thin layer of gold to create a conductive pathway to the SEM stub which is attached to the bottom using copper tape. To create a better conductive pathway for reducing charging artifacts, pieces of copper tape are also placed from the bottom to top of the puck and around the TRISO particles (Figure 2-2(b)). See Figure 2-2(c) for an SEM image of the particles ground and polished to midplane.

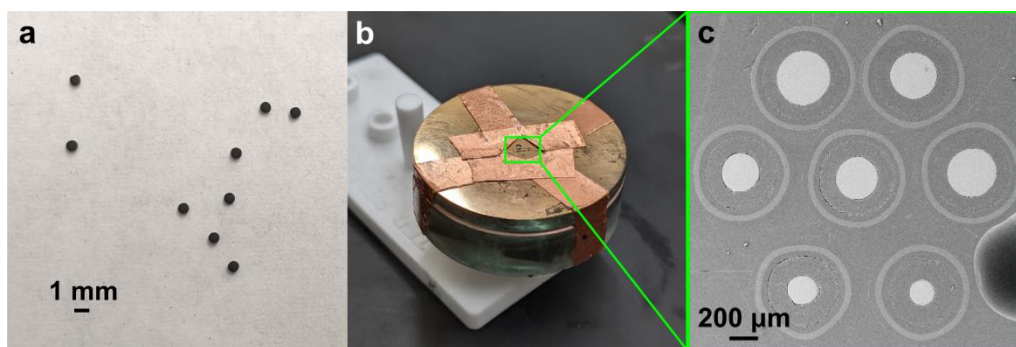


**Figure 2-2: TRISO particle sample preparation** (a) individual surrogate TRISO particles, ~1 mm in diameter, (b) TRISO particles mounted in epoxy puck and ground and polished to midplane; puck prepared for electron microscopy, (c) SEM image of TRISO particles fixed in epoxy puck shown in (b).

### 2.2.3 Fabrication of pillars with a focused ion beam (FIB)

Micropillars for in situ SEM microcompression testing were fabricated using a focused ion beam (FIB). The Zeiss Auriga FIB at the Wisconsin Centers for Nanoscale Technology along with an integrated Nanopatterning and Visualization Engine (NPVE) software were used to set the mill parameters.

To prepare pillars from the as-synthesized Ag microcubes which are monodispersed on a silicon substrate, several mill operations are performed at 54° stage tilt, where the substrate surface is perpendicular to the ion beam. Micropillars with both square and circular cross sections were milled from the as-synthesized cubes to study the effect of external sample shape on the mechanical response. To make a square cross-sectional pillar, rectangular mill shapes were positioned along the edges of the cube to sequentially mill off each edge (Figure 2-3(a)). The thickness of the mill shape was prescribed depending on the final desired size of the pillar. A 30 keV voltage, 50 pA current ion beam was typically used for about 30 seconds with two passes per edge. To make the circular cross-sectional pillars (Figure 2-3(b)), annular mill shapes with progressively smaller internal diameters milled with progressively smaller ion currents were used



to form pillars with a final desired diameter, minimal taper, and low ion beam damage. Typically, three mill operations were performed, with the first mill step (Figure 2-3(b-1)) conducted at a relatively higher current of 300-600 pA and the current reduced for each sequential mill step down to 50 pA for the final mill step (Figure 2-3(b-3)). The low 50 pA current for the final mill step results in a less tapered pillar with minimal ion beam damage [29,30], since the beam is more directed and has a minimal “skirt” to its Gaussian profile.

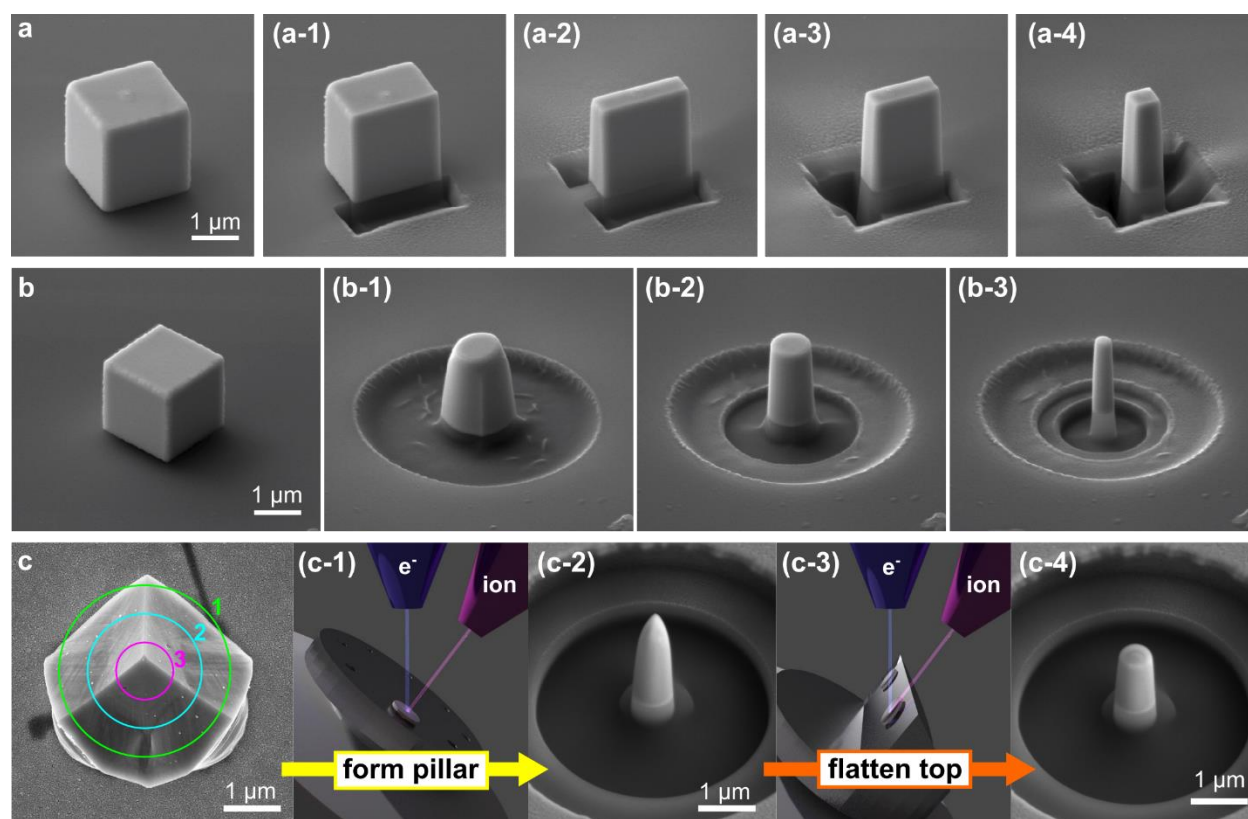


**Figure 2-3: Micropillar fabrication process using a FIB** (a) process to make pillars with square cross sections from single crystal microcubes, (b) process to make circular pillars from single crystal microcubes, (c) process to create circular pillars from impacted cubes.

Micropillars were also fabricated from impacted Ag microcubes (Figure 2-3(c)), using a similar procedure as outlined above for making the circular cross-sectional pillars from the as-synthesized microcubes. However, due to the uneven topography of the impacted cubes, an

additional mill step is required to flatten the surface. To form micropillars of  $\sim 1\ \mu\text{m}$  in diameter from the impacted cubes, the following milling operations are typically performed: i) an annular mill shape with an outer diameter of  $7\ \mu\text{m}$  and inner diameter of  $3\ \mu\text{m}$  (Figure 2-3(c), green - 1) is aligned over the impacted cube, and milled at 30 kV, 300 pA for  $\sim 2$  min, ii) a second annular mill shape with an outer diameter of  $5\ \mu\text{m}$  and inner diameter of  $2\ \mu\text{m}$  (Figure 2-3(c), cyan - 2) is milled at 30 kV, 140 pA for  $\sim 2.5$  min, iii) a third annular mill shape with an outer diameter of  $3\ \mu\text{m}$  and inner diameter of  $1\ \mu\text{m}$  (Figure 2-3(c), magenta - 3) is milled at 30 kV, 50 pA for  $\sim 3$  min. These operations are performed while the sample is fixed to a flat stage and the stage is tilted  $54^\circ$  to the coincidence point (Figure 2-3(c-1)) where top view of the sample is seen in the FIB image (milling perpendicular to the substrate surface). After the pillar has been formed (Figure 2-3(c-2)), the top of the pillar must be flattened so that uniform contact can be made with the flat indenter during uniaxial compression testing. To execute this step, the sample is removed from the chamber and fixed to a  $90^\circ$  pre-tilt stage. The stage is tilted to  $54^\circ$  again and the coincidence point set, so that now the substrate surface is parallel to the ion beam (Figure 2-3(c-3)): with this geometry, the top of the pillar can be milled using a 30 kV, 50 pA ion beam, just until the top surface is flat (Figure 2-3(c-4)).

Only the fabricated micropillars which pass a strict set of quality control parameters are compressed using the in-situ SEM nanoindenter (Section 2.3.3). A taper will affect the elastic and plastic response since the stress field is not uniform as in a perfectly straight pillar with no taper [31]. Additionally, pillars with high aspect ratios ( $>5$ ) may buckle [32]. Therefore, only pillars with taper angles of  $<4^\circ$  (typically  $\sim 2^\circ$ ) and aspect ratios (height/diameter) of 1-3 are selected for further testing. Additionally, for accurate microcompression testing, uniform contact between the substrate and sample and sample and indenter is desired. Since the cubes are impacted onto the

substrate and deformed, perfect contact between the sample and substrate is unlikely. However, to mitigate these effects as much as possible, a layer of gold is deposited on the silicon substrate and any samples which are clearly tilted off the substrate are not tested.

#### 2.2.4 *Fabrication of electron transparent lamella with a FIB*

For high-resolution nanostructural characterization techniques such as transmission electron microscopy (Section 2.4.2) and transmission Kikuchi diffraction (Section 2.4.4), ultra-thin electron transparent lamella must be prepared using a FIB. The typical procedure used to create a TEM lamella is as follows: i) the sample is first coated in a thin layer of platinum using electron beam deposition (~5-10 min) to prevent damage to the sample (Figure 2-4(a)), ii) a thick layer of Pt is then deposited using the ion beam (~2-3  $\mu\text{m}$  thick), iii) with the ion beam oriented  $\pm 3^\circ$  to the sample surface normal ( $54^\circ$  tilt), trenches are milled on either side of the sample (Figure 2-4(b)), typically at 30 kV, 12 nA with a  $45^\circ$  slope down to 10-15  $\mu\text{m}$  depth, iv) sides are milled further at 2 nA until cross section measures ~1-2  $\mu\text{m}$ , v) the sample is tilted to  $0^\circ$  and the micromanipulator is inserted and fixed to the side of the sample using Pt deposition, vi) cuts are made on the sides and under the sample to free the sample from the substrate (typically done at 1 nA), vii) the sample is lifted out using the micromanipulator controls (Figure 2-4(c)), the FIB half-grid brought into view, and the sample aligned and welded to the grid using Pt deposition (Figure 2-4(d)), iix) the stage is tilted to  $54^\circ \pm 2^\circ$  for thinning at 1 nA down to 300 pA until the sample is ~300-500 nm thick, ix) the stage is tilted to  $54^\circ \pm 1^\circ$  for thinning at 140 nA down to 50 pA until the sample is ~100 nm thick, x) the stage is tilted to  $54^\circ \pm 3^\circ$  for final polishing of the sample using a 5 kV, 100 pA beam. This procedure is not followed exactly for every sample. It has been developed as a guide for repeatedly creating high quality lamellas, based on resources [29,33,34]

and experience. However, each sample is unique, and this process is incredibly tedious, time consuming, and fallible; the path to success has been trial and error and experience.

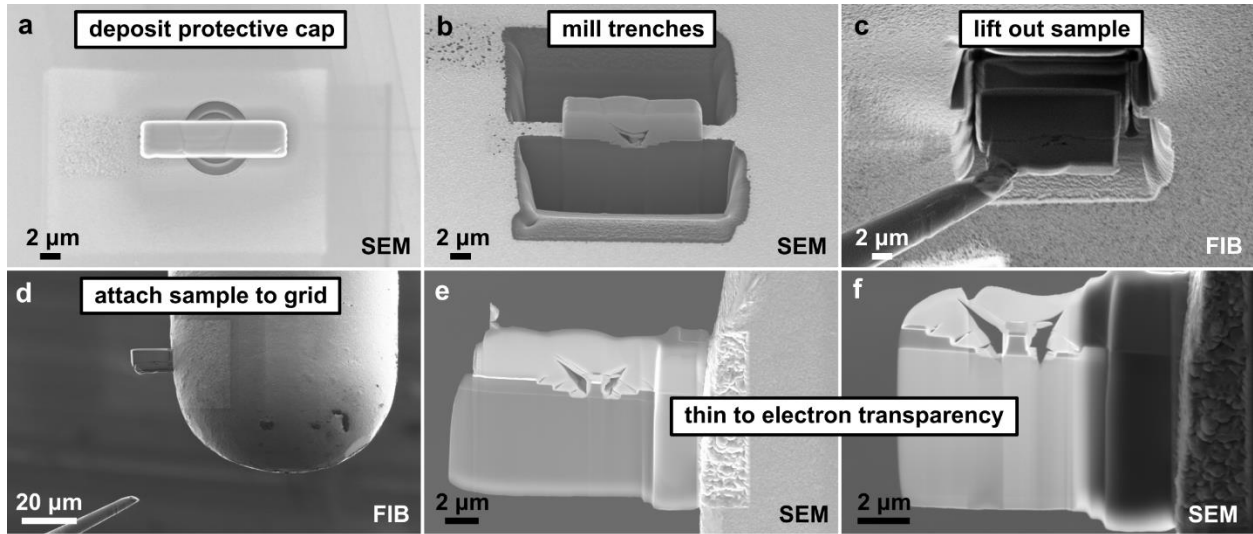


**Figure 2-4: TEM lamella preparation with a FIB** (a) Pt protective cap deposited on sample, (b) trenches made to prepare for lift out, (c) sample is cut free from substrate and lifted out with the micromanipulator, (d) sample is attached to Cu FIB half grid, (e) intermediate sample thinning, (f) final lamella thinned to electron transparency.

## 2.3 Testing apparatus

### 2.3.1 High-velocity impact using a LIPIT apparatus

We use an advanced laser-induced projectile impact testing (LIPIT) apparatus [35,36] to perform high-velocity impact tests on both single crystal Ag microcubes and substrates. The LIPIT apparatus is composed of four main components: the laser, a launch pad, the target, and a multi-exposure imaging system (Figure 2-5). The launch pad is made by depositing a 60 nm layer of gold (Au) on a glass substrate and then spin coating a  $\sim 20\ \mu\text{m}$  crosslinked polydimethylsiloxane (PDMS) layer at 1500 rpm. The Ag microcubes are then drop casted onto the launch pad. A single pulse of the Nd:YAG ablation laser ( $\lambda=1064\ \text{nm}$ ) ablates the Au layer, which causes the rapid formation of a bubble in the PDMS layer. A single microcube aligned with the laser ablation site

is launched by the expanding bubble in the PDMS layer. The PDMS layer prevents sample heating from the laser ablation of Au, in addition to launching the projectile. The microcube hits the target (a silicon substrate coated with ~100 nm gold film) at high velocity. The speed of the projectile is calculated based on the in-flight image of the projectile taken using our custom-built multi-exposure imaging system (Figure 2-5 (b)). This system is composed of a monochromatic camera gated by an acoustic-optic modulator and illuminated by a supercontinuum white laser with a tuneable laser pulse interval.

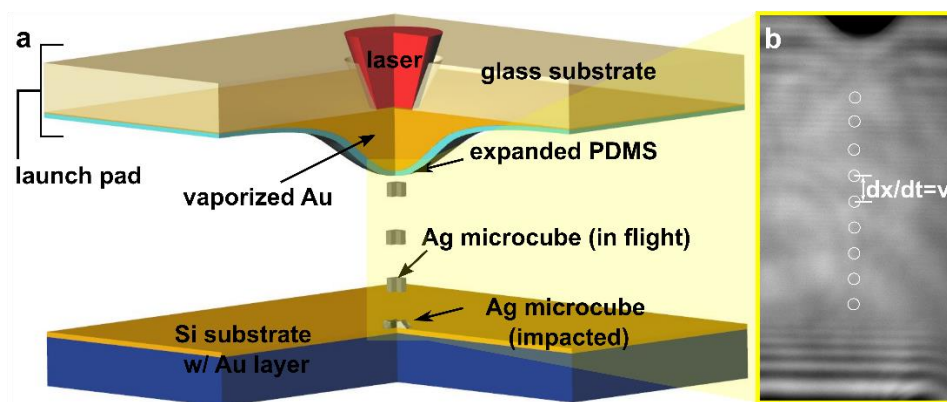


**Figure 2-5: High velocity impact testing** (a) schematic of LIPIT apparatus used to impact single crystal silver microcubes, (b) image of microprojectile in-flight: distance between subsequent projectile locations and light pulse interval.

### 2.3.2 Nanoindentation

Ex-situ nanoindentation is performed using a Bruker Hysitron TI-950 Triboindenter at the Wisconsin Centers for Nanoscale Technology. Nanoindentation can be used to measure the hardness and elastic modulus of a material. We also perform nanoindentation testing on the buffer layer of TRISO particles to record the mechanical properties and investigate crack propagation mechanisms.

The diamond indenter geometry is selected based on the experiment—typically a Berkovich tip is used for hardness testing, and a spherical indenter is used to replicate the craters formed by microprojectile impact testing but at quasi-static strain rates. Samples are adhered to stiff magnetic chips which stick to the sample stage to ensure the sample does not move during testing and the tested sample is much more compliant than anything else. Once loaded, several calibrations are performed, including a transducer calibration and tip-to-optics calibration. Tests are performed in either load-controlled or displacement-controlled mode, with parameters such as the load or displacement rates during loading and unloading and the max load or displacement defined. Specifics for each experiment are outlined in future sections. If hardness measurements are desired, the Oliver and Pharr method [37] is used to calculate the hardness—with a calibrated tip area function used to determine the projected area for a Berkovich indenter and the equations in [38,39] used to calculate the projected area for a spherical indenter.

### 2.3.3 *Quasi-static compression tests using an in-situ SEM nanoindenter*

We used a Hysitron PI85 SEM PicoIndenter (PI) (Figure 2-6) in a Zeiss/LEO 1530 SEM to perform uniaxial compression tests on Ag-cubes with *in-situ* visualization of the deformation. This experimental technique of placing a nanoindenter inside of an SEM was first developed by Greer et. al with their custom-built SEMentor device [40]. With the SEM, micrometer-sized samples can be easily identified and aligned under a flat diamond tip which is used to compress the samples. The sample deformation can be observed while the microcompression test is being performed and videos can be recorded to match deformation events with points of interest on the force displacement curve.

To prepare samples for testing, Ag cubes are dispersed onto a Si substrate by the method discussed in Section 2.2.1 and the substrate is adhered to an SEM stub with carbon paint. The SEM stub can be loaded onto the PI stage and is held by a set screw. The diamond tip is carefully cleaned with a cotton swab drenched in ethanol and then screwed onto the rod extending from the transducer (Figure 2-6(b)). The PI stage piece is slid onto the PI base and fastened once the sample is ~1 mm away from the tip (Figure 2-6(b)). The nanoindenter is slid

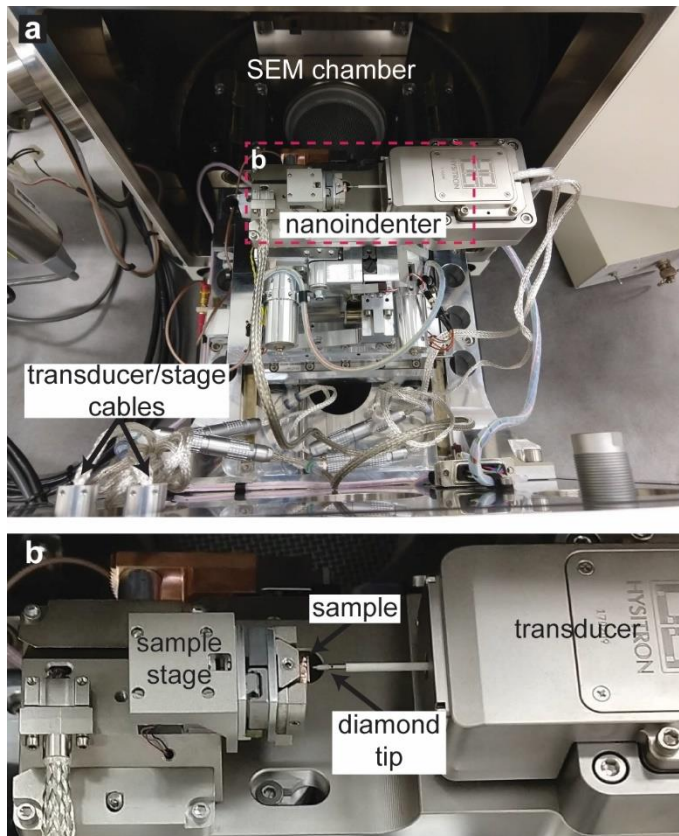


**Figure 2-6: Hysitron PI85 SEM Picoindenter** (a) PI loaded onto the SEM stage, (b) PI components.

into place on the SEM stage (Figure 2-6(a)), and the transducer and sample stage cables are connected to the ports on the SEM chamber door. The SEM door is closed, and chamber pumped.

After the chamber is pumped down, the stage is tilted to 5-10° so that the samples can be seen over the substrate edge. Then the tip and sample surface are brought into view and obtain a good SEM image. A calibration needs to be done to ensure the tip moves smoothly. A unique load function was prescribed for each sample depending on the sample dimensions. Samples were loaded with a constant strain rate of  $0.01 \text{ s}^{-1}$ . The sample dimensions were recorded before testing, including the height which was used to calculate the displacement rate equating to a  $0.01 \text{ s}^{-1}$  strain rate. The indenter was always kept out of contact with the sample surface prior to beginning the test to prevent any pre-damage to the sample.

Since the tests are run in displacement-controlled mode but the system is inherently load controlled, several gains are used in the feedback loop to translate between load and displacement given the prescribed displacement-rate. The displacement rate for each sample is determined by measuring the height of the sample from the SEM image and then calculating the displacement rate that equates to a 0.01/s strain rate. The gain tuning window on the Hysitron software is utilized to find appropriate gains which ensure the actual displacement stays as close as possible to the prescribed displacement-time function. After optimizing with several tests, the gain values in Table 2-2 were used for all tests. Displacement-time functions were set up with a loading segment mirrored by an unloading segment with the same magnitude of displacement-rate and change in displacement which were both customized based on the height of the sample. For some samples, an additional initial loading segment was added with a faster displacement rate to approach the sample faster before testing ensued. It was always ensured that the flat punch did not hit the sample before the test began at the desired displacement-rate.

**Table 2-2: Optimized gains used for displacement-controlled tests**

<b>Gain</b>	<b>Function</b>	<b>Value</b>
Proportional (P)	looks at where result is in relation to the desired result	0
Integral (I)	looks at where the actual result was in relation to the desired result	0.8
Derivative (D)	looks at where the actual result is going to be in relation to desired result	0
Lift Integral Gain (LIG)	controls tip when not in contact with the sample	0.07
Q-control	damps oscillations in a high vacuum environment	1

The data was analyzed using a custom-MATLAB code. The actual dimensions of the samples were calculated from the SEM image measurements based on the stage tilt angle and orientation of the sample. Force-displacement data was converted to engineering stress-strain data



using the original cross-sectional area and height of the sample. The yield stress for each sample was also measured. For samples which exhibited a strain burst (see Section 3.2), the yield point was obvious and directly picked off the graph. For samples with an indistinct yield point, a 0.5% strain offset method was used (0.2% offset not possible because of the scatter in data points).

Since the diamond tip and silicon substrate are much stiffer than silver, their deformation is expected to be negligible. However, a compliance correction was carried out to check this assumption. The total measured displacement contains the pillar deformation but also any other deformations in the system, including in the indenter and substrate. Sneddon developed the formula for calculating the deformation in an elastic half space material from a cylindrical punch [41]. Applied to this scenario, the total compliance of the diamond indenter and substrate is:

$$C_{Sneddon} = \frac{(1-\nu_{ind}^2)}{2E_{ind}(d_{top}/2)} + \frac{(1-\nu_{sub}^2)}{2E_{sub}(d_{base}/2)}, \quad (2-1)$$

where  $E_{ind} = 1141 \text{ GPa}$  (elastic modulus of diamond),  $\nu_{ind} = 0.07$  (Poisson's ratio of diamond),  $E_{sub} = 165 \text{ GPa}$  (elastic modulus of silicon),  $\nu_{sub} = 0.22$  (Poisson's ratio of silicon), and  $r_{base}$  and  $r_{top}$  are the radii at the base and top of the pillar, respectively. The deformation of the pillar is then:

$$\Delta x_{pillar} = \Delta x_{measured} - C_{Sneddon} F \quad (2-2)$$

However, for pillars FIB-fabricated from samples laying on a substrate, a portion of the pillar is the substrate material since the ion beam mills into the substrate. For example, the Ag microcubes are impacted onto a silicon substrate coated with a thin layer (~100 nm) of gold. The fabricated pillar then has three layers: Ag, Au, and Si (Figure 2-7(a)). All three layers contribute to the total deformation of the pillar. Each layer can be represented as a spring with stiffness  $k_i$ . The total deformation of the pillar is the sum of displacements from each spring in series:

$$\Delta x_{pillar} = F \left( \frac{1}{k_{Ag}} + \frac{1}{k_{Au}} + \frac{1}{k_{Si}} \right) \quad (2-3)$$

Equations (2-3) and (2-1) can be substituted into equation (2-2) to find the displacement of the Ag sample:

$$\Delta x_{Ag\ pillar} = \Delta x_{measured} - F \left( \frac{1}{k_{Au}} + \frac{1}{k_{Si}} + \frac{(1-\nu_{ind}^2)}{2E_{ind}(d_{top}/2)} + \frac{(1-\nu_{sub}^2)}{2E_{sub}(d_{base}/2)} \right) \quad (2-4)$$

where  $k_{Au} = \frac{E_{Au}\pi(d_{bottom}/2)^2}{h_{Au}}$  and  $k_{Si} = \frac{E_{Si}\pi(d_{base}/2)^2}{h_{Si}}$ .

The engineering stress and strain are then calculated as:

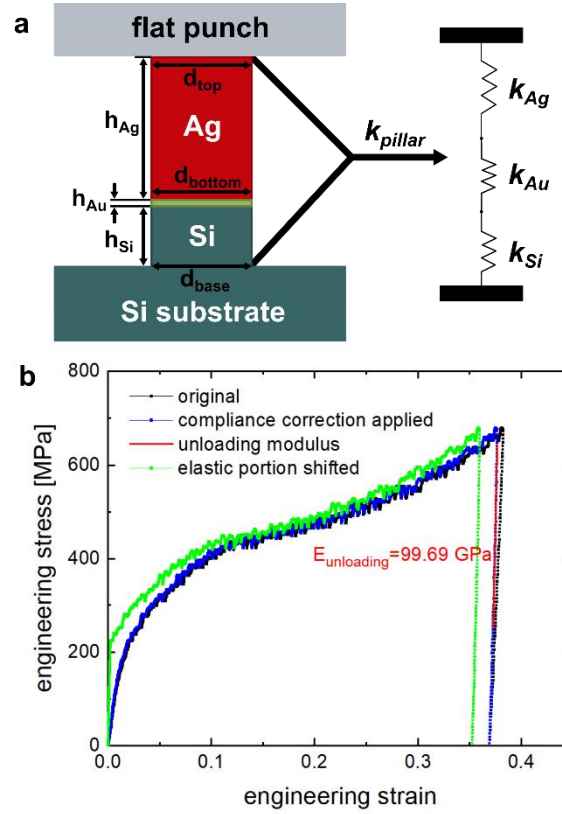


**Figure 2-7: Compliance correction applied to microcompression data** (a) left: all components contributing to measured displacement, right: effective stiffness of pillar is represented by three springs in series, (b) manipulations of original stress strain curve (black): compliance corrected (blue), shift of elastic portion to match unloading modulus (green).

$$\sigma = \frac{F-F_0}{\pi \left( \frac{d_{top}+d_{bottom}}{4} \right)^2}, \quad \varepsilon = \frac{\Delta x_{Ag \text{ pillar}}}{h_{Ag}} \quad (2-5)$$

All dimensions are labeled in (Figure 2-7(a)) and are measured from the SEM images taken before compression testing. Measurements are corrected for stage tilt.

The compliance corrected stress-strain curve (blue) is plotted with the original stress-strain curve (black) in (Figure 2-7(b)). The curve is shifted left slightly, as the true displacement values are slightly less than the measured displacement. However, as expected, the compliance in the system is very small compared to the deformation in the sample. The elastic modulus can be measured from the unloading portion of the compliance-corrected stress strain curve. If measured from the initial elastic portion of the stress-strain curve, an underestimate of the elastic modulus would be obtained. This is due to the inability to achieve perfect contact between the sample and indenter and sample and substrate upon loading, especially since some of the impacted samples are not perfectly flush with the substrate. To correct for this error, the elastic portion of the stress-strain curve can be shifted to match the elastic modulus calculated from the unloading curve. The yield point is found, and the strain values are manipulated as follows:

$$\text{for } \varepsilon < \varepsilon_{yield}: \varepsilon_s = \frac{\sigma}{E}; \quad \text{for } \varepsilon > \varepsilon_{yield}: \varepsilon_s = \varepsilon - \Delta \varepsilon_{yield} \quad (2-6)$$

The resultant stress-strain curve (Figure 2-7(b), green) is shifted farther left and the elastic modulus matches the unloading modulus. This manipulation of the stress-strain curve is beneficial for comparing experimental results to computational results from crystal plasticity simulations, since experimental errors associated with loading the sample are not present in the simulations.

## 2.4 Characterization methods

### 2.4.1 Scanning Electron Microscopy (SEM)

The scanning electron microscopes (SEM) at the Wisconsin Centers for Nanoscale Technology are used for characterization and analysis of all samples studied. The impacted Ag microcubes are imaged to identify the impact orientation and select samples for further testing. During quasi-static compression testing, *in-situ* SEM videos of the deformation are recorded so that interesting deformation events can later be correlated to points on the stress-strain curve. High resolution images of the final deformed geometry are also taken for further analysis. The SEM is also instrumental in being able to align the sample under the flat tip for uniaxial compression testing. When performing compression tests with the *in-situ* SEM nanoindenter, the SEM is usually operated at 25 kV, 8 mm working distance using the *SE2* detector for the best image quality. When imaging the impacted nanocubes at 0° tilt, the SEM is usually operated at 10 kV and 4 mm working distance using the *in-lens* detector for the best image quality. Additionally, an SEM is used in conjunction with the FIB to prepare samples for further testing and analysis (Sections 2.2.3-2.2.4) and to perform FIB-SEM tomography characterization (Section 2.4.5). With additional detectors, the SEM is also used to perform energy-dispersive x-ray spectroscopy (EDS) to attain chemical information and electron backscatter diffraction (EBSD) or transmission Kikuchi diffraction (TKD) to obtain crystallographic information (Section 2.4.4).

### 2.4.2 *Transmission Electron Microscopy (TEM)*<sup>1</sup>

The TEM specimens were analyzed in a FEI Titan Themis<sup>3</sup> Scanning/Transmission Electron Microscope (S/TEM) operated at 300 keV immediately after final polishing. We performed selective area diffraction (SAD) (~200 nm diameter probing area) to investigate the deformed nano/microstructure.

### 2.4.3 *Raman spectroscopy*

Raman spectroscopy is performed on the buffer layer of TRISO nuclear fuel particles to extract nanostructural information about the pyrocarbon in both unirradiated and irradiated samples. A Renishaw inVia confocal Raman microscope is used, which is located at ORNL and approved for the study of select radiological materials. This system provides a mapping feature in which Raman spectrum are acquired over a predetermined area at step sizes as small as ~1  $\mu\text{m}$ . This mapping feature was used to gather spatially dependent changes in the nanostructural features of unirradiated and irradiated buffer. Maps spanning the entire buffer layer thickness (~60 – 100  $\mu\text{m}$ ) and 10 – 20  $\mu\text{m}$  heights are obtained. A 532 nm laser is used at 10% power. Each spectrum is attained with an acquisition time of 15 s and 3 accumulations.

Post-processing of the spectrum data is accomplished using Renishaw's Wire 5.5 software. First, a background correction is applied using a fourth order polynomial and a noise tolerance of 1. Deconvolution of the Raman spectrum is accomplished through curve fitting of six first order and three second order peaks (peaks labeled in Figure 2-8). The labeled "D" peaks are disorder induced bands and are fitted with Gaussian curves. The labeled "G" peaks correspond to bands

---

<sup>1</sup> TEM of impacted silver cubes was done in collaboration with Sadegh Yazdi, who is currently a professor at the University of Colorado-Boulder. TEM of pyrocarbon was done in collaboration with Dr. J. David Arregui-Mena, at Oak Ridge National Laboratory.

originating from the graphitic structure and are fitted using Lorentzian curves. The remaining peaks are fitted using mixed Gaussian-Lorentzian curves.

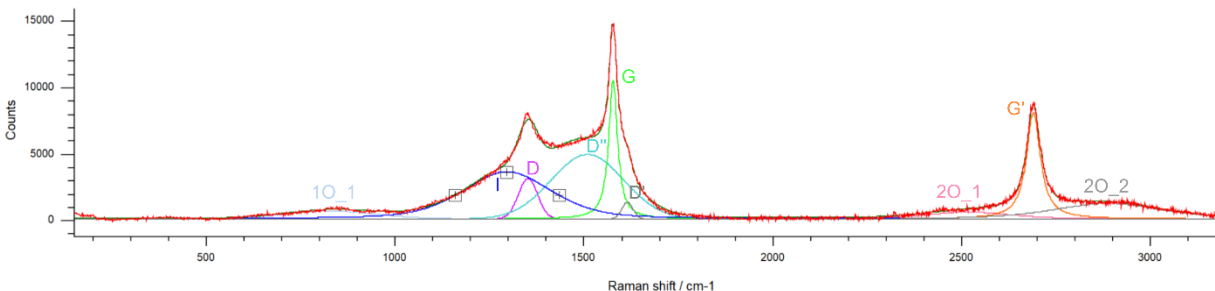


**Figure 2-8: Peak deconvolution of the Raman spectrum with peaks identified**

#### 2.4.4 Transmission Kikuchi Diffraction (TKD)

Transmission Kikuchi diffraction (TKD) is a structural characterization technique similar to electron backscatter diffraction (EBSD), but capable of achieving much finer spatial resolutions [42–44]. The same hardware and software used for EBSD can be used for TKD; the only key difference is that electrons are transmitted through a thin (~100 nm) lamella and structural information from the bottom of the lamella is captured with the detector in TKD, while structural information from electrons backscattered off a bulk sample surface is collected in EBSD. While the optimal spatial resolution for EBSD is ~50-100 nm [45,46], spatial resolutions of 2-10 nm are achievable using TKD [42,47,48]. The finer spatial resolution is due to the smaller interaction volume of electrons being transmitted through the specimen in TKD, rather than backscattered from near the specimen surface as in EBSD [42,43]. Since the smallest expected grain size in the impacted Ag microcubes is on the order of tens of nanometers [36,49], traditional EBSD is not capable of resolving the smallest grains and TKD must be used. Additionally, highly deformed materials often pose problems for traditional EBSD, as the Kikuchi patterns become blurred and are difficult to index near grain boundaries and areas with high dislocation density [46]; however,

the smaller interaction volume of TKD provides detailed information about the local changes in the lattice orientation, providing high quality maps of ultra-fine grained and highly deformed materials [44,50–54].

TKD is performed using the FEI Helios G4 PFIB at the Wisconsin Centers for Nanoscale Technology (WCNT). Although the ion beam is not used, this instrument is equipped with the fastest EBSD CCD camera available at WCNT and is configured to work well for TKD. Data acquisition is performed using the APEX for EBSD software by EDAX. Electron transparent lamellae are prepared from samples using the procedure in Section 2.2.4. The sample tilt, sample thickness, accelerating voltage and current, and grain size all affect the resolution and quality of the obtained Kikuchi patterns [47,48,53,55]. To ensure best results, lamellae are prepared with a uniform thickness of ~100 nm and polished at 5 kV to remove ion damage and smooth the surfaces. TKD is performed on the prepared lamellae immediately after final thinning and polishing to ensure no chemical reactions or problems with sample storage or transference could damage the sample. The FIB half grid with samples attached is mounted on a sample holder which allows for the transmission of electrons through the sample. The sample is tilted to 45° and brought up to a 4 mm working distance. Parameters such as the beam voltage and current, gain, and exposure are optimized for each sample; however, for the impacted Ag microcubes, typically a 30 kV, 3.2 nA electron beam is used, the gain is around 450-550, and the exposure is around 40-50. A square grid with a 10-20 nm step size and 2x2 binning is used. Depending on the settings, the camera typically operates at ~3 frames per second, with total acquisition time ranging from ~20-60 minutes. The crystallographic data file for fcc silver is read in for indexing.

The indexing results obtained during scanning are quite good for a highly deformed sample: for example, the scan in Figure 2-9(b) has a 58% indexing success rate (confidence

index>0.1), which is comparable to TKD results of severely deformed ultrafine-grained samples (indexing success rates of 56-60%) [53]. In these highly deformed samples, the strain and grain size gradients within the sample lead to variation in the quality of the patterns and resultant indexing solutions. For example, in the highly deformed nanograined region (nearest the substrate), the Kikuchi patterns are noisier (Figure 2-9(c)), leading to less reliable indexing. Several steps are taken to improve the quality of the data throughout the sample: i) reindexing of the raw data using the Neighbor Pattern Averaging with Re-indexing (NPAR) algorithm [56] available in OIM v8.6 software, ii) reduce noise through data processing filters in MTEX, iii) estimate pixel by pixel noise during dislocation density calculations.

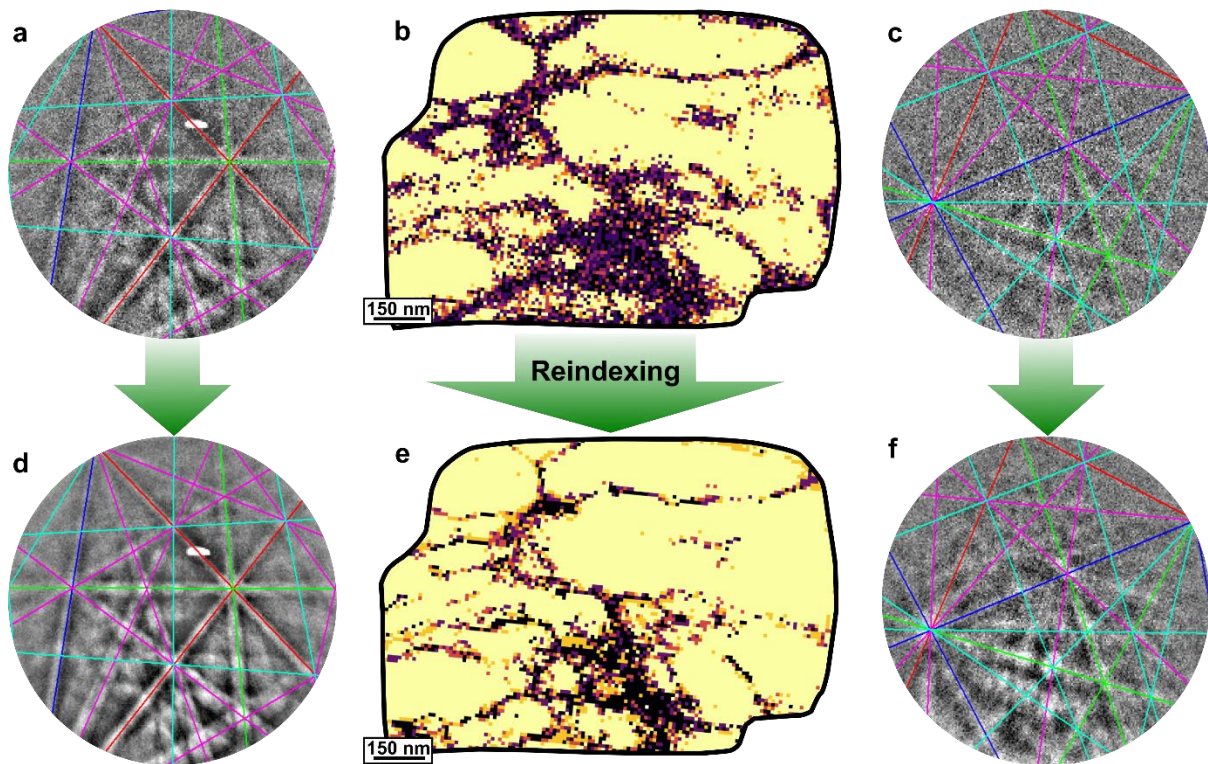


**Figure 2-9: Reindexing Kikuchi patterns** (a) as-captured Kikuchi pattern from the top right of the sample, (b) confidence index map of scan before reindexing; pixels highlighted in yellow are considered correctly indexed when calculating the indexing success rate, (c) as-captured noisy Kikuchi pattern from the highly deformed region at the



bottom of the sample, (d) improved Kikuchi pattern from (a) using NPAR, (e) confidence index map of scan after reindexing, (f) improved Kikuchi pattern from (c) using NPAR.

For reindexing, all Kikuchi patterns are saved during data acquisition, and all data sets are reindexed at a later time using the reindexing tool in OIM v8.6. Dynamic background correction is applied to equalize the intensity gradients throughout the map, and an automatic brightness and contrast correction is applied. NPAR is used during reindexing, which averages unindexable patterns with its neighboring patterns. Parameters for the NPAR reindexing as well as parameters for the Hough transform are iteratively changed and the resultant pattern quality and indexing solutions are checked in many different regions in the sample until the indexing solutions are consistently good for one parameter set. As seen from example patterns before reindexing (Figure 2-9(a,c)) and after reindexing (Figure 2-9(d,f)), the pattern quality significantly improves with the NPAR algorithm. The improvement due to reindexing is also apparent through the indexing success rate: for example, the indexing success rate of this scan was improved from 58% to 75% through reindexing (Figure 2-9(e)).

The reindexed patterns are then analyzed using the MATLAB toolbox MTEX [57], which is an open source software developed for texture analysis of EBSD or pole figure data. Custom scripts are written for each TKD data set, utilizing the functions available through MTEX and MATLAB. After importing the data, the outline of the sample is traced, and the data cropped to this perimeter. Only the data points that were indexed as silver and are within this perimeter are used for further analysis. Missing and noisy data points are fixed by applying a median filter using three nearest neighbors. For grain segmentation, a robust fast multiscale clustering algorithm [58] is used instead of the default grain segmentation algorithm in MTEX. Typically, grain boundaries are determined by sharp transitions in the orientation, however, since the impacted microcube's nanostructure consists of gradual transitions in orientation from grain to grain, pixel-to-pixel

misorientation thresholding is not sufficient for grain boundary detection. Instead, the multiscale clustering algorithm groups pixels into clusters of similar orientation, thus defining the grain boundaries. Parameters for the grain segmentation algorithm are iteratively changed until an acceptable result is obtained based on the inverse pole figure plot with grain boundaries overlaid. Parameters typically used are a threshold angle and variance of  $3^\circ \pm 5^\circ$ , maximum iterations of 10, and a 1.5 inflation power. After applying the grain segmentation once, very small grains of less than 8 pixels are removed, and the grain segmentation applied again. The grain boundaries are then smoothed, and a half quadratic filter applied to the pixels within each grain to conservatively smooth the data and fill in any outliers. An orientation distribution function is extracted from this data and pole figures plotted. After processing the TKD data and segmenting the grains, the grain size distribution is quantified by calculating the average grain size per line and the distance away from the impact plane.

To further characterize the nanostructure, the geometrically necessary dislocation (GND) density is estimated from local misorientations calculated from the TKD data. This technique has been widely used to estimate GND density from EBSD data [59–65], but only recently applied to TKD data [66–70]. Foundational works in continuum dislocation plasticity theory [71,72] relate the dislocation tensor ( $\alpha$ , commonly called the Nye tensor) to the curvature tensor ( $\kappa$ ):

$$\alpha_{ij} = \kappa_{ji} - \delta_{ij}\kappa_{kk} \quad (2-7)$$

where  $i, j, k = 1, 2, 3$ , and  $\delta_{ij} = 1$  for  $i = j$ ,  $\delta_{ij} = 0$   $i \neq j$ . The curvature tensor ( $\kappa$ ) is defined as:

$$\kappa_{ij} = \frac{d\phi_i}{dx_j} \quad (2-8)$$

where  $d\phi_i$  is a lattice rotation over a distance  $dx_j$ . Such values can be directly obtained through orientation data from EBSD or TKD maps. The total dislocation density can be determined by:

$$\rho = \frac{\sum_i \sum_j |\alpha_{ij}|}{|b|} \quad (2-9)$$

where  $b$  is the Burger's vector [63]. However, since data in only two dimensions are collected through EBSD or TKD, not all components of the Nye tensor can be resolved—a maximum of 5 out of 9 components can be obtained [60]. The Nye tensor can also be represented as the sum of the contributions to the total dislocation density from each of the dislocation types ( $\alpha_{ij} = \sum_{t=1}^N \rho^t b_i^t l_j^t$ , where  $b$  and  $l$  are the Burger's vector and line direction for dislocations of type  $t$ ). Several energy minimization approaches have been proposed to extract the dislocation density contribution from each of the 18 dislocation types in fcc materials, using this equation and the components of  $\alpha$  available through EBSD data [60,63,65,67,73].

Although not all components of the dislocation tensor are available through EBSD or TKD data, average local changes in the curvature represented by kernel average misorientation data have been used to provide a good estimate of dislocation density [61,64,65,67,68,70]. Geometrically necessary dislocations accommodate gradients in the strain field, thus, according to mechanism-based strain gradient plasticity theory, the GND density is related to the strain gradient as follows:

$$\rho_G = \frac{\eta}{|b|} \quad (2-10)$$

where  $\rho_G$  is the GND density,  $b$  is the Burgers vector, and  $\eta$  is the effective strain gradient [74]. Considering simple torsion of a cylinder, the strain gradient can be accommodated by the lattice curvature imposed by a screw dislocation lying along the axis of the cylinder [74]. For simplicity, local misorientations are assumed to consist of a series of twist sub-boundaries, accommodated by two perpendicular arrays of screw dislocations [75]. Thus, the dislocation density can be determined by:

$$\eta = \frac{2\theta_{KAM}}{u} \quad (2-11)$$

where  $\kappa$  is the curvature which can be calculated from the kernel average misorientation ( $\theta_{KAM}$ ) divided by the step size ( $u$ ) [68,75]. The kernel average misorientation at each pixel ( $i, j$ ) is calculated using the MTEX function KAM, defined as:

$$\theta_{KAM} = KAM_{i,j} = \frac{1}{|N(i,j)|} \sum_{(k,l) \in N(i,j)} \omega(o_{i,j}, o_{k,l}) \quad (2-12)$$

where  $N(i, j)$  is the set of all neighboring pixels within order  $n$  (see inset in Figure 2-10(b) for a schematic of the 1<sup>st</sup>-6<sup>th</sup> nearest neighbors in a square grid) and with a misorientation angle less than a threshold angle ( $\delta$ ),  $|N(i, j)|$  is the number of neighboring pixels within this set,  $\omega(o_{i,j}, o_{k,l})$  the disorientation angle between the orientation of pixel ( $i, j$ ) and the neighboring pixel ( $k, l$ ).

GND density estimates using Equation (2-11) are very sensitive to the step size ( $u$ ) used for data acquisition [59,62,64,67]. Since geometrically necessary dislocations are, by definition, those required to accommodate gradients in the strain field ([74], Equation (2-10)), reducing the step size will increase the GND density since all dislocations become geometrically necessary at a small enough length scale. Therefore, at the high spatial resolutions obtainable through TKD, a higher estimate of the GND density will be obtained. This sensitivity to step size is compounded with errors associated with measurement noise. If not properly accounted for, measurement noise will lead to higher misorientation values, and thus, artificially higher dislocation density estimates. In order to combat these effects, two solutions are explored: (i) reduce noise using filters [76] as described above, then compute the kernel average misorientations (KAM) from the first order neighbors with a small misorientation threshold ( $2^\circ$ , representative KAM map in Figure 2-10(a)), (ii) use the local misorientation gradient to calculate the dislocation density [61,64]:

$$\eta = \frac{d\theta_{KAM}}{du} \quad (2-13)$$

where  $\frac{d\theta_{KAM}}{du}$  is the slope of a line fitted to  $(u_i, \theta_{KAM,i})$  data points for order  $i = 1:n$  (Figure 2-10(b)). The second method is superior to the first for two reasons: the effect of step size is reduced, and local changes in measurement noise are accounted for. Local changes in measurement noise are likely in these highly deformed heterogeneous nanostructures, especially between the coarse and nanograined regions. If noise is reduced uniformly through filters applied to the entire data set, as in the first method, real misorientation data in more highly deformed regions may mistakenly be considered noise. Therefore, the gradient method is used but parameters such as the order ( $n$ ) of surrounding pixels and threshold angle ( $\delta$ ) must be optimized for the given data sets and TKD conditions. To select these parameters, the same data set is analyzed using both methods with different parameters (Figure 2-10 (c – e)). The line profiles using  $\delta = 2^\circ$  are too flattened since a local gradient is already considered and increasing  $n$  only flattens the curve more. An angle of  $15^\circ$  is a more appropriate choice, since it commonly considered the cutoff between low and high angle grain boundaries. The parameters selected ( $n=5$  and  $\delta=15$ ) preserve the local fluctuations in the data (compared to the KAM method with pre-processing, see Figure 2-10 (d)). The pre-processing method suppresses the underlying GND density gradient; however, by accounting for local noise, the gradient misorientation method uncovers this gradient. Since the GND density distribution using method (i) is comparable, these GND density maps are used for visual representation.

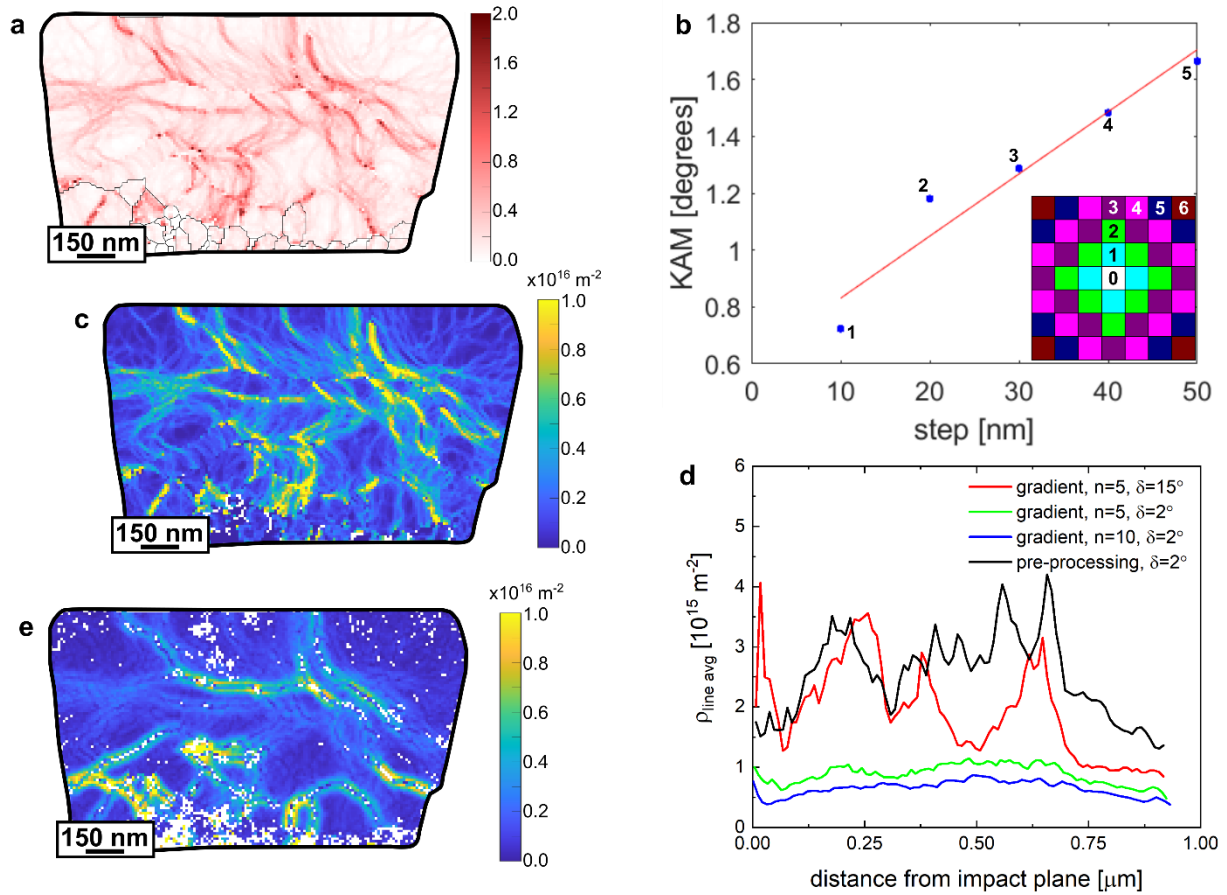


**Figure 2-10: Methods for estimating GND density** (a) kernel average misorientation map after pre-processing the data, (b) local misorientation gradient calculated from KAM values with a maximum of  $n=5$  nearest neighbors considered, (c) dislocation density map from pre-processing method; corresponding average dislocation density line profile plotted in black in (d), (d) dislocation density distributions for different analysis methods used, (e) dislocation density map from gradient method; corresponding average dislocation density line profile plotted in red in (d).

#### 2.4.5 FIB-SEM tomography

FIB-SEM tomography is used to characterize the micropore structure within the buffer layer of TRISO nuclear fuel particles (Sections 4.2 and 4.3). A preliminary investigation of the pore sizes by FIB-milling a cross section of the buffer layer showed pore feature sizes in the range of tens of nanometers to several micrometers. Considering this size range, FIB-SEM tomography is an ideal method to characterize the pore structure since volumes with side lengths of  $>10 \mu\text{m}$

and high spatial resolutions only limited by the FIB resolution are possible [77–84]. FIB-SEM tomography is a serial sectioning and imaging method in which thin slices of material are removed by FIB milling and an SEM image (also possible to do EDS and/or EBSD) is taken every slice. This process results in a stack of SEM images which can be stitched together to recreate the 3D microstructure. From this 3D reconstruction, microstructural analysis, such as porosity analysis can be conducted (Figure 2-11(a)).

The epoxy puck with exposed TRISO particles ground to midplane (Section 2.2.2) is attached to a standard aluminum SEM stub using carbon glue and copper tape. The copper tape is also used to provide a conductive pathway from the base of the sample to the top near and around the TRISO particles. An FEI Helios plasma focused ion beam (PFIB) G4 with the Auto Slice and View 4 software is used for FIB-SEM tomography. To prepare the sample, a region of the buffer layer is identified for analysis through SEM imaging, and trenches on three sides of the region are milled using the FIB (Figure 2-11(b)). A voltage of 30 kV and progressively lower currents of 60 nA, 15 nA, and 1-4 nA are used to mill trenches ~15  $\mu\text{m}$  deep. A fiducial marker for SEM image alignment is made on a milled face parallel to the cross-section to be imaged. The Auto Slice and View 4 software is used to make a fiducial for FIB milling alignment. In setting up the project, this fiducial is registered with respect to the region of interest, enabling precise milling of a specified slice thickness. A slice thickness of 50 nm is typically used, chosen based on optimizing scan time while preserving the fidelity of the microstructural data (see data analysis discussion below). SEM imaging parameters were chosen to provide a resolution at least as good as the resolution in the out-of-plane direction as set by the slice thickness. The immersion lens is used to provide high-resolution and good contrast. Auto focus is performed every 5 slices and a digital y-shift correction is performed to adjust the SEM image acquisition area for stage tilt.

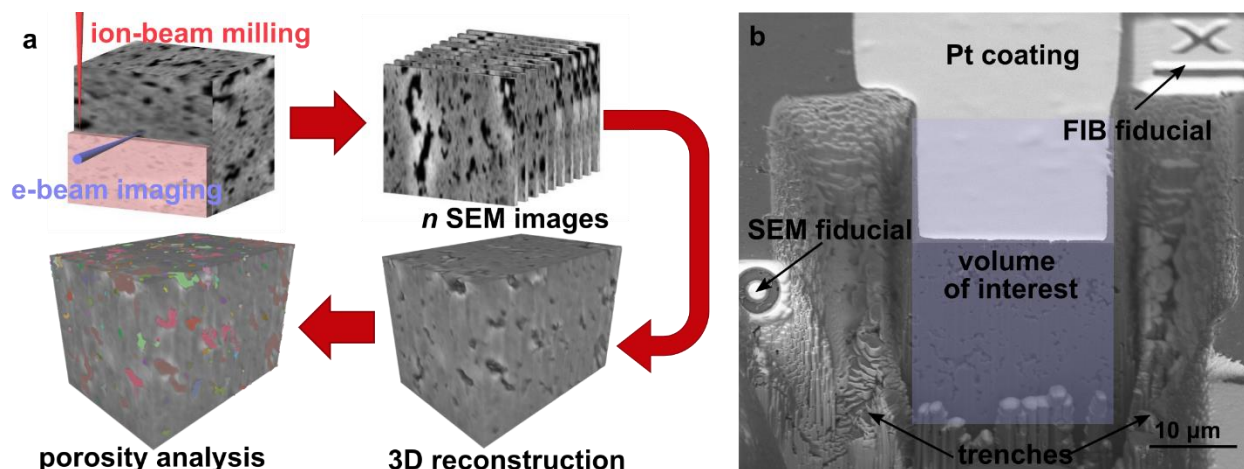


**Figure 2-11: FIB-SEM tomography** (a) workflow of creating 3D reconstructions from slice and view image stacks, (b) sample preparation for FIB-SEM tomography: deposit Pt protective coating, mill trenches, prepare fiducial markers.

Image processing and data analysis are performed using a combination of Avizo 9.5 and Dragonfly 2021.1 software. The Dual Beam 3D Wizard in Avizo is used to perform pre-processing of the image stack—including geometric corrections for the stage tilt, image alignment, and removal of curtaining artifacts. A background detection correction and sigma filter are also applied to reduce noise and normalize the background intensity throughout the image stack. The pre-processed image stack is then exported as tiff files for further processing in Dragonfly. Although Avizo has many of the same image processing and segmentation features, Dragonfly allows more user control and offers more segmentation tools that are necessary for this project.

Image segmentation and feature separation are very important to accurately represent the pore microstructure. Segmentation, the process by which pixels are labeled as belonging to a particular phase or material, is typically done through various intensity thresholding and identification techniques. For these image stacks, up to three phases were identified: pores, buffer, and kernel/IPyC/other. Intensity thresholding and paint tools are used to conservatively identify regions belonging to each phase. Then, a watershed transform is applied to “grow” the labeled



regions until the edge of the feature containing the labeled pixels is reached. Several problems with this intensity-based segmentation method became apparent in our data sets: i) because the pyrocarbon material behind is visible within large pores, pixels inside the pores were misidentified as the buffer or large pores became separated into smaller pores since there is a contrast gradient within the pore, ii) contrast between pores and buffer is inadequate for intensity thresholding, iii) the average intensity of pixels that should be labeled as “pore” or “buffer” changes within an image stack.

Because of these challenges with intensity-based segmentation, Dragonfly’s deep learning segmentation module was tried as an alternative. For this method, a few slices (typically 3-4 slices, ~1-2% of total slices) are manually segmented to be used as the training data set. A deep learning model is then built and trained using this data set and applied to the whole image stack. A convolutional neural network (CNN) called U-Net [85] is used, which was originally developed for biomedical image segmentation. U-Net uses data augmentation to sufficiently reduce the amount of training data needed, while providing excellent segmentation results quickly. Our training data is augmented three times, through horizontal and vertical flipping. The training parameters used are typically as follows: patch size=32, stride ratio=1, epochs number=100, batch size=32, loss function: CategoricalCrossentropy, optimization algorithm: Adadelta. The model is trained until the loss—the error between the neural network’s prediction and reality—is minimized. If the loss is not minimized quickly and effectively, the training parameters are changed slightly until an acceptable result is achieved. After training, the model is applied to the entire data set and segmentation results are outputted and verified for accuracy.

After the data set has been segmented, individual pores must be identified through a separation process. The segmentation process produces an object or region of interest (ROI) for

each phase—in most cases, one for the buffer and one for the pores. To separate the pores ROI into a multi-ROI, where each pore is a separate ROI, a distance map is created from the buffer ROI—which is a greyscale image with higher intensities corresponding to farther distances away from the buffer. From the distance map, intensity thresholding can be used to define the center of each pore. For consistency, the intensity threshold is set at 5% less than the upper-Otsu intensity range. The upper-Otsu threshold can be selected directly in Dragonfly and is based on Otsu’s algorithm which defines two intensity classes, separating pixels with high intensity and low intensity. A threshold value of 5% less than the upper-Otsu intensity range was chosen based on qualitative analysis of the resultant pore separations for different threshold values. Once the pore centers are defined, a new multi-ROI is created by applying a “connected components” analysis which separates each grouping of voxels into a ROI. Then, a watershed transform is applied with the inverted distance map as the landscape and the pores ROI as a mask. The watershed transform allows each pore to “grow” until the boundary of the pores ROI or another pore is reached. This process separates the voxels defined as “pores” through the segmentation process into individual pores. Once separated into individual pores, quantities describing the pore sizes, positions, and shapes can be exported.

Large differences are apparent in the porosity quantification data resulting from the two segmentation methods (Figure 2-12). Looking at the segmentation results in an example area (Figure 2-12(c-e)), the deep learning segmentation method clearly does a better job at capturing the entire pore area, regardless of contrast changes within the pore. These differences propagate into the volumetric porosity data: the number and volume fraction of small pores are significantly higher for the intensity-based segmentation (Figure 2-12(a,b)) because large pores are artificially broken into smaller pores due to contrast gradients within the pore. The total volume fraction of

pores is also much lower for the intensity-based segmentation (10.8%) than the deep learning segmentation (19.3%). This is due to regions within large pores being misidentified as the buffer. Through this analysis, we have determined that the deep learning segmentation method will be more consistent and accurate in characterizing the porosity in our data sets.

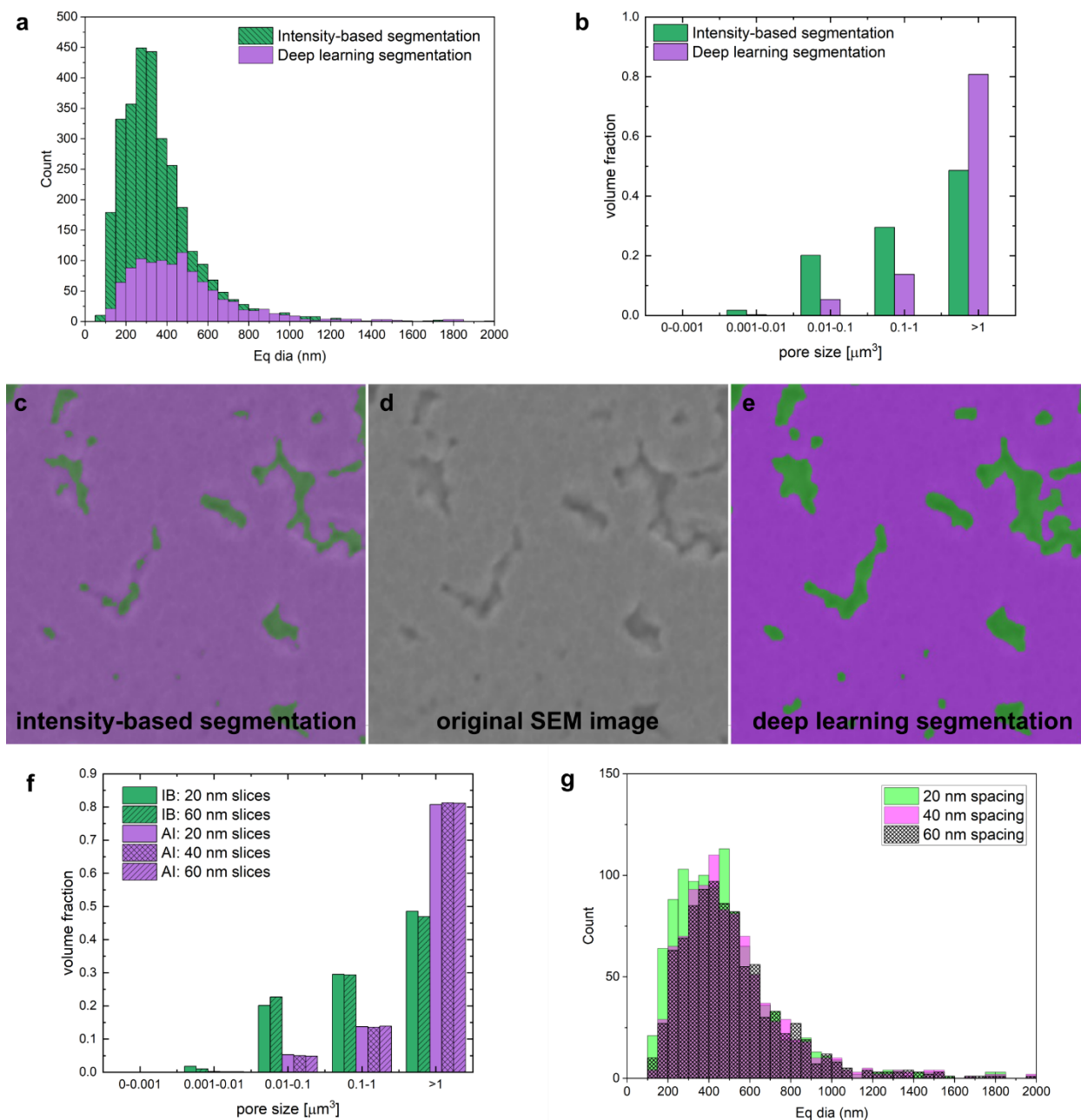


**Figure 2-12: Image processing and data analysis** (a) distribution of pore sizes resulting from intensity-based segmentation and deep learning segmentation methods, (b) volume fractions of pore volume ranges resulting from the two segmentation methods, (c) example of intensity-based segmentation result (pores – green, buffer – purple), (d) unsegmented SEM image of (c) and (e), (e) example of deep learning segmentation result, (f) volume fractions of pore volume ranges compared for various slice thicknesses and segmentation methods, (g) distribution of pore sizes for different slice thicknesses (using deep learning segmentation).

We also performed analysis to determine an optimal slice thickness for fast data acquisition while maintaining high fidelity. A scan taken with 20 nm slice thickness was analyzed three ways to simulate different slice thicknesses: i) every image included – 20 nm slice thickness, ii) every second image included – 40 nm slice thickness, iii) every third image included – 60 nm slice thickness. By analyzing the same data set with some images excluded, we can determine if porosity information is lost with larger slice thicknesses. Figure 2-12(f) shows the volume fractions of pores in each pore volume range for different slice thicknesses and segmentation methods. While differences between 20 and 60 nm slice thicknesses are apparent for intensity-based segmentation, minimal differences exist between data sets analyzed with deep learning segmentation over all slice thicknesses. Therefore, the differences seen in the intensity-based segmentation data sets are attributed to inconsistency in the segmentation method analysis. Looking at the distribution of pore sizes (Figure 2-12(g)) for all slice thicknesses, there are fewer small pores (<300 nm equivalent diameter) identified in the data sets with larger slice thickness, suggesting some information is lost. However, the volume fractions in each pore size category and the total volume fraction of pores ( $19.3\% \pm 0.1\%$ ) remain quite consistent with all slice thicknesses. Therefore, a slice thickness of 50 nm was chosen as an optimal slice thickness to reduce data acquisition time.

## 2.5 Molecular statics (MS) and molecular dynamics (MD) simulations<sup>2</sup>

To understand the microstructural evolution of the Ag microcubes during quasi-static compression and high-velocity impact testing, we performed molecular statics (MS) and molecular dynamics (MD) simulations, respectively. Due to computational limitations, the simulation cell size is limited to a maximum of  $240^3$  fcc unit cells (62 million atoms) which corresponds to a cube with

---

<sup>2</sup> MD simulations were done in collaboration with Prof. Mauricio Ponga at the University of British Columbia, Vancouver.

side length of  $\sim 98$  nm. This cell size approaches the smallest cube size in experiments ( $\sim 100$  nm) and is approximately the limit that one can achieve with the state-of-the-art MD techniques. The simulations can be used to explore the plastic deformation mechanisms that may be active in comparable experiments. All simulations are performed with the LAMMPS code [86,87] and the material (Ag) is modeled with the Embedded atom method interatomic potential developed by Williams et al. [88]. Nanocubes are modeled by constructing the fcc lattice with an initial lattice constant  $a_0 = 0.409$  nm. The initial configuration is relaxed at  $T = 300$  K by allowing the crystal to expand and/or contract independently to minimize the energy and the pressure.

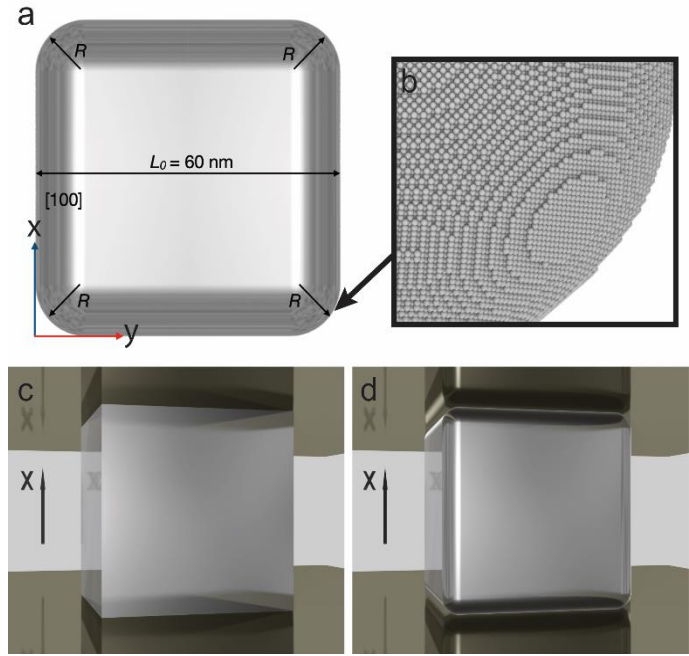


**Figure 2-13: Molecular statics simulation geometry** (a)  $\langle 100 \rangle$  view of cube with rounded edges, edge radius ( $R$ ) and side length ( $L_0$ ) labeled, (b) atomic steps forming the rounded corner, (c) compression of a perfect cube with sharp edges and corners, (d) compression of a cube with rounded edges and corners.

### 2.5.1 Molecular statics (MS) simulations

MS simulations are performed to study the quasi-static compression of Ag nanocubes. Several geometries were considered to match to experiments: nanocubes (several sizes), nanopillars, nanocubes with rounded edges and corners, and nanocubes with porosity. The simulation cell is made up of  $120^3$ - $240^3$  fcc unit cells containing approximately 6 to 62 million atoms ( $L_0 = 20 - 240 a_0$ ). The cylindrical nanopillar was generated with radius of 32 nm and a length of around 64 nm containing 16 million atoms. To investigate the effects of edge roundness,

rounded edges were generated with a python script that removed atoms from the perfect cube. Geometries were generated with a range of cube lengths ( $7.5 < L_0 < 60$  nm) and edge radius sizes ( $0 < R < 12$  nm), to achieve edge roundness ratios ( $r_e = R/L_0$ ) of 0-20%. A schematic cross-section of the rounded particle can be seen in Figure 2-13(a), showing the rounded corners and labeled dimensions. The corners have a spherical surface made of discrete (111) close-pack planes of atoms as shown in Figure 2-13(b). We also studied the effects of vacancy concentration by randomly removing individual atoms from the perfect crystal.

All geometries were generated with the [100]-crystal direction coinciding with the loading direction. Once the geometry is generated, strain-controlled compression of the particle is performed by applying a homogeneous deformation gradient ( $\mathbf{F}$ ) to the atoms along x-direction. The homogeneous deformation gradient is defined as:

$$\mathbf{F} = \begin{bmatrix} 1 + \lambda & 0 & 0 \\ 0 & 1 & 0 \\ 0 & 0 & 1 \end{bmatrix}. \quad (2-14)$$

At each indentation step, the strain is increased by equal increments controlling  $\lambda$ . After the homogeneous deformation gradient is applied, two thin layers ( $\sim 2a_0$ ) at the bottom and top of the particles are restricted to move in the x-direction to generate a strain-controlled compression. The positions of the atoms are optimized to minimize the potential energy of the system using the Polak-Ribière non-linear conjugate gradient (NLCG) method [89]. The tolerances were set to  $10^{-10}$  eV and  $10^{-10}$  eV  $\cdot \text{\AA}^{-1}$  for energy and force convergence, respectively.

The indentation stress was monitored using the virial stress tensor, computed using the expression:

$$\sigma_{ij} = \frac{1}{2\Omega} \sum_{k=1}^N \sum_{\substack{l=1 \\ k \neq l}}^N (r_i^l - r_i^k) f_j^{kl}, \quad (2-15)$$

where  $\Omega$  is the volume of the particle,  $r_i^l$  is the  $i$ -th component of the position vector of atom  $l$ , and  $f_j^{kl}$  is the  $j$ -th component of the force vector applied on  $k$ -th atom by the  $l$ -th atom.  $N$  is the total number of atoms in the simulation. To visualize the yield stress, we use the von Mises equivalent stress as defined in continuum mechanics. Dislocations were identified using the Dislocation Analysis (DXA) [90] implemented in open visualization tool OVITO [91].

### 2.5.2 Molecular dynamics (MD) simulations

MD simulations are performed to study the high-velocity impact of Ag nanocubes. Nanocubes with side lengths of  $\sim 65.5$  nm are constructed ( $\sim 160^3$  fcc unit cells with lattice constant  $\sim 0.409$  nm at 0 K; 16,384,000 atoms), and an initial translational velocity is applied to the atoms to generate the impact velocity. Then, the positions of the atoms are integrated under the NVE ensemble for about 550 ps. The NVE ensemble ensures that no extra energy is added to the computational cell. The rigid wall was generated using a command which includes an atomic interaction at specific location ( $x = 0$ ). The interaction is given by a Lennard-Jones-type potential, i.e.,

$$E_W(r) = \epsilon \left( \frac{2}{15} \left( \frac{\sigma}{r} \right)^9 - \left( \frac{\sigma}{r} \right)^3 \right); \quad r < r_c \quad (2-16)$$

where  $r$  is the minimum distance between the particle and the wall,  $\epsilon = 1$  eV,  $\sigma = 0.1$  nm, and  $r_c = 0.25$  nm is a cut-off radius. Other choices of the wall generate the same results.

From the MD data we compute the average strain rate by using the change of the length of the sample and the time required to do that:

$$\dot{\epsilon} = \frac{\epsilon}{\Delta t} = \frac{\Delta l}{l_0 \Delta t} = \frac{1}{\Delta t} \left( \frac{l - l_0}{l_0} \right), \quad (2-17)$$

where  $l$  is the final length,  $l_0$  is the initial length, and  $\Delta t$  is the elapsed time at which  $l$  and  $l_0$  have been measured. For the [100]-face impact, we estimated the strain rate to be  $\sim 2.4 \times 10^9 \text{ s}^{-1}$ , while the



strain rate for the [110]-edge impact was  $\sim 3.7 \times 10^9 \text{ s}^{-1}$ . These average values of the strain rate are about an order of magnitude larger than that estimated from experiments ( $\sim 1.4 \times 10^8 \text{ s}^{-1}$ , see Appendix A.3 for details) and is mainly due to the size mismatch of the cube.

The strength of the simulation cell is quantified using virial stresses [87] that are computed from,

$$\sigma_{\alpha\beta} = -\frac{1}{V} \left( \sum_i \frac{p_{\alpha}^i p_{\beta}^j}{m} + \sum_i \sum_j r_{\alpha}^{ij} f_{\beta}^{ij} \right); \quad \alpha, \beta = x, y, z \quad (2-18)$$

where  $\sigma_{\alpha\beta}$  are the components of the stress tensor,  $V$  is the total volume of the simulation cell,  $p_{\alpha}^i$  is the component  $\alpha$  of the linear momentum ( $p_{\alpha}^i = m v_{\alpha}^i$ ) of atom  $i$ ,  $r_{\alpha}^{ij} = x_{\alpha}^i - x_{\alpha}^j$  is the component  $\alpha$  of the relative distance vector between atoms  $i$  and  $j$ , and  $f_{\beta}^{ij}$  is the component  $\beta$  of the force vector on atom  $i$  due to atom  $j$ . Since the sample is initially traveling with a large translation speed, we subtracted their center of mass velocity and use the components of linear momentum without the velocity of the center of mass. We use two independent methods to quantify the amount of plastic work generated in the simulation cell. The first quantity is the von Mises equivalent stress given by,

$$\sigma_e = \left( \frac{1}{2} \sum_{\alpha > \beta} (\sigma_{\alpha\alpha} - \sigma_{\beta\beta})^2 + 3 \sum_{\alpha > \beta} \sigma_{\alpha\beta}^2 \right)^{\frac{1}{2}} \quad (2-19)$$

The von Mises equivalent stress allows introducing the stress triaxiality factor, which is a direct measure of the plastic deformation in the sample. The stress triaxiality factor is given by,

$$\xi = \frac{\sigma_m}{\sigma_e} \quad (2-20)$$

where  $\sigma_m = \frac{1}{3}(\sigma_{11} + \sigma_{22} + \sigma_{33})$  is the hydrostatic stress.

In order to provide a more comprehensive study of the impact, we calculated the spatial-temporal evolution of stress and temperature, again using the kinetic energy of the atoms and virial stress. The procedure was reproduced from a laser irradiation simulation where the pressure and temperature were described as a function of the space-time [39]. In order to study the distribution of temperature and stresses, we divided the computational cell into bins of equal size along the  $x$ -direction (normal to the impact plane). For all simulations, we took  $N_{bins} = 40$ . Then, for each bin, we computed the components of the virial stress tensor, and the temperature using the local kinetic energy. Then, we subtracted the temperature of the center of motion. In order to compute the virial stress, we needed to take a reference volume. Here, we used for each bin a volume given by  $V_{bin} = \frac{V_{cube}}{N_{bins}}$  to compute the virial stress. These quantities were processed on the fly, and dumped to a file every 1 ps, for further analysis into the temperature and stress distributions over time and position.

## 2.6 Crystal plasticity simulations<sup>3</sup>

Crystal plasticity simulations are used to investigate the structure-property relations of the heterogeneous nanostructures formed through impact of single-crystal Ag microcubes. Experimental results are compared with simulations of synthetic microstructures formed with experimental input. Additionally, because of the difficulty in preparing, testing, and characterizing samples at the microscale and of limitations in the control over the resultant nanostructure, we use crystal plasticity simulations to explore structure-property relations of heterogeneous nanostructures beyond what can be feasibly achieved with experiments.

---

<sup>3</sup> Crystal plasticity simulations done in collaboration with Prof. Curt Bronkhorst, UW Madison

### 2.6.1 Single crystal constitutive model

The single crystal constitutive model defined by Bronkhorst et al. [92] is used for the simulations, which is based on previous foundational works in the crystal plasticity field [93–102]. The coupled thermo-mechanical elasto-viscoplastic formulation assumes thermally activated slip is the dominant deformation mechanism, tracking the evolution of dislocation density on each slip system and representing grain size effects through an empirical Hall-Petch term. An ABAQUS user subroutine (UMAT) is used to implement the model with the time-integration scheme presented in [98,103]. A brief description of the plasticity model, adapted from Bronkhorst et al. [92], is given here:

As is typical for constitutive models representing large plastic deformations, the deformation gradient is decomposed into the reference (undeformed material), intermediate (plastic deformation), and current (elastic and plastic deformations) configurations:

$$\mathbf{F} \equiv \mathbf{F}^* \mathbf{F}^P \quad (2-21)$$

assuming elastic invertibility and plastic incompressibility. The constitutive relation is given in the intermediate configuration, where the second Piola-Kirchhoff stress ( $\mathbf{T}^*$ ) and elastic Green-Lagrange strain ( $\mathbf{E}^*$ ) are given by

$$\mathbf{T}^* = \mathcal{L}(\theta)[\mathbf{E}^* - \mathbf{A}(\theta - \theta_0)] \quad \text{and} \quad \mathbf{E}^* \equiv \frac{1}{2}(\mathbf{F}^{*T} \mathbf{F}^* - \mathbf{1}) \quad (2-22)$$

where  $\mathcal{L}(\theta)$  is the fourth order elastic stiffness tensor,  $\theta$  and  $\theta_0$  are the current and reference temperatures, respectively, and  $\mathbf{A}$  is the thermal expansion tensor. The stress in the deformed (current) configuration (Cauchy stress,  $\mathbf{T}$ ) can be found by transforming the stress from the intermediate configuration to the current configuration through this relation:

$$\mathbf{T}^* = \mathbf{F}^{*-1}(\det \mathbf{F}^*)\mathbf{T}\mathbf{F}^{*-T} \quad (2-23)$$

Plastic deformation is accommodated by thermally activated dislocation slip, where the plastic velocity gradient is defined by the sum of slip rates ( $\dot{\gamma}^\alpha$ ) in directions defined by the slip system ( $\mathbf{S}_0^\alpha$ ):

$$\mathbf{L}^P = \dot{\mathbf{F}}^P \mathbf{F}^{P-1} = \sum_\alpha \dot{\gamma}^\alpha \mathbf{S}_0^\alpha \quad (2-24)$$

where  $\mathbf{S}_0^\alpha = \mathbf{m}_0^\alpha \otimes \mathbf{n}_0^\alpha$  is the Schmid tensor describing the geometry of the 12 slip systems, composed of combinations of the 4 {111} slip planes and 3 <110> slip directions. Since rotation of the lattice can be described through the elastic deformation gradient ( $\mathbf{F}^*$ ), the slip plane normal directions ( $\mathbf{m}_0^\alpha$ ) and slip directions ( $\mathbf{n}_0^\alpha$ ) which are originally defined in the undeformed (reference) configuration can be converted to the deformed configuration (current) through:

$$\mathbf{m}^\alpha = \mathbf{F}^* \mathbf{m}_0^\alpha \quad \text{and} \quad \mathbf{n}^\alpha = \mathbf{F}^{*-T} \mathbf{n}_0^\alpha \quad (2-25)$$

The slip rate ( $\dot{\gamma}^\alpha$ ) on each slip system ( $\alpha$ ) is calculated by:

$$\dot{\gamma}^\alpha = \dot{\gamma}_0 \exp \left[ -\frac{F_0}{k_B \theta} \left( 1 - \left( \frac{|\tau^\alpha|}{\frac{\mu(\theta)}{\mu} (s_\beta^\alpha + s_l^\alpha)} \right)^p \right)^q \right] \text{sgn}(\tau^\alpha) \quad (2-26)$$

where the terms are constants defined in Table 2-4 or defined by the expressions shown in Table 2-3 for clarity.

The evolution of dislocation density on slip system  $\alpha$  is given by:

$$\dot{\rho}^\alpha = \frac{1}{b} \left( \sqrt{\sum_\beta d^{\alpha\beta} \rho^\beta} - 2r_c \rho^\alpha \right) |\dot{\gamma}^\alpha| \quad (2-27)$$

whose terms are constants (Table 2-4) or defined by the expressions in Table 2-3 or other previously defined expressions.

**Table 2-3: Expressions used to define the variables in equations (2-26) and (2-27); variables given in these expressions are defined in Table 2-4 or in the equations above**

Parameter description	Expression
Resolved shear stress ( $\tau^\alpha$ )	$\tau^\alpha = (\mathbf{F}^{*T} \mathbf{F}^* \mathbf{T}^*) \cdot \mathbf{S}_0^\alpha$
Shear modulus ( $\mu$ )	$\mu(\theta) = \sqrt{C_{44}(\theta) \frac{C_{11}(\theta) - C_{12}(\theta)}{2}},$ <p>where <math>C_{ij}(\theta) = C_{ij}(0K) + m_{ij} \theta</math></p>
Deformation resistance stress due to grain size and dislocation structure ( $s_\rho^\alpha$ )	$s_\rho^\alpha = s_\infty + \frac{k_{gr}}{\sqrt{d_{gr}}} + \mu b \sqrt{\sum_\beta a^{\alpha\beta} \rho^\beta}$
Dislocation multiplication interaction tensor ( $d^{\alpha\beta}$ )	$d^{\alpha\beta} = \frac{a^{\alpha\beta}}{k_c^2}, \text{ for self-interacting and coplanar slip systems}$ $d^{\alpha\beta} = \frac{a^{\alpha\beta}}{k_{nc}^2}, \text{ for intersection non-coplanar systems}$
Capture radius for dislocation annihilation ( $r_c$ )	$r_c = r_{c0} \left( \frac{ \dot{\gamma}^\alpha }{\dot{\gamma}_0} \right)^{\frac{k\theta}{A}}$

### 2.6.2 Parameter determination and fitting

Thirty-six material parameters define the model, whose values are known constants, fitted to experimental data, or a grain-dependent (element set) parameter. Table 2-4 lists these parameters and their values, according to the type. For the parameters that are known constants or from literature: the density ( $\rho$ ), specific heat ( $c_p$ ), thermal expansion coefficient ( $\alpha$ ), elastic constants at 0 K ( $C_{ij}$ ) and temperature dependencies ( $m_{11}$ ), number of slip systems ( $n_{slip}$ ), and Burger's vector magnitude ( $b$ ) are known constants specific to face-centered-cubic silver. The temperature

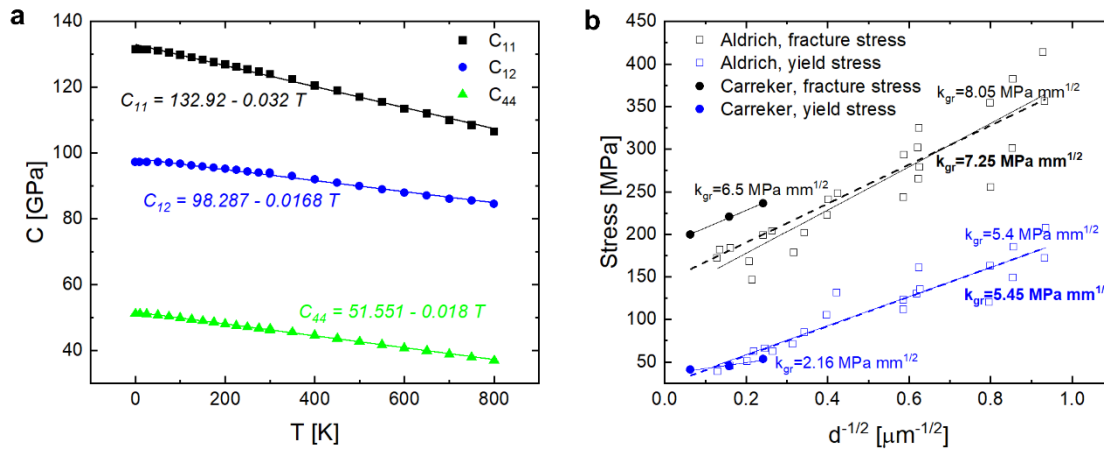


**Figure 2-14: Data from literature used for parameter determination** (a) temperature dependence on elastic constants for silver, data reported in Simons and Wang [104], (b) grain size effect on fracture stress and yield stress, from polycrystal silver data in [106,107].

dependencies for the elastic constants ( $m_{ij}$ ) were found by fitting a line the temperature specific elastic constants for silver from [104] (Figure 2-14(a)). The temperature is taken as room temperature (298 K), as in experiments. Since the simulations are performed at a quasi-static strain rate ( $10^{-2} \text{ s}^{-1}$ ), the Taylor-Quinney coefficient is 0. The strain rate factor ( $\dot{\gamma}_0$ ), long-range resistance ( $s_\infty$ ), intrinsic lattice resistance ( $s_l^\alpha$ ), flow rule barrier exponents ( $p$  and  $q$ ), the six dislocation interaction quantities defining the tensor  $a^{\alpha\beta}$  ( $a_{self}$ ,  $a_{dipolar}$ ,  $a_{Hirth}$ ,  $a_{collinear}$ ,  $a_{glissile}$ ,  $a_{Lomer}$ ) were chosen to be the same values used by Bronkhorst et al. given the assumptions and reasonings

presented in [92]. The grain dependent parameters—the Euler angles representing the grain orientation and grain diameter—are determined from the synthetic microstructures.

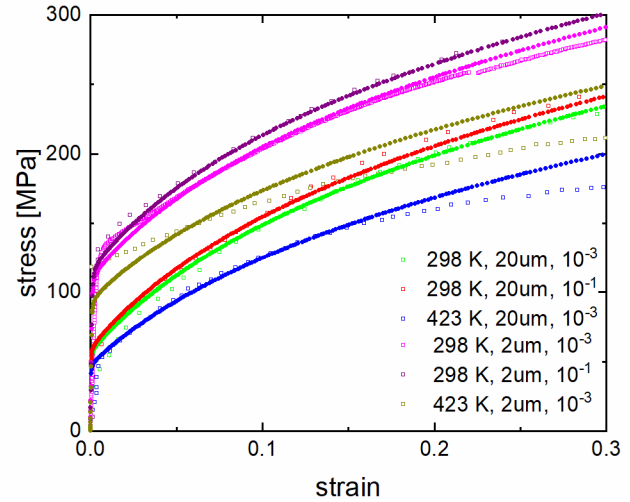
**Table 2-4: Material parameters for single crystal plasticity model**

<i>Known constants or from literature</i>			
Temperature ( $\theta_0$ )	298 K	Burger's vector magnitude ( $b$ )	2.892E-7 mm
Density ( $\rho$ )	10500.0 kg/m <sup>3</sup>	Number of slip systems ( $n_{slip}$ )	12
Specific heat ( $c_p$ )	235.01 J/kg-K	$a_{self}$	0.122
Thermal expansion ( $\alpha$ )	19.0e-6 K <sup>-1</sup>	$a_{dipolar}$	0.122
Taylor-Quinney ( $\eta$ )	0.00	$a_{Hirth}$	0.070
$m_{11}$	-32 MPa/K	$a_{collinear}$	0.625
$C_{11}$ (0 K)	132.92 GPa	$a_{glissile}$	0.137
$m_{12}$	-16.8 MPa/K	$a_{Lomer}$	0.122
$C_{12}$ (0 K)	98.287 GPa	Long-range resistance ( $s_\infty$ )	0 MPa
$m_{44}$	-18 MPa/K	Capture radius ( $r_{c0}$ )	12 mm
$C_{44}$ (0 K)	51.551 GPa	Intrinsic lattice resistance ( $s_l^\alpha$ )	0 MPa
Boltzmann's constant ( $k_B$ )	0.138E-22 J/K	Flow rule barrier exponent: $p$	0.33
Strain rate factor ( $\dot{\gamma}_0$ )	10 <sup>7</sup> s <sup>-1</sup>	Flow rule barrier exponent: $q$	1.66

<i>Fitted</i>		<i>Grain-dependent</i>	
Capture radius constant ( $A$ )	5E-19 J	Euler angle theta	$\theta$ [rad]
Non-coplanar dislocation evolution constant ( $k_{nc}$ )	5.5	Euler angle phi	$\phi$ [rad]
Coplanar dislocation evolution constant ( $k_c$ )	35	Euler angle omega	$\omega$ [rad]
Activation energy ( $F_0$ )	3.5E-18 J	Grain diameter	$d_{gr}$ [mm]
Hall-Petch slope ( $k_{gr}$ )	2.1 MPa√mm		
Dislocation density ( $\rho_0^\alpha$ )	3E6 mm <sup>-2</sup>	Dislocation density	$\rho_0^\alpha$ [mm <sup>-2</sup> ]

The remaining six parameters—the capture radius constant ( $A$ ), dislocation evolution constants ( $k_{nc}$  and  $k_c$ ), activation energy ( $F_0$ ), Hall-Petch slope ( $k_{gr}$ ), and initial dislocation density ( $\rho_0^\alpha$ )—are fitted using experimental uniaxial compression data of polycrystal silver at different temperatures, strain rates, and grain sizes [105]. The Hall-Petch parameter was initially set at  $5.45 \text{ MPa}\sqrt{\text{mm}}$  according to data from size effect studies on silver found in literature [106,107] (Figure 2-14(b)). A polycrystal sample is represented by a one-thousand element cube with random



**Figure 2-15: Parameter fitting to bulk polycrystal silver stress-strain data at different temperatures, strain rates, and average grain size**

crystallographic texture and compressed quasi-statically. The stress-strain curves from simulations with different combinations of the six fitted material parameters are compared to the experimental stress-strain curves with different temperatures (298 K and 423 K), strain rates ( $10^{-1} \text{ s}^{-1}$  and  $10^{-3} \text{ s}^{-1}$ ) and grain sizes (2  $\mu\text{m}$  and 20  $\mu\text{m}$ ). In general, the initial dislocation density was found to have the greatest effect on the flow stress, with higher values increasing the flow stress. Decreasing the capture radius constant or non-coplanar dislocation evolution constant was found to increase the hardening rate. The coplanar dislocation evolution constant has minimal effect on the stress-strain response within these temperatures, strain-rates, and grain sizes studied. Increasing the activation energy was found to increase the flow stress at high strains. The Hall-Petch parameter affected the relative difference in flow stresses achieved by the samples with different grain sizes. After



running many simulations with different combinations of parameters, the values of the fitted parameters shown in Table 2-4 were found to provide the best fit to the experimental data as shown in Figure 2-15. The dislocation density is highlighted in Table 2-4 because the dislocation density fitted through evaluation of the polycrystal model is typically not used in the simulations—instead, experimentally defined functions are used to determine the dislocation density based on the grain size (see Section 2.6.4).

### 2.6.3 *Synthetic microstructure generation*

As described above, the two main goals for the crystal plasticity simulations are to i) compare results to experimental data, thus achieving a better understanding of the plastic deformation of impact-induced heterogeneous nanostructures ii) explore how different parameters defining the nanostructure, beyond what can be feasibly altered experimentally, affect the plastic deformation response. To achieve these goals, the microstructure generation method developed here has the capability of recreating synthetic microstructures from experimental data as well as artificially manipulating the parameters defining the nanostructure to study structural influences beyond those witnessed in experiments. As seen in Section 3.3, the nanostructures formed during high-velocity impact have varied spatial distributions in grain size, dislocation density, and orientation. Furthermore, testing of micropillars with different sample dimensions which are on the same order as the internal feature dimensions introduces complexities that may affect the stress-strain response and must be reproduced in the simulations. Therefore, the synthetic microstructure generation method must be able to recreate a microstructure by accepting experimental inputs such as a grain size distribution, maximum or minimum grain size, orientations, dislocation density, sample shape, and sample dimensions. To expand our structure-property study beyond the experimental results, we want to have full control over these parameters without experimental

input if desired, as well as the ability to specify parameters which cannot be altered in our experiments, such as the direction of the grain size gradient. In addition to all these specifications, there must be a good method to mesh the generated microstructures.

Upon investigating the currently available software for synthetic microstructure generation, it was determined that none of them could fully provide all the requirements outlined above. Two of the most ubiquitous microstructure generation software, Dream3D [108] and Neper [109], boast some fabulous microstructure generation features, but neither encompasses all the features necessary for this project. A new method published recently [110] gets closer to fulfilling the requirements of generating synthetic microstructures from experimental EBSD data while having spatial control over localized features, but it is still being developed and cannot produce meshes. While Dream3D possesses the capabilities of creating samples with different shapes and dimensions, extracting statistical parameters from experimental EBSD data to inform the microstructure generation, and create meshes, its main limitation in regard to this project is the inability to spatially control the grain size distribution. A potential workaround [111] is to generate multiple microstructure layers each with a different average grain size and then stitch them together with a Potts grain growth model [112] to create a gradient in grain size. However, this procedure is not trivial, so alternative microstructure generation methods were investigated. Another option is Neper, which is an open-source software for polycrystal generation and meshing that can be run on any Unix-like operating system. Neper allows for a high degree of user control but does not have nice built-in features for extracting information from EBSD data to build the microstructure like Dream3D does. However, while not directly built-in, there are options to control microstructural features such as the orientations, grain sizes, and approximate positions, which can be based upon EBSD data. In order to control the spatial distribution of grain sizes, a Laguerre-

Voronoi tessellation method [113–115] can be used, in which a set of seed positions and weights are defined which roughly correspond to the grains' centroid positions and sizes ( $\omega_i = r_i^2$ , where  $\omega$  is the weight, and  $r$  is the radius of sphere with equivalent volume). A recent paper published in 2019 [115] demonstrates the effectiveness of this method in controlling the spatial distribution of grain sizes through generation of a 2D bimodal polycrystal structure. We take a similar approach through writing a custom MATLAB code which generates a set of seed positions, weights, and orientations that can be inputted in Neper to create a 3D microstructure with a spatial gradient in grain size.

The seed generation algorithm was written in MATLAB, a summary of which is provided in Figure 2-16. Orientation and grain size distribution data can be extracted from previously analyzed TKD data (see Section 2.4.4) and used to inform the seed generation algorithm. Alternatively, user specified orientations and a grain size function not based on experimental data can be used. Additionally, either the maximum or minimum grain size, sample shape and dimensions, and direction of gradient are defined as inputs to the seed generation algorithm. The first step (Figure 2-16, step 1) is to define the sample geometry based on the inputted sample shape, dimensions, and direction of gradient. Since the seeds are populated within a bounding box in a grid-like fashion, a bounding box is defined which is large enough to contain the rotated volume, with one dimension aligned along the gradient direction. Next, the gradient grain size function ( $g'(s)$ ) is defined (Figure 2-16, step 2), either through a user defined grain size function ( $g_i(s)$ ) or through experimental grain size ( $g$ ) vs position ( $s$ ) data. If experimental data is provided, a smoothing spline is fit to the data which defines a grain size function ( $g_i(s)$ ). The derivative of the initial grain size function ( $dg_i/ds$ ) is the gradient grain size function ( $g'(s)$ ). A synthetic grain

size function ( $g_o(s)$ ) is then determined by integrating the gradient grain size function, with the user defined maximum or minimum grain size ( $g_m$ ) used to find the integration constant.

$$g_o(s) = \int g'(s) ds, \quad g_o(s_m) = g_m \quad (2-28)$$

This function is then discretized by packing seeds as close as possible along the gradient direction, given the space needed ( $\Delta s$ ) for a grain of size  $g_o$ . This formulation allows us to study microstructures with the same gradient grain size function but different extrema conditions or vice versa. Next, the bounding box defined in step 1 is filled with seeds (Figure 2-16, step 3), with their z coordinates determined by the discretized positions ( $s_i$ ) and their x and y coordinates populated through a square array of points with spacing equal to the grain size ( $g_o(s_i)$ ). Therefore, each seed  $i$  has a specified position ( $x(i), y(i), z(i)$ ) and grain size  $g(i)$ . To make the distribution of seeds more representative of a realistic microstructure, the seed positions are perturbed by random increments ( $\Delta x, \Delta y, \Delta z$ ) between 0 and 75% of the radius of the grain ( $g(i)/2$ ) (Figure 2-16, step 4). Penultimately, if the specified gradient direction is different than the z-direction ([001]), the seeds positions are rotated by an angle around an axis defined through a rotation quaternion (Figure 2-16, step 5). Finally, for best tessellation generation results in Neper, extraneous seeds are eliminated (Figure 2-16, step 6) if they are contained within the sample volume or if they are too close to other seeds ( $>threshold\%$  of equivalent spherical volume shared with other seeds). The final seed positions ( $x, y, z$ ) and weights ( $\omega(i) = \left(\frac{g(i)}{2}\right)^2$ ) are outputted to text files, as well as orientation and dislocation density data for each seed.

Once the seeds have been defined through this algorithm, Neper's tessellation module is used to create the synthetic microstructure. The shape and dimensions of the sample are again used as input for the tessellation module, as well as the generated seed position, weight, and orientation

text files. Regularization options are also specified for tessellation, to remove small edges and faces that can negatively affect mesh quality.

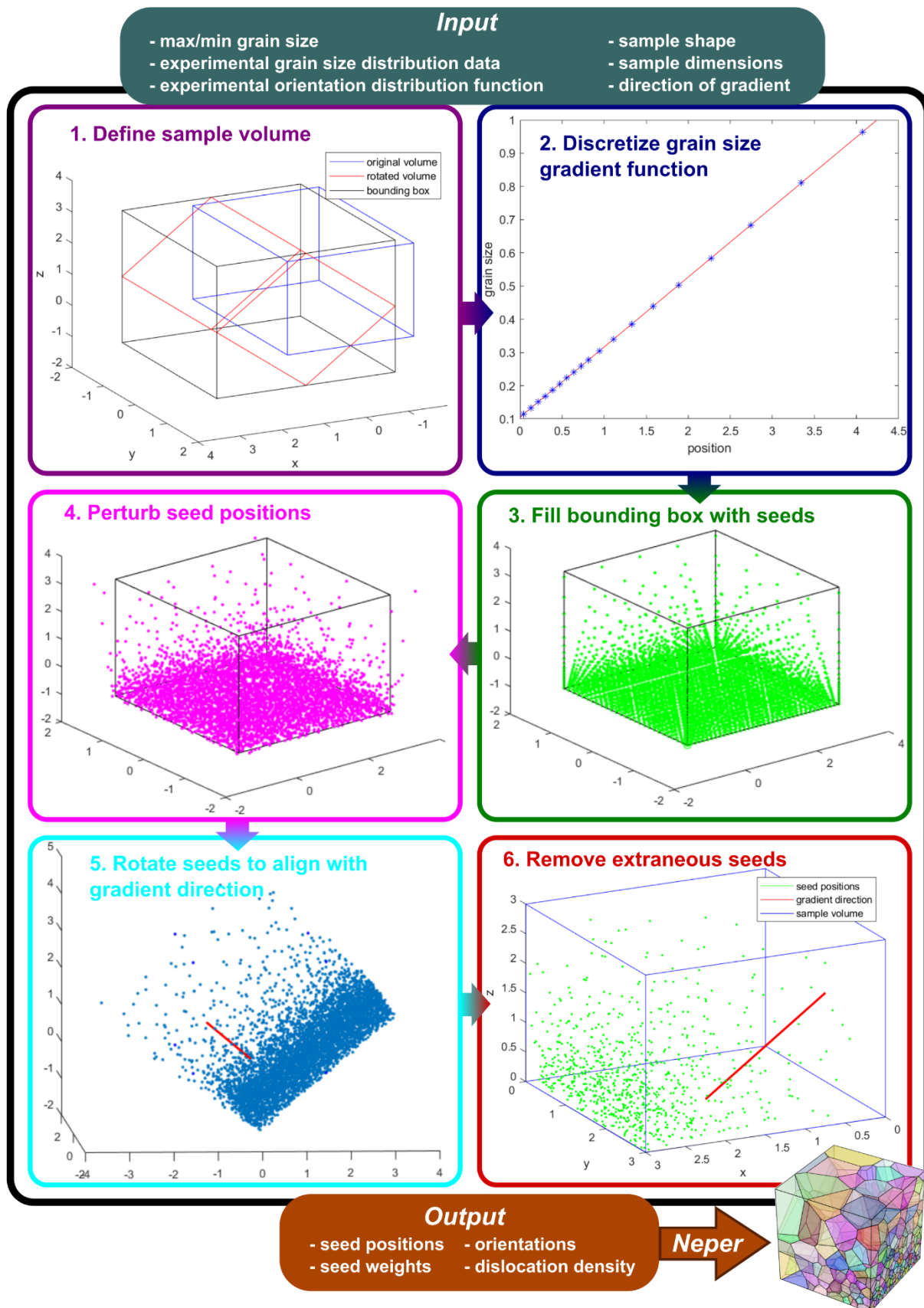


Figure 2-16: Seed generation algorithm

#### 2.6.4 *Incorporating dislocation density and grain size effects into the simulations*

In addition to using the experimental TKD pattern to specify the grain size gradient, minimum grain size, and orientations, we calculated the geometrically necessary dislocation density (GND) from local misorientation data using the approach outlined in Section 2.4.4 and fit a power law curve to data points of average dislocation density vs grain size (examples in Figure 2-17 (a-b)). This relationship between the dislocation density and grain size could be used as an alternative to the empirically derived Hall-Petch parameter. The Hall-Petch effect is a general term for describing the phenomenon of increasing strength with decreasing grain size. Experimental data is typically used to quantify this effect, with little regard for the underlying nanomechanical mechanisms controlling the size effect [116]. In a similar way, the Hall-Petch parameter for silver was derived through fitting to experimental bulk polycrystalline data with different grain sizes (Section 2.6.2). Instead, we investigate if the experimentally defined dislocation density distribution can provide the same effect without relying on the empirically derived Hall-Petch parameter.

Models are run using two methods to represent the grain size effects: i) the fitted Hall-Petch parameter and constant initial dislocation density, or ii) the experimentally defined dislocation density functions without the Hall-Petch parameter. Synthetic microstructures are constructed based on the experimental data using the methods developed in Section 2.6.3. Simulations based on the [100]-impacted microstructure and the [110]-impacted microstructure are run, with the two methods to represent the grain size effects (Figure 2-17 (c-d)). In both the [110] and [100] simulations, the results of method which uses the experimentally defined dislocation density function more closely follows the experimental data compared to the method using the fitted Hall-Petch parameter (Figure 2-17 (c-d)). These results also provide validation for

the experimental methods developed to calculate the dislocation density distributions (Section 2.4.4).

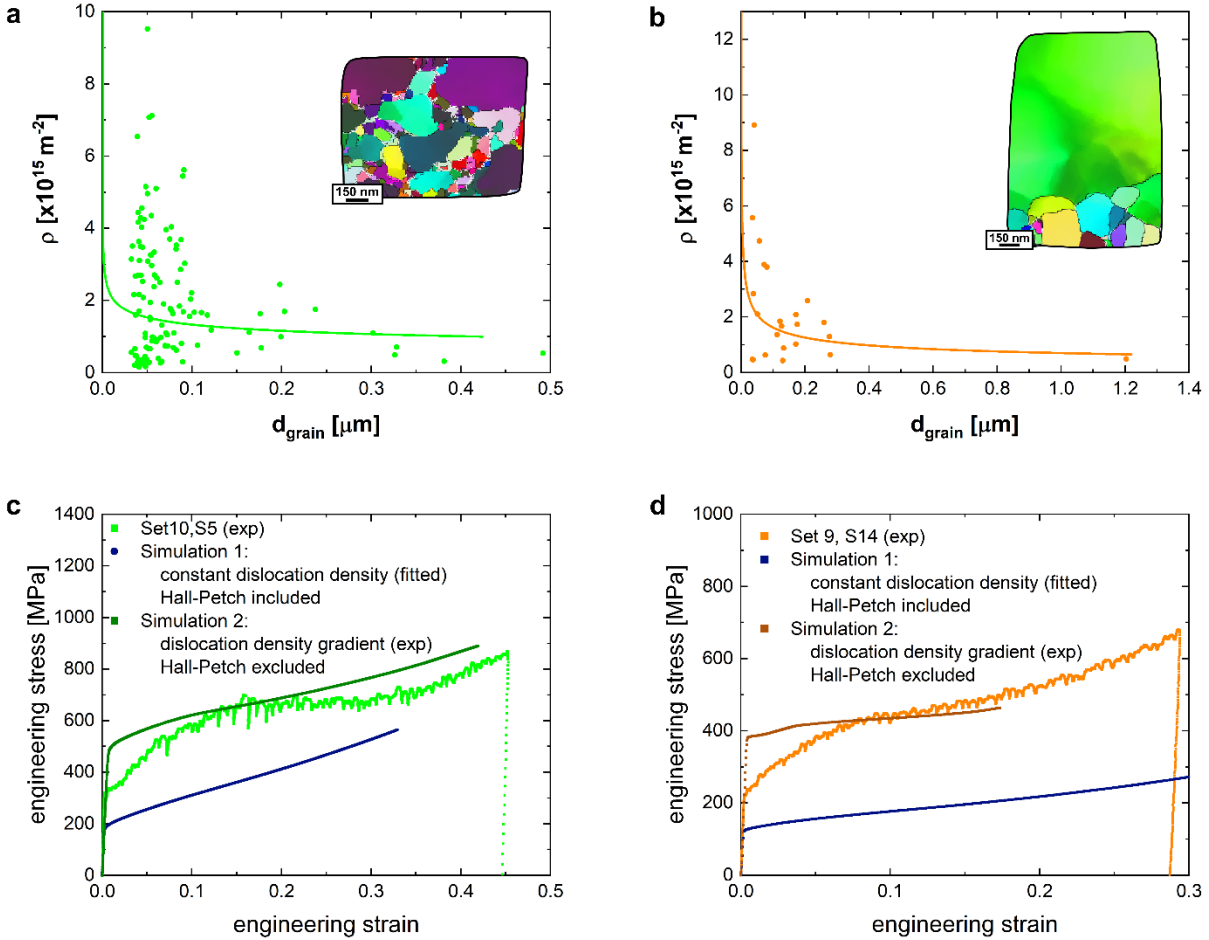


**Figure 2-17: Using experimentally defined GND density distributions in the simulations** (a-b) power law functions fitted to experimental GND density data from [100]-impacted (a) and [110]-impacted (b) samples, (c-d) stress-strain curves from crystal plasticity simulations of [100] samples (c) and [110] samples (d) using different methods to implement the grain size effect.

We can also investigate how the deformed geometries from the simulations compare to the experimental deformed geometry (Figure 2-18). Qualitatively, all simulations do a good job of replicating the deformed geometry of the compressed micropillar from experiments (Figure 2-18 (a)). The most deformation occurs in the coarse-grained region at the top of the sample, whereas



limited deformation occurs towards the bottom of the sample where a line of nanograins reside. This abrupt change in grain size causes the top of the sample to bulge over the bottom. Looking at the deformed geometries of the simulations, the second and third cases with the dislocation density gradient exhibit very similar deformed geometries when viewed from all directions (Figure 2-18 (c)). An unsymmetric bulging occurs in the samples with a dislocation density gradient, while a more symmetric bulging occurs in the sample with a constant dislocation density. For a more quantitative analysis, measurements of the deformed pillar widths along the sample heights were made from the SEM image of the compressed micropillar (Figure 2-18 (b)) and compressed geometries of the first and third simulations (Hall-Petch vs dislocation density gradient) oriented to most closely match the view from the SEM image. We see that the deformed geometry of the simulation with the dislocation density gradient most closely matches the deformed geometry seen in the SEM image (Figure 2-18 (b)). This is the second indicator that the dislocation density gradient is a better representation of the grain size dependent plasticity as compared to the empirically derived Hall-Petch parameter. Therefore, the experimentally derived dislocation density functions are used instead of the Hall-Petch parameter in all simulations.

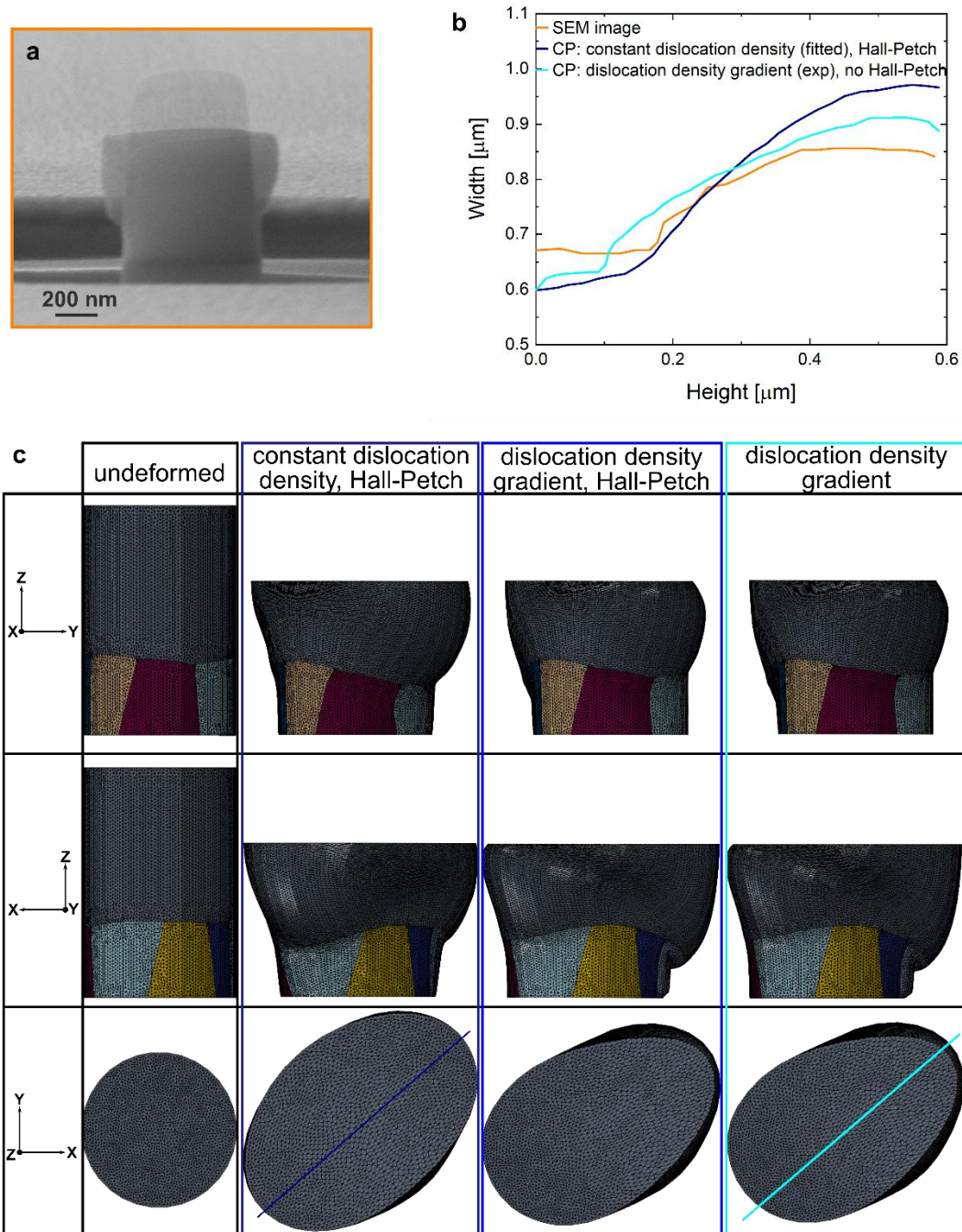


**Figure 2-18: Crystal plasticity simulations of [110]-impacted samples with analysis of different methods used to represent the grain size effect** (a) transparent SEM image of uncompressed pillar overlaid on SEM image of compressed pillar, (b) 2D width vs height profiles of the deformed geometries of samples from experiments and simulations, (c) undeformed and deformed geometries of the synthetic microstructures, viewed along the x, y, and z directions.

### 2.6.5 *Building the models and running simulations*

Neper's mesh module is used to produce an Abaqus input file defining a mesh based on the tessellation microstructure. Mesh generation parameters were altered, and the resultant meshes tested for quality and performance using the crystal plasticity model. Ultimately, first order 4-node tetrahedral elements were selected, as the model did not converge in a reasonable amount of time (several weeks) using second order tetrahedral elements. The relative characteristic length of elements is defined so that the resultant mesh contains ~1 million elements ( $\pm \sim 300,000$ ).

Models are built using meshes of the generated synthetic microstructures and additional nanostructural information from the TKD scan including grain orientations and dislocation density, defining the 36 material parameters for each element set/grain (see Section 2.6.2 for details about parameter determination), and setting loading and boundary conditions. Motion in all three directions is constrained for all nodes on the bottom face to prevent rigid body motion. The pillar is compressed to a true strain of ~40% (or the engineering strain at which the corresponding experiment was stopped at) at a strain rate of  $0.01 \text{ s}^{-1}$ , like experiments (Section 2.3.3). The displacement of each step, the final displacement and final time are calculated based on these quantities and the initial height of the sample. The first time step and max and min time steps are also defined, based on the convergence of the model. Since fully implicit time integration is used, the time step is determined by the rate of convergence not element size—allowing these large models to be run quite efficiently. An ABAQUS user subroutine (UMAT) is used to implement the single crystal plasticity model described in Section 2.6.1. After each model is built, it is checked using the preprocessor and only run if the mesh quality is good enough (~0.01% distorted elements). Depending on how many cpus are used (~7-15), each simulation typically takes

between ~1-4 days to complete, and upwards of 30 days for more complicated microstructures/meshes.

# ***Chapter 3. Improving mechanical properties through impact-induced nanostructural evolution of initially single crystal metals<sup>4</sup>***

## **3.1 Introduction**

The work presented in this chapter focuses on the process-structure-property relations of initially single crystal metals that have been restructured through high-velocity impact. Synthesized single crystal silver micro- and nanocubes and single crystal silver substrates are the model materials used for this study (Section 2.1.1). The single crystals are deformed through microprojectile impact testing (Section 2.3.1), and the resultant nanostructures and mechanical properties are studied. By starting with a single crystal, any nanostructural features observed after impact can be attributed to plastic deformation mechanisms activated through the impact

---

<sup>4</sup> The work presented in this chapter is partially adapted from the following research papers:

- 1) R. Thevamaran, C. Griesbach, S. Yazdi, M. Ponga, H. Alimadadi, O. Lawal, S.J. Jeon, E.L. Thomas, Dynamic martensitic phase transformation in single-crystal silver microcubes, *Acta Materialia* 182 (2020) 131–143
- 2) C. Griesbach, S.-J. Jeon, D.F. Rojas, M. Ponga, S. Yazdi, S. Pathak, N. Mara, E.L. Thomas, R. Thevamaran, Origins of size effects in initially dislocation-free single-crystal silver micro- and nanocubes, *Acta Materialia* 214 (2021)
- 3) C. Griesbach, J. Cai, S.-J. Jeon, R. Thevamaran, Orientation-dependent plasticity mechanisms control synergistic property improvement in dynamically deformed metals, *International Journal of Plasticity* (in review)
- 4) C. Griesbach, J. Cai, S.-J. Jeon, R. Thevamaran, Synergistic strength and toughness through impact-induced nanostructural evolutions in metals, *Extreme Mechanics Letters* (in review)
- 5) C. Griesbach, J. Cai, R. Thevamaran, Crystallographic orientation supersedes reflective shock dynamics during impact induced recrystallization (in preparation)
- 6) C. Griesbach, C. Bronkhorst, R. Thevamaran, Crystal plasticity simulations reveal cooperative plasticity mechanisms leading to enhanced strength and toughness in gradient nanostructured metals (in preparation)

conditions. The objectives defined in Section 1.1.1 are addressed through the carefully designed experiments and simulations presented in this chapter. Before delving into the findings of this research, this introduction provides contextual background for this work.

Before understanding the plasticity mechanisms governing impact-induced structural transformations, we must understand how single crystal face-centered-cubic (fcc) samples deform under quasi-static loading. Metals with an fcc structure readily deform by dislocation slip, through movement of dislocations on the  $\{111\}$  close-packed atomic planes in the  $\langle 110 \rangle$  directions. The set of four  $\{111\}$  planes and three  $\langle 110 \rangle$  directions constitute the twelve slip systems in fcc crystals. A slip system is activated when a critical resolved shear stress is reached, which can be determined through Schmid factor analysis (Appendix A.1). Slip in single crystals can be witnessed experimentally through slip steps apparent on the sample surface, which are especially apparent in quasi-statically compressed single crystal microsamples [40,117–133]. Small jumps in the force-displacement curves of compressed single crystals correspond to the slip events. Similarly, small jumps in the force-displacement curves obtained during nanoindentation testing of single crystal substrates are called pop-ins and are associated with slip events [39,134–137]. In both cases, the defect structure within the stressed volume can affect the mechanical response and the stresses achieved. Nearly-dislocation-free microsamples exhibit massive strain bursts upon yield, which are associated with spontaneous dislocation nucleation on multiple simultaneously activated slip systems [119,121,122,125]. These samples exhibit remarkably high yield strengths as the critical stress for dislocation nucleation must be achieved [123,138,139]. A sample size effect on strength is witnessed in single crystal microsamples, where differing mechanisms have been proposed to explain the size effect, depending on the initial defect content [118,125,126,140–143]. This sample size effect is distinct from the grain size effect, termed the Hall-Petch effect,

where decreasing the average grain size in a polycrystalline sample increases the strength of the material until a critical grain size ( $\sim 20$  nm) is reached [144–146]. In polycrystalline micromaterials, the intrinsic size effect from Hall-Petch strengthening and extrinsic sample size effect are naturally coupled, which introduces a complexity that has not been adequately studied yet [140]. Although the strengths achieved through testing of single crystal nanosamples or bulk nanograined samples are remarkable, they typically come at the cost of dramatically reduced toughness—often in the form of catastrophic failure. Coarse grained materials, on the other hand, exhibit much lower strengths but higher toughness.

This tradeoff between strength and toughness is not limited to the context of size effects but is a ubiquitous problem throughout most engineering materials. However, recent progress has been made to overcome this barrier. Materials containing various forms of nanostructural heterogeneities can exhibit non-homogeneous plastic deformation, providing an optimal combination of strength and ductility [6]. Examples of heterogeneous nanostructures designed to improve the strength and toughness include bimodal or harmonic structures [147], laminated or multilayered nanostructures [148,149], bulk metallic glass composites [150], hierarchical nanotwinned structures [151,152], and gradient nano-grained structures [153–161]. In the case of laminated or multilayered nanostructures, each layer is selected based on the active deformation mechanisms that will contribute positively to either the strength or toughness [148,149]. Hierarchical nanotwin structures provide increased strength with limited reduction in ductility, because twin boundaries are effective blockers to dislocation motion across the boundary, but still allow some plasticity to occur via dislocation glide parallel to the boundary [151,152].

A class of heterogeneous nanostructured materials called gradient nano-grained (GNG) materials have been shown to improve strength while retaining ductility [153]. GNG metals are

typically produced through severe plastic deformation processes such as surface mechanical grinding treatment [162,163], shot peening [164,165], or surface mechanical attrition treatment [154,160], in which surface grain refinement is induced on bulk samples. In several of these methods, imparted shock waves cause pronounced dislocation nucleation near the surface, yielding high dislocation densities on the order of  $10^{14}$ – $10^{17}$  m<sup>-2</sup> [164,166–169]. High dislocation densities are needed to rapidly accommodate the large strains. During such high strain rate deformation, dislocations organize into cellular networks forming subgrains. Upon further straining under high strain rates, these subgrains can progressively rotate into recrystallized grains with high angle grain boundaries [170]. Experimental evidence of the relationship between dislocation density and grain size gradients formed through the shock wave progression is limited. Typically, a nanograined surface layer is produced on bulk coarse grained samples which have an initial dislocation density and complex grain structure; therefore, the dislocation and grain size distributions formed through the shock loading process cannot be isolated and analyzed.

Mechanical testing of bulk GNG materials show improved strength with comparable ductility to the coarse-grained samples [154,160,163–165,171]. These synergistic improvements in strength and toughness are attributed to strain gradients that arise from mechanical incompatibility between layers, causing back stresses which lead to strain hardening in the softer region [154,160,164,165]. During mechanical loading of GNG materials, the coarse grains yield first while the hard nanograined region remains elastic [153]. Geometrically necessary dislocations must accommodate this elastic-plastic mismatch and pile-up at the boundary, producing back-stresses in the soft domain [172]. A discrete dislocation dynamics study of GNG materials clearly shows spikes in the dislocation density at interface regions, supporting this theory [173]. GND pile-up at the boundary also produces forward stresses into the hard domain, which may make the



hard domain softer [172]. Grain growth, a potential softening mechanism, has been reported in the nanograined domains of GNG materials [162,165]. Grain growth can enhance the ductility of nanograined materials when high dislocation densities promote cooperative grain boundary migration and rotation [174,175]. A few studies hypothesize that the GNG structure mitigates these mechanisms through stabilization of the nanograined region by the coarse grained core [162,176]. However, when yielding of the nanograined region eventually occurs, these intergranular plasticity mechanisms are vital for increasing the ductility of nanograined regions. This understanding leads us to wonder whether we could tune the extent to which intergranular and intragranular plasticity mechanisms are active to produce optimal strength-toughness synergy. Through carefully constructed experiments, we probe the full process-structure-property cycle of impact-induced heterogeneous nanostructures and find that dramatic improvements in strength and toughness can be achieved through tuning the active plasticity mechanisms which depend on the impact-orientation dependent nanostructures.

### **3.2 Quasi-static deformation of silver single crystals**

Developing a mechanistic understanding of the quasi-static deformation of silver single crystals sets a foundation for studying the impact-induced nanostructures and resultant changes in mechanical properties. Quasi-static compression tests are performed to measure the stress-strain response of the single crystal samples—forming a basis for comparison to the impact-induced nanostructures’ mechanical properties. In addition to measuring the mechanical response of the single crystal samples, three foundational objectives motivate this work: develop a fundamental understanding of (i) sample size effects on strength, (ii) dislocation nucleation mechanisms, and (iii) the effects of FIB-induced defects. To meet these objectives, quasi-static compression tests are performed on dislocation-free Ag microcubes (Section 2.1.1) and FIB-fabricated micropillars

(Section 2.2.3) of varying sample size (effective diameter: ~100–2000 nm) using an *in situ* SEM nanoindenter (Section 2.3.3). Additionally, transmission electron microscopy (Section 2.4.2) and molecular statics simulations (Section 2.5.1) are used to provide insight on defect nucleation and propagation during compression.

Since we study the mechanical response of micron sized samples, we must clearly understand the origin of sample size effects. Sample size effects have been previously explained through the dislocation starvation [121,126,141,177] and single-arm-source theories [118,140–143]. However, neither of these mechanisms explain a size effect on yield strength in initially dislocation free samples, since they rely on pre-existing mobile dislocations. While most experiments of dislocation-free single-crystal samples reveal that there is a size effect on the yield strength [119,121,123], it is still not well-understood what causes this size effect. Several studies suggest that a truly defect-free single-crystal sample should yield at theoretical strength [122,131,178]. Here, we study the dislocation nucleation mechanisms in initially dislocation-free Ag microcubes to understand the origins of size effects. Furthermore, we investigate what effects surface defects and FIB-induced defects have on the stress-strain response of single crystals and resultant size effects.

### 3.2.1 Quasi-static compression response of initially dislocation-free Ag microcubes

Figure 3-1 shows an example of the quasi-static compression response of an Ag microcube (effective diameter:  $D=2298$  nm). The sample exhibits linear elastic behavior up to a yield strength of  $\sim 550$  MPa (point 2 in Figure 3-1(a)), which is over 9x higher than the bulk yield strength of Ag ( $\sigma_{\text{bulk Ag}} \sim 60$  MPa [7]). The jump in strain between points (2) and (4) on the stress-strain curve (Figure 3-1(a)) corresponds to a spontaneous strain-burst by almost 50% of its original height within a 20 ms interval. This instantaneous strain burst is caused by dislocation avalanches that rapidly propagate through the crystal and exit the sample surface, forming surface slip steps as seen in the SEM image (Figure 3-1(b)). Large strain bursts such as

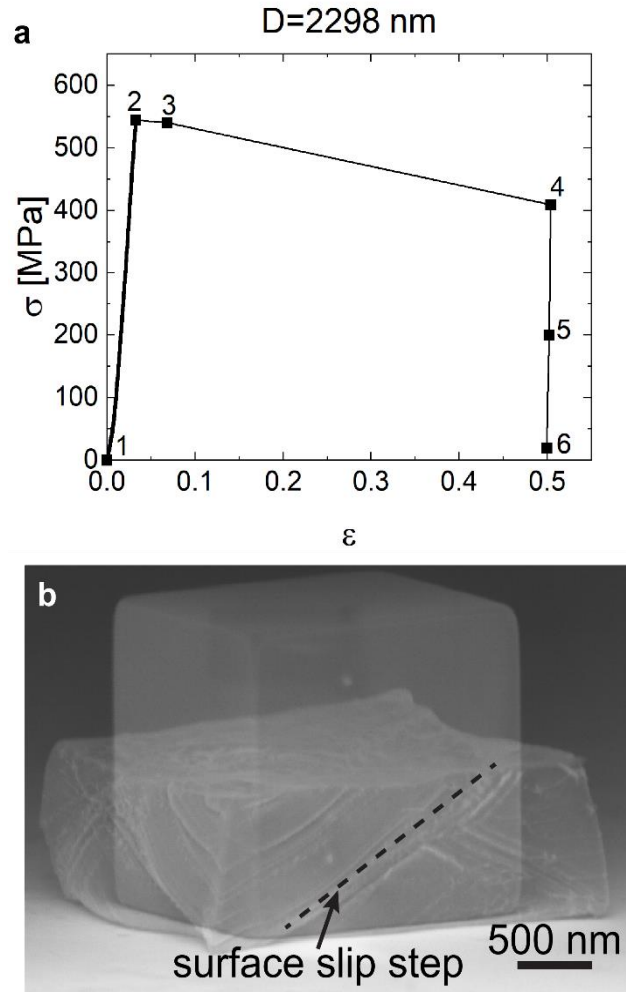


**Figure 3-1: Quasi-static compression response of an Ag microcube** (a) stress-strain response with important features labeled, (b) semi-transparent SEM image of microcube before compression overlaid on SEM image taken after strain burst: notice multiple surface slip steps apparent in the deformed cube.

this are due to simultaneous activation of multiple slip systems. Under a perfect  $\langle 100 \rangle$  loading condition, Schmid factor analysis predicts slip is equally likely to occur on eight different slip systems (see Appendix A.1 for details). Several of these slip systems may have been activated

simultaneously in this sample to accommodate the massive strain burst. Additional details about the massive strain bursts can be found in Appendix B.1.

Through performing TEM (Section 2.4.2) on FIB-prepared electron transparent lamella (Section 2.2.4), we investigated the post-compression microstructure of a sample immediately after the initial large strain-burst, before further compression (Figure 3-2 (a,c)). A high dislocation content is visible in the bright-field TEM images (Figure 3-2 (d,e)). The dark contrast bands intersecting in the sample's interior (Figure 3-2 (d)) are avalanches of dislocations moving through the crystal on the  $\{111\}$  planes. Similar bands are seen at the top left of the sample (Figure 3-2 (d)) but they seem to intersect at the top of the sample. There may have been a surface defect at this point which created a preferential location to nucleate dislocations. The SAD obtained across the cross-section (representative SAD in Figure 3-2 (b)) reveals that the structure remains single crystal even after being compressed by over 20%, albeit with a high-density of dislocation loops.

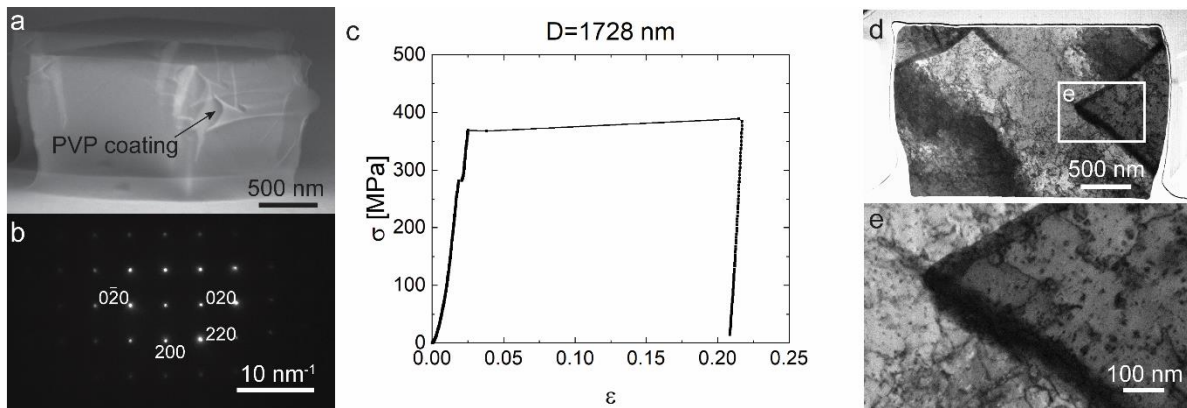


**Figure 3-2: Post-compression microstructure immediately after the massive strain-burst** (a) SEM image of a sample compressed until the massive strain-burst with semi-transparent image of the sample before compression overlaid, (b) SAD pattern showing single-crystal structure was retained, (c) deformation response of the compressed cube in (a), (d) bright-field TEM image of a cross sectional lamellae ( $<100$  nm thick, viewed along the  $<100>$  direction) of the compressed cube in (a) showing large dislocation density throughout sample, (e) magnified view of the region identified in (d) showing dislocation avalanches on  $\{111\}$  planes.

We performed quasi-static compression tests on 25 Ag cubes ranging in size from about 100 nm to 2000 nm. The smallest ~100 nm cubes yield at phenomenal strengths, up to a quarter of the theoretical strength of silver loaded in the  $\langle 100 \rangle$  direction. The massive strain bursts were not witnessed in all samples (Figure 3-3); out of the 25 cubes tested, nine did not exhibit a massive strain burst (see Appendix A.3 for SEM images and stress-strain curves for all samples tested). Instead, these samples exhibit a strain hardening behavior immediately after the initial linear elastic regime. Post-compression SEM images and *in situ* SEM images reveal the samples deform through gradual slip on multiple planes in contrast to the strain-burst samples in which slips in multiple slip systems occur simultaneously. The absence of a massive strain burst suggests conditions were not adequate to induce simultaneous slip on multiple slip systems and parallel planes. SEM images of samples before compression show key differences in the samples which exhibited a strain burst and those that did not (Figure 3-3 (d,e), Appendix B.1). For example, a pristine sample surface and sharp edges and corners are seen in the SEM image of a sample (D=2174 nm) which exhibited a strain burst (Figure 3-3 (d)). In contrast, jagged edges are apparent in the SEM image of a similarly sized sample which did not exhibit a strain burst (Figure 3-3 (e)). The jagged edges could have formed during synthesis or resulted from inter-particle collisions during vortex mixing. These findings suggest that surface and edge defects can significantly alter the deformation response of the cube.

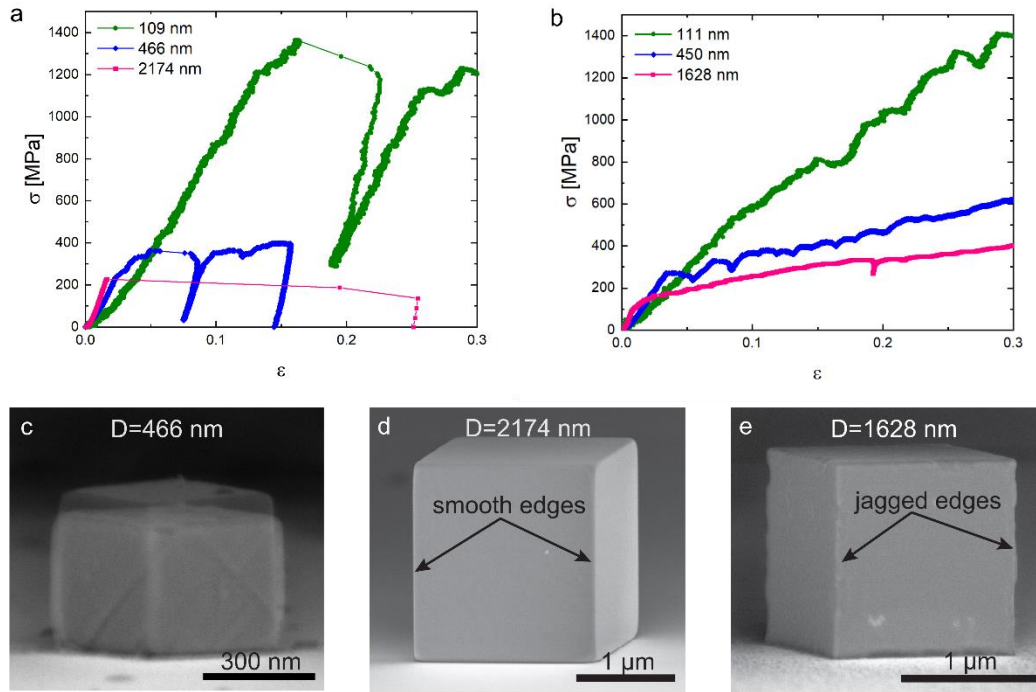


**Figure 3-3: Stochastic deformation nature** (a) stress-strain curves of three representative samples showing a strain burst, (b) stress-strain curves of three representative samples which did not exhibit a large strain burst, (c) semi-transparent SEM image of nanocube ( $D = 466$  nm) before compression overlaid on SEM image taken after strain burst, (d) SEM image of cube which exhibited a strain burst ( $D = 2174$  nm); cube has smooth edges and surfaces, (e) SEM image of cube which did not exhibit a strain burst ( $D = 1628$  nm); cube has jagged edges.

### 3.2.2 Effects of FIB-induced defects on the mechanical response of single crystals

To investigate the influence of potential FIB-induced defects, micropillars were fabricated from pristine Ag microcubes and from a [100]-oriented commercially available Ag substrate. Compression tests were performed on seventeen micropillars FIB-milled from Ag microcubes and six micropillars FIB-milled from the [100]-oriented Ag substrate. Representative stress-strain curves (Figure 3-4 (a)) reveal that FIB milling reduces the yield strength. Additionally, the FIB-milled micropillars do not exhibit a massive strain burst upon yield like the pristine synthesized cubes. However, there are many small strain bursts as evident in the jagged curve post-yield. These

differences in the stress-strain curves suggest that defects were created as a result of the  $\text{Ga}^+$  ion-bombardment during FIB milling. Studies have shown that defects such as vacancies, interstitials, and dislocations can be induced as a result of the ion-bombardment during FIB milling and even when imaging with low ion doses [29,119,179]. Without the need to spontaneously nucleate dislocations, samples exhibit lower yield strength, and the dramatic strain burst does not occur. The average yield strength of micropillars milled from the cubes ( $\sigma_y = 105.9 \text{ MPa}$ ) is very similar to the yield strength of micropillars milled from the substrate ( $\sigma_y = 100.3 \text{ MPa}$ ), but the standard deviation is higher for the pillars from the cubes (cube pillars:  $SD\sigma_y = 23.6 \text{ MPa}$ , substrate pillars:  $SD\sigma_y = 10.4 \text{ MPa}$ ) (Figure 3-4 (b)). These results confirm that the [100]-oriented substrate can be compared to the Ag microcubes (w/ defects). Less variation in the mechanical response of the substrate pillars is likely due to a more consistent defect structure.

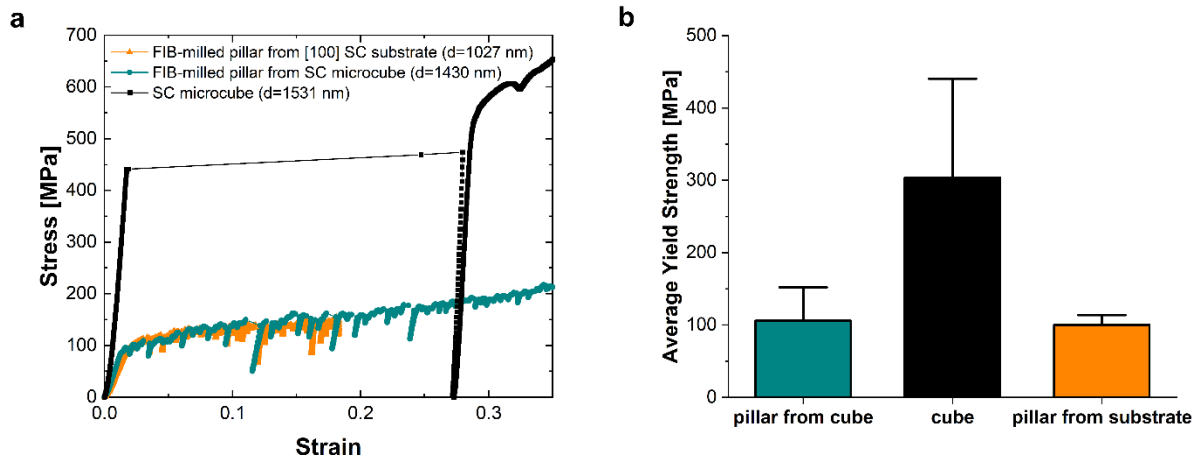


**Figure 3-4: Effects of FIB milling on the mechanical response** (a) stress-strain response of pristine single crystal microcube compared to FIB-milled micropillars fabricated from a microcube and a [100] single crystal substrate, (b) average and standard deviation of yield strength for pristine and FIB-fabricated [100]-loaded samples.

### 3.2.3 *Analysis of dislocation nucleation mechanisms through molecular statics simulations*

Through microcompression tests of Ag single crystals, we have seen that defects greatly affect the mechanical response. To investigate the plasticity mechanisms that govern the stochastic deformation response, we performed molecular statics (MS) simulations (Section 2.5.1) on models of Ag cubes. Since the synthesized Ag microcubes are initially dislocation free (Section 2.1.1), the observed stochasticity in the deformation responses of different cubes must be due to defects other than dislocations. Therefore, we simulated cubes with a perfect face-centered-cubic atomic structure, cubes with high vacancy concentrations (porosity), and cubes with rounded edges and corners. We examine differences in the dislocation nucleation mechanisms and subsequent dislocation evolution in all three cases (Figure 3-5). In the cube with a perfect fcc atomic structure, dislocation nucleation occurs simultaneously at all eight vertices (Figure 3-5(a)). The nucleated dislocations then propagate from each corner on two different  $\{111\}$  slip planes and intersect with each other in the center of the crystal, forming sessile dislocations (Figure 3-5(a), step 7). An evolved dislocation network reflecting the cubic symmetry of the perfect fcc structure is seen in the later stages of deformation (Figure 3-5(a), step 44). The simultaneous dislocation nucleation from each vertex confirms the conclusion drawn from experiments that simultaneous activation of all eight slip systems (predicted by Schmid factor analysis) accommodates the massive strain bursts. To try to replicate the stochastic deformation response seen in experiments, the dislocation nucleation mechanisms of samples with large vacancy concentrations and rounded edges are also examined.

The effect of vacancy concentration on dislocation nucleation can be observed in Figure 3-5 (b-d), where the dislocation emission in samples with no vacancies (Figure 3-5(b)) and a



vacancy concentration of  $p = 0.5\%$  (Figure 3-5(d)) are shown. In the case of the pristine sample, the dislocations are initially emitted from the corners of the sample (mid-cross section shows evolved dislocation structure like in Figure 3-5(a), step 44). On the other hand, when vacancies were placed in the sample (Figure 3-5(d)), the dislocations are now nucleated randomly in the cube. This emission is controlled by the distribution of the defect network, which breaks the symmetry observed for the pristine case. This heterogeneous dislocation nucleation corresponds to a reduction in the peak stresses achieved in samples with non-zero porosity (Figure 3-5(c)). This is likely because stress concentrations develop at the vacancy sites, where the critical stress for dislocation nucleation can be achieved at lower applied force.

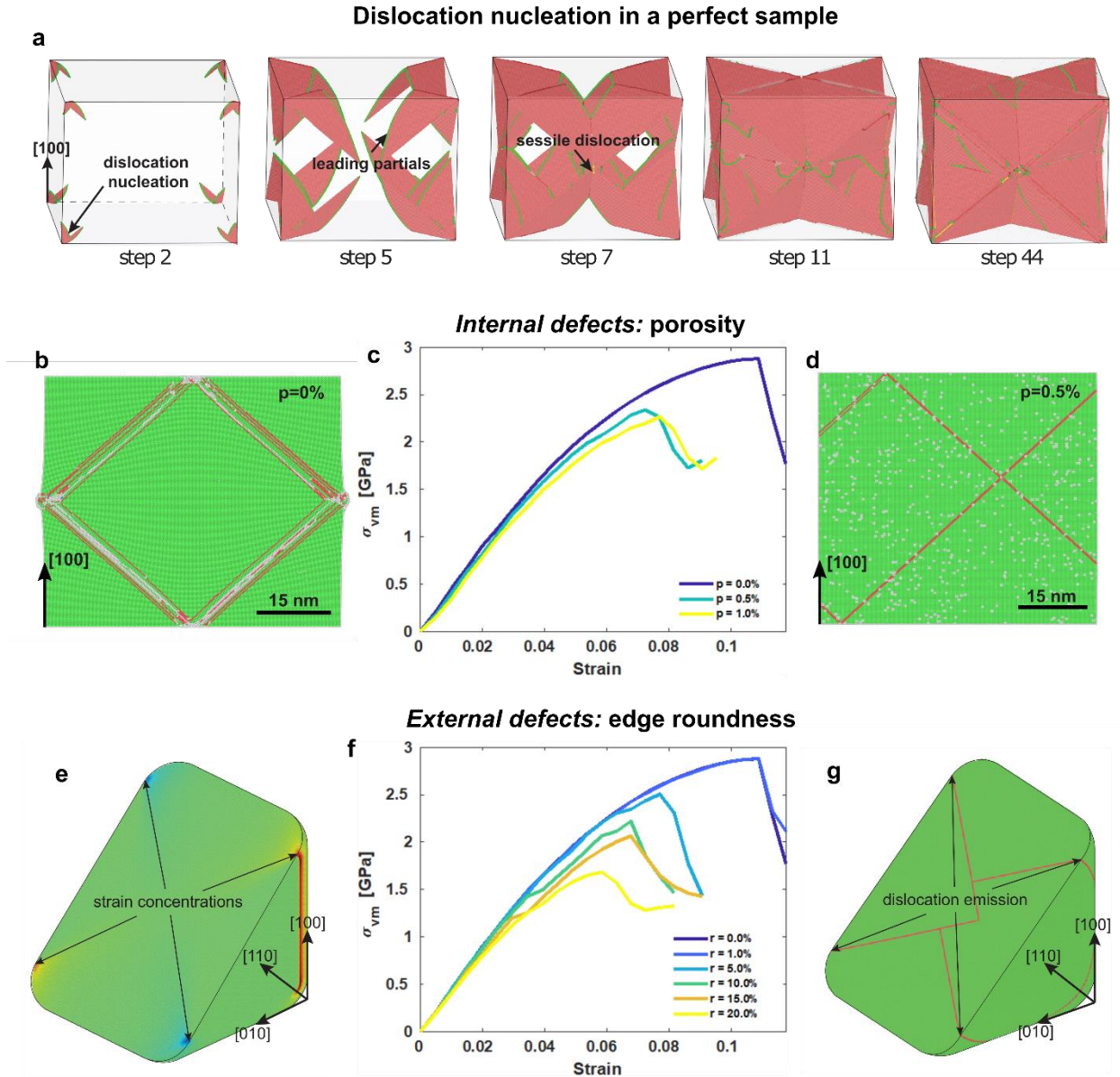


**Figure 3-5: Dislocation nucleation mechanisms revealed through molecular statics simulations** (a) dislocation nucleation and propagation in a perfect cubic sample without internal defects, (b) midsection of perfect sample showing symmetric dislocation structure, (c) stress-strain curves of samples with varying porosity (vacancy conglomerations), (d) midsection of sample with 0.5% porosity showing unsymmetric dislocation structure, (e) sample with rounded edges and corners showing elastic strain localization before first dislocation nucleation event, (f) stress-strain curves of samples with varying edge roundness, (g) stacking faults in red, showing path of partial dislocations nucleated from corners near rounded edges.

The effect of rounding the sample's edges is also investigated through MS simulations (Figure 3-5(e-g)). As evident through the stress-strain curves of samples with different edge

roundness ratios ( $r_e = R/L_0 = 0 - 20\%$ ), edge roundness has a detrimental effect on the peak strength of the particles (Figure 3-5(f)). Again, the dislocation nucleation mechanisms are behind the reduction in strength. Figure 3-5(e) shows a (110) section of a sample with  $r_e = 20\%$  at  $\sim 3\%$  strain. At this level of strain, the sample has not yet emitted any dislocations; however, there are elastic strain localizations near the intersections between the rounded edges and flat surfaces of the particles. These strain localizations coincide with the locations of the first dislocation nucleation events. This can be seen in Figure 3-5(g) where four planes of atoms in stacking fault structure are seen in red. The stacking fault planes indicate that several Shockley partial dislocations have been emitted from these points. This dislocation nucleation mechanism explains the observed trend of reduction in peak stress with increased edge roundness. The rounded edges cause local atomic defects in the perfect cubic geometry comprised of an fcc atomic structure. These surface defects are locations of strain and stress localizations, which are favorable sites for dislocation nucleation. As more rounded edges are simply longer surface defects, it will make dislocation nucleation easier, initiating plasticity at lower stresses and strains.

### 3.2.4 *Origins of sample size effects*

Clearly, external and internal defects affect the dislocation nucleation mechanisms, which determine the material's yield strength. This understanding provides insight into origins of sample size effects. All samples tested exhibit a size effect on yield strength (Figure 3-6). Our experimental data sets all have a similar degree of size effect (slope: exponent of  $(D/b)$ ) and are similar to values found in literature. The as-synthesized cubes (red and blue) have a slightly stronger size effect than the FIB-fabricated pillars (teal and pink). The stochastic nature of the “strain-burst” samples' deformation (red) is indicated by the large scatter in data points. We also see a less pronounced, but clear size effect in the MS data from the cubes with 15% rounded edges

(orange). This size effect originates from the defects caused by removing the edge and corner atoms. These MS simulations, in addition to the comparison of the cube and pillar data from experiments, confirms that the external geometry influences the size effect.

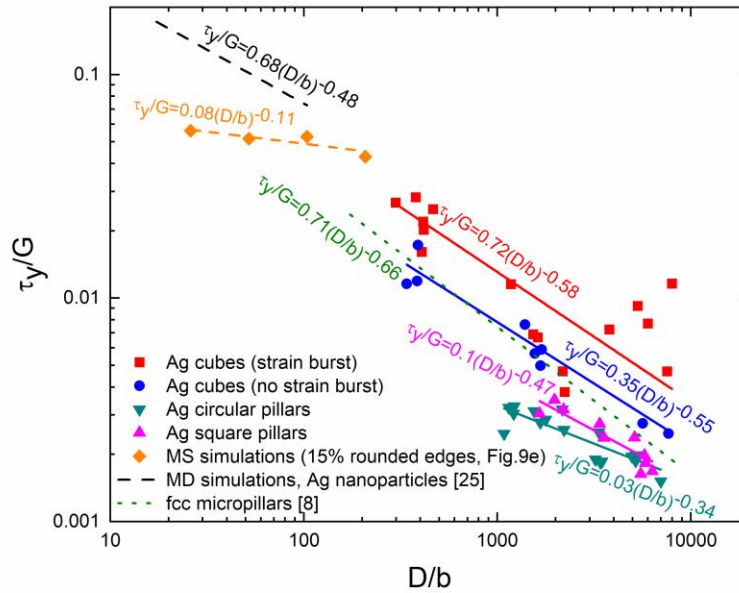


**Figure 3-6: Size effect on yield strength:** log-log plot of normalized shear yield strengths versus normalized sample sizes; power law fits of our experimental data: Ag strain-burst (red), no-strain-burst (blue), FIB-fabricated circular pillar (teal), and FIB-fabricated square pillar (pink) sample sets, and our MS simulations of samples with 15% edge roundness (orange) compared to data from literature (modeled Ag nanoparticles [138] (black), compilation of fcc micropillars [180] (green)).

While the size effects (slopes) of the experimental data sets are similar (Figure 3-6), the intercept of the fitted curves vary along the y-axis—demonstrating that each sample set achieves different strengths across sample sizes. For example, the FIB-fabricated pillars (teal and pink) yield at strengths consistently lower than those of the as-synthesized cubic samples without FIB exposure (both those that exhibited strain bursts and those that did not). We attribute the lower strength to a higher initial defect content, whether that be FIB-induced dislocations or  $\text{Ga}^+$

implantation. This is consistent with the trend that the higher the initial defects, the lower the yield strength is: the MD simulations of Ag nanoparticles [138] and our MS simulations of Ag nanocubes show the highest yield strengths since they are free of any internal defects. Feruz and Mordehai explain that the size effect seen in their MD simulations is due to the faceted particle shape, which elicits differing stress gradients depending on the particle size [138]. We were also able to produce a size effect in our MS simulations by rounding the cube edges, which creates atomic-level surface defects of lengths proportional to the sample size. Our Ag microcubes which exhibited a large strain burst yield at slightly lower strength, followed by the cubes which did not exhibit a strain burst, which had more initial surface defects. Lastly, the Ag micropillars yield at even lower strengths since the FIB fabrication process introduces more defects from  $\text{Ga}^+$  ion bombardment. These results show that slight differences in the initial defect structure have an immense influence on the mechanical performance of the material.

We also considered how slight differences in the initial defect structure could influence the size effect. Particularly, because our as-synthesized cubes are initially dislocation-free but still exhibit a size effect, we investigated what defects (other than dislocations) could be contributing to the size effect. The samples which exhibited a strain-burst are initially dislocation free as shown in the HRTEM image in Figure 2-1. Without any preexisting dislocations, the observed size effect on yield strength must be due to differing dislocation nucleation mechanisms. Dislocations can be nucleated homogeneously or heterogeneously [181]. Heterogeneous nucleation is favored as it requires much lower levels of stress than homogeneous nucleation [122]. Dislocations are nucleated heterogeneously at areas of high stress concentration [121,122,133,138,139,181]. If the stress state is perfectly uniform—free of any stress concentrations—homogenous nucleation at the theoretical stress may occur; however, this is generally not experimentally achievable. More

commonly, heterogenous nucleation occurs, driven by factors that disrupt the perfect cubic symmetry and elicit stress or strain concentrations. We have investigated several of these potential factors in this work, including the external defects such as surface asperities and edge roundedness, and internal defects such as vacancy conglomerations.

External defects such as surface asperities or rounded edges can cause stress and strain concentrations to develop at localized regions and at the sample-indenter interface, initiating early dislocation nucleation at these locations. Larger cubes may have a greater probability of surface defects, which has been used to describe the size effect in terms of a weakest-link model through Weibull statistics [119,142,143]. We have also investigated the effects of external geometry and edge roundness on the size effect, both through MS simulations and experiments. In experiments, the larger cubes have sharper edges and corners than the smallest 100 nm cubes ( $r_e = 2.3\%$  for microcubes,  $r_e = 13.8\%$  for 100nm cubes). Since the smallest cubes yielded at higher strengths than the larger cubes (defining the size effect), this may suggest that rounder edges correlate with dislocation nucleation at higher stresses. However, MS simulations reveal that rounding the cube edges and corners will actually have a detrimental effect on the strength, since rounded edges break the perfect cubic symmetry at the atomic scale and create strain localizations where the rounded edge meet the cube faces—prime locations for dislocation nucleation. With this understanding, we can conclude that the edge roundness ratio ( $r_e = R/L_0$ ) may not be as important as the actual edge radius size ( $R$ ), as the disruption of the perfect cubic atomic structure is what creates the local strain concentrations, initiating dislocation nucleation at the rounded edges.

In addition to external defects, internal defects can also break the perfect cubic symmetry and influence dislocation nucleation mechanisms. The MS simulations of cubes with varying vacancy concentrations reveal that vacancy conglomerations have a strong detrimental effect on

the strength since dislocations are preferentially nucleated at the stress concentrations near the voids. Combining the effects of vacancy concentration and edge roundness, the vacancy concentration has greater control over nanocrystal plasticity than edge roundness—illuminating the coupled effects of external and internal atomic-level symmetry breakers. Additional studies into the vacancy concentrations or void generations resulting from a seed-mediated growth synthesis method could provide further validation.

Through quasi-static compression of single crystal Ag microsamples, we have gained a mechanistic understanding of the origins of sample size effects and the influence of defects on heterogeneous dislocation nucleation. Sample size effects are attributed to various internal and external defects, which break the perfect cubic crystal structure and initiate heterogeneous dislocation nucleation at lower stresses: smaller samples have a lower probability of containing such defects. This study provides a foundation for studying the process-structure-property relations of dynamically deformed single crystals.

### 3.3 Impact-induced nanostructural evolution of single crystals

With a foundational understanding of the quasi-static deformation mechanisms of single crystal silver, we study the distinct plasticity mechanisms that arise during ultra-high strain rate deformation ( $\sim 10^8 \text{ s}^{-1}$ ). High strain rate deformation is used in various material processing methods to induce dramatic nano and microstructural changes. Extensive structural changes can arise through mechanistic pathways such as dynamic recrystallization and martensitic phase transformations. We can use these mechanistic pathways to produce desired nanostructures if we understand the favorable conditions to active such mechanisms. Clearly correlating processing conditions to the resultant nanostructures is possible by studying the impact-induced structural changes of initially single crystals. The work presented in this section provides a fundamental understanding of the influence of three processing conditions—the strain-rate, crystal orientation, and reflective shock dynamics—on the nanostructural evolution of single crystal silver.

To achieve this understanding, complementary sets of experiments and molecular dynamics simulations were performed. High strain rate deformation of Ag microcubes (Section 2.1.1) is studied through high velocity impact of microcubes onto a rigid target using the LIPIT apparatus (Section 2.3.1) and post-impact nanostructural characterization using TEM (Section 2.4.2) or TKD (Section 2.4.4). Nanostructural characterization is performed on electron transparent lamellae (Section 2.2.4) FIB-milled from cross sections of cubes impacted on their faces ([100] crystal orientation), edges ([110] crystal orientation) and corners ([111] crystal orientation). These three orientations are studied throughout this work to investigate the effect of crystal orientation on the process-structure-property relations of impact-induced nanostructured metals. MD simulations of Ag nanocubes impacted along the [100] and [110] directions are performed to investigate the nanostructural evolution and corresponding temporal and spatial



distributions of stress and temperature during impact (Section 2.5.2). Additionally, to investigate how free surfaces play a role in the impact-induced nanostructural evolution, we perform similar experiments on single crystal Ag substrates with [100], [110], and [111] surface normal directions (Section 2.1.1) impacted with rigid spherical projectiles using the LIPIT apparatus. Electron transparent lamellae are extracted from the regions under the impact craters (along a particular direction of interest) and TKD is performed to characterize the deformed nanostructures.

### 3.3.1 *High strain rate deformation of initially single crystal Ag microcubes*

Using our custom built LIPIT apparatus, we launch single crystal Ag microcubes at ~400 m/s. Upon hitting a rigid Si substrate at supersonic velocity, the Ag microcube dynamically deforms at strain rates on the order of  $10^8 \text{ s}^{-1}$ . At ten orders of magnitude higher strain rate than the quasi-static compression strain rate ( $10^{-2} \text{ s}^{-1}$ ), we can investigate what effect dramatically different strain rates have on the plastic deformation. Microcubes impacted on their faces are selected for comparison to the quasi-statically compressed cubes, since the loading direction with respect to the crystallographic orientation ([100]) is the same. Differences in the plastic deformation due to strain rate are immediately apparent in the external deformed geometries (Figure 3-7). The quasi-statically compressed cube shows more uniform deformation along the sample height (Figure 3-7 (a)), while the impacted cube shows more outward material flow near the impact plane than on top (Figure 3-7 (c))—indicating a strain gradient emerges during impact-induced deformation. This distinction is a direct result of the differing strain rates resulting in varying stress states. At a strain rate of  $0.01 \text{ s}^{-1}$ , inertial effects can be neglected, and the entire body uniformly deforms under the uniaxial compressive loading (the bulging observed in the mid region at large strain is due to the frictional restraints by the indenter and the substrate, though it is minimized by the thin PVP layer). Since the synthesized microcubes are initially dislocation free, uniform uniaxial loading induces

spontaneous dislocation nucleation from both the top and bottom surfaces. The surface slip steps on parallel  $\{111\}$  crystallographic planes reveal pronounced dislocation slip events which accommodate the plastic deformation throughout the sample. In contrast, at the high strain rate ( $10^8 \text{ s}^{-1}$ ) achieved during impact, a shock wave develops at the bottom of the sample (near the impact plane) and propagates towards the top region of the cube. This results in dislocations being initially nucleated from only the bottom surface. The propagation of the impact-induced shock wave results in gradient plastic deformation of the sample, producing the deformed shape in Figure 3-7 (c).

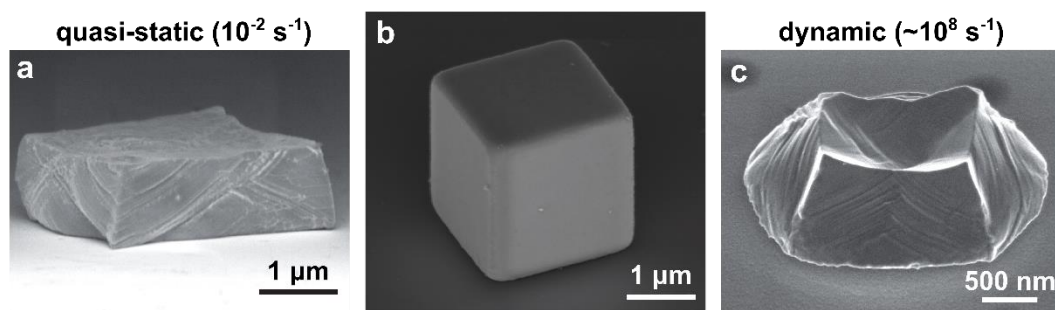


**Figure 3-7: Distinct deformed geometries depending on strain rate: SEM images of (a) Ag microcube deformed under quasi-static loading, (b) undeformed Ag microcube, and (c) Ag microcube deformed under dynamic loading.**

TEM analysis of the quasi-statically compressed microcubes revealed that although significant dislocation plasticity occurred during compression, the compressed cube remained single crystal. At high strain rates, the dynamic stress state may initiate additional plastic deformation mechanisms which significantly alter the crystal structure of the cube. To investigate potential impact-induced nanostructural changes, an Ag microcube impacted along the  $[100]$  direction (face impact) was cross sectioned and thinned to electron transparency for subsequent TEM analysis within 24 hours after impact. Stitched bright field TEM images reveal a highly disordered nanostructure (Figure 3-8 (a)). Selected area diffraction (SAD) patterns were taken at the positions indicated by circles in Figure 3-8 (a). The SAD patterns in Figure 3-8 (b–d) are not consistent with a face-centered-cubic

(fcc) crystal structure. Additionally, streaks and multiple symmetric spot patterns of varying intensities reveal a nanocrystalline structure (multiple grains were probed within the small area of the aperture). Instead of an fcc structure, the SAD patterns exhibit an hcp crystal structure (Figure 3-8 (b-d)). Each diffraction pattern was examined with several different zone axes of the 2H (Figure 3-8(g)) and 4H (Figure 3-8(h)) polytypes to find the best fit. We performed detailed error analysis to determine the most probable polytype and zone axis for each pattern (Appendix B.2). Overall, 4H was consistently a better fit for all SAD patterns.

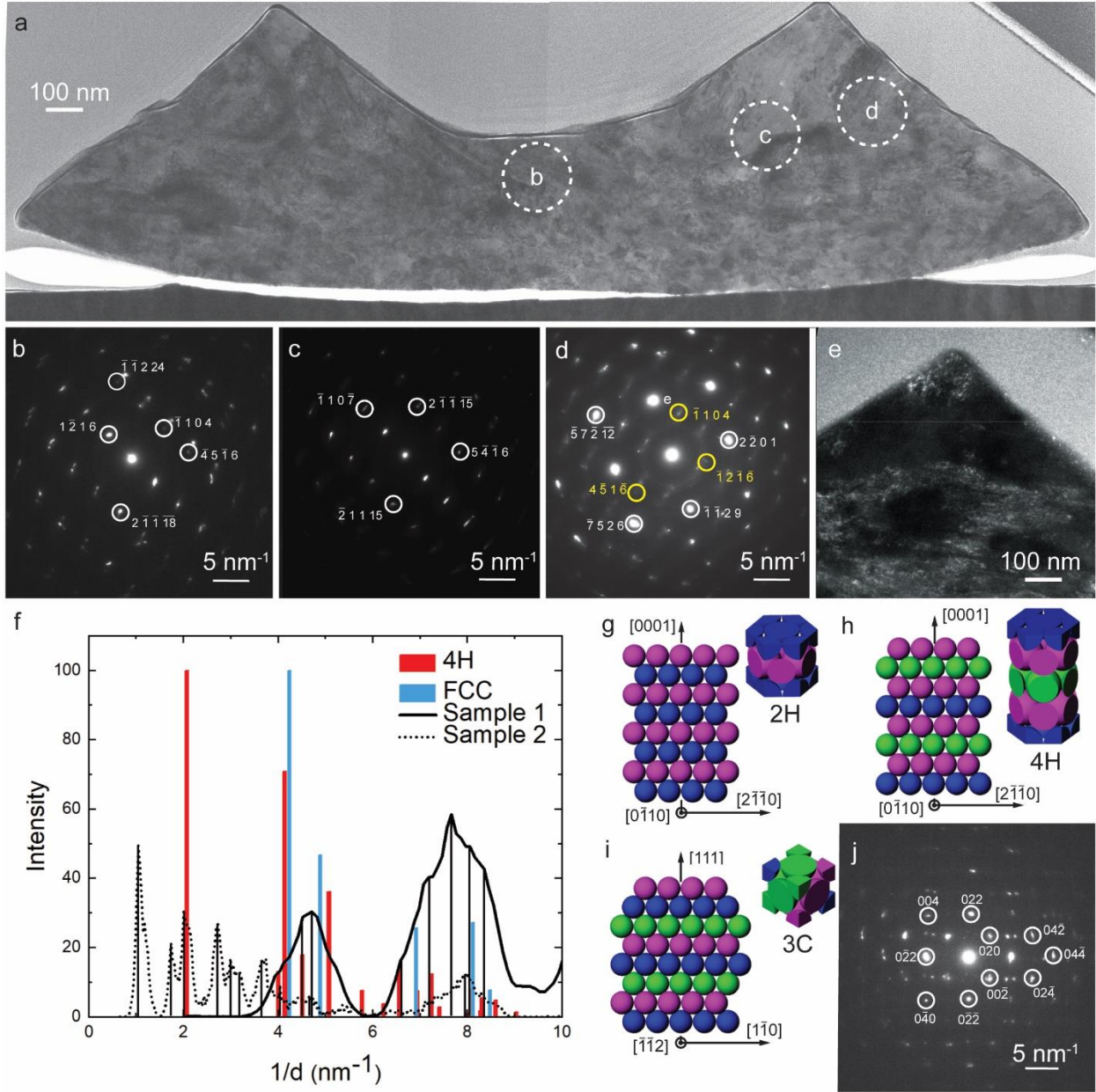


**Figure 3-8: Phase transformation in [100]-impacted Ag microcube** (a) TEM image of a thin lamella obtained from the middle section of the impacted sample within 24 hours from impact, (b-d) SAD patterns seen at the location indicated as 'b' (hcp zone axis:  $[10\bar{2}83]$ ), 'c' (hcp zone axis:  $[\bar{2}19\bar{17}3]$ ), and 'd' (hcp grain 1 (indicated in white) zone axis:  $[13\bar{4}4]$ , hcp grain 2 (indicated in yellow) zone axis:  $[10\bar{2}83]$ ) in d showing diffraction from hcp grains; diffraction from two of the multiple adjacent hcp grains are indexed in white and yellow in d, (e) dark field TEM image corresponding to  $[\bar{1}104]$  diffraction spot indicated as 'e' in d, showing hcp grains as small as 10 nm, (f) intensity peak curves of compiled diffraction data from two samples with 4H and FCC peaks from the database overlaid, (g-i) illustrations of the close-packed planes of Ag in 2H (g), 4H (h), and fcc (i) phases; insets show unit cells of respective phases (blue, purple, and green colors indicate the atoms that belong to A, B, and C stacking planes,

respectively). (j) SAD pattern obtained after further ion-beam thinning showing the characteristics of reverted fcc grains.

Since the hcp grain orientations were not primarily in low-order zone axes, we additionally performed diffraction peak analysis and compared our data to diffraction peak data of various Ag polytypes from the American Mineralogist Crystal Structure Database. The benefit of this method is that it does not rely on the determination of a zone axis or an indexed pattern from the software and the data is extracted directly from the diffraction pattern. The intensity curve for each diffraction pattern is calculated by integrating the intensities over  $\theta=0$  to  $2\pi$  for each distance  $d$  from the zone axis spot:  $I(d) = \int_0^{2\pi} I(d, \theta) d\theta$ . Intensities are normalized by the maximum intensity and then the data from all diffraction patterns are averaged together to create the intensity curve for one sample. Figure 3-8(f) shows diffraction data compiled from two different samples with intensity peaks for fcc and 4H Ag-polytypes overlaid. Sample-1 and Sample-2 intensity plots are averages of 21 and 51 SAD patterns obtained at various locations on the TEM lamellae, respectively. Each sample has a different range of  $d$ -spacings, likely due to different diffraction conditions. The peaks of Sample-2 are much more distinct due to consistency between individual diffraction patterns. Sample-1, on the other hand, has very broad peaks since the individual diffraction patterns have varied peak positions and intensities. This can be attributed to a larger degree of micro-strain or various different polytypes being present in the sample. Several peaks in each sample correspond to 4H peaks, while only one peak in Sample-1 at around  $8.12 \text{ nm}^{-1}$  shows closer agreement with 3C. This suggests most of the sample has transformed to 4H while a small amount of fcc phase may still be present. Differences in our diffraction data compared to the intensity peaks from the database are potentially due to the different diffraction method used; data from the American Mineralogist Crystal Structure Database is obtained via x-ray diffraction while our data was obtained using TEM diffraction for which artifacts such as double diffraction are possible.

Our detailed analysis reveals the presence of an hcp phase in [100] impacted samples, most likely of a 4H structure containing ABCB stacking sequence. This suggests that a martensitic dynamic phase transformation must have occurred due to impact, transforming the fcc crystal structure to an hcp structure in the nanosecond timescale. Upon further thinning of the same sample to less than 50 nm using FIB, we observe that the SAD patterns (Figure 3-8(j)) now represent the characteristics of an fcc structure. This suggests a secondary phase transformation that transforms the 4H phase back to an fcc (3C) structure can occur due to stress-relaxation [182] in a thinned sample that has undergone significant exposure to ion beam and electron beam radiation [18]. We have investigated the relative stability of the hcp polytypes and found that within a few days after impact, the metastable hcp phase transforms back to the fcc phase through continuous recrystallization [49].

We also created an MD simulation (Section 2.5.2) of a [100]-impacted nanocube which allows us to track the temporal evolution of the atomic structure (Figure 3-9(a)). We investigate the deformation nano- and atomic-structures of the sample using the local atomic structure calculated by the common neighbor analysis (CNA) algorithm implemented in OVITO [183]. Initially (0 ps), ~97% of atoms are in the fcc crystal structure while ~3% are found to be of other crystal symmetries, which primarily includes the surface atoms all around the nanocube. After impact, the local structure significantly changes as a function of time. At 4 ps, 92% of the atoms are in fcc structure while 1.4% are in body-centered-cubic (bcc) structure and 5.6% are in other crystal structures. This change is due to the shock wave propagation in the sample that generates lattice distortion and eventually results in plastic deformation. At 34 ps, the sample contains only 62.5% of fcc atoms while 19.4% of the atoms have transformed into a new hcp phase (remainder in: bcc ~2.6%, other ~14.7%). The hcp phase forms due to high emission of partial dislocations that form stacking faults. Large regions of hcp phase form in the sample as the deformation progresses (hcp regions are shown in red in Figure 3-9(b)).

Closer examination of the large hcp regions that have formed due to impact (Figure 3-9(b) inset) shows a stacking sequence of 2H polytype (stacking sequence AB, lattice constants  $a = 0.283$  nm and  $c = 0.638$  nm) rather than 4H polytype (stacking sequence ABCB, lattice constants  $a = 0.288$  nm,  $c = 1.0$  nm) as found from the experimental SAD patterns. After 51 ps, the percentage of hcp phase reaches steady state. However, other types of atoms dynamically recrystallize into an fcc structure. The final sample at 500 ps contains 69.9% fcc phase, 14.0% hcp phase, 0.8% bcc phase, and 15.2% in other phases.

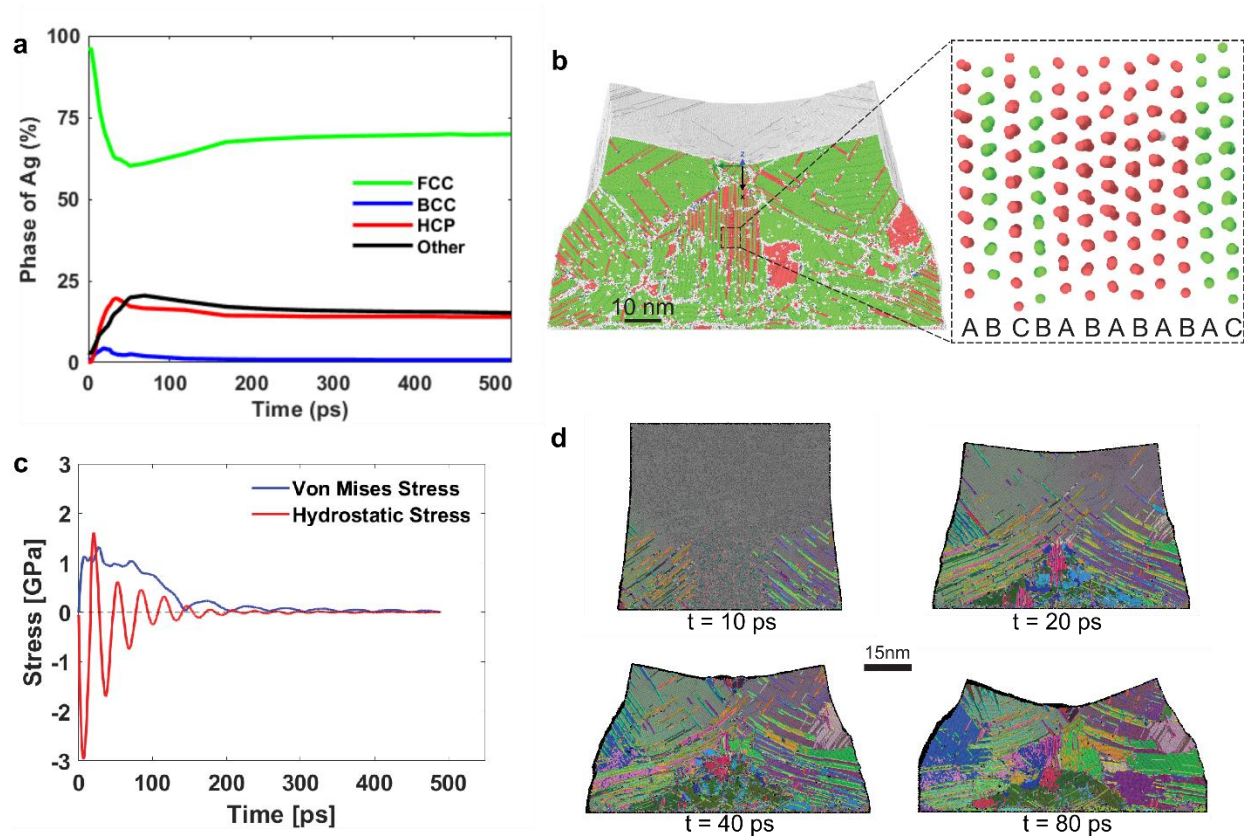


**Figure 3-9: Structural evolution of [100]-impacted cube found in MD simulations** (a) relative amount of various phases present as a function of time in the [100] impacted Ag nanocube, (b) (001) mid-section of the sample showing large regions with the new hcp (2H) phase; inset shows the magnified view of the stacking sequence where the red and green indicate atoms in hcp and fcc phases, respectively, (c) the von Mises equivalent stress and hydrostatic stress as a function of time, (d) nanostructural evolution of the [100] impacted Ag nanocube as a function of time.

To determine how the fcc to hcp phase transition occurs in [100] impacted samples, we examined the atomic-structure evolution and stress-time histories provided by the MD simulations (Figure 3-9(c-d)). As the sample impacts the rigid target in the [100] orientation, an elastic shock wave develops and propagates through the sample. The oscillatory behaviour apparent in the hydrostatic stress curve (Figure 3-9(c)) is characteristic of shock wave propagation and interaction with the sample surface. The period of this fluctuation is between 26 to 32 ps, which is very close to the time the elastic shock wave takes to travel twice the length of the ~65.5 nm sized nanocube sample. On the other hand, the von Mises equivalent stress (Figure 3-9(c)) initially increases higher than 1.3 GPa in a very short time (~10 ps) and remains higher than 1 GPa for around ~80 ps. The von Mises equivalent stress then gradually reaches zero as the kinetic energy due to the impact velocity is converted to plastic work.

The shock wave which propagates between the sample's surfaces is the key driving force for creating stacking faults which lead to the martensitic phase transformation. Avalanches of partial dislocations are nucleated at the bottom lateral edges of the sample (Figure 3-9(d);  $t=10$  ps) and propagate on  $\{111\}$  planes along  $\langle 110 \rangle$  directions, forming large stacking faults. Shortly after impact, dislocations interact in the mid-region of the sample leading to phase-transformation, formation and rotation of new grains, and dynamic recrystallization of the grains (Figure 3-9(d);  $t=20$  ps). Once the compressive shock wave reaches the top free surface of the sample, it reflects back as a tensile wave with additional dislocations nucleated from the top free surface (Figure 3-9(d);  $t=40$  ps). During this period, the dislocations multiply in the bottom and middle impacted regions of the samples, leading to large hcp regions (indicated by red atoms in Figure 3-9 (b)). After 80 ps (Figure 3-9(d);  $t=80$  ps) the microstructural changes slow and the microstructure remains approximately the same at future time steps.



To experimentally investigate the dynamic recrystallization and dislocation nucleation mechanisms, we performed transmission Kikuchi diffraction (TKD) on a [100]-impacted sample two days after impact (Figure 3-10). Both fcc and hcp crystallographic information files were read in for indexing, but the Kikuchi patterns were automatically indexed as fcc, revealing that at this point in time after impact, the metastable hcp phase has fully relaxed back to an fcc structure [49]. This [100]-impacted sample underwent extensive recrystallization as seen in the TKD orientation map (Figure 3-10 (a)). The most recrystallization occurs near the impact plane (bottom of the sample), with the grain size progressively increasing with the distance away from the impact plane. To quantify the nanostructural changes across the sample height, we calculated the average grain size ( $d_{line\ avg}$ ) and average dislocation density ( $\rho_{line\ avg}$ ) at each point (pixel) in the vertical direction (Figure 3-10 (c)). The gradient in grain size is clearly shown in the line profile of average grain size vs distance from impact plane (Figure 3-10 (c), black left axis). Also notice the smooth transitions among various colors in Figure 3-10 (a), indicating gradual changes in orientation. Even the largest grains identified contain a gradient of colors which correspond to subgrain boundaries. This myriad of orientations is reflected in the pole figures (Figure 3-10 (e)), in which limited texture emerges with smooth transitions between orientations. The impact-induced recrystallization produces these orientation changes from the original perfect (100) crystal orientation (Figure 3-10 (d)).

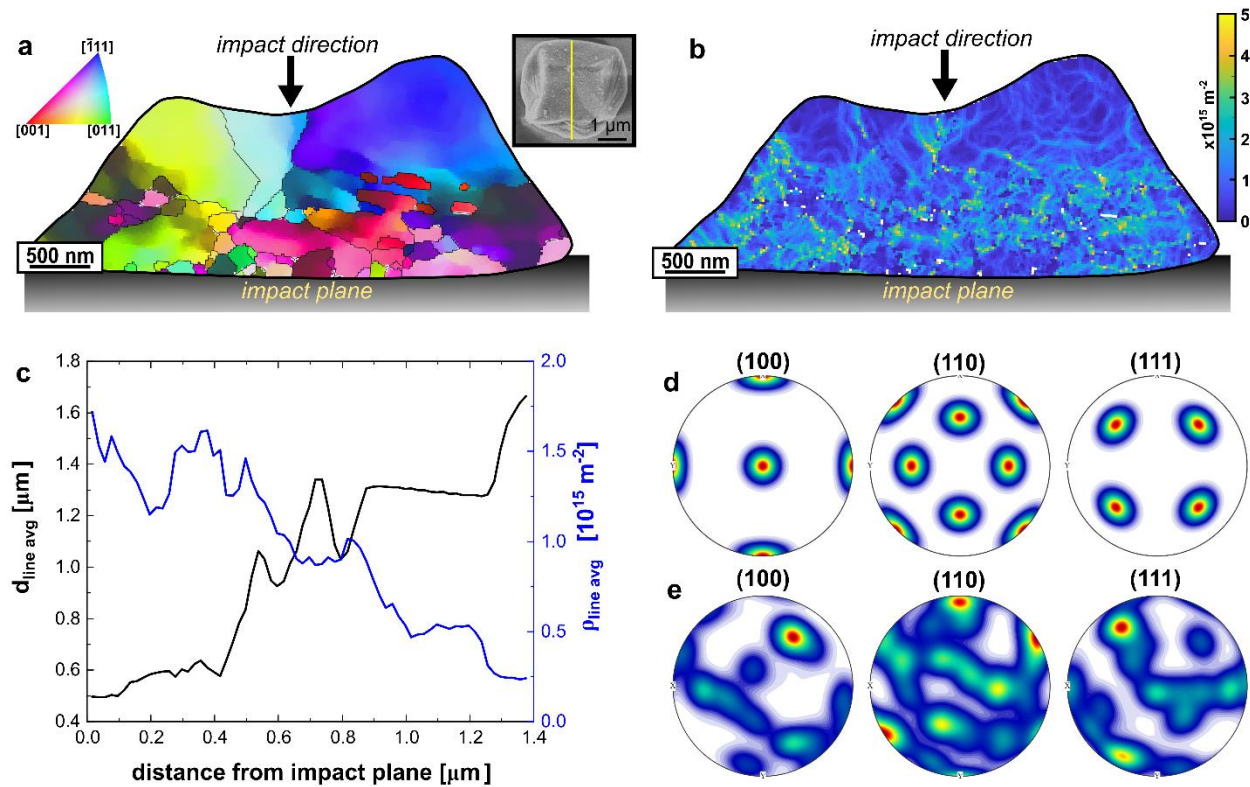


**Figure 3-10: Nanostructure of impacted microcubes** (a) orientation map from TKD analysis showing the GNG structure, (b) GND density map from TKD, (c) line profiles of average dislocation density and average grain size as functions of the distance from impact plane, (d) perfect (100) texture representative of an undeformed cube's crystal structure, (e) orientation data shown in (a) plotted on (100), (110), and (111) pole figures.

A map of the GND density throughout the sample is shown in Figure 3-10 (b). When comparing the dislocation density map (Figure 3-10 (b)) to the corresponding orientation map (Figure 3-10 (a)), we observe that regions of high GND density correlate with the gradual orientation changes seen within grains. Looking at the distribution of average dislocation density along the sample height (Figure 3-10 (c), blue right axis), a gradient in dislocation density is apparent with the highest dislocation density near the impact plane which progressively decreases with increasing distance away from the impact plane. This is the opposite trend compared to the grain size gradient, where the grain size increases moving away from the impact plane. These observations reveal that in the [100]-impacted samples, the dislocation density increases with

decreasing grain size. The shock dynamics and evolving stress state within the impacted cube lead to these dislocation and grain size gradients: since plasticity initiates in the bottom of the cube where it impacts the substrate, the plastic deformation gradient naturally follows the progression of the shock wave whose strength attenuates as it propagates [36,49,168,184].

### 3.3.2 *Impact-orientation dependent nanostructural evolution*

To investigate the effects of impact orientation on the resultant nanostructures, we perform nanostructural characterization on samples impacted along their [100]-face, [110]-edge, and [111]-corner orientations. Since subsequent microcompression tests are performed on pillars FIB-fabricated from the impacted cubes, pillars are formed prior to fabrication of the electron transparent lamellae so that representative nanostructures of undeformed pillars can be characterized. Nanostructural characterizations of these undeformed pillars are also used as input for crystal plasticity simulations. The nanostructures of pillars fabricated from [100], [110], and [111] impacted microcubes are shown in Figure 3-11. The pillars were formed from the center of the impacted cubes as indicated by the blue circles in SEM image insets of Figure 3-11, and lamellae formed from the cross-sections identified by yellow lines. The grain maps colored by crystal orientation reveal distinct nanostructural evolutions depending on the crystal orientation upon impact. The [100]-face impacted sample (Figure 3-11(a)) exhibits extensive grain refinement. In contrast, only limited grain refinement occurs in the [110]-edge (Figure 3-11 (b)) and [111]-corner (Figure 3-11 (c)) impacted samples, and the nanograins are primarily localized near the impact surface. The largest grain in the [110]-impacted sample remains in the original (110) orientation; however, contrast changes in the orientation color map within large grains suggest the formation of subgrain boundaries (Figure 3-11 (b)). Similarly, the [111] impacted sample exhibits most of the grain refinement closest to the impact plane (Figure 3-11 (c)); whereas,

the top of the pillar is split into two large grains, with a few nanograins and geometrically necessary dislocations accommodating the drastic shift in orientation between the grains. Orientation changes within large grains are clearly accommodated through GND density networks—denoting subgrain boundaries. These subgrains may have formed into distinct grains upon further extreme strain rate deformation. Formation and rotation of subgrains under high strain or strain rate loading are precursors to grain formation; this recrystallization mechanism—termed progressive subgrain misorientation (PRiSM) recrystallization—has been observed in adiabatic shear bands [185].

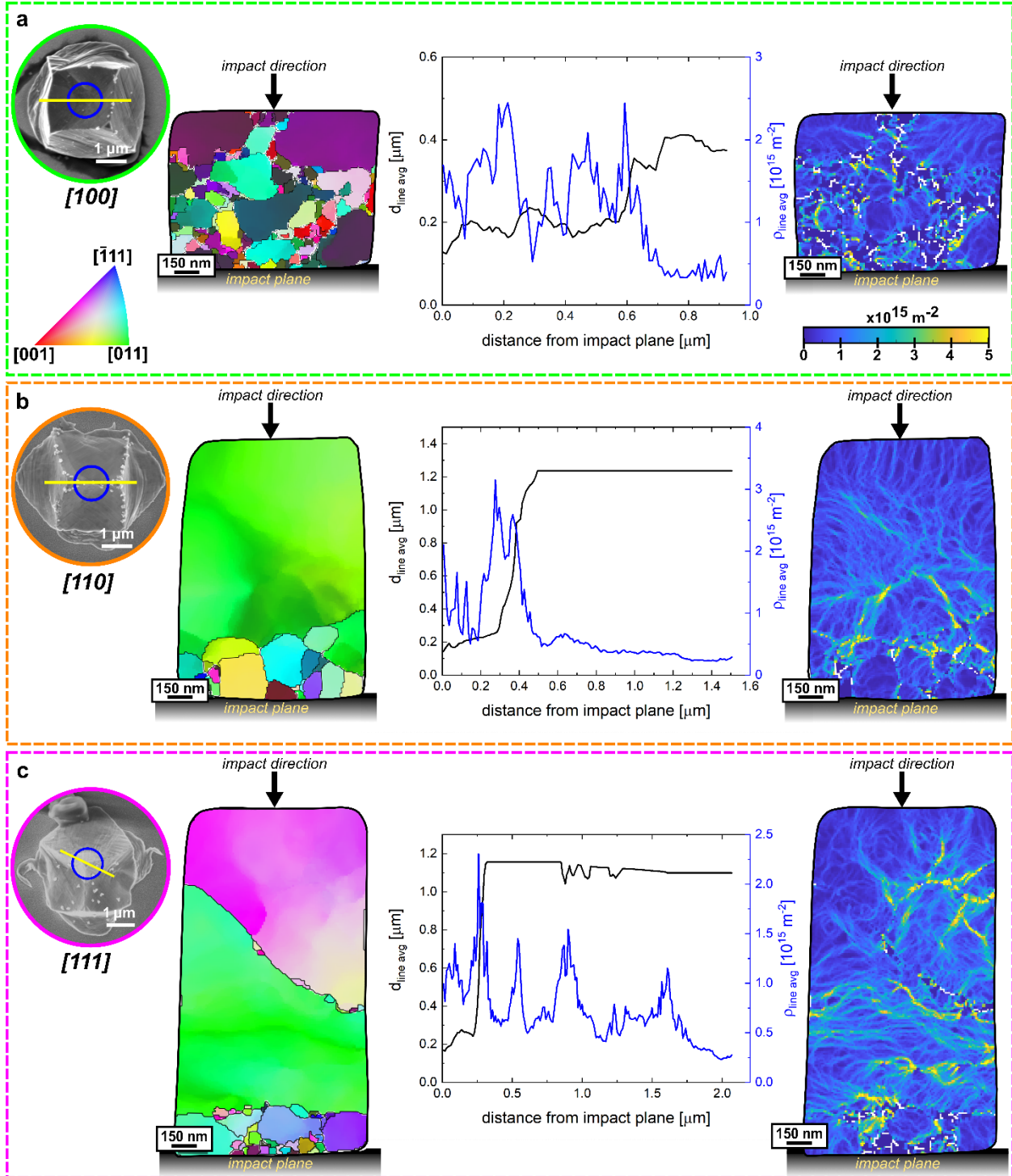


**Figure 3-11: Nanostructural characterization of uncompressed pillars formed from (a) [100], (b) [110], and (c) [111] impacted microcubes—each panel showing (from left to right): (i) SEM images of the impacted microcubes with locations of the pillars denoted by blue circles and lamella orientations denoted by yellow line, (ii) TKD orientation maps, (iii) grain size and GND density distributions, (iv) GND density maps.**

The plots in Figure 3-11 show the relationship between grain size and GND density as a function of the distance away from the impact plane. Inversely correlated grain size and dislocation gradients result from the high-strain rate plastic deformation induced through impact. As shown through simulations, dislocation nucleation and gradients in dislocation density result from shock wave progression and attenuation: shock-induced dislocation densities are dependent on the strain rate, crystal orientation, and resultant stress and temperature distributions [49,166,168,184]. Our experiments clearly show that the crystal orientation upon impact influences the impact-induced dislocation densities and recrystallization: sustained grain refinement and high GND densities are produced across the pillar height in the [100]-face impacted sample, while in the [110]-edge and [111]-corner impacted samples, high GND densities and grain refinement are primarily confined to the bottom ~250–400 nm, near the impact plane. Spikes in average GND density accompany the transition between the recrystallized nanogained region and coarse-grained region, revealing that GNDs accommodate the strain gradient between hard nanogained regions and softer coarse-grained regions. Additionally, local peaks in the GND density correspond to local minimums in the grain size (i.e. at ~900 nm in Figure 3-11 (c) plot).

Since the [110]-impacted sample's nanostructure was found to be the most different compared to the [100] sample, we performed additional TEM analysis and MD simulations on representative [110]-impacted samples. Unlike the [100] impacted sample, in which an hcp phase transformation occurs during impact (Section 3.3.1), the experimental results and simulations show that an hcp phase transformation does not occur in [110] impacted samples. Selected area diffraction (SAD) patterns taken at different areas within the lamella all show an fcc structure (Figure 3-12(a-e)). The SAD patterns in Figure 3-12(a-b) show distinct spots in an fcc structure, revealing that the top region of the sample contains large crystalline fcc regions. In contrast, the SAD pattern taken

from the bottom left of the sample (Figure 3-12(d)) shows diffuse spots forming rings, indicating this region consists of a nanocrystalline fcc structure. These findings are consistent with the TKD results of the [110]-impacted sample (Figure 3-11 (b)). The MD simulation of an impacted [110] nanocube confirms that a phase transformation does not occur (Figure 3-12(f-g)). The small percentage of atoms in an hcp structure correspond to stacking fault defects emitted between Shockley partial dislocations (Figure 3-12(g), inset) and does not reflect a large hcp phased domain as in the [100] impacted sample (Figure 3-9). However, the large percentage of atoms in the “other” phase corresponds to amorphous regions near the bottom of the sample which were formed due to melting.

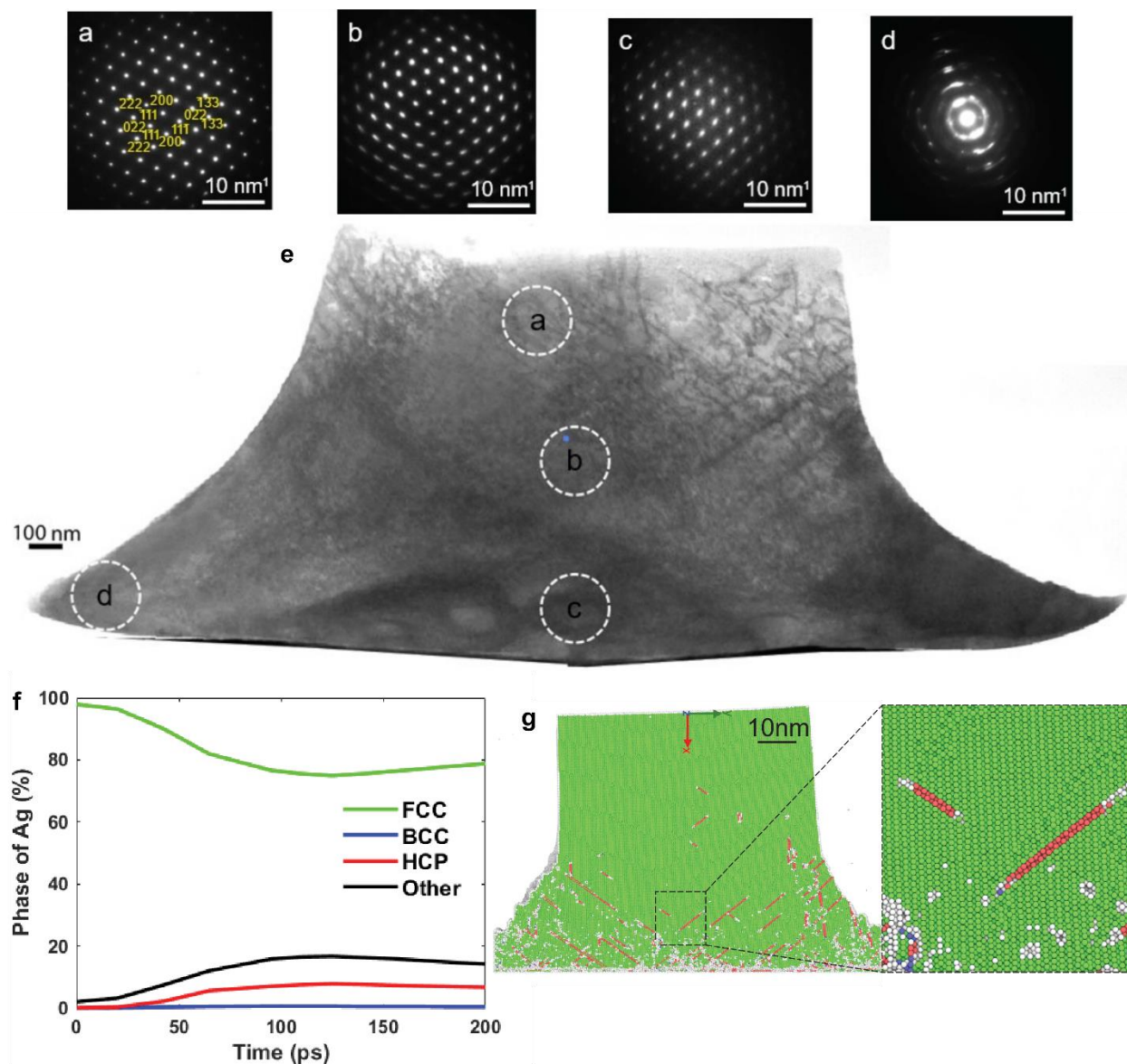


**Figure 3-12: No phase transformation in [110] impacted sample** (a-d) SAD patterns obtained at various locations as indicated in (e) showing single crystalline pattern at the top and middle regions and highly nanocrystalline pattern and amorphous Ag (diffused rings) at the bottom edge regions, (e) TEM image of a thin lamella obtained from the middle section of the impacted sample within 24 h from impact, (f) relative amount of various phases present as a function of time for the [110] impacted Ag nanocube as determined through MD simulations, (g) (001) mid-section of the sample with no hcp regions; inset shows the magnified view of small stacking faults.

To investigate why a phase transformation occurs in the [100] case but not in the [110] case and why melting appears to occur in the [110] case but not the [100] case, we look at the evolution of stress and temperature throughout the samples and compare these to the nanostructural



changes taking place (Figure 3-13). A key distinction between the [110] and the [100] impacted samples is that the hydrostatic stress is always negative during [110] impact (Figure 3-13(f)) with few oscillations, while a highly oscillatory hydrostatic stress state develops in the [100]-impacted sample, with a large initial magnitude which decays with time (Figure 3-13(b)). As discussed in Section 3.3.1, this oscillatory behaviour is indicative of shock wave propagation and interaction with the sample surface. Shock wave propagation and reflection are necessary for the hcp phase transformation and grain refinement that occurs in the [100] sample (Figure 3-13(a)). Because these qualities are lacking in the stress-state of the [110]-impacted sample, a phase transformation and extensive recrystallization do not occur (Figure 3-13(e)). The von Mises stress and stress triaxiality in the [110]-impacted sample indicate why the sustained shock and large hydrostatic stress state does not occur in the [100] sample. The von Mises stress in the [110]-impacted sample (Figure 3-13(f)) immediately increases upon impact, reaching values of  $\sim 0.9$  GPa. Such a large value is mainly achieved by the relatively large normal stress in the impact direction (first diagonal component of the stress tensor) as compared to the two other components of the stress tensor. This is an indication that the stress is primarily uniaxial. The stress triaxiality shown in (Figure 3-13(g)) also suggests that the large hydrostatic stress state does not develop in the [110] impacted sample. Initially, the stress triaxiality increases very quickly, and then decays and stabilizes after 10 ps. The initial peak is due to almost zero shear stresses for the first 50 ps which coincides with melting in a portion of the atoms in the simulation cell. The shear stresses build-up after 60 ps where several dislocations can be seen in the sample. After 10 ps, while some fluctuations of the magnitude of the stress triaxiality are seen, the absolute values of the stress triaxiality are around  $\pm 0.6$ , which is considerably smaller than in the [100] case (Figure 3-13(c)).

The presence of melting in the [110] sample can be confirmed by examining the space-time temperature profile (Figure 3-13(h)). Regions near the impact plane reach temperatures over 2600 K, which is well above the melting point of Ag (~1230 K). The heat is mainly concentrated near the impacted area while the rest of the sample remains at a much lower temperature. These extremely high localized temperatures are not achieved in the [100] sample (Figure 3-13(d)), confirming that melting does not occur in this case.

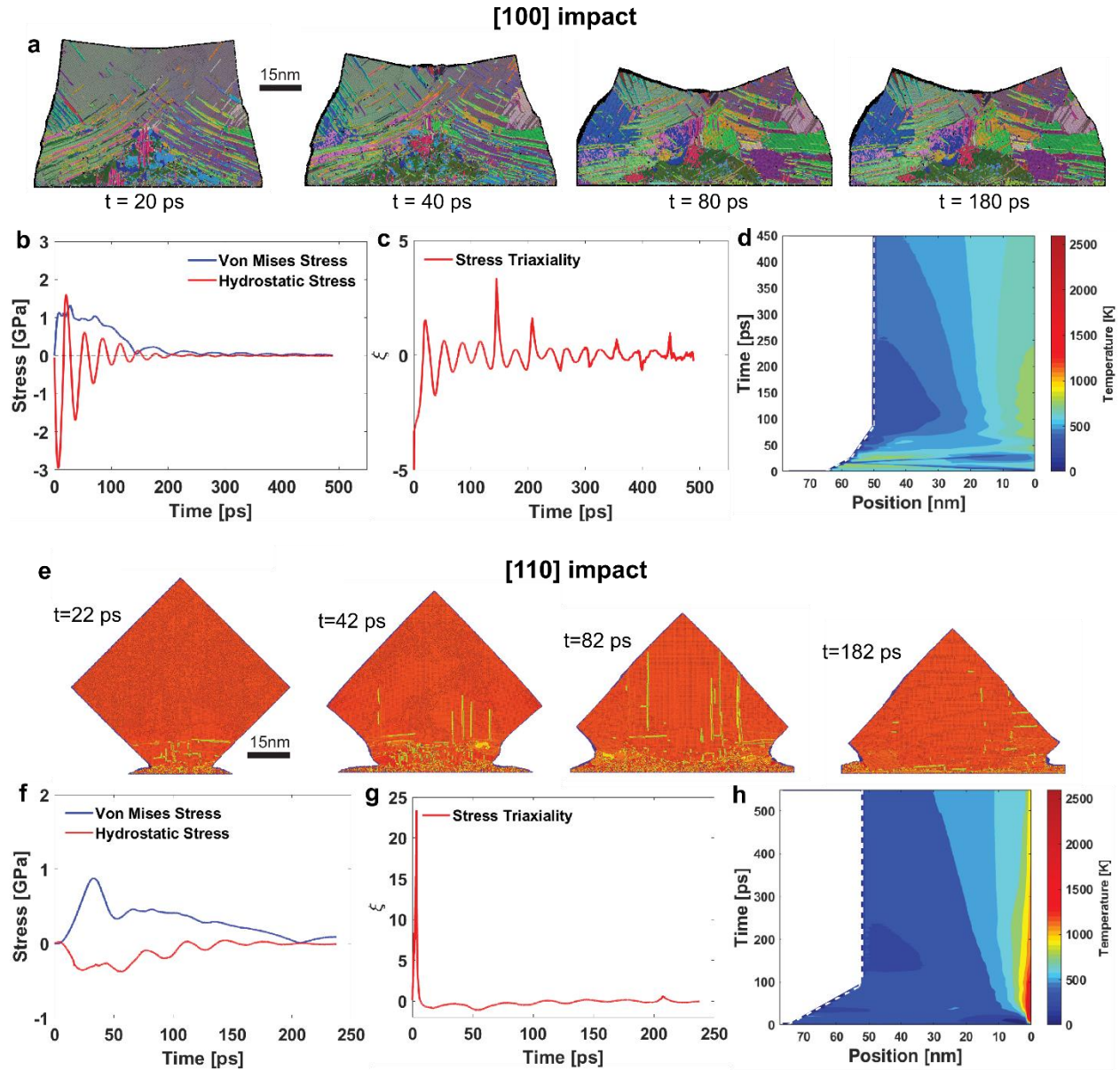


**Figure 3-13: Nanostructural evolution of [100] and [110] impacted nanocubes** (a) nanostructural evolution of the [100] impacted Ag nanocube as a function of time, (b) von Mises and hydrostatic stress as a function of time in the [100] impacted nanocube, (c) stress triaxiality as a function of time in the [100] impacted nanocube, (d) temperature distribution in the [100] impacted nanocube as a function of position from the impact plane and time, (e) nanostructural evolution of the [110] impacted Ag nanocube as a function of time, (f) von Mises and hydrostatic stress as a function of time in the [110] impacted nanocube, (g) stress triaxiality as a function of time in the [110] impacted nanocube, (h) temperature distribution in the [110] impacted nanocube as a function of position from the impact plane and time.

Our experiments and complementary MD simulations show clear orientation-dependent differences in the resultant impact-induced nanostructures. Although all three samples show

inversely correlated grain size and GND density gradients due to impact-induced shock wave progression, interactions, and attenuation, the extent of dynamic recrystallization differs depending on the impact orientation. The crystal orientation or cube orientation may be the predominant factor governing recrystallization: either (i) the internal crystal orientation along the impact direction is the predominant factor which enables favorable defect nucleation that influences the plastic deformation, or (ii) the orientation of the external geometry upon impact (ie. edge, corner, or face impact of the cube) significantly alters the imposed stress state and resultant nanostructure. In this system, the orientation of the cube and crystal orientation cannot be decoupled because of the single-crystal growth mechanisms; however, they can be decoupled through MD simulations. Our collaborators have shown that both appear to influence the extent of recrystallization, but impacted samples oriented along the [100] crystal direction always exhibit the largest degree of recrystallization, regardless of the particle orientation [168]. This is likely due to the high number of simultaneously activated slip systems, promoting dislocation plasticity. Since the crystal orientation seems to be the predominant factor affecting dynamic recrystallization, the resultant nanostructures of these impacted microcubes are mainly crystal-orientation dependent, rather than particle shape dependent.

### 3.3.3 *Effect of loading conditions on dislocation nucleation and recrystallization*

The detailed experimental analysis and MD simulations presented in the previous section revealed that defect nucleation and interaction leading to recrystallization are dependent on shock wave propagation, attenuation, and reflection in the impacted Ag microcubes. The shock dynamics and stress state are dependent on the impact orientation: the oscillatory hydrostatic stress state that develops during impact of [100]-face oriented microcubes is necessary for significant nanostructural changes to occur. This stress state is absent in the [110]-edge impacted microcubes,

where extensive recrystallization and phase transformations do not occur. With this understanding, we now wonder whether shock wave reflection leading to the oscillatory stress state is necessary for dynamic recrystallization or if the crystallographic orientation primarily governs the recrystallization mechanisms.

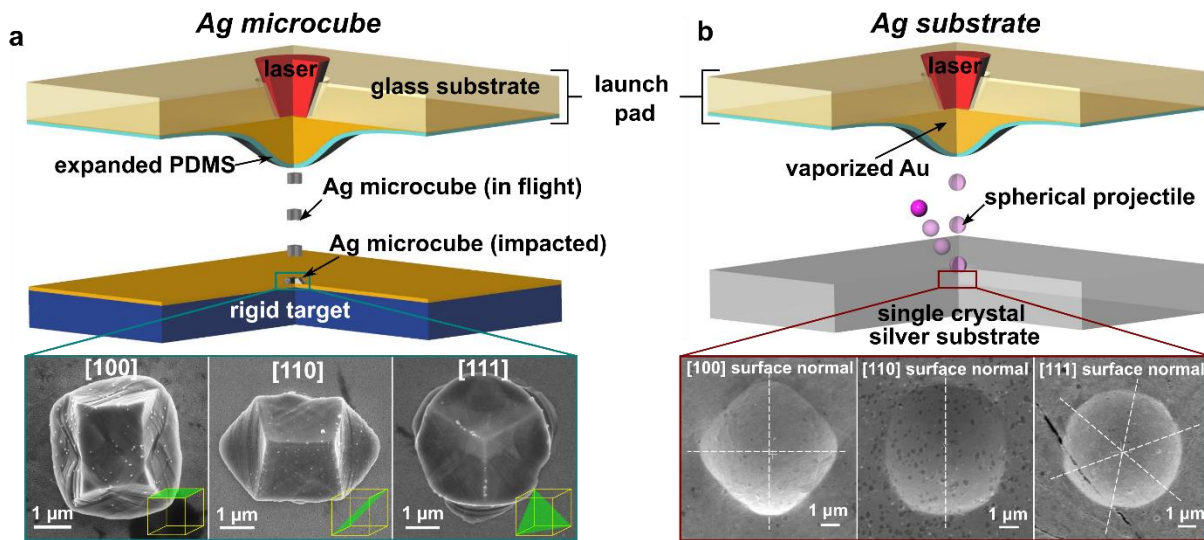


**Figure 3-14: LIPIT on single crystal Ag cubes and substrates** (a) Schematic of the high-velocity impact of an Ag microcube onto a rigid target in the LIPIT; SEM images of [100]-face, [110]-edge, and [111]-corner impacted cubes, (b) Schematic of the high-velocity impact of rigid spherical projectile onto a deformable single crystal Ag substrate with the LIPIT; SEM images of impact craters on Ag substrates with [100], [110], and [111] surface normal directions.

Without nearby free surfaces to reflect the impact-induced shock wave, the shock wave will continue to propagate and attenuate in the impact direction. Such a condition can be experimentally achieved through high-velocity impact of rigid spherical microprojectiles onto a deformable substrate. The microprojectile size ( $\sim 9 \mu\text{m}$ ) is significantly smaller than the substrate thickness ( $\sim 500 \mu\text{m}$ ) to ensure dissipation of the shock wave well before reaching the bottom surface. We perform microprojectile impact tests on single crystal Ag substrates, with surface normal directions of [100], [110], and [111]. Studying these three orientations in both the impacted microcubes and impacted substrates allows for clear determination of whether the reflective shock

dynamics or crystallographic orientation primarily governs the dynamic recrystallization. Consistent with studies of quasi-static indentation on single crystal metals [186–190], pile-up patterns with symmetries reflecting the internal symmetry of the crystal lattice are visible in the SEM images of the impact craters (Figure 3-14 (b)). Even though the impact projectile is spherical, a square shaped indent is seen in the top view SEM image of an impact crater on the [100] Ag substrate (Figure 3-14 (b)). Material piles up along the  $\langle 110 \rangle$  directions, creating a 4-fold symmetry pile-up pattern which reflects the internal 4-fold cubic symmetry of the Ag crystal when viewed along the  $\langle 100 \rangle$  direction. Similarly, a 2-fold symmetry pile-up pattern is visible when looking at the SEM images of an impact crater on the [110] Ag substrate, which reflects the crystal symmetry when viewed along the  $\langle 110 \rangle$  direction (Figure 3-14 (b)). Finally, 6-fold symmetry is apparent from the top view SEM image of the [111] impacted substrate (Figure 3-14 (b)). The four-, two-, and six-fold symmetries are also apparent in the top view SEM images of the [100], [110], and [111] impacted microcubes (Figure 3-14 (a)).

To compare the impact-induced nanostructural evolution of Ag substrates to the previous characterization we have done on impacted Ag microcubes, we formed electron transparent lamella from beneath the impact craters and performed transmission Kikuchi diffraction (TKD) to capture the crystallographic information at spatial resolutions as low as 10 nm. From the TKD scans taken below the impact craters (Figure 3-15), we see distinct differences between the three substrates of different orientations. The impacted [100] Ag substrate shows an extensive amount of grain refinement, with a collection of the smallest ( $\sim 100$  nm) grains located  $\sim 2$   $\mu\text{m}$  below the crater surface (Figure 3-15 (a)). Sharp orientation changes denote clear grain boundaries. In contrast, the [110] substrate does not undergo extensive recrystallization to form distinct grains (Figure 3-15 (b)). However, there is a gradual and continuous change from a  $\sim(100)$  orientation on

the left side of the crater to a  $\sim(111)$  orientation on the right side of the crater (Figure 3-15 (b)). This suggests that some lattice rotation occurs due to impact, but not enough to form distinct recrystallized grains. The  $[111]$  substrate exhibits minimal grain refinement near the crater surface and gradual orientation changes throughout the remaining influence zone (Figure 3-15 (c)).

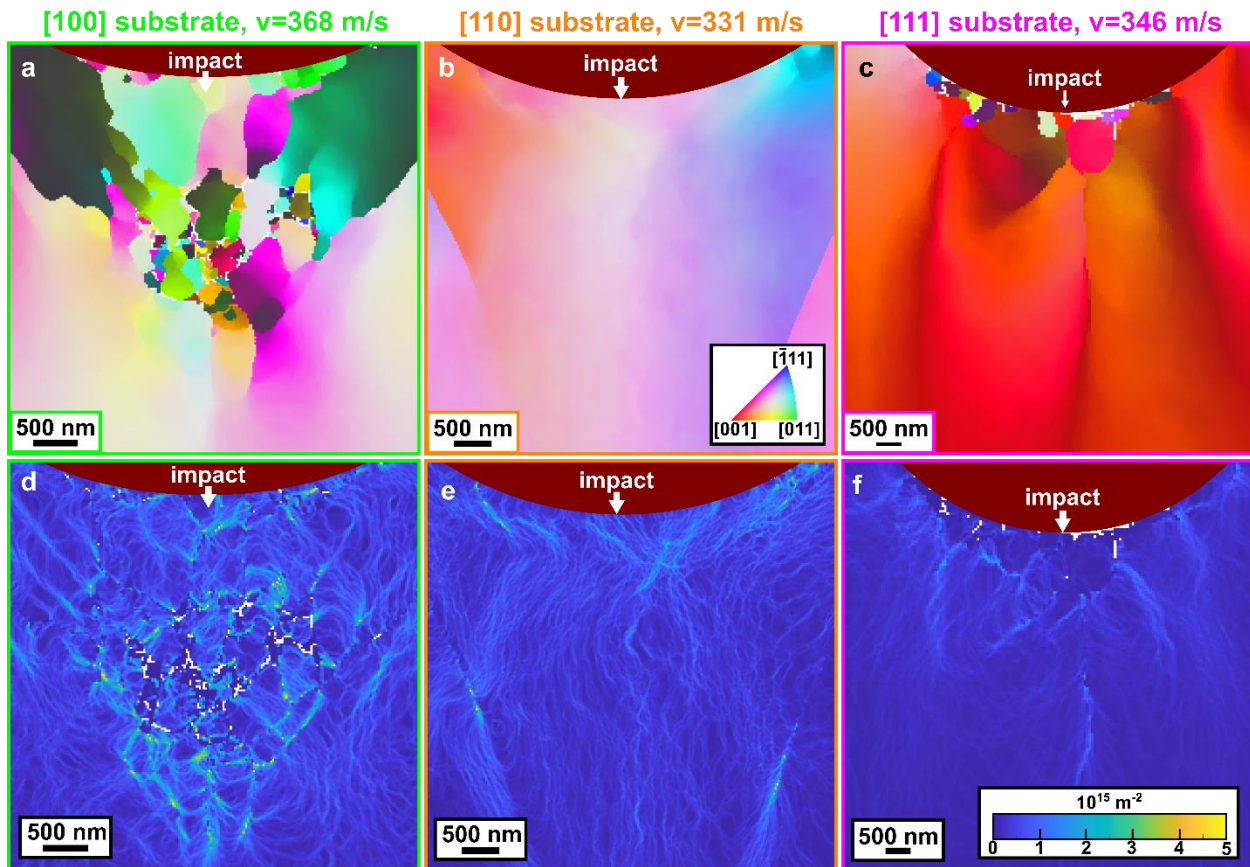


**Figure 3-15: TKD scans beneath impact craters** (a-c) TKD orientation maps taken beneath the impact craters on a  $[100]$  impacted substrate (a), a  $[110]$  impacted Ag substrate (b), and a  $[111]$  impacted Ag substrate (c), (d-f) geometrically necessary dislocation density maps of  $[100]$  (d),  $[110]$  (e), and  $[111]$  (f) impacted substrates.

The dislocation networks accommodating the crystal rotation in each substrate are visible in the geometrically necessary dislocation density plots (Figure 3-15 (d-f)). The highly torturous dislocation networks (Figure 3-15 (d)) accommodate the large misorientations between neighboring grains in the  $[100]$  substrate (Figure 3-15 (a)). In contrast, the dislocation networks in



the [110] and [111] substrates (Figure 3-15 (e,f)) are less concentrated and torturous, accommodating the gradual orientation changes but not forming the dislocation cell structures leading to grain formation. In all three substrates, the regions with the highest dislocation density are close to and directly beneath the impact crater surface (Figure 3-15 (d-f)). The region with high dislocation density tapers off with increased depths: marking a conically shaped influence zone beneath the crater. This influence zone is clearly visible in the orientation maps and dislocation density maps of the [100] (Figure 3-15 (a,d)) and [110] (Figure 3-15 (b,e)) substrates. The grain refinement and crystal rotation is primarily isolated to this conical zone, whereas the orientation of the crystal outside of this zone is the original single crystal orientation. In the [110] substrate, although the orientation changes within the influence zone are very gradual, abrupt orientation changes can be traced on either side of the crater from the outside edges towards the middle (Figure 3-15 (b)). These boundaries can be associated with the planes of high dislocation density visible in (Figure 3-15 (e)), clearly marking the edge of the influence zone.

To quantify the extent of impact-induced nanostructural evolution with increasing depths, we calculated the average dislocation density and grain size at each position ( $z$ ) beneath the substrate surface. The average grain diameter at each  $z$  position is normalized by the diameter of the largest grain (representing the single crystal): thus, a value of 1 corresponds to a single crystal (no recrystallization). Figure 3-16(a) shows the normalized average grain size and average dislocation density as a function of the distance from the substrate surface. For all three substrates, the average dislocation density is highest close to the surface and tapers off at larger depths. At  $\sim 5 \mu\text{m}$  from the substrate surface, the average dislocation density in all three samples approaches approximately the same value of  $\sim 0.5 \times 10^{14} \text{ m}^{-2}$ , which is likely the average bulk dislocation density of the substrates before the impact event. Impact-induced dislocation nucleation, either through



activation of pre-existing sources or heterogeneous dislocation nucleation at the contact surface, must have been prevalent to increase the local dislocation density up 14x that of the original bulk dislocation density. This localized increase in dislocation density is likely to increase the material's hardness, as we have shown through dynamic hardness measurements of single crystal aluminum substrates [169]. Within the surface region of high dislocation density, local peaks in the average dislocation density in each substrate reveal more nuanced differences in the impact-induced plastic deformation. For example, the dislocation density in the [111] substrate peaks at  $\sim 1 \mu\text{m}$  below the substrate surface (Figure 3-16 (a), bottom, magenta), which corresponds to the small region that exhibits grain refinement (Figure 3-15 (c), Figure 3-16(a) – top, magenta). Similarly, the peak in dislocation density for the [100] substrate corresponds to the region of maximum grain refinement located  $\sim 2 \mu\text{m}$  below the substrate surface (Figure 3-15 (a), Figure 3-16(a) – green). We also see that the [100] substrate exhibits the highest sustained dislocation densities compared to the other substrates, which accommodates the large degree of crystal rotation necessary for recrystallization.

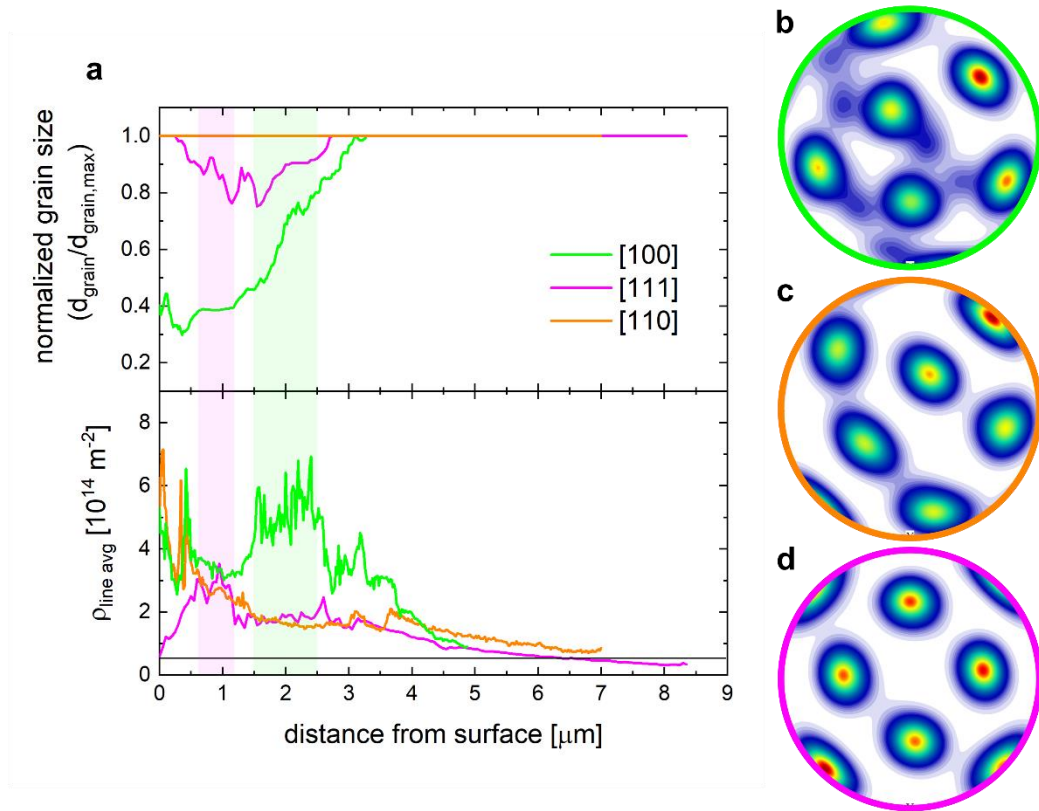


**Figure 3-16: Distributions of nanostructural features below impact craters** (a) average normalized grain size (top) and dislocation density (bottom) with increasing depth from the surface, (b-d) (110) pole figures corresponding to the orientation maps of [100] (b), [110] (c), and [111] (d) impacted substrates.

The [100] substrate has the lowest average grain sizes and exhibits a spatial gradient of increasing grain size with increasing depths (Figure 3-16(a)). Although we noted that the smallest grains lie  $\sim 2 \mu\text{m}$  below the substrate surface, this does not correspond to the location of smallest average grain size due to the decreasing width of the recrystallized region (i.e., most of the sample to either side remains single crystal). The extensive amount of recrystallization induced in the [100] substrate is also reflected in the (100) pole figure in (Figure 3-16 (b)), showing a weak texture. The average grain size distribution of the [111] substrate shows a small dip in grain size while most of the sample has not recrystallized like the [110] sample (Figure 3-16(a)).

Correspondingly, the pole figures of the [110] (Figure 3-16(c)) and [111] substrates (Figure 3-16(d)) show stronger textures when compared to the [100] sample's pole figure (Figure 3-16(a)).

Clearly, the dynamic recrystallization is primarily governed by the crystallographic orientation. The same conclusion is drawn from the impact-induced nanostructural transformations seen in single crystal silver microcubes: [100]-face impacted microcubes exhibit the most grain refinement, while limited grain refinement occurs in [110]-edge and [111]-corner impacted samples (Figure 3-11, Figure 3-17 (a)). Plots of the normalized grain size as a function of the distance from the impact site show the formation of smooth gradient nano-grained structures in the samples impacted along the [100] direction (Figure 3-17 (a-b)–green). Samples loaded in the [111] direction show limited grain refinement isolated to the impact surface (Figure 3-17 (a-b)–magenta), while the [110]-impacted samples show limited to no grain refinement (Figure 3-17 (a-b)–orange). These similarities are surprising, given the different boundary conditions of these shock loaded crystals: the microcubes have free surfaces which allows for reflection of the imparted shock wave while the shock wave would continue in the same direction of the substrate without reflection. MD simulations of the impact of Ag microcubes show that the oscillatory hydrostatic stress state that develops as a result of the shock wave reflection from the cube's free surfaces leads to the formation of stacking faults, phase transformation, and recrystallization [49] (Section 3.3.2). However, this oscillatory stress state would not arise in impacted substrates due to the primarily unidirectional propagation of the shock wave through an apparent infinite medium (see schematic in Figure 3-17 (f)). Our results signify the importance of the crystal orientation during high strain rate plastic deformation, irrespective of reflective shock dynamics.

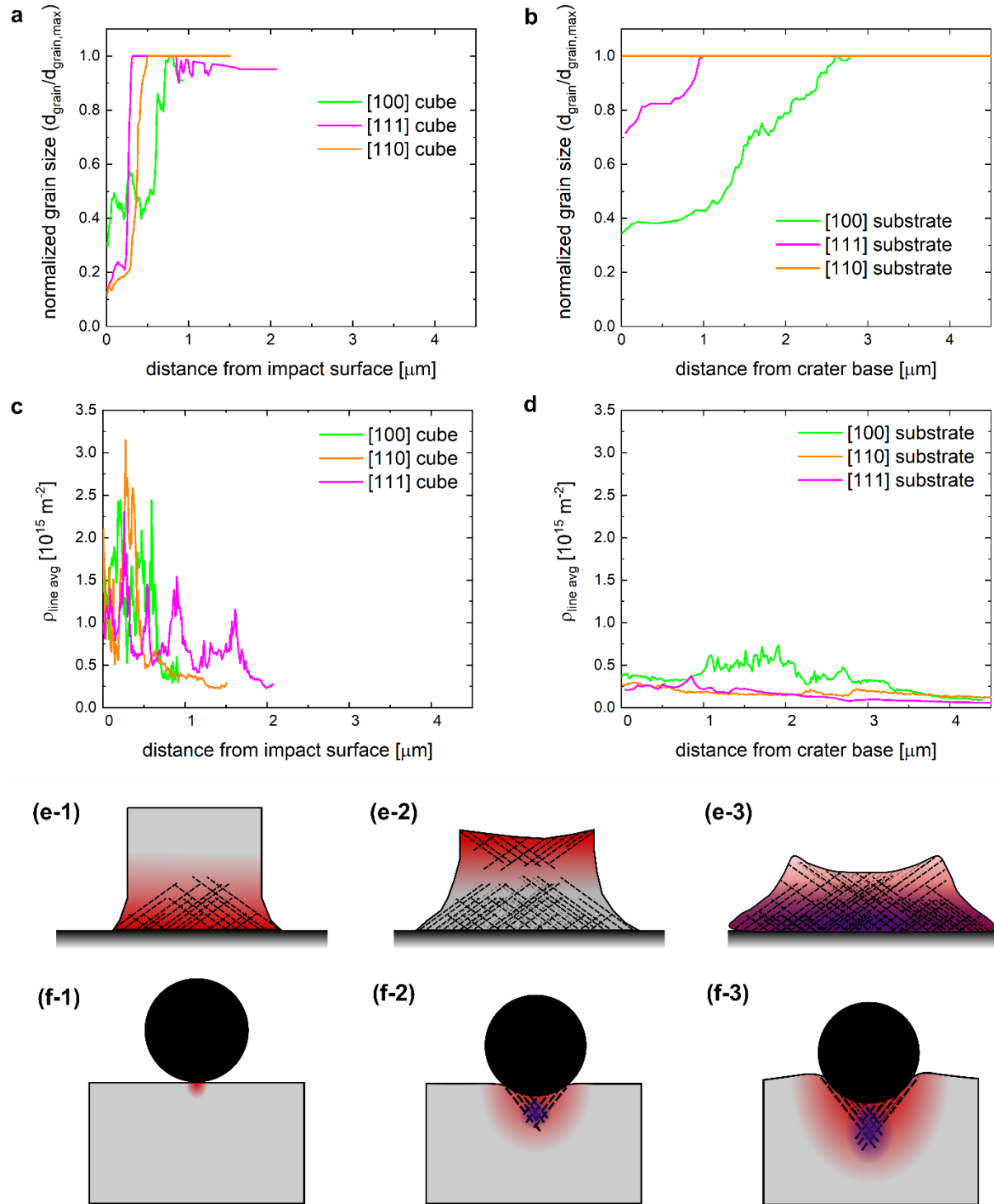


**Figure 3-17: Impact-induced nanostructural evolution in single crystal microcubes and substrates** (a-b) normalized grain size distributions of impacted Ag microcubes (a) and substrates (b), (c-d) dislocation density distributions in impacted microcubes (c) and substrates (d), (e-f) schematics showing dislocation evolution (dashed

lines), shock wave propagation (red shading), and regions of grain refinement (purple) in the impacted Ag microcubes (e) and substrates (f).

To understand why dynamic recrystallization occurs in the [100] impacted substrate even though the oscillatory hydrostatic stress state is likely absent, we must understand the orientation-dependent mechanisms controlling the nucleation, propagation, and interaction of dislocations. From Schmid factor analysis of  $\langle 100 \rangle$ ,  $\langle 110 \rangle$  and  $\langle 111 \rangle$  loaded fcc crystals (Appendix A.1), we find that eight, six, and four slip systems share the maximum Schmid factor for each respective orientation. This reveals that more slip systems would be simultaneously activated in  $\langle 100 \rangle$  loaded fcc crystals than the other two orientations. Additionally, although six slip systems share the same Schmid factor for a  $\langle 111 \rangle$  loading direction, the maximum Schmid factor of 0.272 is less than the maximum Schmid factor for  $\langle 100 \rangle$  loading (0.408)—meaning for the same applied normal stress, the shear stress exhibited on the slip systems in the  $\langle 111 \rangle$  loaded crystal would be less. Due to the higher shear stresses and higher number of simultaneously activated slip systems, more dislocations are likely nucleated in the [100] impacted samples. Our experimental data of GND density distributions confirm this hypothesis: both the [100] impacted cubes and substrates exhibit the highest average GND densities compared to the other two orientations (Figure 3-17 (c-d)). The higher GND densities and higher number of activated slip systems in the [100] impacted samples would also promote enhanced dislocation interaction, leading to the formation of dislocation subcells.

We hypothesize that rapid and continuous dislocation nucleation as the projectile impacts deeper into the sample leads to recrystallization. With a spherical projectile, the contact area progressively increases during impact, which would cause continuous dislocation nucleation over a larger and larger area (Figure 3-17 (f)). This progressive nucleation of dislocations is similar to that seen in the MD simulations of [100] impacted microcubes. In the substrate, these dislocations

would then propagate on the  $\{111\}$  planes and interact in the middle region of the sample, below the impact crater. This mechanism would also explain why the most grain refinement occurs below the sample surface in the  $[100]$ -impacted substrate.

During high strain rate loading of single crystals, homogeneous dislocation nucleation occurs since preexisting dislocations and sources are unable to accommodate the rapid deformation. The Orowan equation relates the shear strain rate to the dislocation dynamics:

$$\dot{\gamma} = \rho_{\perp} b \frac{dx}{dt} + x b \frac{d\rho_{\perp}}{dt},$$

where  $\rho_{\perp}$  and  $\frac{d\rho_{\perp}}{dt}$  are the density and rate of change of edge dislocations,  $b$  is the Burgers' vector, and  $x$  and  $\frac{dx}{dt}$  are the displacement and velocity of the dislocations. This relationship reveals that to accommodate higher strain rates, corresponding increases in the dislocation density, dislocation velocity, and/or dislocation nucleation rate must occur. Enhanced dislocation production is clearly evidenced by the dislocation gradients formed in the impacted substrates and cubes (Figure 3-17 (c-d)). However, comparing the dislocation distributions and magnitudes formed in the cubes versus the substrates reveals dislocation densities in the cubes up to an order of magnitude higher than in the substrates. Furthermore, the synthesized microcubes are dislocation free, which makes the high density of impact-nucleated dislocations even more impressive. We hypothesize that the reflective shock dynamics play a role in ultra-high dislocation densities formed in the impacted cubes. From MD simulations, we know that dislocations are initially nucleated at the nanocube's surfaces that first come in contact with the substrate, and as the shock wave propagates to the opposite surface and reflects, more dislocations are nucleated from the top surface (Section 3.3.1, Figure 3-17 (e)). This mechanism continues until the shock wave has dissipated in the crystal and there is insufficient stress for homogeneous dislocation nucleation. Since the substrates do not

have any nearby free surfaces, this shock reflection mechanism leading to sustained dislocation nucleation cannot occur.

Given this new understanding of the optimal dislocation nucleation and interaction conditions which lead to grain refinement, we hypothesize that enhanced grain refinement could be induced in [111] oriented samples through higher impact velocity. To negate the possibility of melting, we performed microprojectile impacts on the [111] oriented Ag substrate at impact velocities of ~600 m/s which is well below the predicted impact velocity which would impart enough energy to melt the sample (~818 m/s, see Appendix A.3). Figure 3-18 shows the TKD results from beneath the crater of the [111] substrate impacted with a microprojectile at 571 m/s. The TKD orientation map (Figure 3-18 (a)) shows grain refinement near the surface of the crater. The GND density map shows a more tortuous dislocation network (Figure 3-18 (b)), much like the [100] impacted sample. Comparing the normalized grain size and GND density distributions of the two [111] impacted samples (Figure 3-18 (c)) reveals smaller average grain size and higher dislocation density—both sustained for larger depths—in the sample with higher impact velocity. Finally, the corresponding (110) pole figures reveal a more diffuse texture in the sample impacted at a higher velocity (Figure 3-18 (d-e)). These observations point to more grain refinement through enhanced dislocation activity due to the higher strain rate. The higher impact velocity leads to faster dislocation nucleation. Even though only six slip systems would be simultaneously activated, the increased dislocation activity leads to a similar degree of grain refinement as the [100] impacted samples.

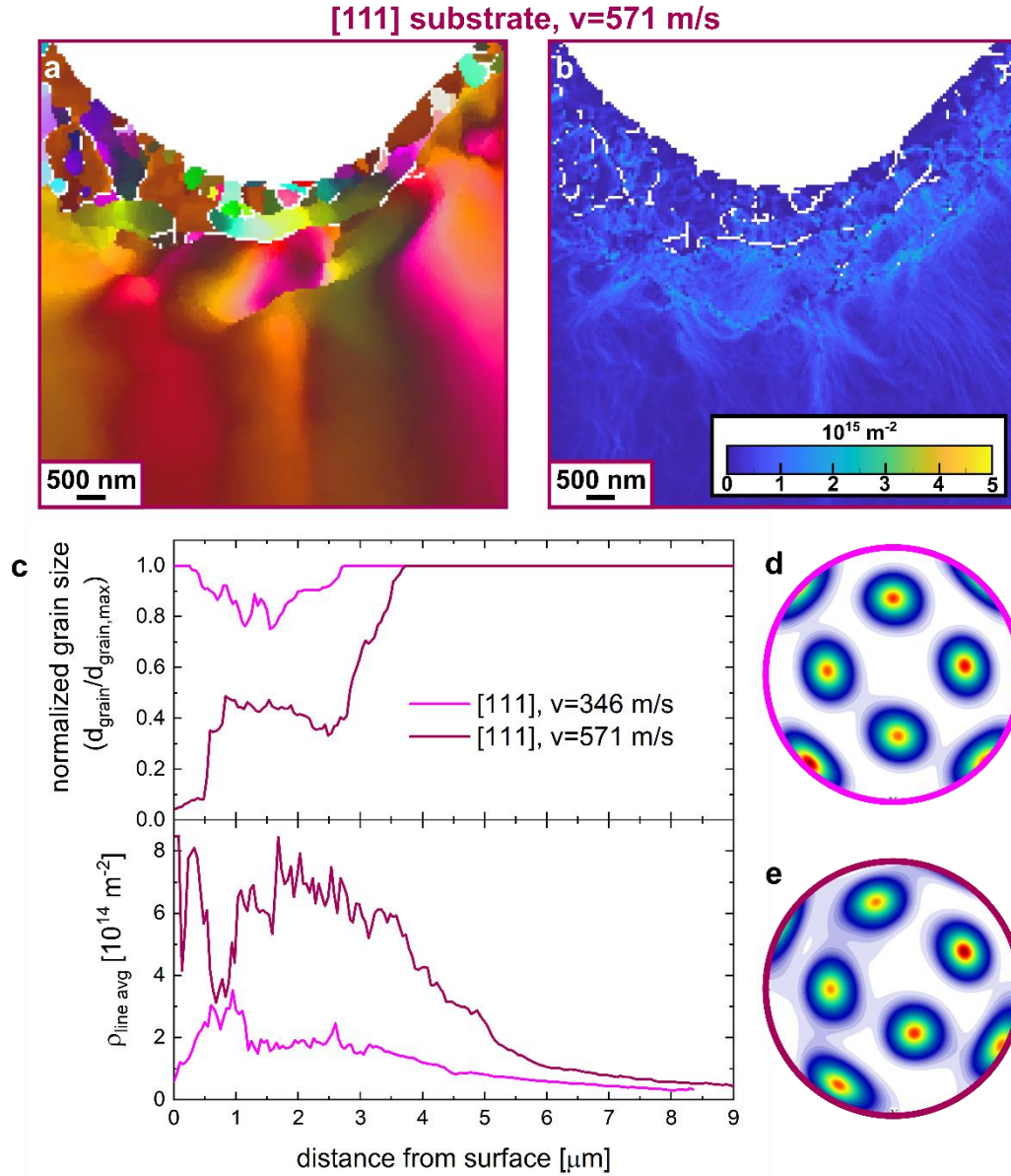


**Figure 3-18: High-velocity impact of the [111] Ag substrate** (a) TKD orientation map of nanostructure under crater, (b) corresponding GND density map, (c) normalized grain size and GND density distributions from low and high velocity impacts of the [111] substrate, (d-e) (110) pole figures corresponding to the orientation maps of the low and high velocity [111] substrate impacts.



### 3.4 Synergistic property improvement in impact-induced heterogeneous nanostructures

To study the effects of impact-induced structural changes on the mechanical properties, we perform compression tests on micropillars formed from impacted Ag microcubes. Single crystal Ag cubes with  $\sim 2\ \mu\text{m}$  side lengths (Section 2.1.1) are impacted onto a rigid target at speeds of  $\sim 400\ \text{m/s}$  using a LIPIT apparatus (Section 2.3.1). Particles impacted along three principal directions—[100]-face, [110]-edge, and [111]-corner impacts—are identified through SEM analysis (Section 2.4.1) and selected for further study. Micropillars  $\sim 1\ \mu\text{m}$  in diameter are formed from the impacted samples using a FIB (Section 2.2.3) and compressed at  $0.01\ \text{s}^{-1}$  constant strain rate using an *in situ* SEM nanoindenter equipped with a flat diamond tip (Section 2.3.3).

To study the mechanical response of these heterogeneous nanostructures in more detail, we perform crystal plasticity simulations on synthetic microstructures which were generated based on the experimentally characterized nanostructures. Details about the model can be found in Section 2.6—including details on the coupled thermo-mechanical elasto-viscoplastic crystal plasticity model, parameter fitting for fcc silver, the synthetic microstructure generation method, and model evaluation. The crystal plasticity simulations provide valuable information not attainable through experiments—including stress and strain distributions and three-dimensional evaluation of nanostructural changes during compression.

#### 3.4.1 Mechanical responses of impacted samples compared to single crystals

Representative engineering stress-strain responses obtained from the microcompression tests of an as-synthesized microcube, a single crystal pillar formed from a synthesized microcube, and a pillar formed from a [100]-impacted microcube are shown in Figure 3-19(d). All three

samples have a similar effective diameter (624 nm - 642 nm), to eliminate contributions from sample size effects. The single crystal microcubes exhibit an initial linear elastic behavior followed by an abrupt massive strain burst due to the spontaneous nucleation of dislocations. Many slip steps along the  $\{111\}$  planes are visible on the surface of the deformed microcube (Figure 3-19(a)). The single crystal pillars show a similar response of an initial linear elastic behavior up to a distinct yield point where slip starts to occur, but the massive strain burst is absent because of the presence of surface defects that result from FIB milling [125]. The plastic portion of the single crystal pillar's deformation contains many strain bursts which mark slip events. Without any grain boundaries to stop the dislocations, they exit the sample forming slip steps. A large slip step, where the top portion of the sample has sheared along a particular  $\{111\}$  plane relative to the bottom portion, is visible in the SEM image of the deformed micropillar (Figure 3-19(a)). The stress-strain response of the [100]-impacted sample is a stark contrast to the responses of the single crystal samples. The linear elastic region is difficult to distinguish from the plastic region, making a prediction of the yield strength difficult—even with the strain offset method. The plastic response at higher strains ( $>0.15 \epsilon$ ) indicates intragranular slip also occurs in this sample, although the smaller serrations correspond to smaller slip events. Large slip steps are not visible on the SEM image of the deformed pillar ([100]-impacted sample, Figure 3-19(c)), in contrast to the deformed geometries of the single crystal samples (Figure 3-19(a-b)).

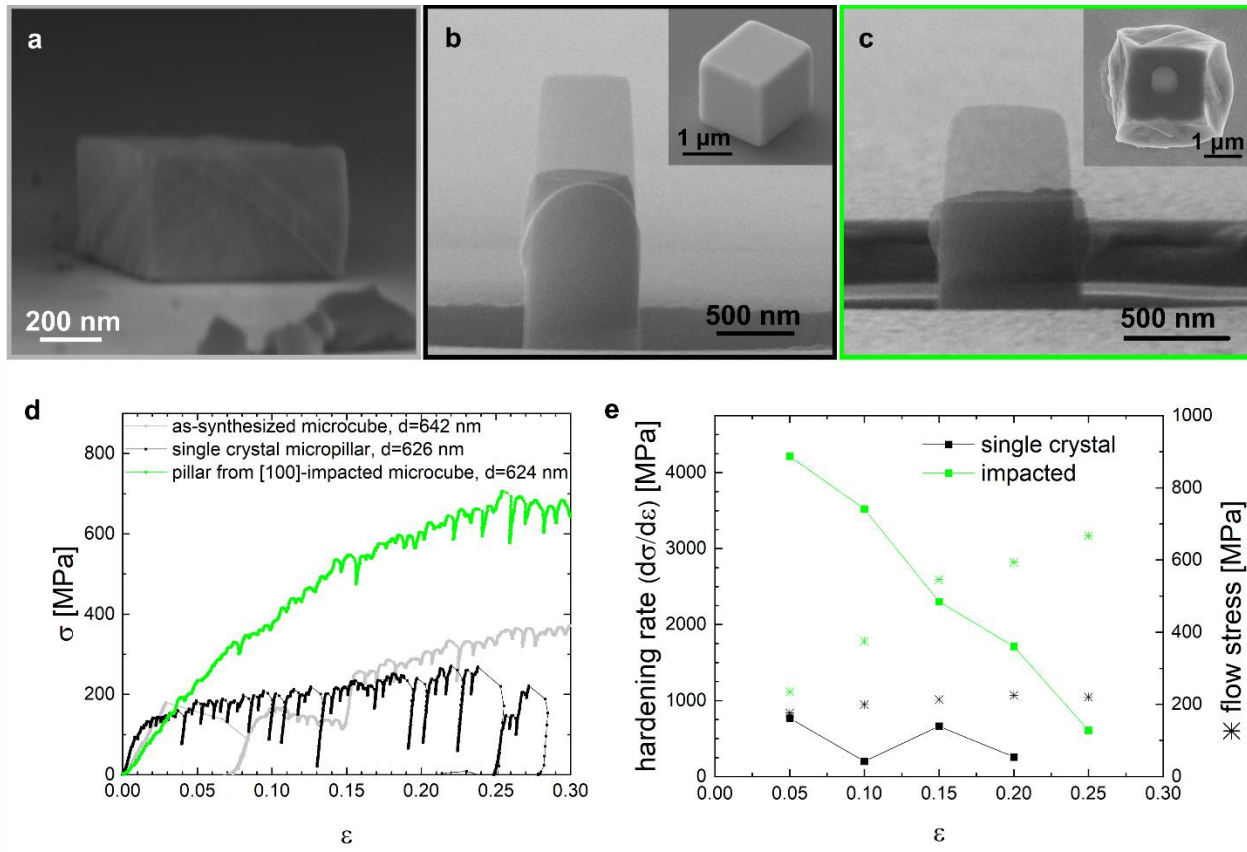


**Figure 3-19: Microcompression testing of single crystal and impacted samples** (a) SEM image of compressed microcube ( $d=642$  nm), with stress-strain curve shown in (d), (b) transparent SEM image of FIB-fabricated micropillar from single crystal microcube (insert) overlaid on SEM image of compressed micropillar; corresponding stress-strain curve in (d), (c) transparent SEM image of FIB-fabricated micropillar from [100]-impacted microcube (insert) overlaid on SEM image of compressed micropillar; corresponding stress-strain curve in (d), (d) stress-strain curves of samples in (a-c), (e) hardening rates and flow stresses at 0.05 strain increments from stress-strain curves of single crystal pillar and impacted samples in (d).

Additionally, the impacted sample exhibits much greater strain hardening than the single crystal samples. This can be seen in the stress-strain curves of (Figure 3-19(d)) and is clearly shown in (Figure 3-19(e)) where the hardening rates ( $\theta$ ) at different strains are shown for each sample. The hardening rates at 5-25% strain are calculated by fitting a line to a portion of stress-strain curve at  $\varepsilon_i = \pm 0.01$ ; the slope of this line ( $d\sigma/d\varepsilon$ ) is the hardening rate at that strain ( $\varepsilon_i$ ). The plot of hardening rate as a function of strain (Figure 3-19(e)) reveals that the [100]-impacted sample

exhibits much higher hardening than the single crystal sample, at all strains ( $\sim 3.5$ - $17.6\times$  greater, depending on the strain. At early stages of deformation ( $0.05$ - $0.1 \epsilon$ ), the hardening rate of the impacted sample is very high ( $\theta(\epsilon=0.1)=3519.9$  MPa,  $17.6\times$  the hardening rate of the single crystal sample). The unusually high hardening rates before  $\sim 0.1$  strain make it difficult to distinguish the yield point—a new challenge that arises in the gradient nano grained metals. As deformation progresses, the stress-strain curve of this impacted sample begins to level off, with a reduction in the strain hardening rate. The high hardening rate in the impacted sample corresponds to a dramatic increase in the flow stress with increasing strain, while the flow stress in the single crystal sample remains approximately constant (Figure 3-19(e)). At 25% strain, the flow stress of the impacted sample is over 300% that of the single crystal sample.

Microcompression tests were performed on micropillars formed from single crystal microcubes and impacted microcubes with [100], [110], and [111] impact orientations. Stress-strain responses from the compression of micropillars with diameters of  $\sim 600$ - $1500$  nm, taper angles of less than  $4^\circ$ , aspect ratios of  $\sim 1$ - $3$ , and with good contact with the substrate and indenter during deformation are selected for comparison and further analysis (see Appendix B.3 for details of each sample). This strict set of pillar quality parameters ensures that differences in the mechanical responses are due to nanostructural differences rather than changes in sample preparation, shape, or size. Within the diameter range of  $600$ - $1500$  nm, the sample size effect should be minimal [125] (Section 3.2). In all, nine single crystal samples, eight [100]-impacted samples, twelve [110]-impacted samples, and twelve [111]-impacted samples are selected for further analysis. [100]-impact is the least common and the samples are often tilted off the substrate. Although any impacted samples which are noticeably titled off the substrate are not tested, any sample which is lying on a substrate is not going to have perfect uniform contact with the substrate.

Therefore, the portion of the stress-strain curve which should represent the linear elastic response of the material with slope equal to the elastic modulus of the material is often nonlinear and compliant resulting in underestimation of the elastic modulus. Small differences in the contact conditions upon loading can influence this initial linear elastic portion; therefore, a compliance correction and shifting of the elastic portion to match the unloading modulus, as outlined in Section 2.3.3, are applied to the data. The corrected engineering stress-strain curves for all micropillars from [100], [110], and [111] impacted samples, as well as the single crystal samples, are plotted in (Figure 3-20).

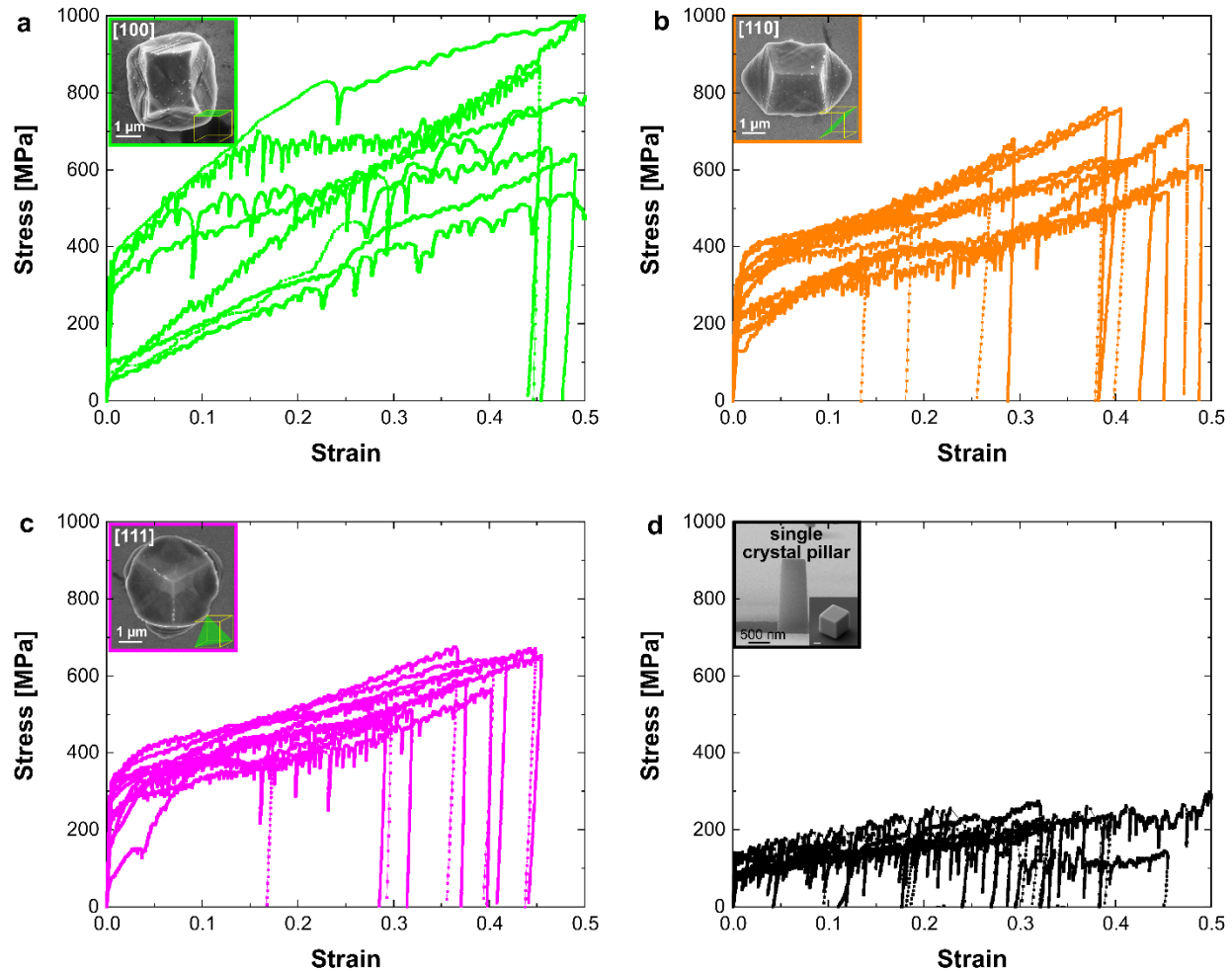


**Figure 3-20: Engineering stress-strain curves from microcompression tests of [100]-impacted samples (a), [110]-impacted samples (b), [111]-impacted samples (c), and single crystal samples (d).**

To compare the stress-strain responses, the data for [100]-impacted, [110]-impacted, [111]-impacted, and single crystal samples are separated but plotted with the same scales for stress and strain. Henceforth, the data for the impacted samples is color coded by impact orientation: [100]-green, [110]-orange, [111]-magenta. Immediately apparent is the stark contrast between the high stresses achieved in the impacted samples and the consistently low stress achieved in the single crystal samples. In accordance with the observations made from Figure 3-19, it appears that all impacted samples—regardless of impact orientation—exhibit higher strain hardening and achieve

higher flow stresses compared to the single crystal samples. Appreciable strain hardening cannot be achieved in the single crystal sample since dislocations are continuously exiting the crystal through large, localized slip events—indicated by the large serrations in the stress-strain curve (Figure 3-20 (d)). Without any nanostructural features to act as barriers to their motion, nucleated dislocations propagate across the crystal on the slip planes and annihilate at the free surfaces. In contrast, the impacted samples exhibit ultra-high strain hardening (Figure 3-20 (a-c)). The smaller serrations in the stress-strain responses of the impacted samples (Figure 3-20 (a-c)) reveal that dislocation slips are arrested by the complex nanostructure formed from impact.

Comparing the stress-strain curves for the different impact orientations (Figure 3-20 (a-c)), it appears that the [110] and [111] impacted samples behave similarly (Figure 3-20 (b-c)), while the [100]-impacted samples tend to exhibit higher strain hardening and achieve higher flow stresses at high strains (Figure 3-20 (a)). Interestingly, there is also less scatter in the stress-strain curves of the [110] and [111] samples as compared to the [100] samples, suggesting the impact-induced nanostructures are more predictable and vary less with different processing parameters in the aforementioned cases. Since the [100]-impacted samples undergo the most extensive nanostructural changes—including a phase transformation (Section 3.3.1), variations in the formed nanostructures may be more extreme than in the other orientations, which would explain the increased scatter in the mechanical responses.

To obtain a mechanistic understanding of the sources of variation in mechanical responses and which nanostructural features elicit improved performance, we perform crystal plasticity simulations on synthetic microstructures based on experimental input. The single crystal constitutive model defined by Bronkhorst et al. [92] is used for the simulations, which assumes thermally activated slip is the dominant deformation mechanism (Section 2.6.1). Experimental

TKD data from samples of each impact orientation (Figure 3-21 (a-e)) is used to generate synthetic microstructures. Grain size gradient functions are defined by curve fitting the experimental average grain size vs position data (Figure 3-21 (a)). The seed positions and weights used to generate the synthetic microstructures are determined based on these gradient grain size functions (Section 2.6.3). The initial dislocation density for each grain is defined based on power law curves fitted to experimental GND density data (Figure 3-21 (a)). This method is used to incorporate grain size effects on strength, rather than relying on an empirically derived Hall-Petch term (Section 2.6.4). Grain orientations are randomly assigned from the experimentally defined orientation distribution function. The synthetic sample geometries are based off the experimental micropillar sizes. Experimental data from five micropillars of each impact orientation are used for input and comparison to the simulations. In all, fifteen synthetic microstructures are generated based on experimental data. Details for these fifteen samples are listed in Table 3-1.

**Table 3-1: Details for simulation samples**

Simulation ID	Experiment ID	Dislocation density power law	Pillar diameter [μm]	Pillar height [μm]	Strain	# grains	# elements
100_1	Set52_S5	$8.3908 \times 10^{14} d^{-0.2001}$	0.9935	0.78	40%	700	992,717
100_2	Set33_S1		0.74	0.704	49%	371	1,558,297
100_3	Set10_S5		0.62	0.958	45%	284	1,596,130
100_4	Set9_S12		0.66	0.783	53%	309	1,068,233
100_5	Set52_S3		0.966	0.795	46%	675	1,006,331
110_1	Set25_S1	$6.985 \times 10^{14} d^{-0.3651}$	0.913	0.988	40%	100	1,322,231
110_2	Set26_S2		0.918	0.983	39%	105	1,266,253
110_3	Set9_S9		0.642	1.484	47%	52	1,291,663
110_4	Set9_S10		0.64	1.329	14%	53	1,214,815
110_5	Set9_S14		0.594	1.072	30%	46	1,231,346
111_1	Set26_S3	$5.7575 \times 10^{14} d^{-0.5336}$	0.929	1.455	40%	20	1,347,673
111_2	Set32_S4		0.917	1.405	38%	22	1,140,717
111_3	Set9_S13		0.62	1.502	29%	12	1,189,908
111_4	Set4_S10		1.496	1.465	40%	30	1,281,297
111_5	Set0_S11		0.919	1.926	30%	22	1,159,423



Examples of synthetic microstructures are shown in Figure 3-21 (c-e) and can be compared to the corresponding experimental TKD patterns. Note that the TKD patterns are two-dimensional, and the synthetic microstructures are actually three dimensional but side views are shown here. The synthetic microstructures are colored by grain orientation (left) and average dislocation density (right) based off the colormaps shown in Figure 3-21 (c). The similarities between the synthetic microstructures and corresponding experimental data confirms that our synthetic microstructure generation algorithm produces statistically equivalent microstructures. The experimental grain size and dislocation density distributions are well represented in the synthetic microstructures. This is also illustrated well in Figure 3-21 (f-g): even though the sample dimensions vary, the experimental grain size gradients are well represented in the synthetic microstructures Figure 3-21 (f). Additionally, Figure 3-21 (g) shows that average dislocation density within the synthetic “grains” follow the experimentally defined power law functions (Figure 3-21 (b)).

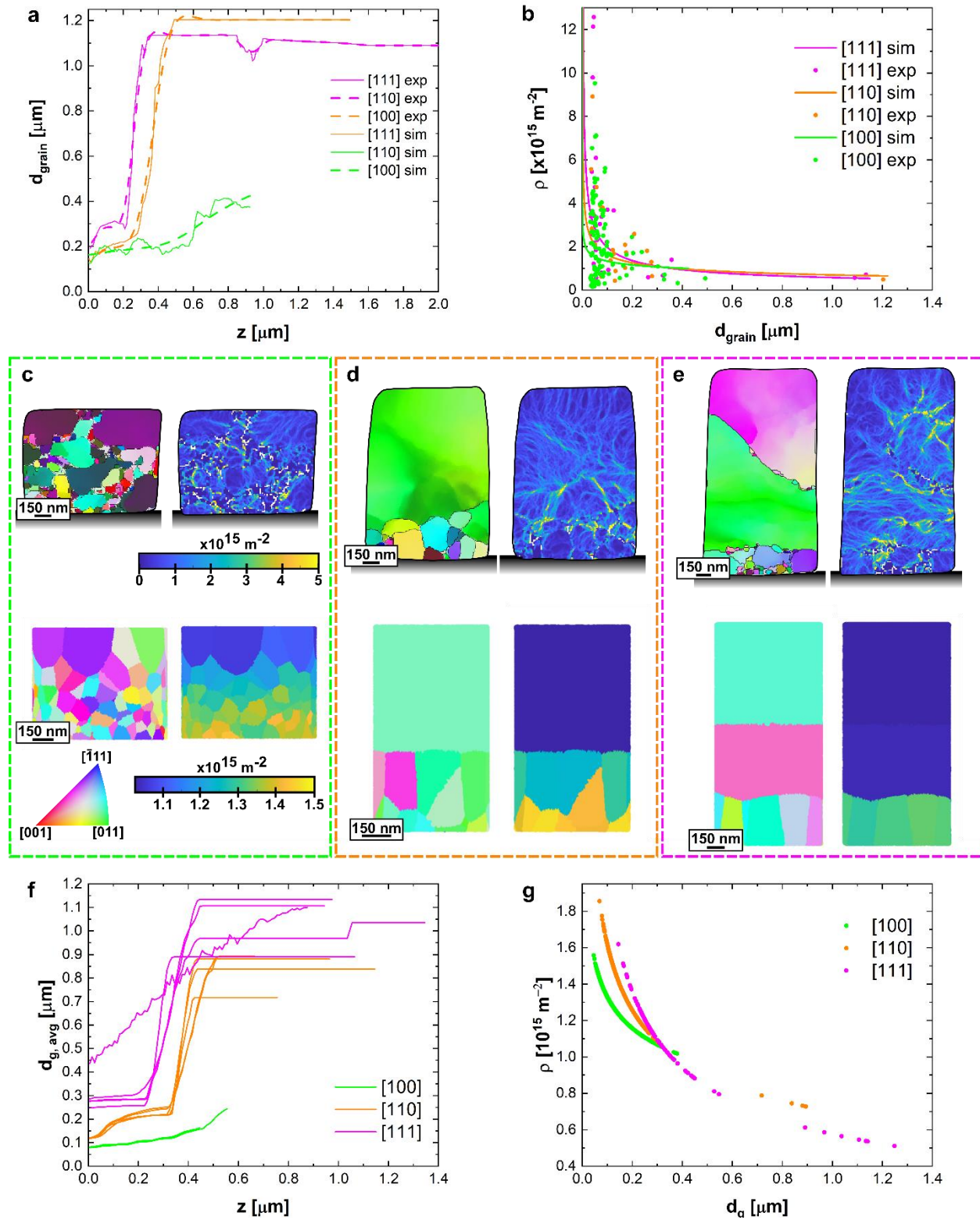


**Figure 3-21: Synthetic microstructures based on experimental data** (a) curves fitted to experimental grain size distributions, (b) power law curves fitted to experimental data of average dislocation density vs grain diameter, (c-e)

examples of synthetic microstructures based on [100] (c), [110] (d), and [111] (e) impacted samples, (f) average grain size vs z position for each of the 15 synthetic microstructures, (g) average dislocation density vs grain diameter for each of the 15 synthetic microstructures.

Now that we have established that the synthetic microstructures accurately represent the experimentally characterized nanostructures, we can compare the results of the crystal plasticity simulations to the experimentally measured mechanical responses. Overall, the stress-strain responses from simulations are very similar to those obtained from microcompression tests (Figure 3-22 (a-b)). The experiments and simulations for the [110] and [111] samples are especially well aligned. However, the large scatter in the mechanical responses of [100] impacted samples is not well captured in the simulations. In the experiments, some [100] impacted samples show lower yield strengths, but in the simulations, all [100] samples exhibit higher yield strengths than the [110] and [111] samples. This discrepancy is likely due to larger variations in the [100]-impacted samples' nanostructures due to the extensive grain refinement and the martensitic phase transformation. Nanostructural data from only one TKD map is used to create the [100] synthetic microstructures; therefore, potential variations between different [100]-impacted samples' nanostructures would not be captured in the simulations.

The average flow stresses and hardening rates in the simulations are comparable to the experiments (Figure 3-22 (c-f)). All samples exhibit increasing flow stress with increasing strain—indicating strain hardening. Like experiments, the [110] and [111] samples exhibit similar mechanical responses: the average flow stresses and hardening rates in these samples are very similar (Figure 3-22 (d, f)). The standard deviations in flow stress are also very comparable for the [110] and [111] samples in experiments and simulations, revealing that the simulations accurately capture variability between samples of these orientations. This confirms that the [110] and [111] impacted nanostructures are more predictable than the [100] impacted nanostructures. The

simulations show a clear distinction between the flow stresses and hardening rates achieved in [100] samples compared to the other orientations. As seen in experiments, the [100] samples exhibit ultra-high strain hardening rates. The simulations also show consistently higher yield strengths and flow stresses achieved in the [100] samples. We hypothesize that the improved mechanical performance of the [100] samples is due to the impact-induced nanostructural gradients. These gradients likely induce heterogeneous deformation, which is assumed to be a main driver of improved mechanical performance in GNG metals.

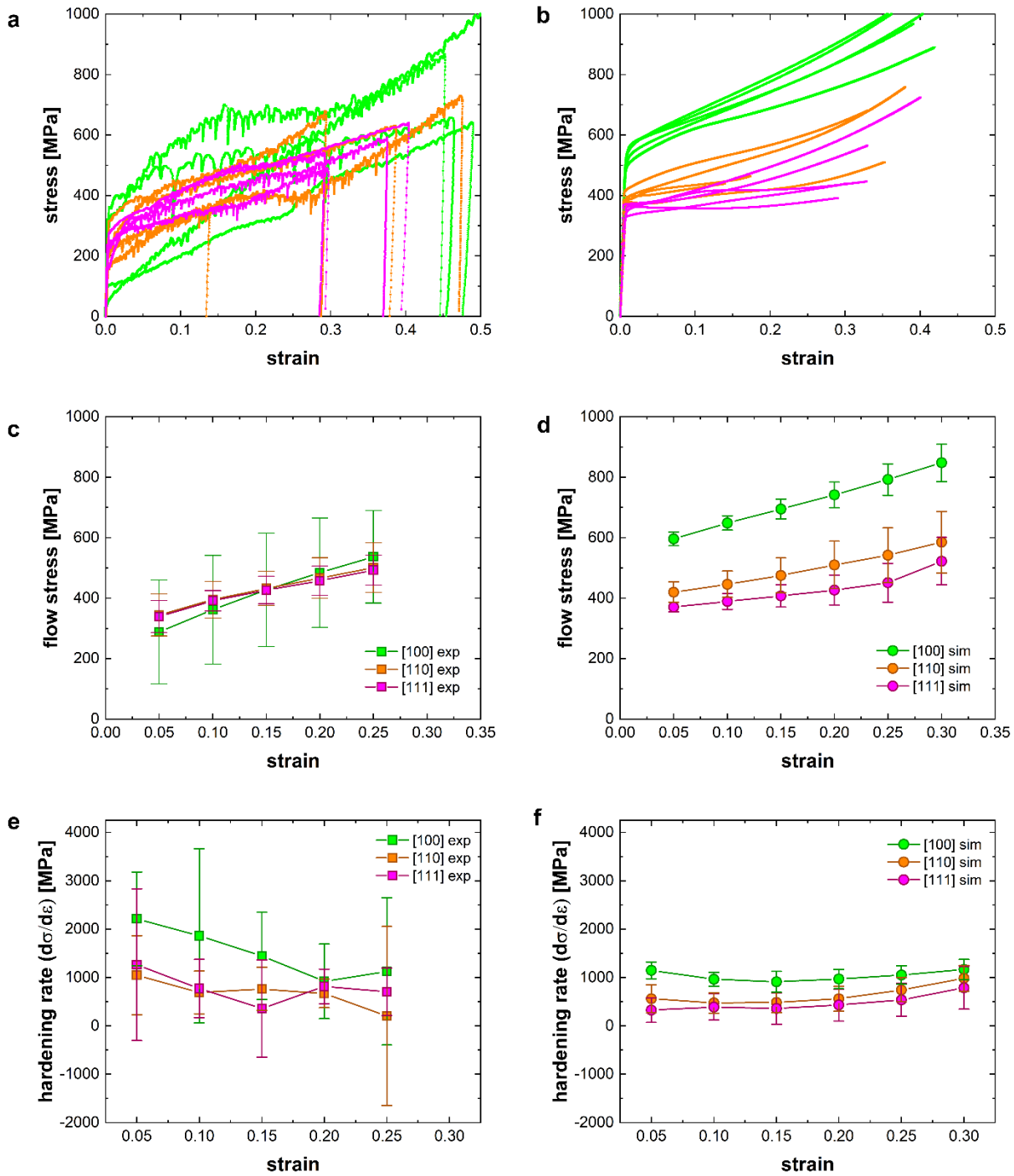


**Figure 3-22: Comparison of mechanical responses obtained through experiments and simulations** (a-b) stress-strain responses from microcompression tests (a) and crystal plasticity simulations (b), (c-d) averages and standard deviations of flow stresses for each orientation at 0.05 strain increments from experimental (c) and computational (d) stress-strain curves, (e-f) averages and standard deviations of local hardening rates for each orientation at 0.05 strain increments from experimental (c) and computational (d) stress-strain curves.

### 3.4.2 *Heterogenous deformation induced strengthening*

Evidence of heterogeneous deformation can be seen in the SEM images of the compressed pillars and is quantifiable through the simulations (Figure 3-23). SEM images of representative compressed pillars clearly show localized deformation at the top of the pillars (Figure 3-23 (a, c, e)). Like their similar stress-strain responses, the [110] and [111] impacted samples exhibit similar deformed geometries (Figure 3-23 (c, e)). Strain localization is extreme in these two cases, as the bulging of the sample top over the pillar base indicates. These deformed geometries are mirrored in the simulations (Figure 3-23 (d, f)), where the displacement field shows localization of deformation to the top of the pillar. The banded contour lines suggest that shear localization develops on the slip planes of the large coarse grains within these samples. The sharp transition between the nanogained region with high intrinsic strength to the ductile coarse-grained region in the [110] and [111] impacted samples (Figure 3-21) corresponds to the region of extreme deformation localization seen in the deformed geometries. The compressed [100]-impacted sample, in contrast, exhibits less extreme deformation localization at the top and exhibits deformation across the sample (Figure 3-23 (a)). However, a gradient in the displacement field still exists (Figure 3-23 (b)). Under uniaxial compressive loading, sequential yielding of the gradient nano-grained structure occurs, with the coarse-grained regions plastically deforming before the nanogained regions. This strain gradient plasticity is distinct from that which arises from nonuniform loading such as bending and torsion: here, the strain gradient is due to the intrinsic heterogeneous nanostructures rather than the deformation mode.

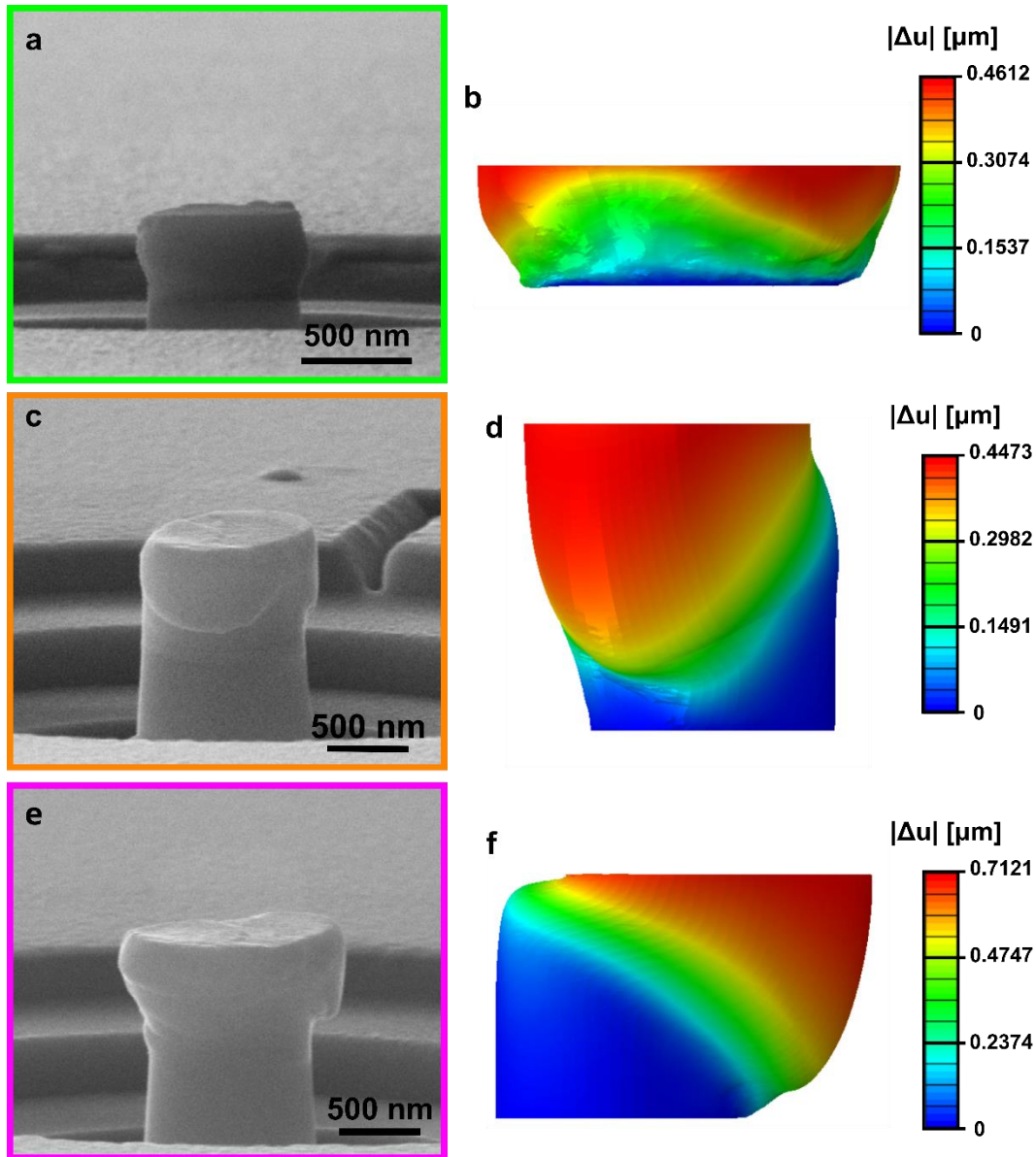


**Figure 3-23: Heterogeneous deformation** shown through post-compression SEM images of [100]-impacted (a), [110]-impacted (c), and [111]-impacted (e) samples, and colormaps showing displacement magnitude on the deformed geometries of [100] (b), [110] (d), and [111] (f) synthetic microstructures.

Now that we have confirmed that heterogeneous deformation occurs, we can delve into how this affects the stress and strain distributions and the overall mechanical response. Considering the imposed stress state of uniaxial compression, we first investigate the normal stress and strain components in the compression direction ( $z$ , 3). We have selected the two samples which

exhibit the “best” (high yield strength/hardening rate) and “worst” (low yield strength/hardening rate) mechanical responses to study their stress and strain distributions in more detail. The initial microstructures of these two samples are shown in Figure 3-24 (b-c). The sample which exhibited the “best” mechanical response (Figure 3-24 (a)—dark green) corresponds to a [100]-impacted sample with a smooth grain size gradient (Figure 3-24 (b)). The sample which exhibited the “worst” mechanical response (Figure 3-24 (a)—maroon) corresponds to a [111]-impacted sample with a sharp transition in grain size and a large coarse grain filling up much of the sample volume (Figure 3-24 (c)). Since the majority of the sample is a single grain, this sample may behave more similarly to a single crystal than a GNG sample. The corresponding colormaps in Figure 3-24 (e-f) showing the  $\epsilon_{33}$  strain distribution clearly show strain localization at the top of the samples. However, in the [100] sample with a smooth GNG structure, there appears to be a gradient of increasing strain magnitude with increasing z position (height). The average  $\epsilon_{33}$  every 0.01  $\mu\text{m}$  is plotted against the z position (Figure 3-24 (d)). Most samples do exhibit a strain gradient, but the [100] samples show the most extreme gradient in  $\epsilon_{33}$ . Comparing the two samples of interest, the sample which exhibited the better mechanical performance has a steeper and more consistent strain gradient. Similarly, we can look at the  $\sigma_{33}$  stress distributions in the samples (Figure 3-24 (g-i)). A stress gradient is apparent in the [100] GNG sample, but not in the [111] sample. The stress gradient follows the grain size gradient, with larger compressive stresses in regions of smaller grain sizes. These results reveal the role of heterogeneous deformation induced stresses. From sequential yielding of the GNG layers, back stresses are produced in the softer region and forward stresses are produced in the harder region. The back stresses reduce the compressive stress applied in the coarser grained regions. The colormap in Figure 3-24 (h) shows that the  $\sigma_{33}$  stress component in some elements within coarse grains can even become tensile.



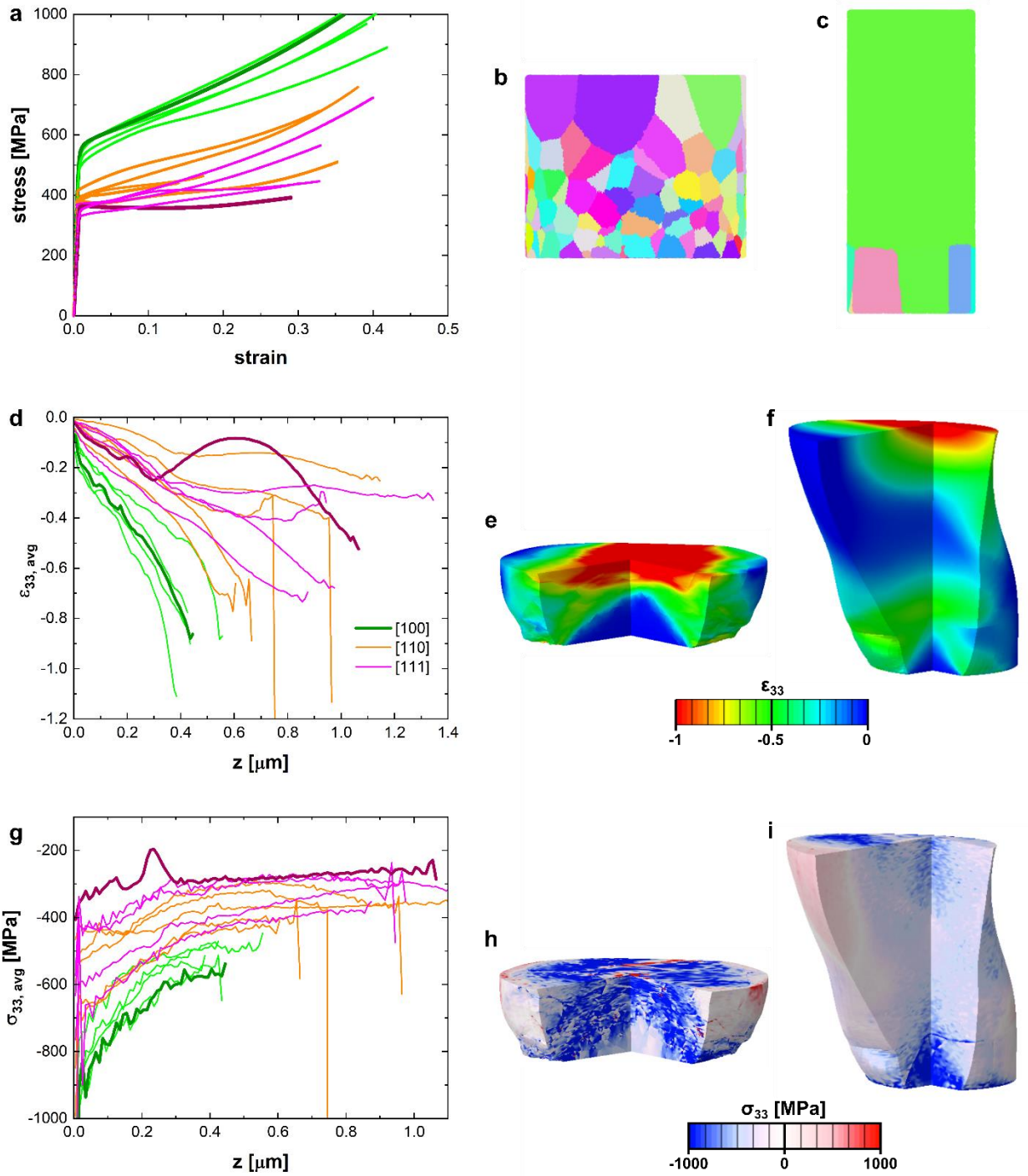


**Figure 3-24: Heterogeneous deformation induced strengthening** (a) stress-strain responses of all simulations with the “best” and “worst” mechanical responses highlighted, (b) initial microstructure of sample exhibiting the “best” stress-strain response, (c) initial microstructure of sample exhibiting the “worst” stress-strain response, (d) average  $\epsilon_{33}$  along the sample height ( $z$ ), (e) colormap of  $\epsilon_{33}$  corresponding to the sample in (b), (f) colormap of  $\epsilon_{33}$

corresponding to the sample in (c), (g)  $\sigma_{33}$  along the sample height (z), (h) colormap of  $\sigma_{33}$  corresponding to the sample in (b), (i) colormap of  $\sigma_{33}$  corresponding to the sample in (c).

We can also investigate the multiaxial stress and strain states within the sample by calculating the von Mises stress and strain and the Lode parameter. The components of the stress and strain tensors and/or principle stresses are used to calculate the equivalent stress and strain and the Lode parameter in each element through the following equations:

$$\text{Equivalent stress: } \sigma_e = \frac{1}{\sqrt{2}} \sqrt{(\sigma_{11} - \sigma_{22})^2 + (\sigma_{11} - \sigma_{33})^2 + (\sigma_{22} - \sigma_{33})^2 + 6(\sigma_{12}^2 + \sigma_{13}^2 + \sigma_{23}^2)}$$

$$\text{Equivalent strain: } \varepsilon_e = \frac{\sqrt{2}}{3} \sqrt{(\varepsilon_{11} - \varepsilon_{22})^2 + (\varepsilon_{11} - \varepsilon_{33})^2 + (\varepsilon_{22} - \varepsilon_{33})^2 + 6(\varepsilon_{12}^2 + \varepsilon_{13}^2 + \varepsilon_{23}^2)}$$

$$\text{Lode parameter: } \mu_\sigma = \frac{2\sigma_2 - \sigma_1 - \sigma_3}{\sigma_1 - \sigma_3}$$

These values are calculated for each element and then the average values along the sample height (binned every 0.01  $\mu\text{m}$ ) are computed and plotted against the z position (Figure 3-25).

Like the strain component in the compression direction (Figure 3-24 (d)), the equivalent strain exhibits a gradient along the sample height (Figure 3-25 (a)). This strain gradient is most extreme in the [100] samples—again pointing to the role of heterogeneous deformation in the improvement of mechanical properties. The von Mises stress distributions along the sample height reveal higher stress in the nanograined regions (Figure 3-25 (b)). In the [110] and [111] samples, the von Mises stress is relatively constant at larger z—which corresponds to the coarse-grained regions (Figure 3-25 (b)). In contrast, the [100] samples exhibit a smooth and constant decrease in average von Mises stress after peaking in the nanograined region. All samples show relatively lower von Mises stress at z=0, which then steeply increases with increasing z. This is likely due to the fixed boundary condition at the pillar base. We are planning to run additional simulations with altered orientations of the grain size gradient to understand the influence of gradient direction and

grain size location with respect to the loading and boundary conditions (i.e., inverse gradients with coarse grains at the pillar base, gradients oriented at different angles with respect to the compression direction, etc).

The Lode parameter provides a measure of the deviatoric stress and reveals whether a material element is in a state of overall tension or compression. Three extreme cases of the Lode parameter are illustrated through the Mohr circle plots in Figure 3-25 (c): a Lode parameter of 1 can correspond to a state of uniaxial compression, a Lode parameter of -1 can correspond to a state of uniaxial tension, while a Lode parameter of 0 can correspond to a state of pure shear. Most samples remain in a state of compression across the sample height; however, the average Lode parameter in some samples turns negative at larger  $z$ —revealing a state of overall tension (Figure 3-25 (c)). A clear gradient of decreasing Lode parameter with increasing  $z$  is seen in the [100] samples—revealing the influence of gradient heterogeneous deformation on the multiaxial stress state. In contrast, the [111] and [110] samples do not exhibit such clear gradients in the Lode parameter.

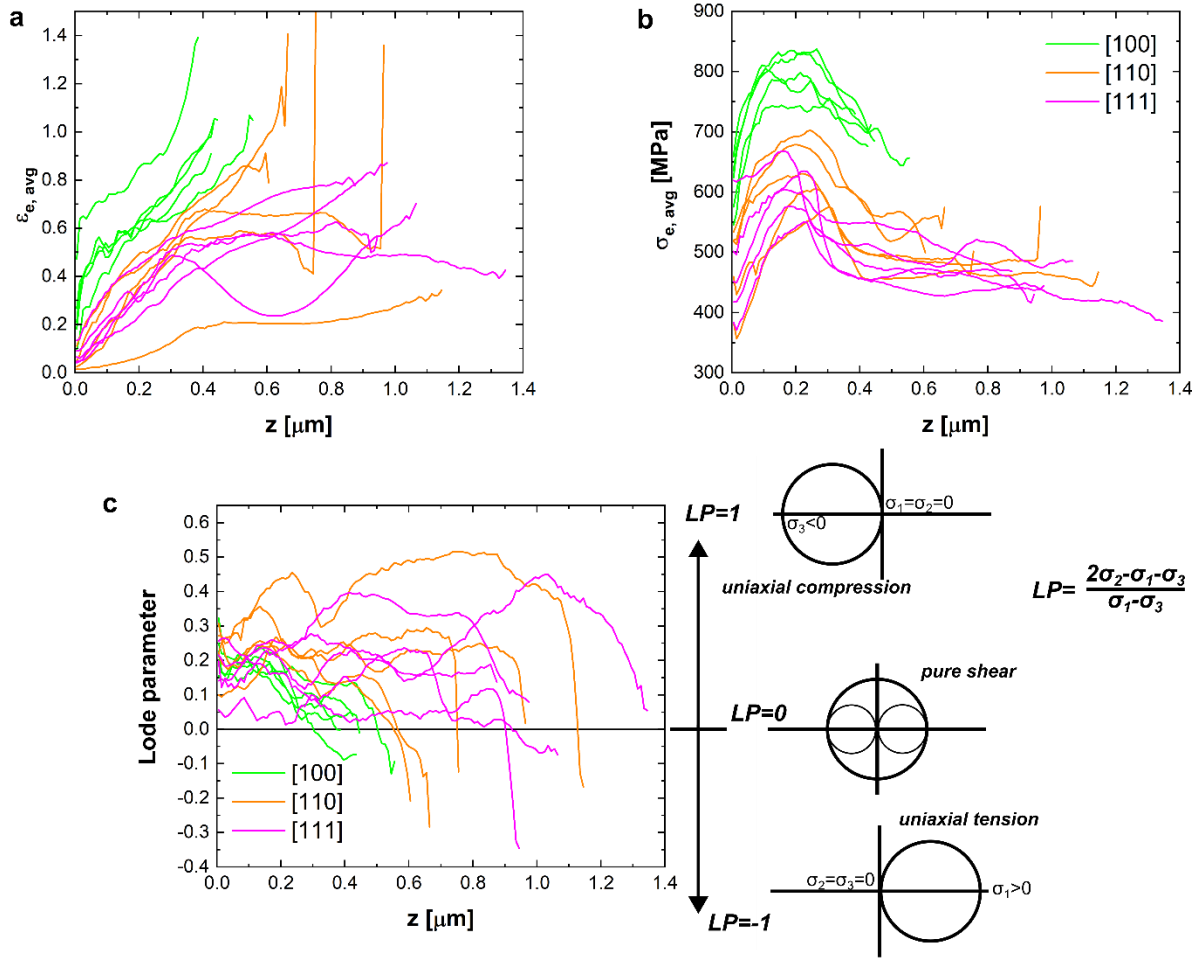


**Figure 3-25: Multi-axial stress and strain states along the sample heights** (a) average equivalent strain along the sample heights, (b) average equivalent stress along the sample heights, (c) average Lode parameter along the samples heights with key values illustrated through Mohr circle plots.

### 3.4.3 Synergistic property improvements

To quantify the improved mechanical responses of the impact-induced nanostructures, we calculate the average yield strengths, compressive toughness, elastic moduli, flow strengths, and hardening rates for samples of each impact orientation. The averages and standard deviations of the hardening rates ( $d\sigma/d\varepsilon$ ) and flow stresses at strains of 5-25% for each sample type are plotted in Figure 3-26 (a-b). Again, all impacted samples outperform the single crystal samples, with higher hardening rates and flow stresses at all strains analyzed. For the single crystal samples, the

average flow stress remains approximately constant with increasing strain, corresponding to the very low strain hardening rates and even turning negative (softening) at higher strains. In contrast, a steady increase in the flow stresses of impacted samples with increasing strain corresponds to higher average hardening rates. The [100]-impacted samples exhibit the highest average strain hardening rates and the largest standard deviations in values. Again, this suggests that the nanostructural changes induced through [100]-impact are extensive and can vary greatly.

Figure 3-26 (c) summarizes the differences in the average mechanical properties of the impacted and single crystal samples. The yield strength, compressive toughness, and elastic modulus were calculated for each sample. The yield strength was obtained by the offset method with 0.5% strain if the yield point was indistinguishable, or if obvious, as in the case of a strain burst upon yield, the yield point was selected. The toughness was found by calculating the area under the stress-strain curve from 0-0.3 strain—which is a measure of the strain energy the material can absorb up to 30% strain. The elastic modulus was determined from the slope of a line fit to the unloading curve of the engineering stress-strain curve with a compliance correction applied (this modulus is also used to shift the linear elastic portion of the stress-strain curve, Section 2.3.3). Averages and standard deviations of these properties for the [100], [110], and [111] impacted samples and the single crystal samples are displayed in the bar chart of Figure 3-26 (c). The [100] samples display the most variance in properties, in accordance with the large scatter in the stress-strain responses of different samples displayed in Figure 3-20 (a). Again, this points to larger potential variations in the [100]-impacted nanostructures. The average toughness values for all three impact orientations are very similar and  $\sim 2.8\times$  higher than the average toughness of single crystal samples (Figure 3-26 (c)). The average yield strengths of all impacted samples are also much higher than the single crystal samples ( $\sim 2.2\text{-}2.7\times$  higher).

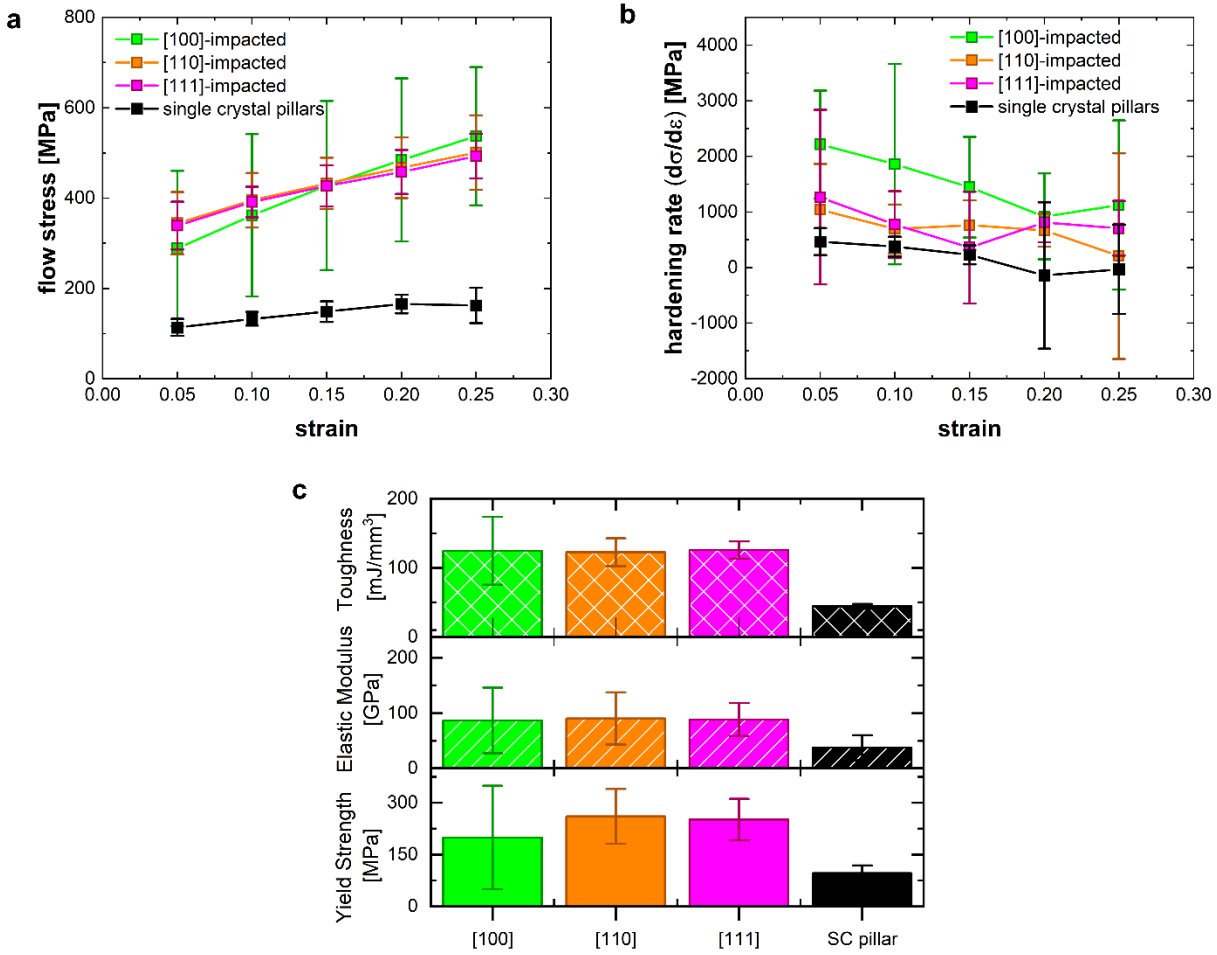


**Figure 3-26: Average mechanical properties of impacted samples compared to single crystal samples** (a) average flow stresses at select strains, (b) average hardening rates at select strains, (c) averages and standard deviations of toughness (up to 30% strain), elastic modulus (calculated from unloading curve), and yield strength (0.5% offset method).

The elastic modulus of each sample depends on the grain structure within the sample. The elastic modulus for grains of different orientations can be calculated from elasticity theory using the elastic constants for silver and coordinate transformations: the theoretical elastic moduli for [100], [110], and [111] oriented crystals of silver are  $E_{[100]} = 43.67 \text{ GPa}$ ,  $E_{[110]} = 83.61 \text{ GPa}$ , and  $E_{[111]} = 120.29 \text{ GPa}$  (see Appendix A.2). The experimentally measured average elastic modulus of the [100] oriented single-crystal pillars is  $37.1 \pm 23.1 \text{ GPa}$ , which is close to the

theoretical value of 43.67 GPa. The average elastic moduli for the impacted samples all differ from the theoretical elastic moduli of their original orientations—the closest is [110]-impacted samples which have an average value and standard deviation of  $90.3 \pm 47.5$  GPa (compared to  $E_{[110]} = 83.61$  GPa). These results are in accordance with the nanostructural characterization in Section 3.3.2, which revealed that the majority of a [110]-impacted sample remains in a single-crystal [110] orientation. In contrast, extensive restructuring occurs in the [100] sample—which would lead to a composite elastic modulus (measured elastic moduli for [100]-impacted samples:  $E = 86.6 \pm 59.5$  GPa) much different than that of its original [100] orientation (43.67 GPa). However, it should be recognized that this analysis is based on the elastic moduli calculated from the unloading portion of stress-strain curves obtained through microcompression testing, which may not produce as accurate elastic modulus as in tensile tests [191]. In a microcompression testing setup, there are many factors that can contribute to inaccurate measurement of the elastic modulus. Compliance of the indenter tip, substrate, and portion of the FIB-milled pillar that is not the sample (eg. Si and Au) must be accounted for and subtracted from the recorded displacement to calculate the actual displacement of the Ag sample (Section 2.3.3). Since there is some uncertainty in values used for the compliance correction (e.g. dimensions and properties), this can introduce uncertainty in the elastic modulus measurements.

A plot of toughness vs yield strength (Figure 3-27) shows the improvements in both properties attained by the impacted samples compared to both single-crystal and bulk polycrystalline Ag [105]. The toughness and yield strengths were calculated using the same method for bulk polycrystalline silver (2 and 20  $\mu\text{m}$  grains) from stress-strain data found in literature [105]. On average, an increase of over 250% in both the average yield strength and toughness is attained in the impacted samples ( $\sigma_y = 242 \pm 97.9$  MPa,  $u_T = 124 \pm 30.2$  mJ/

$mm^3$ ) when compared to the single-crystal pillars ( $\sigma_y = 96.1 \pm 22.7 \text{ MPa}$ ,  $u_T = 44.3 \pm 3.41 \text{ mJ/mm}^3$ ). A maximum improvement of 4.7x in strength and 5x in toughness is achieved in the impacted samples compared to the single-crystal pillars. The impacted samples also show a synergistic improvement in strength and toughness compared to bulk polycrystalline Ag—up to 7.4x and 4x, respectively. On average, the impacted samples show improved strength ( $\sim 2.7x$ ) and toughness ( $\sim 2.1x$ ) compared to the properties of bulk polycrystalline Ag found in literature. As typically mutually exclusive properties, a synergistic improvement in both strength and toughness is remarkable.

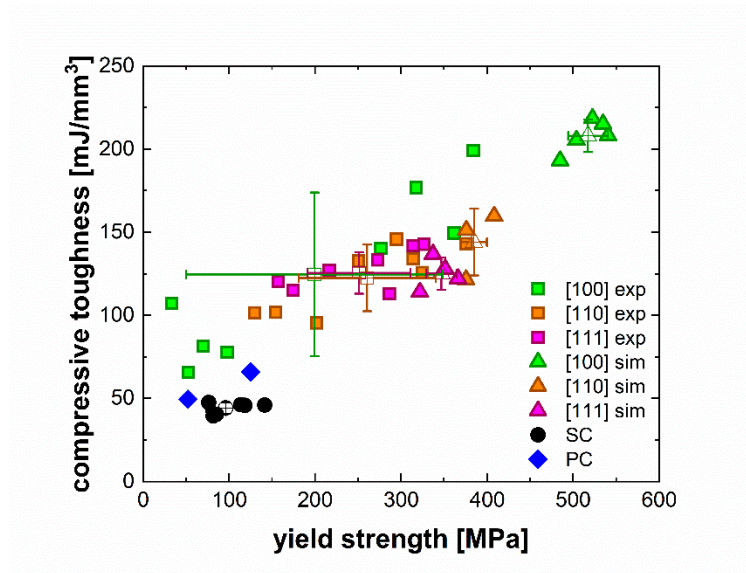


**Figure 3-27: Synergistic improvements in strength and toughness**

The simulations show similar average values compared to the experiments, with the exception of the [100] samples (Figure 3-27). By orientation, the simulations show 2.6, 1.5, and 1.4 times the strength and 1.7, 1.2, 1 times the toughness compared to the average experimental data for [100], [110], and [111] samples, respectively. The averages for the [110] and [111] samples are very similar to experiments. The [100] samples show consistently higher strength and toughness values in the simulations. In contrast, the [100] samples in experiments show a bimodal



behavior, where some [100] samples exhibit the highest strengths and toughness of all impacted samples, while other experimental [100] samples have low strengths and thus lower toughness. If the nanostructure formed does not contain pronounced grain size and GND density gradients, significantly improved properties from gradient plasticity will not occur. The synthetic structures for the [100] simulations all have clear grain size and dislocation density gradients—thus, consistently high strengths and toughness are achieved. With such variation in properties, we must understand the plasticity mechanisms governing the mechanical response to be able to improve impact processing conditions that yield heterogeneous nanostructures with the most desirable properties.

### **3.5 Activation of complementary plasticity mechanisms provides synergistic property improvements**

To investigate the plasticity mechanisms which lead to improved mechanical performance, we perform nanostructural characterization post-compression to identify the nanostructural changes which occurred during quasi-static compression. We can also track the structural changes during compression in the crystal plasticity simulations. We performed TKD on the three compressed micropillars whose mechanical responses are highlighted in Figure 3-28. The three samples chosen for microcompression testing and subsequent nanostructural characterization had similar impact conditions as the three corresponding uncompressed samples (Figure 3-11). We compare the nanostructures of the corresponding compressed and uncompressed samples to gain insight into the active deformation mechanisms during compression. The dominant plasticity mechanisms may differ between the unique impact orientation dependent nanostructures.

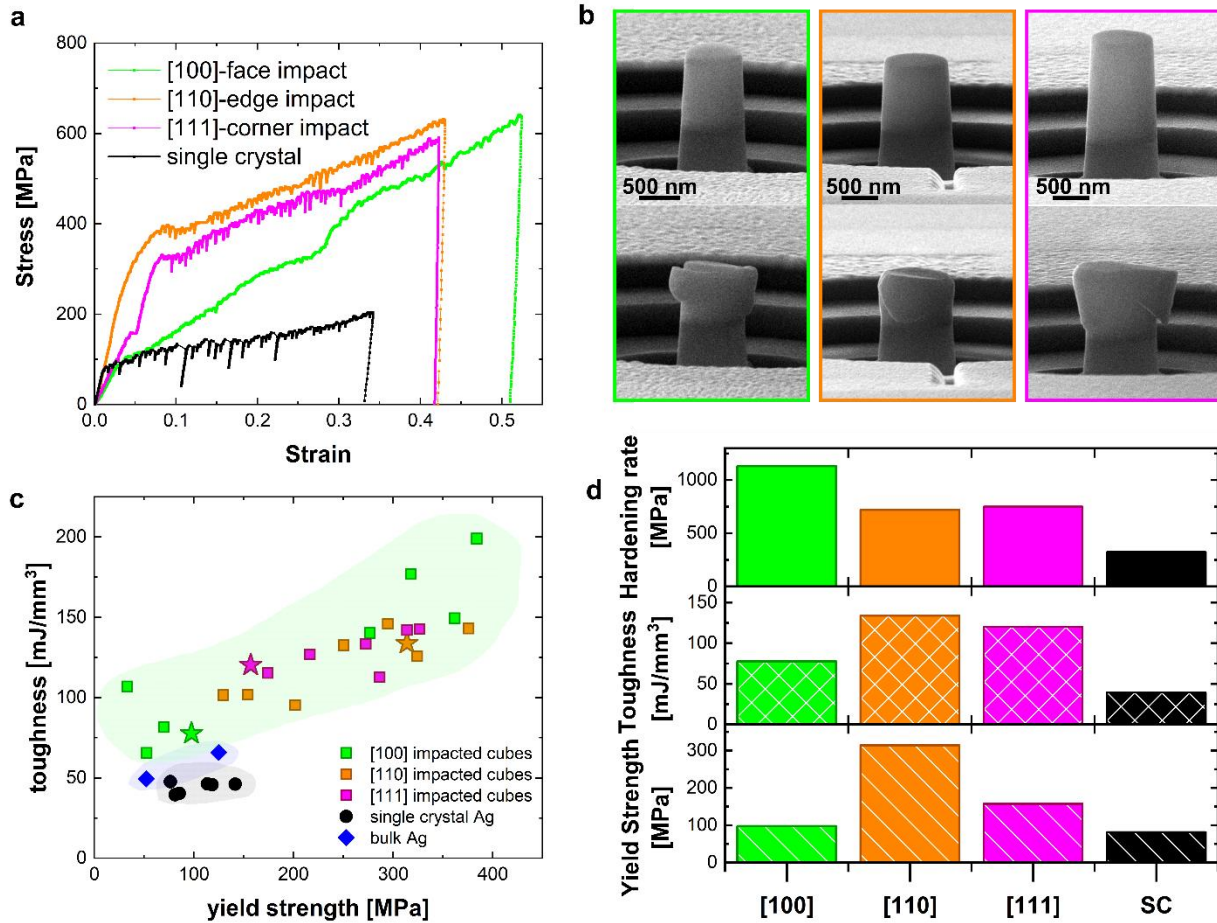


**Figure 3-28: Mechanical performance of samples selected for further nanostructural characterization** (a) stress-strain curves corresponding to the samples selected for post-compression nanostructural characterization with the stress-strain curve of a compressed single crystal Ag pillar shown for reference, (b) SEM images of the micropillars (impacted samples) before and after compression, (c) toughnesses vs yield strengths of single crystal Ag pillars (black), bulk Ag (blue), and impacted Ag microcubes (green – [100], orange – [110], and magenta – [111]); starred data points correspond to the three impacted samples that were further processed for TKD nanostructural analysis, (d) hardening rates ( $d\sigma/d\epsilon$ ), toughnesses, and yield strengths computed from the stress-strain curves in (a).

### 3.5.1 Dominant plasticity mechanisms in [110]-impacted samples

The nanostructural changes during compression of a [110]-impacted sample are illustrated in Figure 3-29. A TKD scan is acquired on the entire cross-sectional area of the compressed pillar (Figure 3-29 (a)). The [110] compressed sample, like its uncompressed counterpart, exhibits a step-function-like grain size gradient (Figure 3-29 (e))—containing nanograins mostly near the impact

plane, while the remainder of the sample is a large single crystal (Figure 3-29 (b)). The similarity between the grain size distributions in the [110] samples reveals that the plastic deformation is dominated by intragranular slip, since intergranular plasticity can significantly change the grain structure in the nanograined region. A strong (110) texture is apparent in both the compressed and uncompressed samples (Figure 3-29 (d)), with the texture being slightly more diffuse in the compressed case because of the intragranular crystal rotations and high dislocation activity leading to the formation of subgrain boundaries. Misorientation across subgrain boundaries is accommodated by dense GND networks (Figure 3-29 (b–c)). Such subgrain formation and rotation accommodates large strain in the coarse-grained region and may eventually lead to the formation of high angle grain boundaries under severe plasticity. Higher average GND density in the compressed sample is resultant from the increased GND activity in the coarse-grained region (Figure 3-29 (e)).

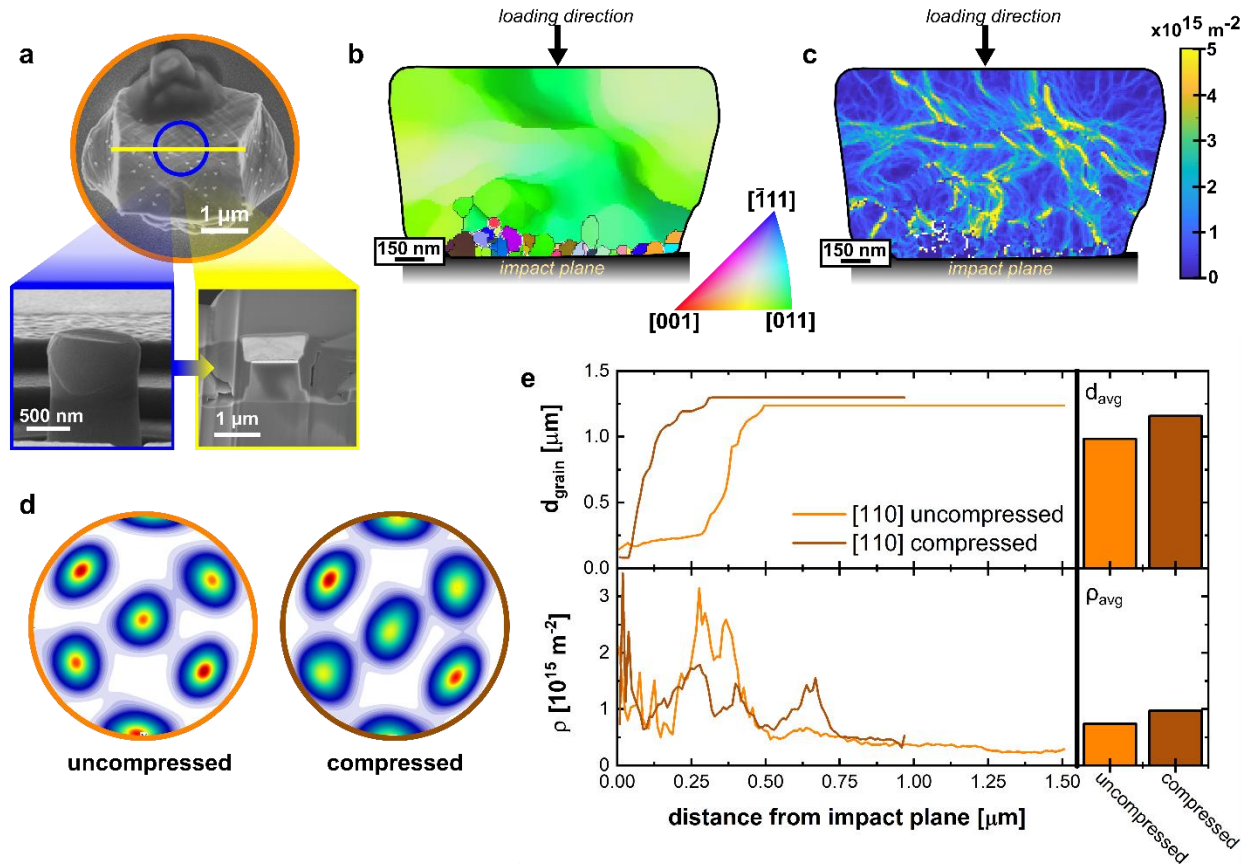


**Figure 3-29: Nanostructural changes due to quasistatic compression of a [110]-impacted sample** (a) SEM images of impacted microcube, compressed pillar, and pillar cross-section for TKD analysis, (b) TKD orientation map, (c) GND density map, (d) (110) pole figures of uncompressed and compressed samples, (e) grain size and GND density distributions and respective averages for uncompressed and compressed [110]-impacted samples.

To confirm these observations and assess differences in the nanostructural evolution during compression of different [110] samples, we study the dislocation density and grain orientation changes tracked in the crystal plasticity simulations. Unlike experiments, we can track the nanostructural changes within the same sample. In experiments, we need to rely on the assumption that samples impacted under similar conditions have similar nanostructures, since the same sample before and after compression cannot be characterized. Figure 3-30 (a) shows the stress-strain responses of the [110] simulations. To examine what nanostructural changes lead to the variation in stress-strain responses, we selected the two samples with the most different responses for further

analysis: Simulation 110\_1 (Figure 3-30 (a), black – high yield strength and hardening rate) and Simulation 110\_3 (Figure 3-30 (a), magenta – low yield strength and hardening rate). First, we investigate the change in dislocation density within these two samples as large increases in dislocation density would explain high strain hardening. Figure 3-30 (b) shows the average change in dislocation density per grain for each simulation (final state vs initial state), while the average change in dislocation density per element is shown in the colormaps of Figure 3-30 (c-d). As determined from the experimental nanostructural characterization, pronounced intragranular dislocation activity accommodates the large strain localization in the coarse-grained region (Figure 3-30 (b-d)). Comparing these two [110] simulations, the sample which exhibits higher strain hardening (110\_1) shows larger changes in dislocation density per grain compared to the simulation which exhibited the lowest strain hardening (110\_3) (Figure 3-30 (b)). The  $\Delta\rho$  colormap for simulation 110\_3 (Figure 3-30 (c)) shows a band of high dislocation density in the top large grain, revealing shear localization on one of the slip systems. Such shear localization is similar to that which we observed in the quasi-statically compressed single crystal silver samples (Section 3.2). Since the plastic deformation of this sample is dominated by single crystal-like behavior, high strain hardening cannot be achieved. The yield strength, however, is higher than the single crystals (~100 MPa, Section 3.2.2) due to the hardening effect of the nanograined layer with initially higher dislocation density. In contrast, the sample which exhibited high strain hardening (110\_1) shows large changes in dislocation density throughout all grain sizes (Figure 3-30 (b) – black). This is also seen in the  $\Delta\rho$  colormap for simulation 110\_1 (Figure 3-30 (d)), where large changes in dislocation density appear throughout the large grain and into the nanograins. In this sample, the pronounced dislocation activity in the large grain accommodates

much of the strain, but due to heterogeneous-induced stresses (Section 3.4.2), intragranular plasticity is also activated in the nanograin region.

The effects of these different intragranular plasticity mechanisms are seen in the orientation maps of these two samples (Figure 3-30 (e-f)). In Simulation 110\_3, minimal orientation changes occur (Figure 3-30 (e, g)), but any orientation changes are primarily isolated to the shear band. In contrast, large orientation changes are seen within both the large and small grains of Simulation 110\_1 (Figure 3-30 (f, h)). The orientation changes within grains reveal the formation of subgrain boundaries, as seen in the experimental results (Figure 3-29 (b-c)). High crystal rotation is seen along the nanograin-to-coarse grain boundary and within some of the nanograins (Figure 3-30 (f, h)). The final orientations within some of the nanograins are closer to neighboring grains' orientations than the grain's initial orientation (Figure 3-30 (f)). This reveals that intragranular plasticity may lead to intergranular plasticity.

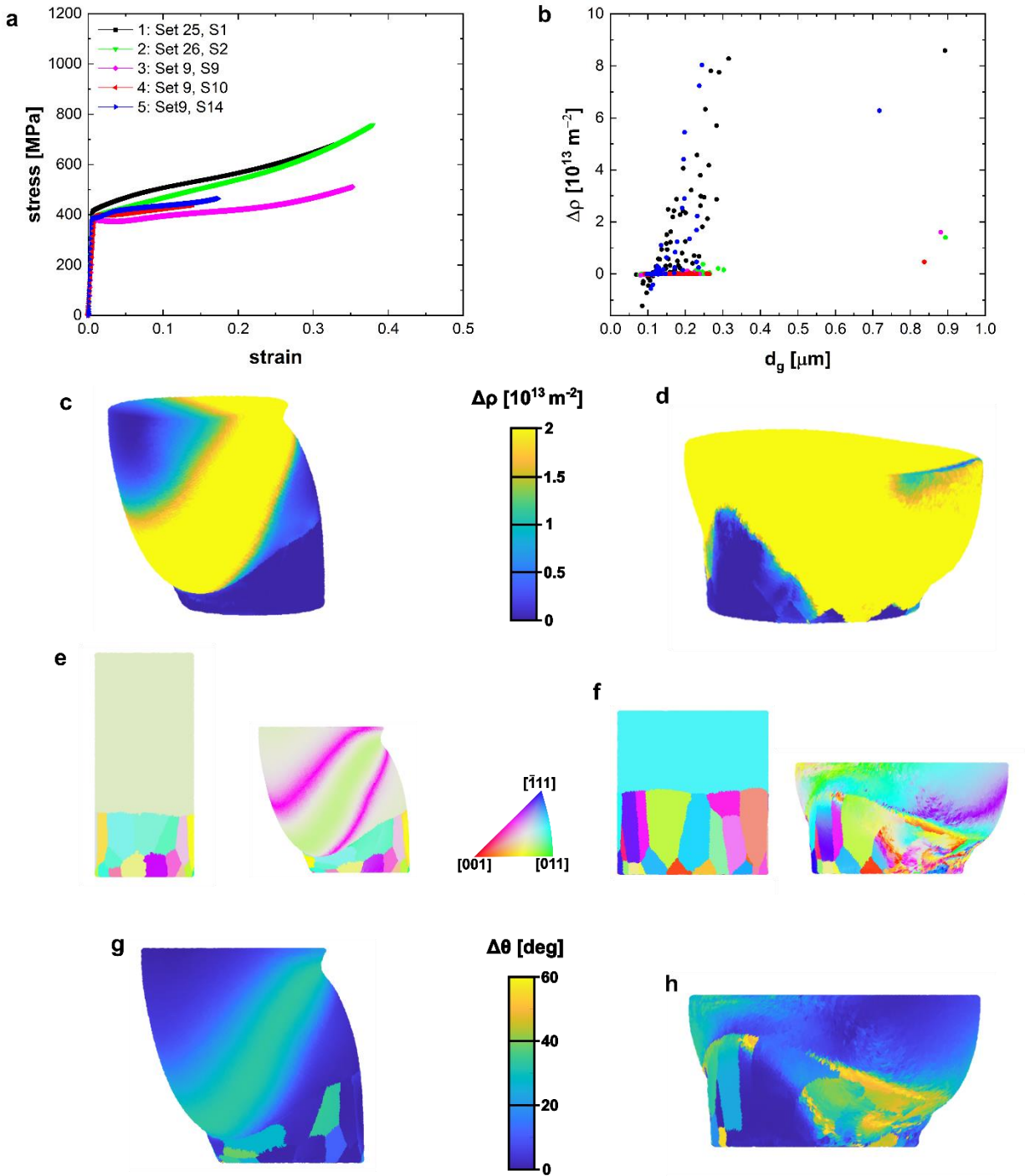


**Figure 3-30: Nanostructural changes in [110] samples tracked through CP simulations** (a) stress-strain curves from the five simulations of [110] samples, (b) average change in dislocation density vs grain size – color coded based on the legend in (a), (c-d) average dislocation density change per element in simulation 110\_3 (c) and simulation 110\_1 (d), (e-f) grain orientation plots before and after compression for simulation 110\_3 (e) and simulation 110\_1 (f), (g-h) angle between initial and final orientation per element in simulation 110\_3 (g) and simulation 110\_1 (h).

### 3.5.2 *Dominant plasticity mechanisms in [100]-impacted samples*

TKD analysis of the compressed [100]-impacted sample reveals a different dominant plasticity mechanism than the [110] samples. Pronounced intergranular plasticity is evident from the changes in grain sizes, orientations, and GND density. The TKD grain map shows large sprawling grains with internal orientation gradients and nanograins interspersed throughout the sample (Figure 3-31 (b)). As in the uncompressed sample, a gradual increase in average grain size with increased distance still exists, but the average grain size is larger in the compressed sample compared to the uncompressed (Figure 3-31 (e)). Furthermore, the compressed sample shows a stronger texture than the uncompressed (Figure 3-31 (d)). These changes in the grain structure suggest that pronounced intergranular plasticity must have occurred—leading to grain coalescence. Mechanically driven grain coalescence can be accommodated through cooperative nanograin rotation and grain boundary migration in the presence of high dislocation densities. The high dislocation densities induced through impact drive nanograin formation, and high GND density remains in the nanograined regions after impact. To reduce the high strain energy stored in these regions, subsequent loading initiates intergranular plasticity (through dislocation activity at the nanograin boundaries) leading to grain coalescence. Pronounced intergranular plasticity is also evident in the decreased average GND density in the compressed sample (Figure 3-31 (e)), in addition to the changes in the grain structure.



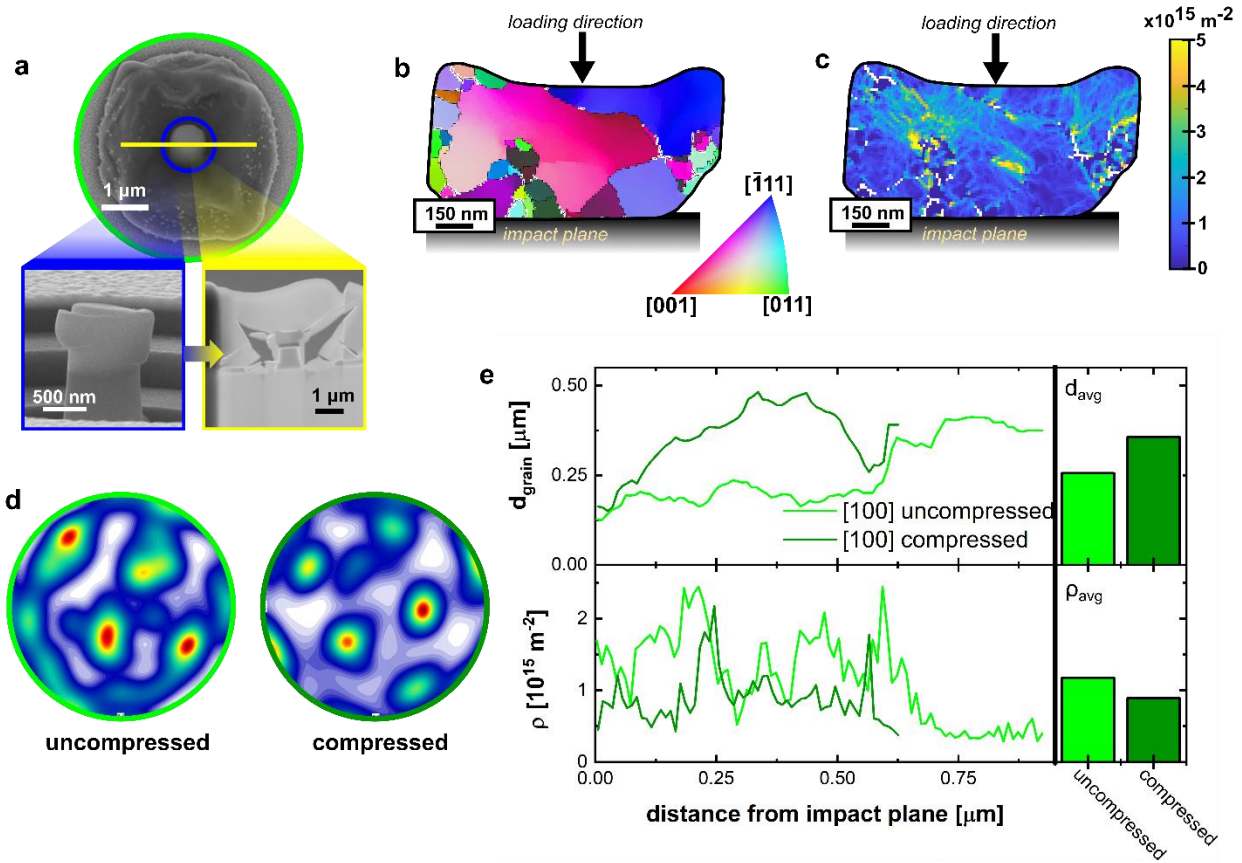


**Figure 3-31: Nanostructural changes due to quasistatic compression of a [100]-impacted sample** (a) SEM images of impacted microcube, compressed pillar, and pillar cross-section for TKD analysis, (b) TKD orientation map, (c) GND density map, (d) (110) pole figures of uncompressed and compressed samples, (e) grain size and GND density distributions and respective averages for uncompressed and compressed [100]-impacted samples.

Once again, we turn to the crystal plasticity simulations for additional clues about the active plasticity mechanisms (Figure 3-32). Special attention is placed on the simulations with the most varied mechanical responses: Simulation 100\_5 (Figure 3-32 (a), blue – high yield strength and hardening rate) and Simulation 100\_3 (Figure 3-32 (a), magenta – low yield strength and hardening rate). Like the [110] simulations, the sample which exhibits high strain hardening shows large changes in dislocation density throughout all grain sizes (Figure 3-32 (b)). There is a clear gradient of increasing  $\Delta\rho$  with increasing grain size (Figure 3-32 (b, d)). This nicely reflects the large strain gradient seen in the [100] samples (Figure 3-25 (a))—revealing that enhanced intragranular

dislocation plasticity accommodates the larger strains in the larger grains. In contrast, there is little change in the dislocation density of Simulation 100\_3 (Figure 3-32 (b, c)), corresponding to the lower strain hardening rates achieved in this sample.

The enhanced intragranular dislocation plasticity in Simulation 100\_5 appears to lead to intragranular crystal rotation (Figure 3-32 (f, h)). Orientation changes within grains point to the formation of subgrain boundaries (Figure 3-32 (f, h)). Additionally, some of the visible deformed grains seem to have similar orientations to their neighboring grains (Figure 3-32 (f)). This points to a combination of intra- and inter-granular plasticity leading to grain coalescence, as hypothesized from the experiments.

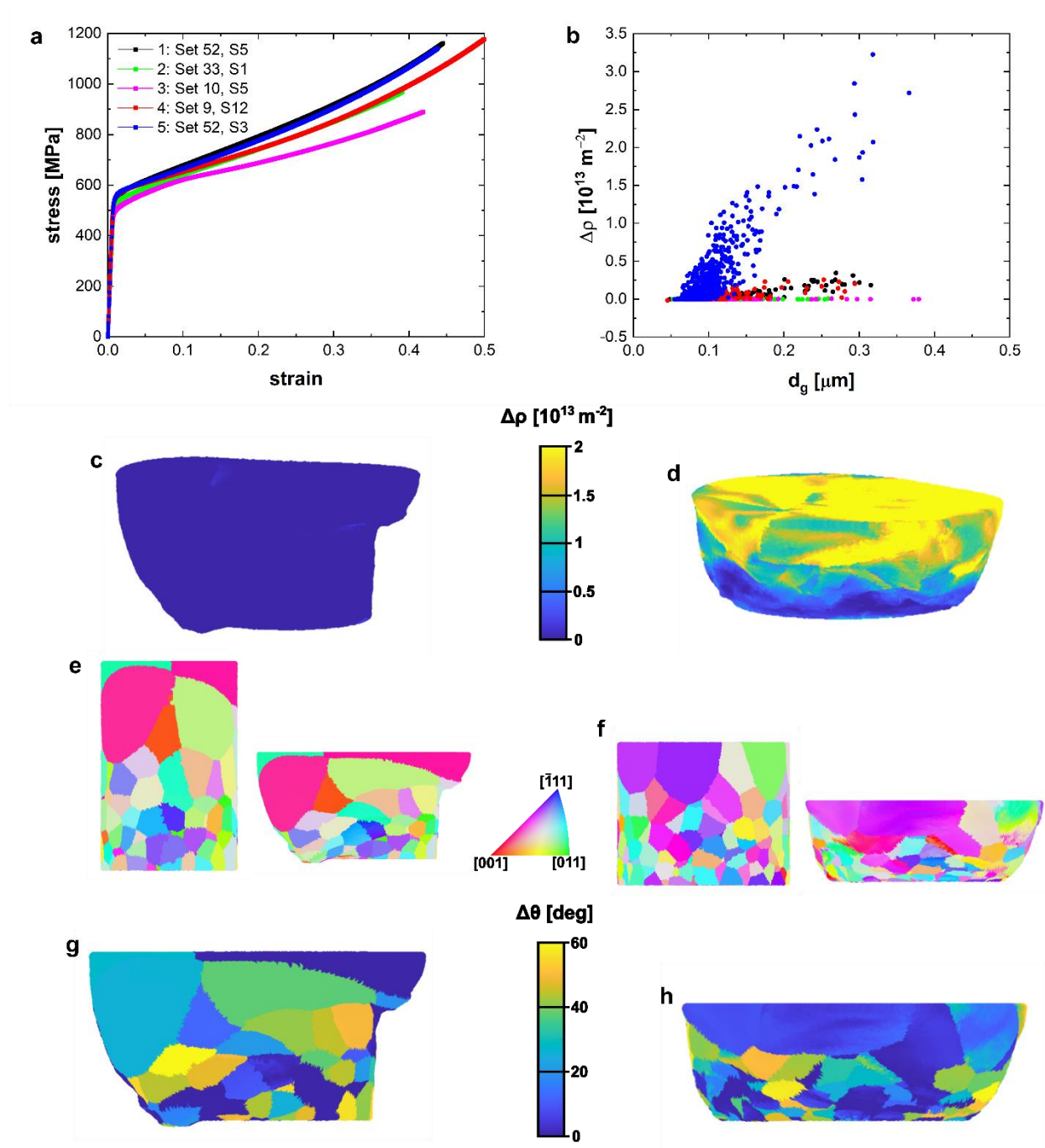


**Figure 3-32: Nanostructural changes in [100] samples tracked through CP simulations** (a) stress-strain curves from the five simulations of [100] samples, (b) average change in dislocation density vs grain size – color coded based on the legend in (a), (c-d) average dislocation density change per element in simulation 100\_3 (c) and simulation 100\_5 (d), (e-f) grain orientation plots before and after compression for simulation 100\_3 (e) and simulation 100\_5 (f), (g-h) angle between initial and final orientation per element in simulation 100\_3 (g) and simulation 100\_5 (h).

### 3.5.3 *Dominant plasticity mechanisms in [111]-impacted samples*

The dominant plasticity mechanism in the [111]-impacted samples is more challenging to deduce. In the [111] samples, increased texture (marking grain coalescence, Figure 3-33 (d)) and a more gradual grain size gradient (Figure 3-33 (e)) are juxtaposed with an increase in GND density and smaller average grain size further from the impact plane (Figure 3-33 (e)). These results indicate both intragranular and intergranular plasticity playing dominant roles. The TKD grain and GND density maps of the compressed [111] sample (Figure 3-33 (b, c)) show the result of these mechanisms. During compression, strain localization in the coarse-grained region is accommodated by pronounced dislocation activity. To reduce the strain energy, dislocations form subgrain boundaries which could eventually turn into new grains. The increase in GND density is from this intragranular plasticity. The opposite occurs in the nanograined region: grain coalescence reduces the high stored strain energy from impact-induced dislocations accommodating nanograin boundary misorientations. Thus, a complex interplay between intergranular and intragranular plasticity exists in the [111] samples.

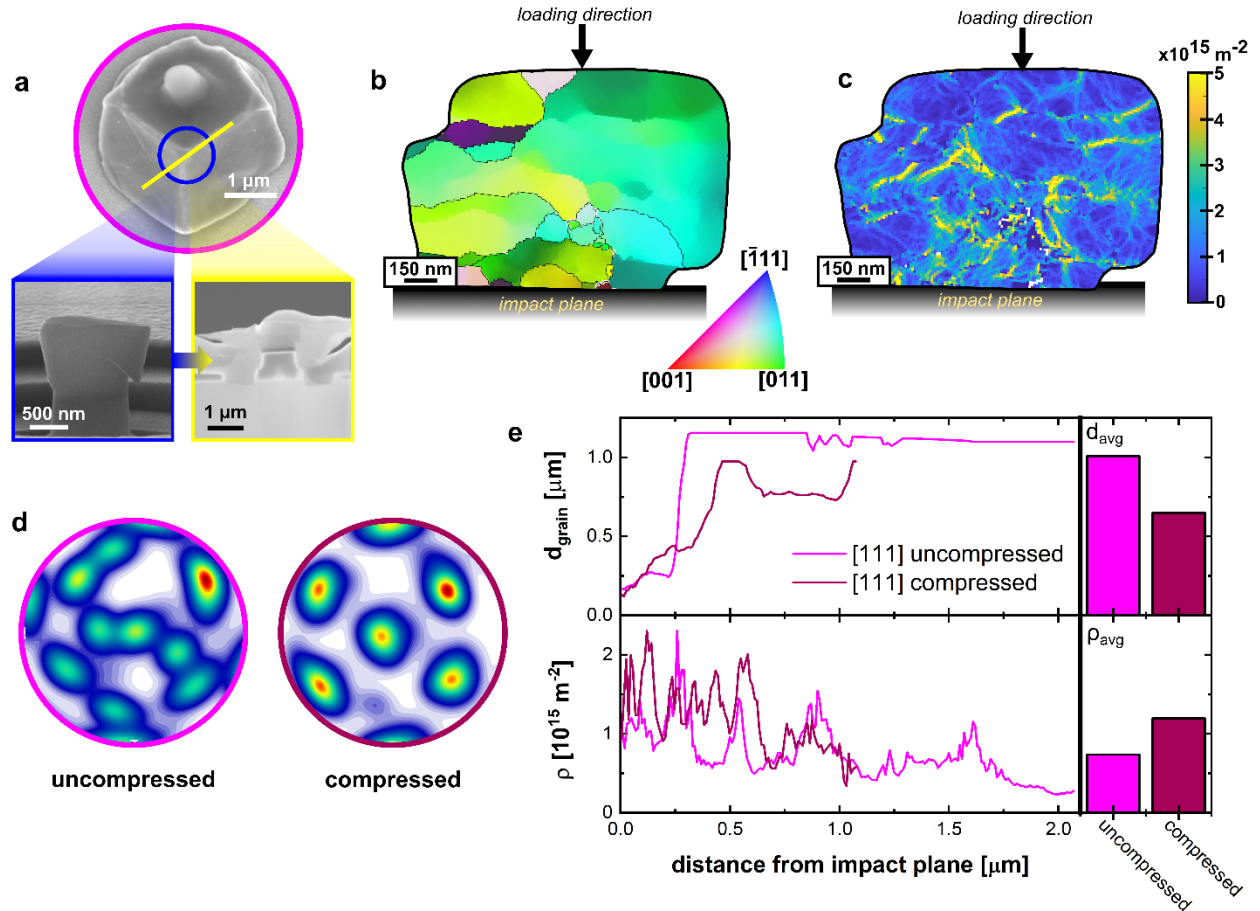


**Figure 3-33: Nanostructural changes due to quasistatic compression of a [111]-impacted sample** (a) SEM images of impacted microcube, compressed pillar, and pillar cross-section for TKD analysis, (b) TKD orientation map, (c) GND density map, (d) (110) pole figures of uncompressed and compressed samples, (e) grain size and GND density distributions and respective averages for uncompressed and compressed [111]-impacted samples.

The crystal plasticity simulation results tell a similar story as the other two orientations (Figure 3-34). The sample which exhibited the highest strain hardening (Simulation 111\_4; Figure 3-34 (a) – red) shows enhanced dislocation activity throughout the sample, but especially in the largest grains (Figure 3-34 (b) – red, Figure 3-34 (d)). In contrast, the sample with low strain hardening (Simulation 111\_3; Figure 3-34 (a) – magenta) shows an isolated band of increased dislocation density in the largest grain (Figure 3-34 (c))—much like Simulation 110\_3 (Figure 3-30 (c)). The enhanced dislocation activity in Simulation 111\_4 causes intragranular crystal

rotation (Figure 3-30 (f, h)), with influence from neighboring grains. Like the experiments, the simulations provide evidence for complementary intra- and inter-granular plasticity mechanisms.

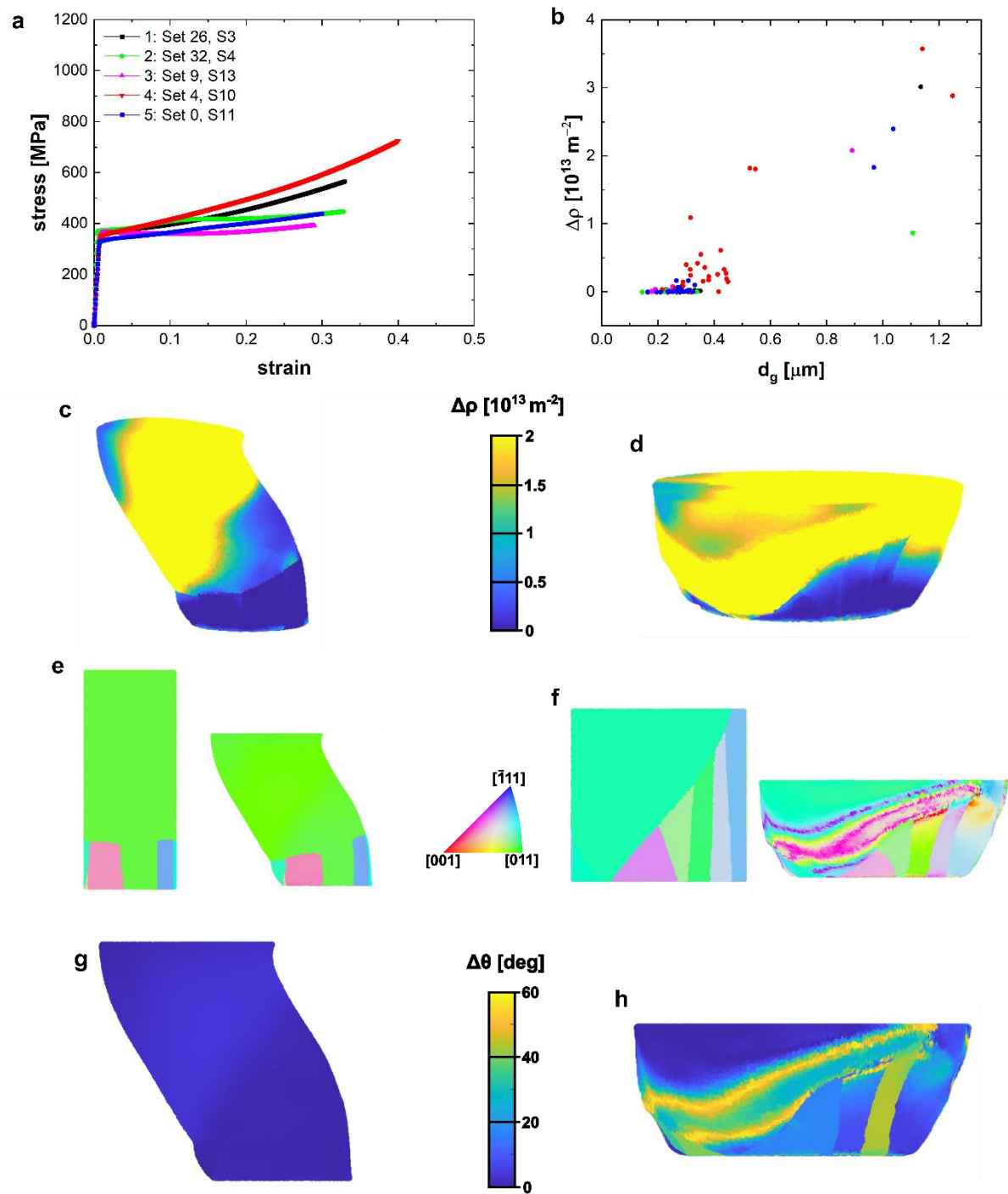


**Figure 3-34: Nanostructural changes in [111] samples tracked through CP simulations** (a) stress-strain curves from the five simulations of [111] samples, (b) average change in dislocation density vs grain size – color coded based on the legend in (a), (c-d) average dislocation density change per element in simulation 111\_3 (c) and simulation 111\_4 (d), (e-f) grain orientation plots before and after compression for simulation 111\_3 (e) and simulation 111\_4 (f), (g-h) angle between initial and final orientation per element in simulation 111\_3 (g) and simulation 111\_4 (h).

### 3.5.4 *Activation of complementary plasticity mechanisms through heterogeneous deformation*

Both intergranular and intragranular plasticity are present in all samples; what differs is the extent to which each of these mechanisms is present. Through experiments, we have shown that intragranular plasticity dominates in the [110]-impacted sample, intergranular plasticity dominates in [100]-impacted sample, and both types are prominent in [111]-impacted sample. Due to the extensive impact-induced recrystallization and high GND densities in the [100]-impacted sample (Figure 3-35 (a, c)), intergranular grain rotation and grain boundary migration lead to grain coalescence (Figure 3-35 (b)). Cooperative nanograin rotation and grain boundary migration enabled through high dislocation activity has been shown to enhance the ductility in nanocrystalline metals [174,175,192]. In contrast, intragranular plasticity dominates in the [110]-impacted samples, with high dislocation activity in the coarse-grained region accommodating much of the strain (Figure 3-35 (a, c, d)). Heterogeneous plasticity arises in all samples due to the grain size and GND gradients, but stress and strain gradients are most pronounced in the [100] samples (Section 3.4.2). Since soft coarse-grained regions yield before hard nanograin domains, GNDs pile-up at the boundary to accommodate the elastic-plastic mismatch. Pile-up of dislocations at the domain boundaries is especially apparent in the [110]-impacted sample, where a spike in GND density occurs at the sharp transition in grain size. Such pile-up of dislocations has been shown to induce back-stress in the soft domain and forward-stress in the hard domain ([172], Figure 3-35 (d)). These heterogeneous-deformation-induced stresses produce unusual mechanical responses, including increased strain hardening in soft domains and increased ductility in hard domains. Our results indicate that dislocation generation and accumulation within coarse grains leads to high strain hardening, promoted by hetero-deformation induced back stresses. Forward



stresses and high impact-induced dislocation densities in the nanogained regions promote cooperative intergranular plasticity mechanisms leading to grain growth and ductility in nanogained domains.

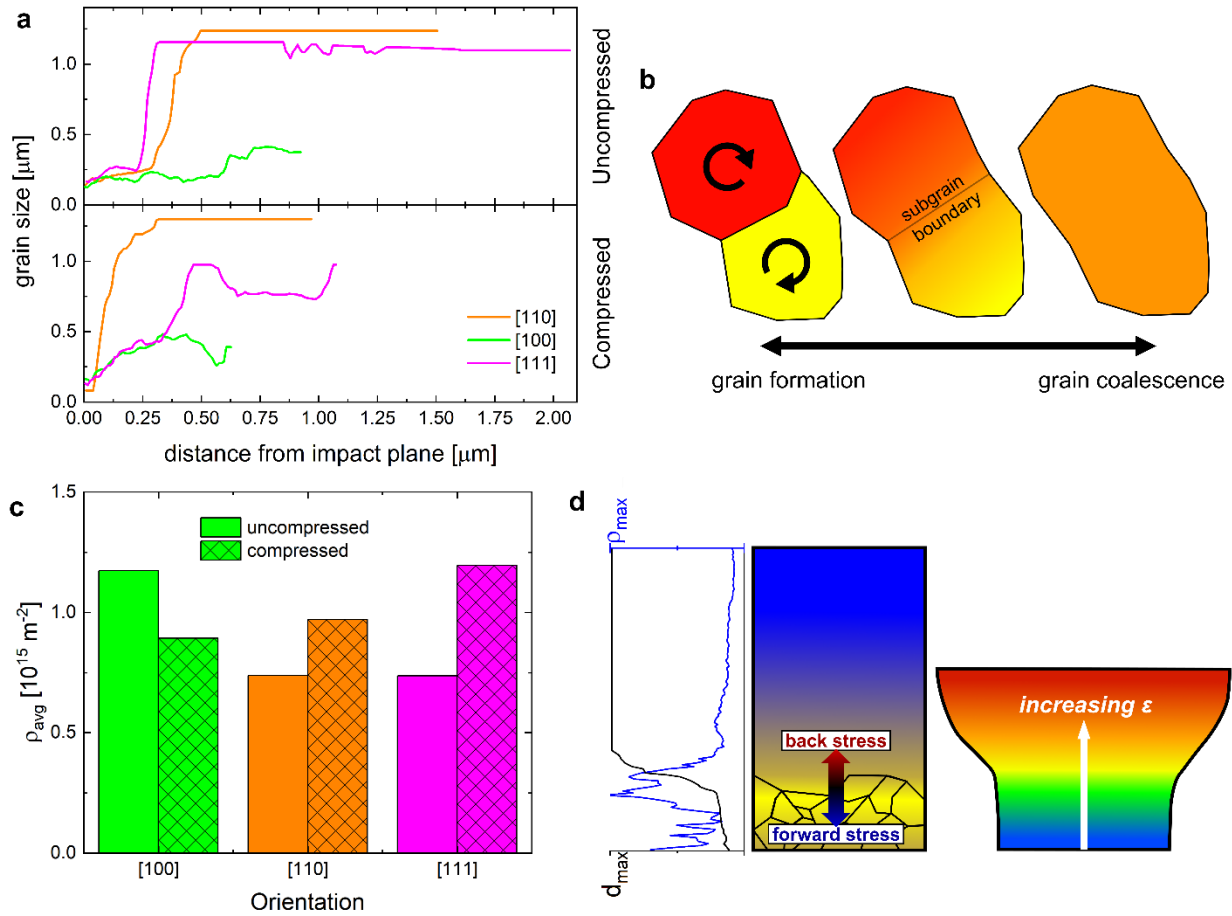


**Figure 3-35: Impact orientation-dependent plasticity mechanisms** (a) grain size gradients for uncompressed and compressed samples of the three impact orientation cases, (b) schematic of grain coalescence/formation, (c) average dislocation densities of uncompressed and compressed samples of the three impact orientation cases, (d) heterogeneous deformation induced by grain size and GND density gradients.

### 3.6 Conclusion

The work presented in this chapter provides a comprehensive understanding of the process-structure-property relations of impact-induced heterogeneous nanostructures. Single crystal silver is used as the model material, which has a face-centered cubic structure and low stacking fault energy. Beginning with pristine single crystal samples allows for clear determination of the process-structure-property relations. Before delving into the complexities of the nanostructural evolution and resultant properties of the single crystals deformed at high strain rates, we studied the quasi-static mechanical behavior and origins of size effects in single crystal microsamples. We found that dislocation-free nanocubes yield at near-theoretical strengths due to the high strengths needed for homogeneous dislocation nucleation. The effects of pre-existing defects such as edge and corner roundness, surface asperities, vacancy concentrations, and FIB-induced defects are systematically investigated through experiments and MD simulations. We find that any defect which breaks the perfect cubic crystal structures initiates heterogeneous dislocation nucleation at lower stresses. This understanding is used to explain the observed sample size effect on strength, since smaller samples have a lower probability of containing such defects. This study provides a foundation for studying the process-structure-property relations of dynamically deformed single crystal microsamples.

In contrast to the quasi-statically compressed microcubes which remain single crystal even after loading to 40-50% strain, microcubes impacted on their face while traveling at velocities of  $\sim 400$  m/s (corresponding to a strain rate of  $\sim 10^8$  m/s) show dramatic nanostructural changes. Through TEM and MD simulations, we reveal a martensitic phase transformation from an fcc to an hcp structure in [100]-face impacted microcubes. Extensive grain refinement also occurs, forming a gradient-nano-grained structure. The impact-induced shock wave propagates and

attenuates within the sample, inducing pronounced dislocation nucleation as it interacts with the free surfaces. The attenuation of the shock wave leads to gradient plasticity, forming inversely correlated grain size and dislocation density gradients along the sample height. These dislocation density and grain size gradients are found to depend on the orientation of the cube upon impact: [100]-face impacted samples show the most grain refinement, with smooth grain size and dislocation density gradients. In contrast, the [110]-edge and [111]-corner impacted samples show only limited grain refinement near the impact plane, with corresponding peaks in dislocation density accommodating the boundary between the coarse and nanograined regions. The internal crystallographic orientation and external cubic shape are coupled in the synthesized microcubes, so to investigate which predominately governs the dynamic recrystallization, we performed microprojectile impact tests on [100], [110], and [111] orientated single crystal silver substrates. This study revealed that the crystal orientation—rather than the reflective shock dynamics which are altered based on the external shape—is the predominant factor governing dynamic recrystallization. Extensive recrystallization occurs in [100] oriented single crystals due to the high number of simultaneously activated slip systems and high critically resolved shear stresses promoting enhanced dislocation nucleation, propagation, and interaction. Dynamic recrystallization can be induced in [111] oriented single crystals by increasing the impact velocity, which increases the rate of dislocation nucleation and interaction.

With this understanding of the impact-induced nanostructures and corresponding orientation-dependent recrystallization mechanisms, we studied the resultant mechanical responses of these heterogenous nanostructures. Through microcompression tests of micropillars formed from the impacted cubes, we found that the impacted samples exhibit increased strength and strain hardening compared to the original single crystal microsamples. Synergistic

improvements in strength and toughness are attained, with maximum improvements of 4.7x the yield strength and 5x the toughness as the single-crystal silver micropillars, and up to 7.4x the yield strength and 4x the toughness as bulk coarse-grained silver. Such enhanced mechanical performance is attributed to heterogeneous deformation induced strengthening. Crystal plasticity simulations of synthetic microstructures based on experimental data reveal the emergence of strain and stress gradients due to the original grain size and dislocation density gradients. This gradient plasticity is more pronounced in [100] samples which have a smooth grain size gradient. The heterogeneous deformation induces back stresses in the soft domain and forward stresses in the hard domain. These heterogeneous deformation induced stresses are shown through gradients in the stress distribution and Lode parameter: high compressive stresses are seen in the nanograin regions, and the stress state progressively becomes more tensile with increasing grain size.

To investigate what plasticity mechanisms are elicited through heterogeneous deformation, we study the nanostructural changes due to quasi-static compression. Post-compression TKD analysis reveals that both intergranular and intragranular plasticity are present in all samples, but the dominant plasticity mechanisms can be tuned based on the distinct impact-orientation dependent nanostructures. Through experiments, we have shown that intragranular plasticity dominates in the [110]-impacted sample, intergranular plasticity dominates in [100]-impacted sample, and both types are prominent in [111]-impacted sample. The nanostructural changes are tracked in the crystal plasticity simulations, and different plastic deformation responses can be attributed to positive or negative effects on the mechanical response. We find that samples with large increases in average dislocation density exhibit high strain hardening. Increases in dislocation density are higher in larger grains, which corresponds to the strain localization. Enhanced intragranular dislocation activity leads to crystal rotation within grains. The orientation changes

appear within grains of all sizes and seem to be influenced by neighboring grains. These complementary intra- and inter-granular plasticity mechanisms provide enhanced mechanical properties.

## ***Chapter 4. Investigating the fracture and densification behavior in the pyrocarbon buffer layer of TRISO nuclear fuel particles<sup>5</sup>***

### **4.1 Introduction**

The work presented in this chapter focuses on the process-structure-property relations of the buffer layer in tristructural isotropic (TRISO) coated nuclear fuel particles (Section 2.1.2). The objectives defined in Section 1.1.2 are addressed through the carefully designed experiments on unirradiated and irradiated particles. The heterogeneity of the porous buffer layer is characterized and its effects on the local mechanical properties and failure modes analyzed. Post-irradiation examination reveals dramatic micro- and nanostructural changes within the porous pyrocarbon. Structural changes are found to depend on the irradiation conditions and dictate the buffer fracture and densification response. This work aims to provide a better understanding of the buffer layer response to irradiation, providing guidance for improvements in future iterations of TRISO particle design and fabrication. Before delving into the findings of this research, this introduction provides contextual background for this work.

---

<sup>5</sup> The work presented in this chapter is partially adapted from the following research papers:

- 1) C. Griesbach, T. Gerczak, Y. Zhang, R. Thevamaran, Microstructural heterogeneity of the buffer layer of TRISO nuclear fuel particles, *Journal of Nuclear Materials* 574 (2022)
- 2) C. Griesbach, C. McKinney, Y. Zhang, T. Gerczak, R. Thevamaran, Irradiation-induced changes in the porous buffer microstructure of TRISO nuclear fuel particles (in preparation)
- 3) C. Griesbach, J.D. Arregui Mena, E. Lopez, Y. Zhang, T. Gerczak, R. Thevamaran, Irradiation-induced nanostructural changes in porous pyrocarbon (in preparation)
- 4) C. Griesbach, T. Gerczak, Y. Zhang, R. Thevamaran, Super elasticity and anisotropic mechanical response in porous pyrocarbon (in preparation)

Tristructural isotropic (TRISO) coated fuel particles have been developed as a high-performance fuel for High Temperature Gas-cooled Reactors (HTGRs) [24,193]. HTGRs are a high performance clean-energy alternative to fossil-fuel energy types, providing the potential to alleviate some of the negative effects of climate change [194]. Recently, TRISO particles are also being considered for other nuclear applications—including several advanced reactor types, modular reactors, and space nuclear propulsion. Depending on the application, thousands of small spherical (~1 mm diameter) TRISO particles are held together with a matrix material (typically graphite) through a compaction process. In HTGRs, cylindrical fuel compacts are organized into large prismatic graphite blocks compacts which go into the nuclear reactor [195]. The TRISO coating surrounds a spherical kernel containing uranium and is designed to retain the fissile by-products caused by irradiation. The modern architecture of TRISO particles was based on the German TRISO-coated fuel particles developed for the AVR (Arbeitsgemeinschaft Versuchsreaktor) reactor [196,197]. The US Department of Energy's Advanced Gas Reactor (AGR) Fuel Development and Qualification Program has continued the exploration of the established TRISO architecture and conducted irradiation experiments containing several fuel variants [198]. The AGR-1 irradiation experiment contained laboratory-scale fuel particles with uranium oxycarbide (UCO) kernels [199], whereas the AGR-2 experiment contained capsules with UCO particles and capsules containing particles with  $\text{UO}_2$  kernels [200]. In the AGR-2 experiments, several changes were made to the particle fabrication process, including to the kernel and coating processes, and to the process used to set the particles in cylindrical compacts; additionally, the TRISO particles for the AGR-2 experiments were produced by manufacturers at the industrial scale [198]. In both irradiation experiments, the particle architecture is relatively the same: surrounding the spherical kernel is a multilayered spherical shell consisting of a porous

pyrocarbon buffer layer, a dense inner pyrolytic carbon layer (IPyC), a silicon carbide layer (SiC), and a dense outer pyrolytic carbon (OPyC) layer. A fluidized bed chemical vapor deposition (FBCVD) coating furnace was used to fabricate the layers of the coating [25].

The TRISO particles tested in the AGR experiments have been shown to be robust under irradiation at HTGR relevant temperatures [25,27]. Failure can occur when the outer SiC layer is locally corroded or fractured, allowing fission products to be released from individual particles [201–203]. In testing AGR-1 particles under normal irradiation conditions and enhanced temperatures of 1600–1800 °C out-of-pile, the percentage of particles that showed SiC failure was only 0.0013% under normal irradiation conditions and 0.0091–0.14% during the 1800 °C safety tests [201]. Here, the 1800 °C safety test condition represents a margin temperature higher than predicted fuel temperatures relevant to off-normal accident conditions expected for typical HTGR designs [204]. Although these failure events are less probable, release of fission products limits the acceptable lifetime of the fuel compacts to ensure safe operation; thus, failure must be mitigated.

Post irradiation examination (PIE) of the particles tested in the AGR-1 and AGR-2 irradiation experiments reveal common failure modes within the TRISO coating [25,26,202,203]. Examination of AGR-1 particles revealed that failure often begins in the buffer layer with fracture—including radial buffer fracture and circumferential internal tearing of the buffer—that leads to the initiation of cracks in surrounding layers and the transference of fission products, which locally corrode the exposed SiC layer, eventually leading to failure of the SiC layer and the release of fission products [201,202,205]. Therefore, it is imperative that we understand the causes of buffer fracture and which modes of buffer failure led to IPyC and SiC failure. A complex stress state exists within the buffer layer during irradiation due to kernel swelling and thermal stress,



leading to buffer densification and fracture [206]. The different responses of the buffer layer to irradiation have been characterized through optical imaging and x-ray computed tomography and classified based on whether the buffer fractures and/or internally tears away from the IPyC layer [207–209]. Radial and/or circumferential cracking of the buffer layer can occur: radial cracks can propagate into the IPyC layer if the buffer/IPyC layers are not separated, whereas incomplete tearing of the buffer away from the IPyC layer through circumferential cracking can lead to high stress concentrations at still-bonded locations that induce cracking within the IPyC layer [207,208]. Both buffer responses can lead to failed SiC layers due to transmission of a crack into the IPyC layer and subsequent local corrosion at the IPyC-SiC interface [201,202,205]

To understand the complex stress state and structural changes that occur during irradiation, we must fully characterize the structure of both as-fabricated and irradiated particles across different length scales. Of critical importance to understanding fracture and densification within the buffer layer is comprehensive characterization of the microscale pore structure—including the porosity and its spatial distribution, typical pore size, shape, and orientation, and variations in the porosity between particles. This comprehensive characterization of the pore structure will provide insight into the buffer fracture modes, the role of the pore structure in densification, and the stochasticity of buffer behavior. Modeling efforts have sought to predict TRISO particle failure but fall short partly due to the lack of structural characterization of the buffer layer [210–212]. Such characterizations have been done on the PyC layers and the SiC layer [28,84,205,213–218]; however, little characterization of the buffer microstructure has been done relative to the other TRISO layers. Past buffer layer characterizations were performed using micro- to macro-scale characterization techniques such as x-ray tomography, mercury intrusion porosimetry, or macroscale relative density measurements [27,193,216,219]. These micro- and macro-scale

characterizations are insufficient to accurately describe the spatial dependence of buffer porosity and the pore size and shape, which are necessary for prediction of buffer and TRISO particle failure. Of relevance to fracture initiation and propagation in the buffer is the porosity and its spatial distribution, which affect the irradiation-induced dimensional changes, stress distribution, and local fracture resistance.

Like the porous microstructure, irradiation-induced changes within the pyrocarbon nanostructure can have pronounced influence on the buffer densification and fracture response. There have been some separate effects studies into the influence of various temperatures and/or neutron fluences on the dimensional changes of graphite and pyrolytic carbon [220–223]. Heat treatment of pyrocarbon produced through fluidized bed chemical vapor deposition showed an increase in graphitization (increased anisotropy, domain size, and degree of stacking order) with increasing heat treatment temperatures [223]. Increased temperature has also been shown to increase the rate of dimensional change in irradiated graphite and pyrocarbon [220,222]. Additionally, the initial anisotropy and crystal size influences the densification rate [221]. To understand the irradiation-induced densification of the pyrocarbon buffer layer, we must characterize the nanostructural changes that occur within the pyrocarbon nanostructure. X-ray tomography studies have revealed that the densification and radial fracture fractions of the buffer layer depend on the irradiation conditions [224]. Here, we study the effects of different irradiation conditions on the micro- and nanostructural changes in the porous pyrocarbon buffer layer.

## 4.2 Implications of microstructural heterogeneity in the as-fabricated buffer layer of TRISO particles

### 4.2.1 Experimental design

To fully characterize the buffer porosity and investigate the heterogeneity of the buffer microstructure, we perform FIB-SEM tomography (Section 2.4.5) on several different regions within the buffer layer and on multiple particles. Additionally, several scans are performed sequentially along the radial direction,

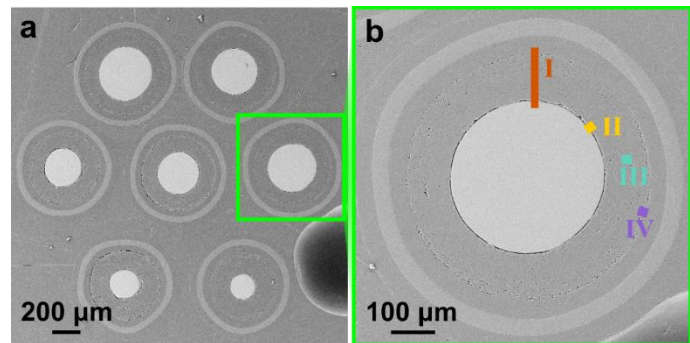


**Figure 4-1: FIB-SEM tomography on TRISO particles** (a) SEM image of cross-sectioned TRISO particles mounted in an epoxy puck, (b) regions of interest identified, corresponding to objectives of the porosity characterization plan (Table 4-1).

traversing the entire buffer layer thickness, which provides a continuous description of the variation in porosity along this direction. The experimental plan outlined in Table 4-1 yields a robust characterization of the buffer layer porosity.

**Table 4-1** Porosity characterization plan using FIB-SEM tomography

ID	Description	Sample Volume	Number of iterations
I	Section traversing entire buffer layer	$\sim 10 \times 100 \times 10 \text{ } \mu\text{m}^3$ ( $\sim 8$ separate scans)	1 (8 parts)
II	Volume near kernel	$\sim 15 \times 15 \times 15 \text{ } \mu\text{m}^3$	5 (different particles or locations)
III	Volume in center	$\sim 15 \times 15 \times 15 \text{ } \mu\text{m}^3$	5 (different particles or locations)
IV	Volume near iPyC layer	$\sim 15 \times 15 \times 15 \text{ } \mu\text{m}^3$	5 (different particles or locations)

To investigate how the microstructural heterogeneity affects the mechanical properties in different directions, we also perform nanoindentation (Section 2.3.2) and microcompression tests (2.3.3). Several locations within the buffer layer are mechanically tested, and strategically milled micropillars are compressed in the radial and tangential directions.

#### 4.2.2 Porosity characterization across the radial direction of a single particle

The pores were identified through the segmentation and separation workflow outlined in Section 2.4.5. Visuals of the porosity across the buffer layer are shown in Figure 4-2 (c), with pores colored according to the scan. To quantify the porosity along the buffer thickness, the porosity of slice  $n$  in scan  $m$  is defined as

$$P_{n,m} = P(r_{buffer}) = \frac{A_{pores,n} t_{slice}}{A_m t_{slice}} \quad (29)$$

where  $A_{pores,n}$  is the area of the pixels segmented as pores in slice  $n$ ,  $A_m$  is the cross-sectional area of scan  $m$ , and  $t_{slice}$  is the slice thickness (50 nm). The slice position along the radial direction in the buffer ( $r_{buffer}$ ) is defined as

$$r_{buffer} = r_{0,m} + nt_{slice} \quad (30)$$

where  $r_{0,m}$  is the start position of scan  $m$ ,  $n$  is the slice number, and  $t_{slice} = 50$  nm. The porosity (per slice) is plotted as a function of  $r_{buffer}$  in Figure 4-2 (a). A general trend of increasing porosity with increasing  $r_{buffer}$  is observed (Figure 4-2 (a)). However, there are significant local fluctuations in the porosity which appear to increase in magnitude with increasing  $r_{buffer}$ . To more clearly visualize the changes in porosity and its fluctuation with increasing  $r_{buffer}$ , box plots are shown to represent the data statistics of each 10  $\mu\text{m}$  interval across the buffer thickness (Figure 4-2 (b)). From this representation, we see that in general, the mean and median values increase

with larger  $r_{buffer}$ . However, there are a few exceptions, particularly in the 60 – 90  $\mu\text{m}$  range where there is a local decrease in porosity due to large fluctuations shown though the large error bars and interquartile ranges of the box plots in this region. Given the large error bars which overlap each other, we performed a Mann-Kendall test to determine if the observed trend of increasing porosity with  $r_{buffer}$  is statistically significant. The Mann-Kendall test accesses whether a monotonic upward trend exists in the data by looking at the differences between each data point and all preceding data points [225,226]. The test statistic ( $Z_{MK}$ ) was found to be 18.32, which is greater than the Z-value obtained at the 95<sup>th</sup> percentile of a standard normal distribution ( $Z_{0.95} = 1.6449$ ). Therefore, the null hypothesis that there is no monotonic trend is rejected, and we confirm that there exists a statistically significant upward monotonic trend in the data.

The increase in porosity along the radial direction is expected to be resultant of the processing route: the particles are fabricated through an FBCVD process [25], in which layers grow on the particle in the radial direction. Although the diameter of the particle is increasing during deposition, the processing conditions—including the coating gas fraction and total gas flow—are not typically changed to account for the increase in surface area over the course of the deposition [227]. The constant deposition conditions with time-dependent change in bed surface area may influence the FBCVD coating process and result in an increase in porosity with increasing distance from the kernel, as seen in our data. The increase in porosity and variability as well as the location of maximum porosity at  $\sim 5 \mu\text{m}$  from the buffer-IPyC interface correlates well with the radial location of circumferential cracking that leads to buffer-IPyC tearing, as seen in PIE of TRISO particles [25,26]. The average porosity within the total scan volume is 13.5%. We can also calculate the average porosity in the buffer layer by considering the radial distribution of porosity ( $\rho(r)$ ) to be representative of the entire buffer layer and integrating over the whole buffer

volume ( $\rho_{avg} = \int_{r_1}^{r_2} \rho(r) 4\pi r^2 dr / V_{total}$ ), which is calculated to be 14.0%. This average porosity of 14% does not account for the approximate buffer density of 50% of the theoretical density of graphite [207,228,229]. Therefore, the buffer matrix or nanoscale porosity below the resolution of the serial sectioning approach used here must account for the reduced buffer density. Considering the 14% porosity and 50% theoretical density, we can calculate the expected density of the buffer matrix (solid pyrocarbon) to be 1.31 g/cc or ~58% of the theoretical density of graphite. A pyrocarbon with such a low density would have a very disordered nanostructure with large interplanar spacing between the graphene planes as shown in a recent molecular dynamics study [230].

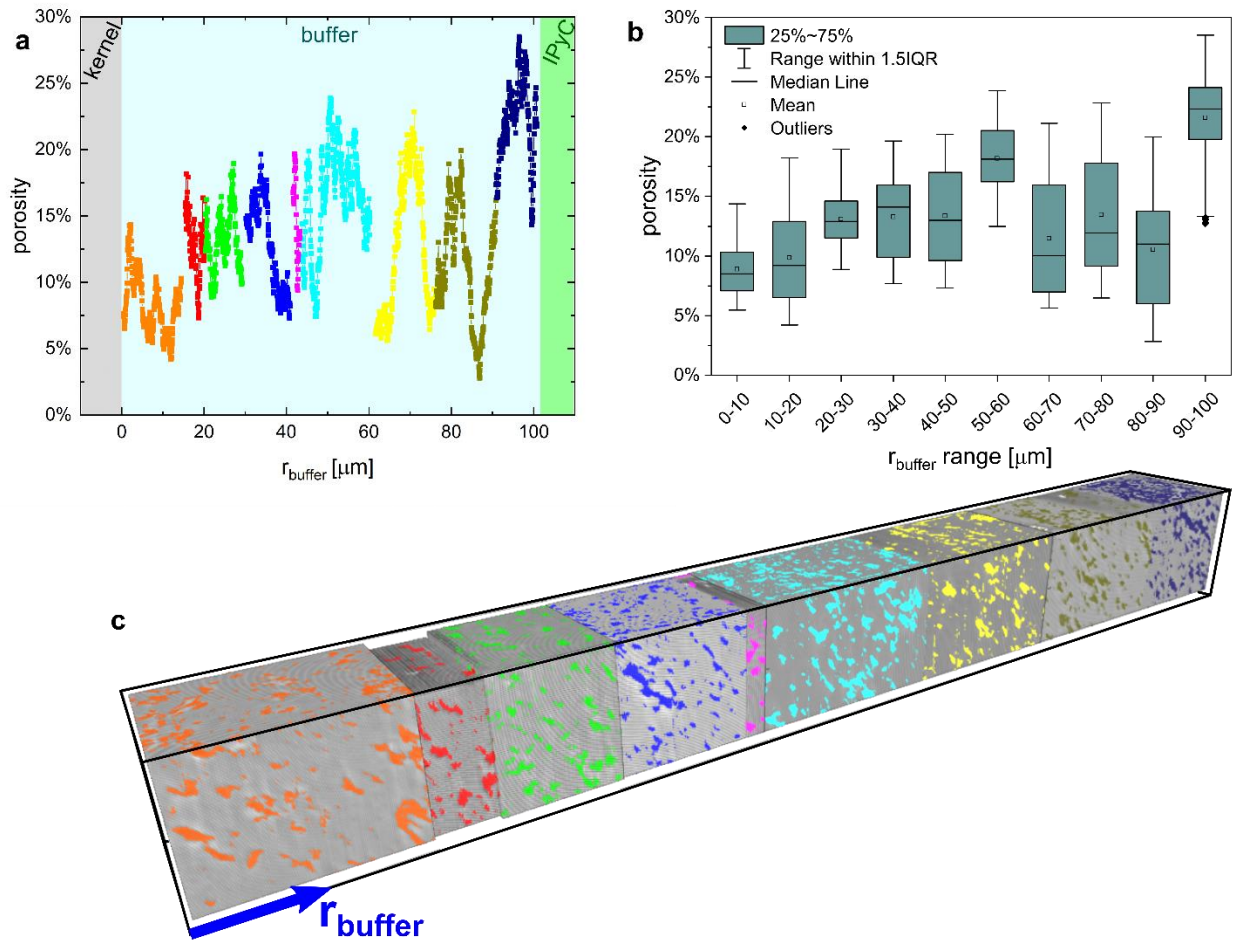


**Figure 4-2: Porosity distribution along buffer layer thickness** (a) per slice porosity across buffer layer—average porosity in each scan denoted with black square, with error bars denoting standard deviation, (b) box plots showing statistics of data in (a) separated into 10  $\mu\text{m}$  intervals, (c) 3D reconstruction of buffer microstructure, with porosity in each scan highlighted—colors correspond to scan data in (a) and in Figure 4 (a–b).

We further characterize the porosity by examining the pore size. Each pore's volume and equivalent diameter (calculated by equating the pore volume to a spherical volume) is plotted against its centroid location in the buffer along the radial direction (Figure 4-3 (a–b)), colored corresponding to the scan. The pore volumes range from  $4.7\text{E-}4 \mu\text{m}^3$  to  $174 \mu\text{m}^3$  (corresponding to diameters of equivalent spherical volumes of approximately  $0.097 \mu\text{m}$  and  $6.9 \mu\text{m}$ , respectively). Since the scan resolution is  $50 \text{ nm}$ , it is possible that smaller pores exist but are not resolved by this method. However, as the highest concentration of pores are within the  $0.001\text{--}0.01 \mu\text{m}^3$  size range, and the number of pores identified with volumes  $<0.001 \mu\text{m}^3$  is much lower (Figure 4-3(b–c)), we conclude that the identified pores adequately represent the actual porosity in the sample. Additionally, the smallest pores—although numerous—contribute very little to the total porosity (Figure 4-3 (d)).

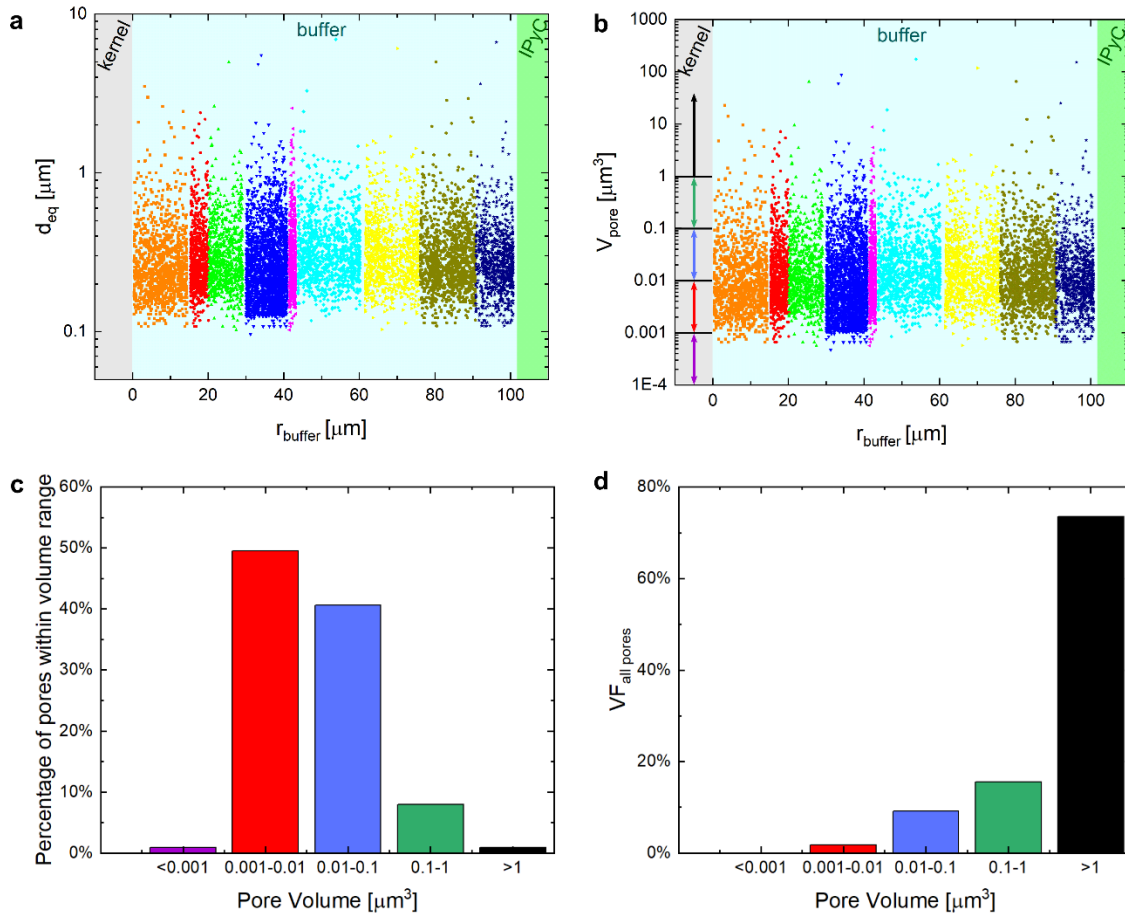


**Figure 4-3: Pore size distribution** (a) each pore's equivalent diameter and centroid position plotted in the color corresponding to the scan, (b) each pore's volume and centroid position plotted in the color corresponding to the scan; volume ranges identified by colored arrows corresponding to colors used in (c) and (d), (c) percentage of pores in each volume range, (d) volume fraction of pores in each volume range.

We identified five volume bins to examine the pore size distribution in more detail (colored arrows in Figure 4-3 (b)):  $V < 0.001 \mu\text{m}^3$  (purple),  $0.001 \mu\text{m}^3 < V < 0.01 \mu\text{m}^3$  (red),  $0.01 \mu\text{m}^3 < V < 0.1 \mu\text{m}^3$  (blue),  $0.1 \mu\text{m}^3 < V < 1 \mu\text{m}^3$  (green), and  $V > 1 \mu\text{m}^3$  (black). These colors representing the volume bins are used in Figure 4-3 (c-d) and Figure 4-4. Figure 4-3 (c) shows the percentage of pores within each volume range ( $N_{\text{pores} \in V_{\text{range},i}} / N_{\text{pores}}$ ), whereas Figure 4-3 (d) shows volume fraction of pores within each volume range ( $\sum V_{\text{pores} \in V_{\text{range},i}} / \sum V_{\text{pores}}$ ). Although some of the smallest pores ( $0.001 \mu\text{m}^3 < V < 0.01 \mu\text{m}^3$  – red) constitute a large percentage of pores (~50%), they provide



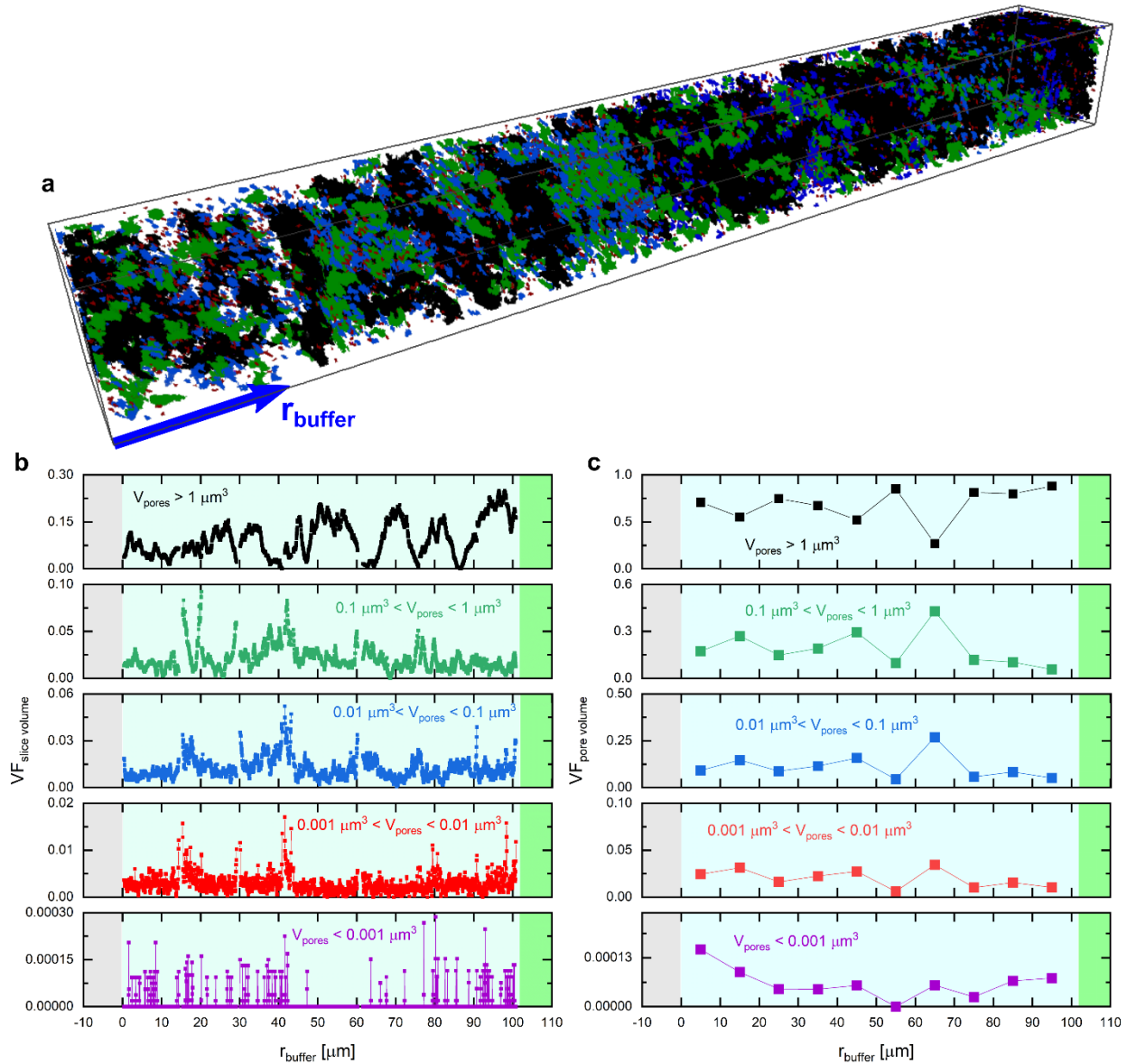
only ~1.7% of the total pore volume. Conversely, the largest pores ( $V > 1 \mu\text{m}^3$  – black) represent only 0.9% of the pores but make up 74% of the total pore volume. This inverse relationship between the number of pores and contribution to total porosity hints at the pore structure: that of large sprawling networks of connected voids surrounded by numerous interspersed small pores. However, several questions about the pore structure remain, including the distribution of pore sizes throughout the buffer layer thickness, and whether any pore size grouping is primarily responsible for the increase in porosity toward the IPyC layer or if the porosity from all pore sizes increases.

Figure 4-4 (a) shows a 3D volume rendering of the pores along the buffer thickness. The pores are colored according to the volume ranges defined previously. From this visualization, it appears that there are fewer smaller pores (green, blue, red) where the largest pores (black –  $V > 1 \mu\text{m}^3$ ) dominate. Additionally, the largest pores (black –  $V > 1 \mu\text{m}^3$ ) seem to dominate closest to the IPyC layer, which may explain the increase in overall porosity (Figure 4-4 (a)). To verify these observations, the volume fraction within each volume range ( $VF_{slice\ volume}$ ) was plotted against the distance from the kernel in the radial direction (Figure 4-4 (b)). Calculated for every slice, the volume fraction of pores from volume range  $i$  on slice  $n$  is defined as

$$VF_{i,n} = VF_{slice\ volume}(r_{buffer}) = \frac{A_{n,pores \in V_{range,i}}}{A_n} \quad (31)$$

where  $A_{n,pores \in V_{range,i}}$  is the total area of all pores on slice  $n$ , whose size is within the volume range  $i$ ;  $A_n$  is the cross-sectional area of slice  $n$ ;  $r_{buffer}$  is calculated according to Eq. (2); and  $i$  is the index corresponding to a volume range (5 in total). The continuous line profiles of the volume fractions with distance from the buffer (Figure 4-4 (b)) show the local and global changes in porosity within each pore size grouping. The largest variation occurs within the largest pore size range ( $V > 1 \mu\text{m}^3$  – black). Additionally, the variation in the volume fraction and the mean volume

fraction seem to increase with increasing  $r_{buffer}$ , which correlates with the increase in the standard deviation and average porosity in the entire sample (Figure 4-3 (a)). This suggests that the largest pores are the driving component of overall porosity in the sample, and they are the primary source of the porosity fluctuation along the radial direction seen in Figure 4-3 (a).



**Figure 4-4: Pore size distribution across buffer thickness** (a) pores colored by pore size ( $V > 1 \mu m^3$  – black,  $0.1 \mu m^3 < V < 1 \mu m^3$  – green,  $0.01 \mu m^3 < V < 0.1 \mu m^3$  – blue,  $0.001 \mu m^3 < V < 0.01 \mu m^3$  – red,  $V < 0.001 \mu m^3$  – purple), (b) volume fraction per slice of pores within each volume range plotted against position along the radial direction within the buffer, (c) volume fraction of total pore volume in each 10  $\mu m$  section.

We can also analyze how each pore size's contribution to the total porosity changes across the buffer layer. For each 10  $\mu\text{m}$  section, the volume fraction of pores within volume range  $i$  ( $\sum V_{pores \in V_{range,i}} / \sum V_{pores}$ ) is plotted against the median  $r_{buffer}$  value of the 10  $\mu\text{m}$  section (Figure 4-4 (c)). Looking at the trends in volume fractions for the different pore sizes, it becomes apparent that the smaller pores all follow the opposite trend as the largest pore size ( $V > 1 \mu\text{m}^3$  – black). For example, at  $r_{buffer} = 65 \mu\text{m}$ , the contribution to the overall porosity from the largest pores is at a minimum, whereas the contributions to the overall porosity from the smaller pores ( $0.001 \mu\text{m}^3 < V < 1 \mu\text{m}^3$  – red, blue, green) are at the maxima values in the buffer layer. This suggests that when there is a deficit of large pores in a region, the porosity is primarily made up of smaller pores and vice versa. Additionally, the contribution to the total porosity from the largest pores is high near the IPyC layer, whereas all other pore sizes contribute very little to the porosity near the IPyC layer. These data confirm the observations made from the 3D volume rendering of the pore structure (Figure 4-4 (a)). The increased porosity near the IPyC layer, which is driven by the largest pores, may be able to accommodate large compressive strains during densification of the buffer layer.

To investigate the pore shapes, we adopted a particle form analysis method commonly used in sedimentology [231]. A particle's form can be described using three dimensions: the length or longest dimension ( $L$ ), breadth or intermediate dimension ( $I$ ), and thickness or smallest dimension ( $S$ ). These three dimensions are perpendicular to each other. Typically, the length is taken to be the maximum caliper diameter,  $I$  is the maximum caliper diameter perpendicular to  $L$ , and  $S$  is perpendicular to both  $L$  and  $I$ . However, in some cases, these definitions do not produce the smallest volume containing the object. Therefore, we used an alternative method, in which the three dimensions correspond to the side lengths of a bounding box with minimum volume

surrounding the pore. Meshes of the pores are outputted from the Dragonfly model, and a MATLAB script is used to find the minimum bounding box surrounding each pore. All three dimensions are unique;  $L$  is defined as the longest dimension,  $S$  is defined as the smallest dimension, and  $I$  is defined as the intermediate dimension. We describe the particle form through ratios of these side lengths: an elongation parameter ( $I/L$ ) and a flatness parameter ( $S/I$ ).

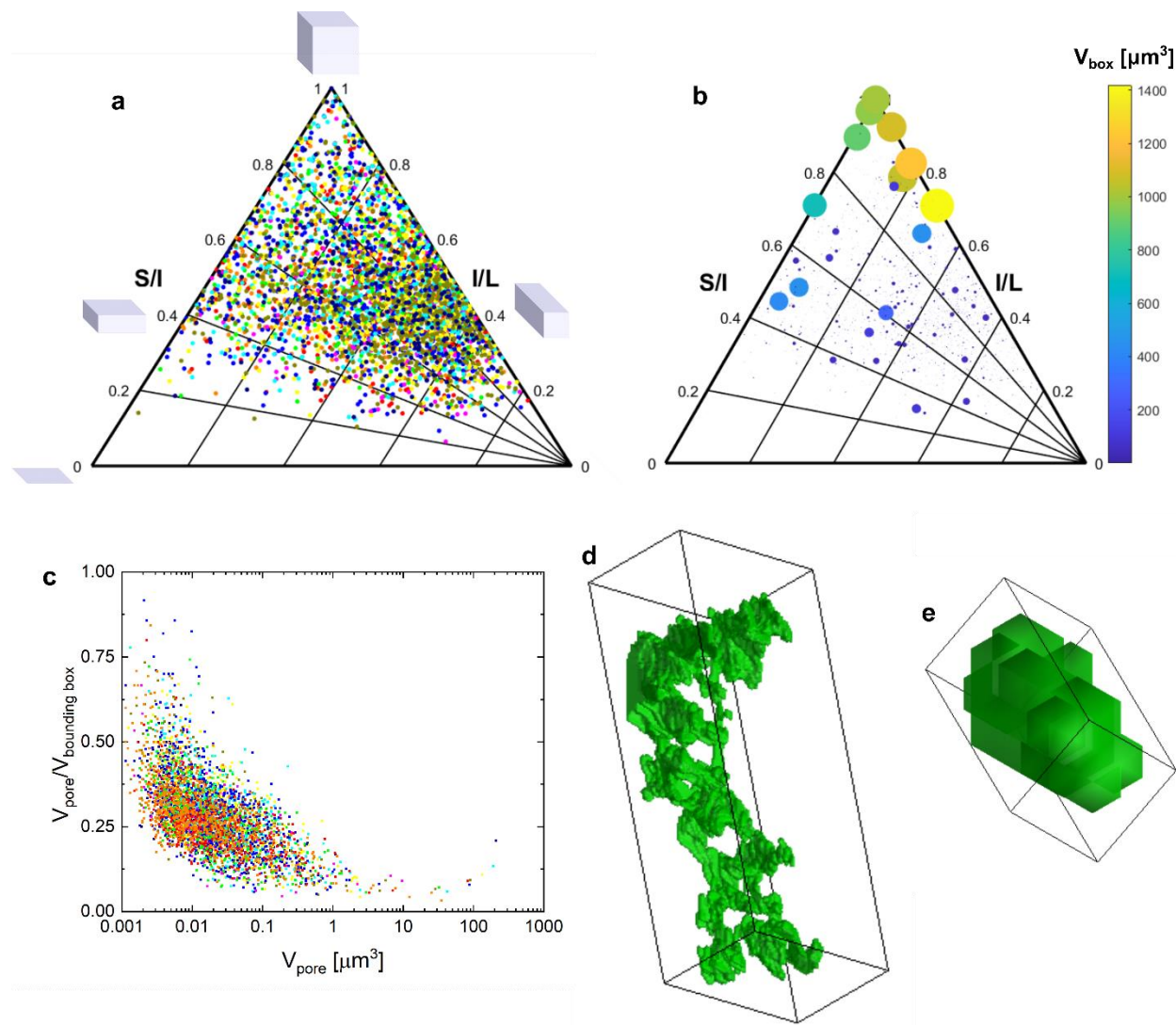


**Figure 4-5: Pore shape distribution** (a) flatness and elongation factors ( $S/I$  and  $I/L$ , respectively) for each pore plotted on a ternary plot and colored by scan, (b) same data in (a) colored and scaled by the volume of the pore's

bounding box, (c) a measure of the pore fill volume of the bounding box vs. pore volume, (d) mesh and bounding box of a representative large pore:  $V_{\text{pore}}=2.958 \mu\text{m}^3$ ,  $V_{\text{pore}}/V_{\text{bounding box}}=0.056$ , (e) mesh and bounding box of a representative small pore:  $V_{\text{pore}}=0.003 \mu\text{m}^3$ ,  $V_{\text{pore}}/V_{\text{bounding box}}=0.417$ .

The flatness and elongation ratios for each pore are plotted on the ternary plots in Figure 4-5 (a-b). The data points in Figure 4-5 (a) are color coded by scan, and the data points in Figure 4-5 (b) are scaled and colored by the volume of each pore's bounding box. From Figure 4-5 (a), we can see that there is not a segregation of pore shapes by scan (or position along the buffer layer thickness). There is a congregation of data points near the  $I/L = 0.5$ ,  $S/I = 0.9$  region, revealing that many pores are elongated and not flat. In fact, the lower region of the ternary plot is devoid of data points, revealing that the pores are not flat. Figure 4-5 (b) shows the relationship between pore shape and size. We see that the large congregation of data points near the  $I/L = 0.5$ ,  $S/I = 0.9$  region was composed mostly of smaller pores. In contrast, the largest pores tend to have larger  $I/L$  ratios and are more cubic in shape. However, the largest pores have bounding box volumes of 1000–1400  $\mu\text{m}^3$ , which approaches the scan volumes. Thus, these largest pores may continue outside of the scan volume, introducing some error in the pore shape.

Figure 4-5 (c–e) provides further insight into the relationship between pore shape and size. The ratio of the pore's volume to the volume of its bounding box is plotted against the pore's volume (Figure 4-5 (c)). A ratio of one would mean the entire bounding box is filled by the pore. We observe that the smallest pores have larger  $V_{\text{pore}}/V_{\text{bounding box}}$  ratios than the larger pores. This suggests that the largest pores consist of sprawling networks of interconnected voids with the pyrocarbon matrix between the voids, giving a smaller fraction of pore volume per buffer volume unit. This observation is confirmed by analyzing representative pores in each volume range. Figure 4-5 (d) shows the mesh and bounding box of a large pore with a volume of  $2.958 \mu\text{m}^3$ , and Figure 4-5 (e) shows the mesh and bounding box of a small pore with a volume of  $0.003 \mu\text{m}^3$ . The smaller

pore in Figure 4-5 (e) fills ~42% of the bounding box. In contrast, the larger pore has many branching components, leading to a smaller  $V_{\text{pore}}/V_{\text{bounding box}}$  ratio of 0.056. This confirms the conclusion from the previous analysis that the large pores consist of sprawling networks of interconnected voids that may be able to accommodate larger strains in a given volume during densification due to compression of material into the empty space.

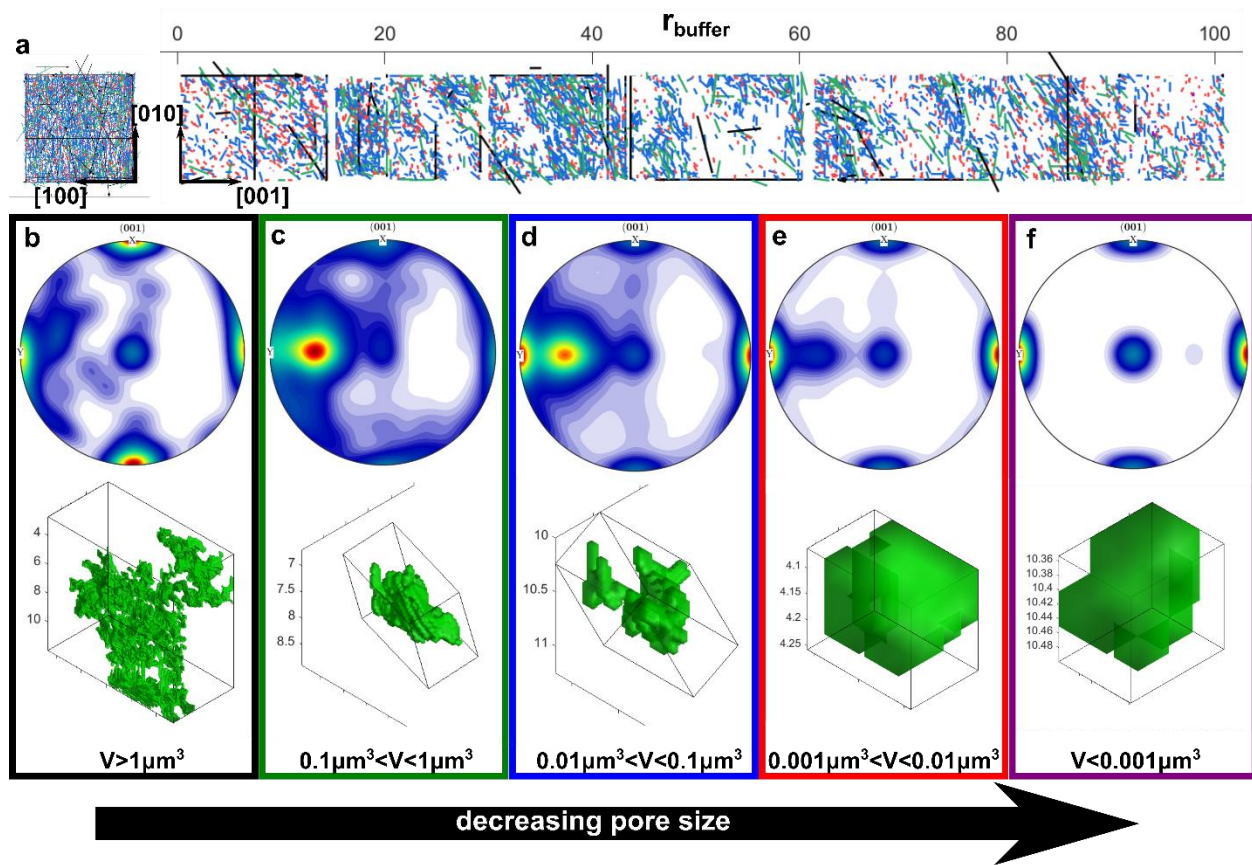


**Figure 4-6: Pore orientation distribution** (a) front view (left) and side view (right) of vectors describing the magnitude and orientation of each pore's L dimension (longest side length of bounding box)—color coded by pore volume bin, (b–f) top: (001) pole figures of the L-vector orientations for different pore volume bins with respect to the [001] direction (radial/buffer thickness direction); bottom: examples of pores from each pore volume bin showing orientation of bounding box.

Since most pores are elongated and not equiaxed, we examine the orientation of pores within the buffer and whether a predominant texture emerges. Vectors describing the magnitude

and orientation of each pore's  $L$  dimension ("L-vectors") are plotted in Figure 4-6 (a). The vectors are color coded by the pore volume bins defined previously. Miller indices are used to define the directions, as in crystallography: the radial direction (or scan "z" direction) identified in Figure 4-6 (a) corresponds to the [001] direction, and the cross section plane is defined by the [010] (height) and [100] (width) directions. The Euler angles describing the rotation between these "L-vectors" and the [001] direction are computed and plotted on the (001) pole figures in Figure 4-6 (b–f) (top panel) using MTEX [57]. Orthorhombic crystal symmetry is invoked to reflect the symmetry of the bounding boxes. If all pores' long axes were aligned with the [001] direction, for example, then the pole figures would exhibit a bright spot in the center. Pole figures for each pore volume bin are plotted in Figure 4-6 (b–f), with decreasing pore volume, in addition to example pores from each bin. A clear texture emerges, which evolves as a function of the pore size. A near  $\langle 100 \rangle$  texture emerges in the largest ( $V > 1 \mu\text{m}^3$ ) and smallest ( $V < 0.001 \mu\text{m}^3$ ) pores, revealing that the bounding boxes of these pores are commonly oriented along three principal axes. In both cases, the [001] texture (central spot) is weaker relative to the [100] and [010] directions, revealing that the pore's longest axis is more commonly aligned along a circumferential direction. For the smallest pores, the near  $\langle 100 \rangle$  texture can be attributed to the cubic mesh dictating the bounding box orientation, as only a few voxels make up these pores (see Figure 4-6 (f), bottom). For the largest pores ( $V > 1 \mu\text{m}^3$ ), the  $\langle 100 \rangle$  texture is weaker; however, many pores are still oriented with the L-vector along the [100], [010], or [001] direction. As mentioned previously, these large pores often span the entire scan volume, so the bounding box would naturally be oriented the same as the scan volume.

The orientation of the intermediate pores is of greater interest and may provide insight into the processing conditions and buffer performance during irradiation. In the pole figures of Figure

4-6 (c-e), we see a high concentration of orientations around  $[0\bar{2}1]$ , which becomes more diffuse with decreasing pore volume. However, the smaller pore volume bin ( $0.001\text{--}0.01\ \mu\text{m}^3$ , red) contains small pores, which may also be susceptible to the artifact of the cubic mesh described earlier. The emergence of the  $[0\bar{2}1]$  texture, as well as the diffuse spread of orientations around the pole figure perimeter in Figure 4-6 (c–d), provides a clear indicator that the elongated pores tend to be oriented along particular directions. Perhaps more enlightening is the absence of pores with orientations on the right side of the pole figures. This can also be observed in the L-vector plot (Figure 4-6 (a), right), in which many vectors are oriented in a left-to-right, down-diagonal fashion, but very few are oriented in a left-to-right, up-diagonal fashion. These observations lead us to suspect that the particle was not ground to precisely mid-plane, and the elongated pores are typically oriented with their long axis perpendicular to the true radial direction of the particle (i.e., in a circumferential direction). If this is the case, then the pore shapes and orientations defined here could be used to predict stress concentrations and the fracture modes within the buffer layer. Additional FIB-SEM tomography experiments on several different particles are needed to confirm these observations.

#### 4.2.3 *Heterogeneity in porosity and mechanical properties*

To examine if the observed microstructural features are consistent between particles, we performed FIB-SEM tomography at three distinct regions—near the kernel-buffer interface, mid-buffer, and near the buffer-IPyC interface—on five different particles. The measured porosity as a function of  $r_{buffer}$  is shown in Figure 4-7 (a) for the five particles, and the average and standard deviation in porosity for each scan (3 on each particle) are shown in Figure 4-7 (b). While local fluctuations in porosity are different between particles, most particles exhibit high porosity and larger variations in porosity near the buffer-IPyC interface. The exception is sample S3P3, for



which a low average porosity of ~10% is recorded for the third scan near the IPyC. However, given the average location (~105  $\mu\text{m}$ ), this scan likely encompassed some of the IPyC layer which contains much lower porosity. The large local fluctuations in porosity can be attributed to the fluid dynamics within the fluidized bed chemical vapor deposition chamber. During deposition, the particles continuously flow throughout the chamber, and their position and velocity with respect to the gas inflow nozzle affects the rate of deposition. If all particles follow the same trajectory and are exposed to the exact same deposition conditions, their porous microstructures would be very similar. However, due to the geometry of the chamber and nozzle, the velocity of the particles will vary throughout their trajectory causing banded fluctuations in porosity. Furthermore, particle flow may stagnate in some regions, causing heterogeneity between particles. However, the overall average porosity is quite consistent—an average of 14.7% with a standard deviation of 3.8% between particles. These findings confirm two main conclusions found in the previous section (Section 4.2.2): (i) the porosity and its fluctuation tend to be higher near the buffer-IPyC interface, and (ii) the average porosity (around 14%) is much too low to account for the low density of the buffer layer (50% theoretical density).

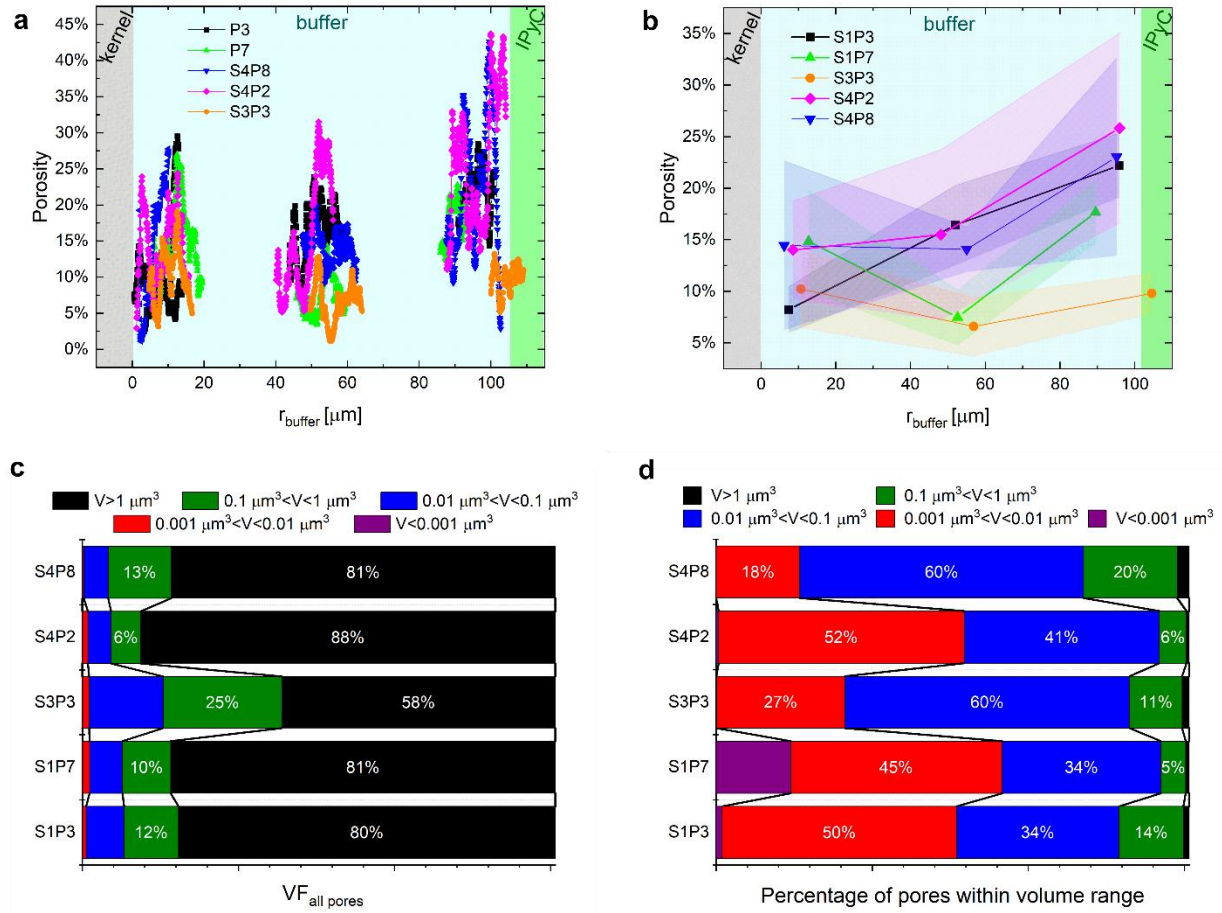


**Figure 4-7: Porosity heterogeneity between particles** (a) porosity measured every slice (50 nm) in each of the 15 scans (3 scans each on 5 particles), (b) average and standard deviation of porosity in each of the 15 scans plotted against average position within the buffer layer, (c) volume fraction of pores in each volume range, (d) percentage of pores in each volume range.

The pore sizes and their contribution to the overall porosity are also quite consistent between the particles. Pores are split into the same five volume bins used in Section 4.2.2, each spanning an order of magnitude from less than  $10^{-3} \mu\text{m}^3$  to greater than  $1 \mu\text{m}^3$ . While the largest pores ( $>1 \mu\text{m}^3$ ) make up most of the pore volume (up to 88%), they represent a very small percentage of the total pores ( $<2\%$ ). The pores with volumes between  $10^{-3} \mu\text{m}^3$  and  $10^{-1} \mu\text{m}^3$  make up the majority of the pores but contribute very little to the overall pore volume. These results

indicate similarity between pore sizes and the relative contribution to overall porosity within these five samples.

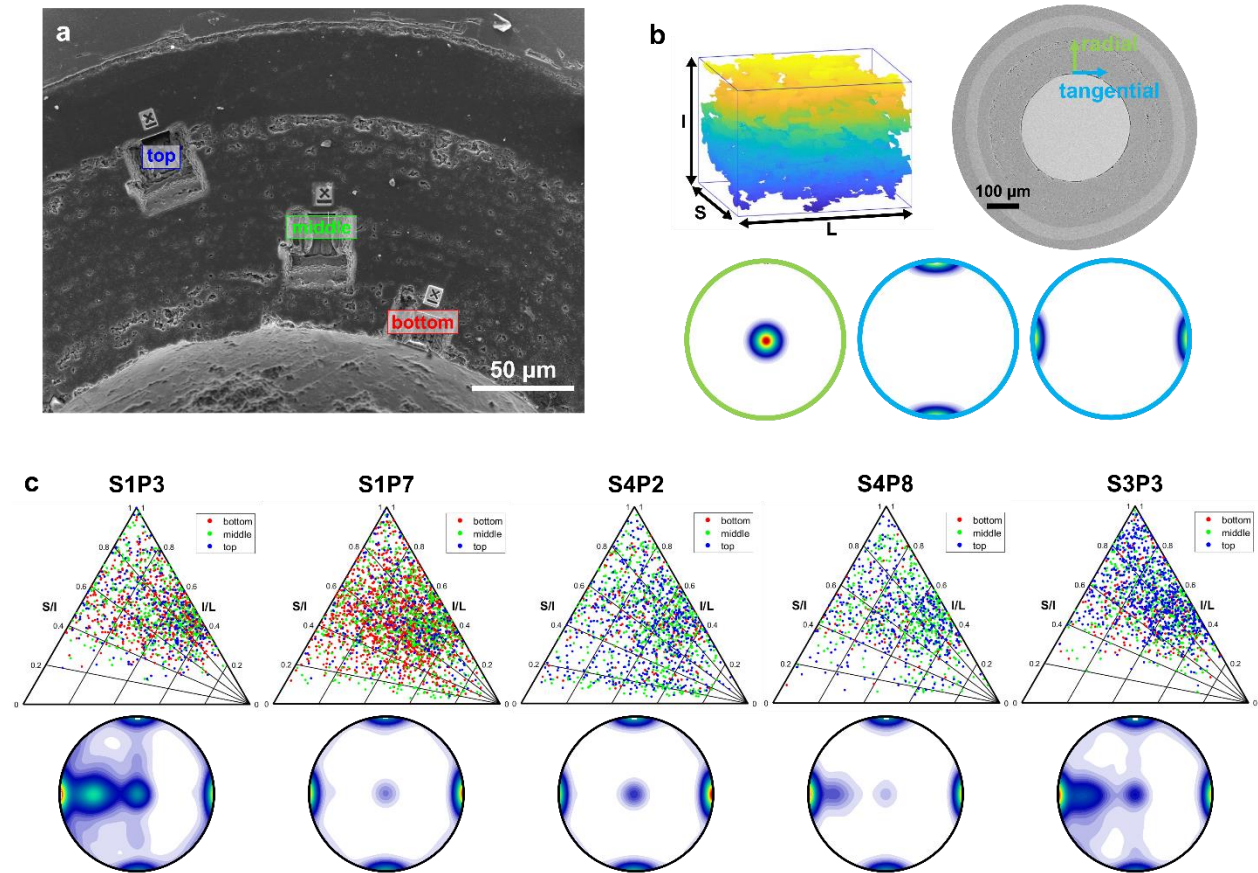


**Figure 4-8: Pore shape and orientation** (a) SEM image indicating locations of scans, (b) definitions of pore dimensions and orientation of the L dimension with respect to the r-t coordinate system, (c) ternary plots representing pore shapes (top) and pole figures showing orientation distributions of elongated pores (bottom).

To further analyze pore structure heterogeneity between particles, we analyzed the pore shapes and their orientations using the same methods described in Section 4.2.2. Ternary plots (Figure 4-8 (c)) show increased scatter in pore shape within some particles (i.e., S1P7, S4P2); however, all particles have very few pores with small S/I ratios, indicating most pores are not flat. Additionally, concentrations of pores with intermediate I/L ratios indicates most pores are slightly elongated. Finally, in all particles, there does not appear to be a clear trend of changing pore shape

with position in the buffer (bottom, middle, top). Since pores are elongated and not flat, we performed orientation analysis on pores longest dimension (L) with respect to the particle's radial and tangential directions (Figure 4-8 (b)). Orientations concentrated on the [100] and [010] poles of the (001) pole figure correspond to tangential directions, while orientations concentrated on the [001] pole (center) indicates elongation of pores in the radial direction. Most samples show stronger concentrations of orientations along the tangential directions, while a concentration in the  $[0\bar{2}1]$  direction emerges in samples S1P3 and S3P3. These samples were likely not ground precisely to midplane and the  $[0\bar{2}1]$  direction corresponds to a tangential direction. These results confirm the hypothesis that elongated pores tend to be oriented along tangential directions.

With a comprehensive characterization of the porous microstructure, we performed mechanical tests designed to assess the effects of microstructural heterogeneity on the mechanical response. Nanoindentation tests were performed in situ SEM with a sharp cube corner diamond tip. Nanoindentation of brittle materials using a sharp faceted tip produces cracks which propagate radially from the edges of the tip. The length of these cracks can be used to estimate the fracture toughness [232]. As a graphitic material, pyrocarbon is brittle, so we expected to use this method for an initial estimate of fracture toughness. However, even using the high load transducer at a maximum load of  $\sim 300$  mN, radial cracks are not produced. Instead, the nanoindentation tests reveal super elasticity of the buffer (Figure 4-9 (a)). Indents in the buffer layer were made to depths of  $\sim 4\text{--}11$   $\mu\text{m}$  (Figure 4-9 (a-2)). Upon unloading, most of the deformation is elastically recovered (Figure 4-9 (a-3)). High elasticity of the buffer is also demonstrated through microcompression tests of pillars FIB-milled from the buffer layer (Figure 4-9 (b)). Two microcompression tests were performed on the same micropillar: in the first test, the test was stopped before the yield point, and in the second test, the pillar was compressed until brittle failure had occurred. SEM images of the

pillar before (Figure 4-9 (b-1)) and after (Figure 4-9 (b-2)) the first test show that the pillar made a full elastic recovery. In contrast, remnants of the pillar after brittle failure are seen in (Figure 4-9 (b-c)). The stress-strain curves of these two tests (Figure 4-9 (b)) show that the pillar elastically deforms until at least 10% strain and doesn't exhibit brittle failure until ~22% strain. We hypothesize that microporosity provides space for enhanced elasticity within the pyrocarbon matrix.

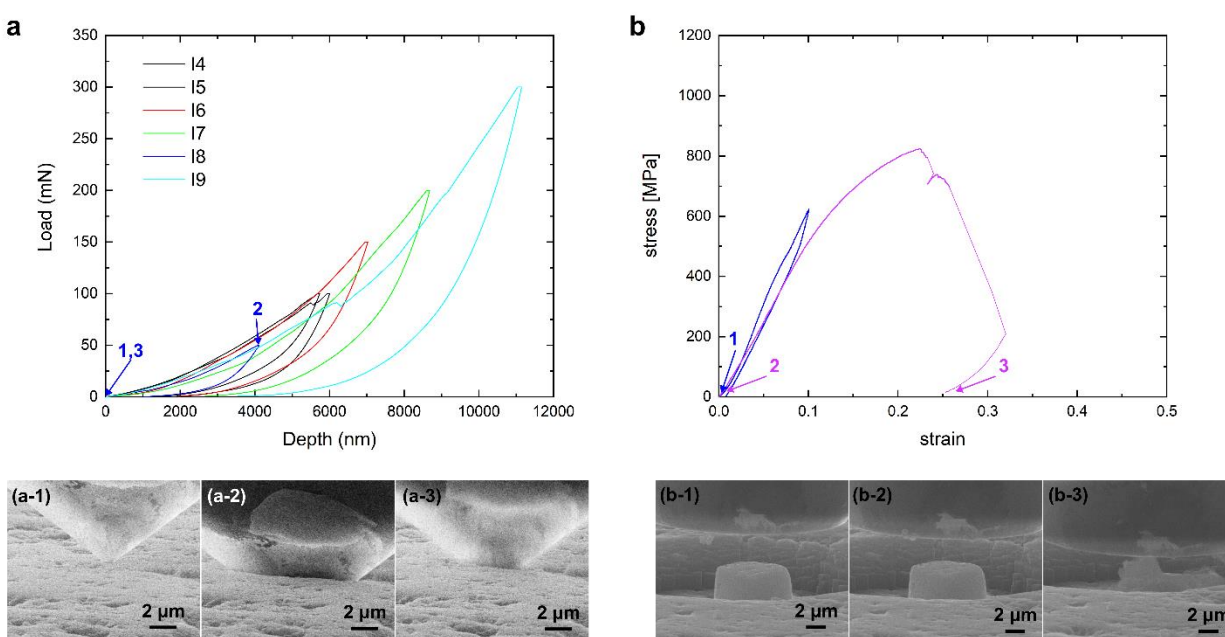


**Figure 4-9: Super-elasticity of pyrocarbon buffer** (a) force-displacement curves from in situ SEM nanoindentation experiments with SEM images at select points during deformation in (a-1) – (a-3) , (b) stress-strain curves from in situ SEM microcompression experiments on the same sample compressed to ~10% strain without yielding (blue curve) and to ~30% strain exhibiting brittle failure; SEM images at select points during deformation in (b-1) – (b-3).

Additional microcompression tests were performed on pillars in the radial and circumferential directions of the spherical particle. To accomplish circumferential compression, the particles were ground to approximately midplane and pillars were fabricated by FIB-milling annular patterns on the surface (Figure 4-10 (c)). Pillars were milled at different positions along

the radial direction of the buffer to correlate the mechanical properties to the radial porosity gradient revealed through FIB-SEM tomography. A large pillar diameter ( $\sim 7\ \mu\text{m}$ ) was chosen to include a representative pore structure—similar to the volumes probed in FIB-SEM tomography. To accomplish compression in the radial direction, particles were ground past mid-plane until the kernel disappeared and the central circular area of the particle was all buffer. Pillars fabricated at the center of this exposed buffer cross-section are axially aligned with the radial direction of the particle (Figure 4-10 (c)). The radial position of this pillar within the buffer layer is calculated by measuring geometric features of the cross section. Pillars are compressed at a constant strain rate of  $0.01\ \text{s}^{-1}$ . Engineering stress-strain curves of radially compressed and circumferentially compressed pillars are shown in Figure 4-10 (a) and (b), respectively. A light to dark color map is used to denote increasing radial position within the buffer layer. The yield strength of each pillar is plotted against the pillar's radial position in Figure 4-10 (d). Again, super elasticity is witnessed, with brittle failure deferred until 10-25% strain. Interestingly, a trend of increasing yield strength with increasing radial position emerges in both radial and circumferential compressed pillars (Figure 4-10 (d)). Considering that the pillars located closer to the IPyC layer would have higher porosity, the higher yield strength in these pillars is counterintuitive. Simple consideration of the rule of mixtures would suggest that the increased void space would reduce the composite yield strength. Additionally, stress concentrations would develop at points around pores, which could cause premature fracture, thereby reducing the yield strength. The experimental data counters these arguments, suggesting a more nuanced mechanistic explanation is required. A potential explanation, which we are investigating through ongoing MD simulations with our collaborators, is that the porous microstructure allows for enhanced plasticity in the pyrocarbon nanostructure.

With increased void space within the material, nanostructural rearrangement (i.e. rotation of crystallites, bond forming/breaking between graphene layers, etc) is made possible.

Although we expect to see differences in the mechanical responses of radially and circumferentially compressed pillars, clear trends cannot be confirmed with this limited sample size. However, the two radially compressed pillars exhibit slightly lower yield strength than circumferentially compressed pillars at similar positions (Figure 4-10 (d)). This observation can be rationalized through a simple mechanics argument: The pore shape analysis revealed that elongated pores tend to be oriented with their long axis parallel to the tangential direction (see Figure 4-10 (d) for schematics representing the orientation of pores with respect to the compression direction). Therefore, considering the equation for the stress concentration factor around elliptical voids ( $K_t = 1 + 2\frac{a}{b}$ ), pillars compressed in the radial direction would have higher stress concentrations at the void sides, potentially causing premature yield at lower applied stress. More microcompression tests on pillars, especially in the radial direction, need to be performed to confirm this hypothesis. Additionally, it is important to note the complex and heterogeneous nature of the pore structure, which has pronounced effects on the stress distribution in any given sample.

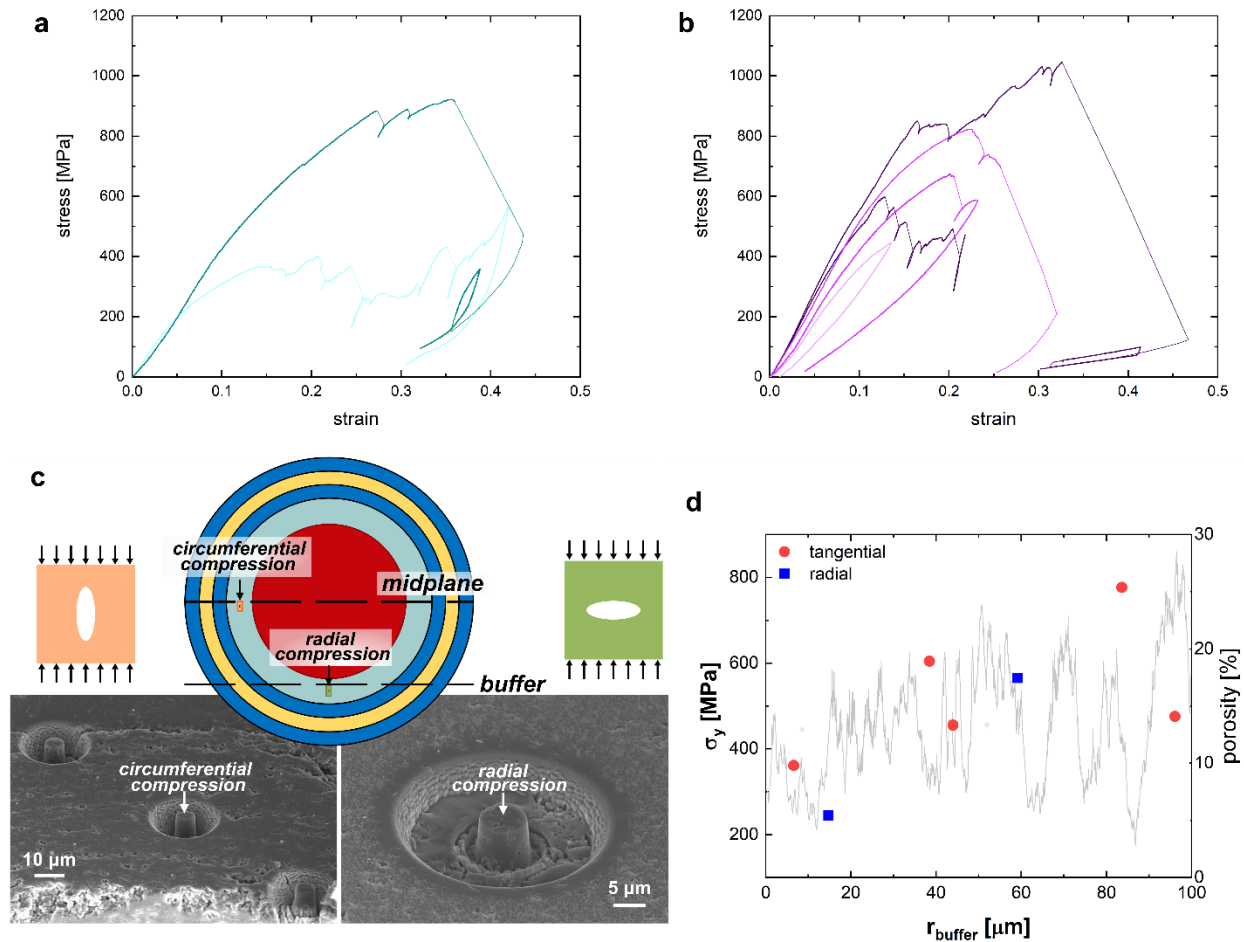


**Figure 4-10: Compression of buffer micropillars in the radial and tangential directions** (a) stress-strain curves of pillars compressed in the radial direction (darker color corresponds to increased distance into the buffer layer), (b) stress-strain curves of pillars compressed in the tangential direction (darker color corresponds to increased distance into the buffer layer), (c) schematic and SEM images showing pillar orientation for radial and circumferential compression, (d) yield strength plotted against radially position within buffer.

#### 4.2.4 Potential implications to fracture and densification behavior

The extensive microstructural analysis presented here provides insight into the observed irradiation response of the buffer layer. The spatial distribution of porosity, pore shapes, sizes, and orientations are expected to influence the initiation and propagation of fractures within the buffer layer. A commonly witnessed fracture mode within the buffer layer is circumferential fracture located near the buffer-IPyC interface, which leads to partial or full tearing away of the buffer



from the IPyC layer [25,26,207]. Such tearing near the buffer-IPyC interface can lead to either the arrest of cracks—which may have otherwise continued into the IPyC layer—or transmission of new cracks into the IPyC layer due to local stress concentrations in still-bonded regions of the interface [25,26,202,207,208]. With such drastically different outcomes—one positive and one negative—this fracture mode must be mechanistically understood for prediction of particle failure. Our results provide some insight into why circumferential fracture near the buffer-IPyC interface is common: we see an increase in porosity and fluctuation in porosity with increasing distance from the kernel, with a local maximum in porosity located at  $\sim 5\text{ }\mu\text{m}$  from the buffer-IPyC interface (Figure 4-11 (a-b)). Higher porosity translates to larger stresses in the pyrocarbon matrix, and stress concentrations at pore sides are prime locations for crack initiation. The location of maximum porosity correlates well with PIE observations of circumferential fracture in the buffer: commonly, a few microns of the buffer material are still attached to the IPyC layer after interface tearing [26,206]. However, full buffer-IPyC tearing does not always occur and a portion of the buffer-IPyC interface remains intact with the final state of the attached buffer expected to be resultant from tensile and shear stresses experienced during tear progression of which fast fluence and fuel temperature influence [224]. The local variability in the pore structure affects the local stress distribution and may determine whether fracture continues to propagate or is arrested. Predicting the extent of circumferential tearing at the buffer-IPyC interface is extremely important to understanding TRISO particle performance, as partial tearing can lead to the initiation of fracture in surrounding layers due to local stress concentrations [207,208], and can also cause asymmetric temperature and fission product distributions [233].

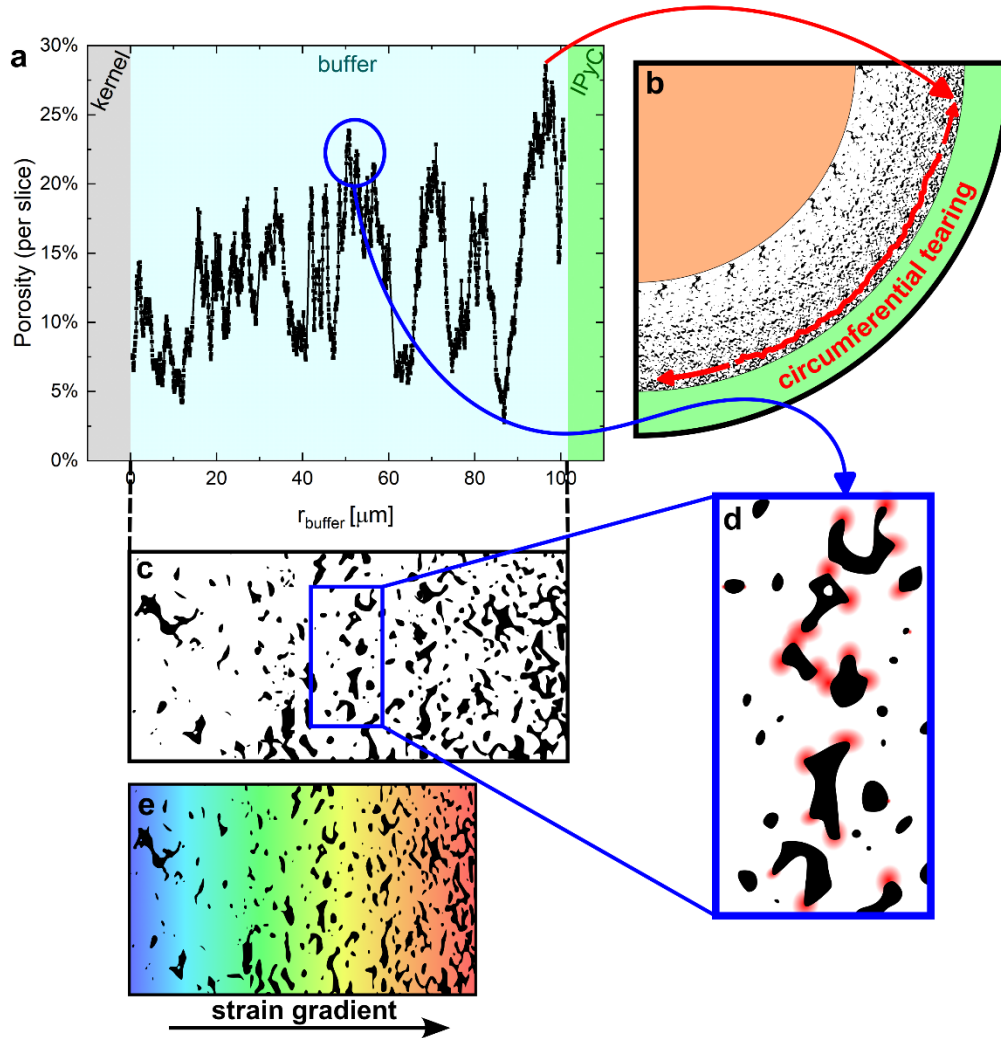


**Figure 4-11: Microstructural features dictating buffer response to irradiation** (a) experimental porosity distribution obtained through this work (Figure 4-2 (a)), (b) schematic showing potential circumferential tearing mechanism at the location of maximum porosity (identified in (a)) near the buffer-IPyC interface, (c) pictorial representation of the porosity gradient seen in experimental data in (a), (d) representation of an area of locally high porosity with sites of potential stress concentrations identified, (e) representation of irradiation-induced densification of the buffer layer, with regions of higher porosity accommodating more strain (shown in red).

Circumferential tearing near the buffer-IPyC interface is not the only mode of buffer fracture witnessed. In fact, the irradiation behavior of buffer fracture is very stochastic, with circumferential cracks, radial cracks, or a combination of the two nucleating and propagating at different regions of the buffer layer [25,26,207]. At the extremes, radial cracks can cause through-

layer fracture, and circumferential cracks can cause full tearing near the buffer-IPyC interface [25,26,207]. With such a stochastic response, we must understand which features of the buffer microstructure dictate the response to predict buffer layer failure and, ultimately, particle failure. Our results point to key features that may be impactful, including the pore structure heterogeneity, pore size distributions, and the pore shapes and orientations. As seen in (Figure 4-11 (a)), local fluctuations in porosity are quite extreme, with increasing magnitude toward the buffer-IPyC interface. Such extreme fluctuations in the porosity will significantly impact the stress state within the buffer layer and induce local stress concentrations at which fracture initiation can readily occur. In addition, we find that these local fluctuations in porosity are primarily governed by the largest ( $V > 1 \mu\text{m}^3$ ) pores (Figure 4-4 (b)). This, in combination with the knowledge of the morphology of the largest pores—that of large sprawling networks of smaller, interconnected voids (Figure 4-5)—suggests that stress concentrations are likely to develop within these complex networks of high porosity (Figure 4-11 (d)). Additionally, our analysis of the pore shapes and orientations (Figure 4-6, Figure 4-8) provides insight into the likely locations of high stress concentrations and expected fracture propagation directions. We find that most pores are elongated along a particular axis, which is typically oriented along the circumferential directions rather than the radial direction. The pore shape and orientation as well as its proximity and position with respect to other pores have all been shown to be integral factors to determining stress concentrations and the resultant fracture modes and propagation directions [234–237]. Although the stress state within the buffer layer is complex given the heterogeneity of the pore structure, we can assume an overall compressive stress in the radial direction due to densification and a tensile stress in the hoop (circumferential) direction due to kernel expansion. Comparing our results to simplified numerical models and

experiments [234–237] in the literature provides insight into the potential microstructure-dependent fracture modes:

- (i) Pores that are elongated along the axis perpendicular to the loading direction exhibit higher stresses at the pore sides [234,235]. This compares well to our pore structure: the pores are elongated along the circumferential direction.
- (ii) Under compression, pores spaced closely in the direction perpendicular to the loading direction exhibit higher compressive stresses at the pore sides, whereas pores positioned diagonally from each other exhibit higher tensile stresses at the pore poles [234,237]. Compressive stresses at the pore sides lead to shear cracking, which can propagate to link pores together [234,237]. In the buffer, elongated pores are spaced closely together in the regions of high porosity near the buffer-IPyC interface: high compressive stresses at the pore sides may lead to shear cracking and linking of pores, resulting in circumferential tearing. Conversely, radial cracks may form due to higher tensile stresses at the pore poles of offset nearby pores.

This simple analysis supports the common fracture modes witnessed within the buffer layer of irradiated TRISO particles. The stochastic fracture behavior can be further understood through quantification of differences in the buffer microstructure and investigation into irradiation conditions, such as temperature and fast fluence, which can affect the stress state and resultant fracture behavior within the buffer.

Finally, though the complex stress state within the heterogeneous porous buffer layer leads to myriad fracture responses, it also leads to buffer densification [25,26,206,238]. We suspect that the porosity gradient along the buffer layer thickness (Figure 4-11(a,c)) leads to a strain gradient

during densification: regions of higher porosity may accommodate more of the strain under a compressive load (Figure 4-11(c,e)). Characterization of the pore structure along the buffer thickness of irradiated particles would test this hypothesis. Additionally, little is known about what proportion of densification is accommodated by compression of the porous microstructure vs. changes in the pyrocarbon matrix. These points are addressed in the next two sections.

## **4.3 Irradiation-induced changes in the porous buffer microstructure**

### *4.3.1 Experimental design*

The irradiation-induced microstructural changes are investigated through FIB-SEM tomography experiments on select TRISO particles from the AGR-2 irradiation experiment. Experiments were conducted within Oak Ridge National Laboratory's Irradiated Fuels Examination Laboratory, to ensure containment and safe handling of the irradiated particles. The effects of temperature and fast neutron fluence are probed by selecting particles with irradiation conditions spanning across the range of the AGR-2 experiment's irradiation conditions (Figure 4-12). Three dimensional volumes spanning the entire buffer layer thickness (~40–100  $\mu\text{m}$ ) are reconstructed to investigate changes in the porosity, pore size distribution, pore shapes, and microstructural heterogeneity due to irradiation. These experiments provide insight into the microstructural changes associated with densification and fracture of the buffer layer. It is imperative that we understand how the irradiation conditions affect the densification and fracture behavior, since certain buffer failure modes are associated with a higher probability of particle failure. To improve the safety and performance of TRISO nuclear fuel particles, we must understand how the highly porous and heterogeneous pyrocarbon buffer layer evolves during

irradiation, leading to altered mechanical properties and dictating buffer—and potentially particle—failure modes.

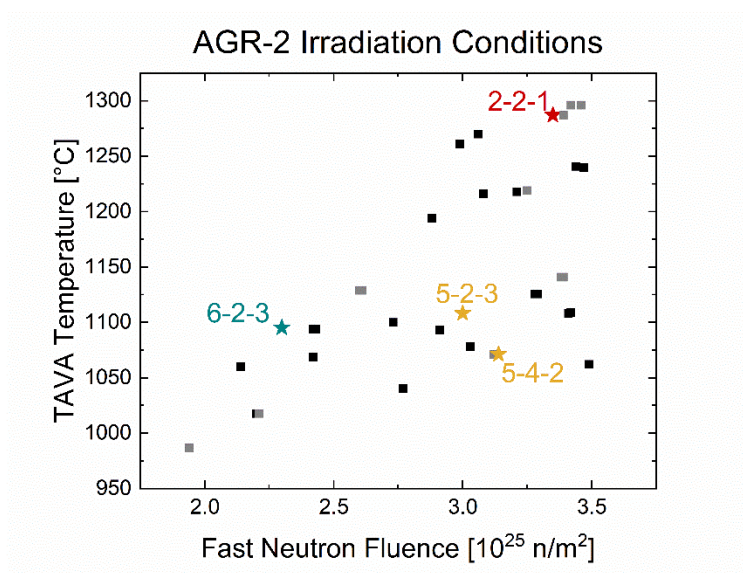


**Figure 4-12: Irradiation conditions of the AGR-2 experiment’s fuel compacts**

The experiment matrix designed to achieve these goals is briefly described here and outlined in Table 4-2. Representative compacts from three irradiation condition groups are selected from the AGR-2 compacts with UCO kernels (Figure 4-12): one with relatively low temperature and fluence (6-2-3), two compacts with relatively low temperature and higher fluence (5-4-2 and 5-2-3) and one compact with high temperature and high fluence (2-2-1). Three particles from each of these three irradiation condition groups are selected for analysis. Particles with approximately average silver retention in each compact are selected ( $M_{\text{part}}/M_{\text{avg}}$ ), which is used as an indicator that the temperature in that particle was not significantly different from the time average volume average (TAVA) temperature recorded for that compact [26]. The TAVA temperatures, fluences, and average silver retention for each particle analyzed are shown in Table 4-2. For each of the 9 irradiated particles studied, experiments conducted on that particle are noted in the last three columns. At least four full-buffer thickness FIB-SEM tomography scans are conducted for each of

the three irradiation condition groups to investigate microstructural heterogeneity between particles with similar irradiation conditions. Additionally, two full-buffer scans are performed on at least one particle in each group to investigate intraparticle heterogeneity. In addition to the irradiated samples, a full-buffer FIB-SEM tomography scan is also performed on a representative as-fabricated AGR-2 particle—serving as a control to ascertain irradiation-induced microstructural changes from the as-fabricated microstructure.

**Table 4-2: Experiment matrix designed to investigate the irradiation-induced changes in the buffer layer's micro- and nanostructure**

Compact	Mount	Particle	Ag (M <sub>part</sub> /M <sub>avg</sub> )	Temperature [°C]	Fluence [10 <sup>25</sup> n/m <sup>2</sup> ]	#full buffer scans	Raman	TEM
221	MM-D67	RS43	1.12	1287	3.35	2	X	X
221	MM-D67	RS46	1.8	1287	3.35	2		X
221	MM-D68	RS39	0.83	1287	3.35	1		
523	MM-D12	RS11	0.48	1108	3.00	1		X
523	MM-D12	RS28	0.43	1108	3.00	1		
542	MM-D55	RS25	1.59	1071	3.14	2	X	
623	MM-D69	RS18	1.87	1095	2.30	2		X
623	MM-D69	RS07	1.72	1095	2.30	1		X
623	MM-D70	RS35	0.81	1095	2.30	1	X	X
As fabricated AGR-2			N/A			1	X	X

The data acquisition and analysis workflow presented in Section 2.4.5 is used to acquire quantitative data on the buffer microstructure. To prepare for FIB-SEM tomography, a volume spanning the entire buffer thickness (with a  $\sim 14 \times 14 \mu\text{m}^2$  cross section) was isolated by milling trenches around 3 sides (Figure 4-13 (b)). Prior to milling, a Pt protective layer was deposited on the surface to prevent ion damage to the region of interest. Depending on the particle (how much the buffer layer densified during irradiation), the buffer layer can be between 30 and 100  $\mu\text{m}$  thick.

Between 1 and 3 separate FIB-SEM tomography runs are needed to traverse the entire buffer layer thickness. Each run takes approximately 18 hours to complete. A constant slice thickness of 50 nm is used for every scan, and the SEM image resolution is set to obtain a pixel size of  $<50 \times 50$  nm. Between ~700 and 2100 SEM images are acquired for each full-buffer FIB-SEM tomography scan. These 2D images are aligned and combined to form a 3D virtual reconstruction of the microstructure (Figure 4-13 (d)). Image processing techniques are used to segment the greyscale SEM images into different phases and provide quantitative analysis on the microstructural features. Image segmentation is performed using a deep learning model (Section 2.4.5) trained to identify the pyrocarbon, pores, fission products, and cracks (Figure 4-13 (c-e)). The segmented regions representing the pores and fission products are separated into individual components based on connectivity analysis. From this, individual pore sizes, shapes, positions, etc. can be quantified.



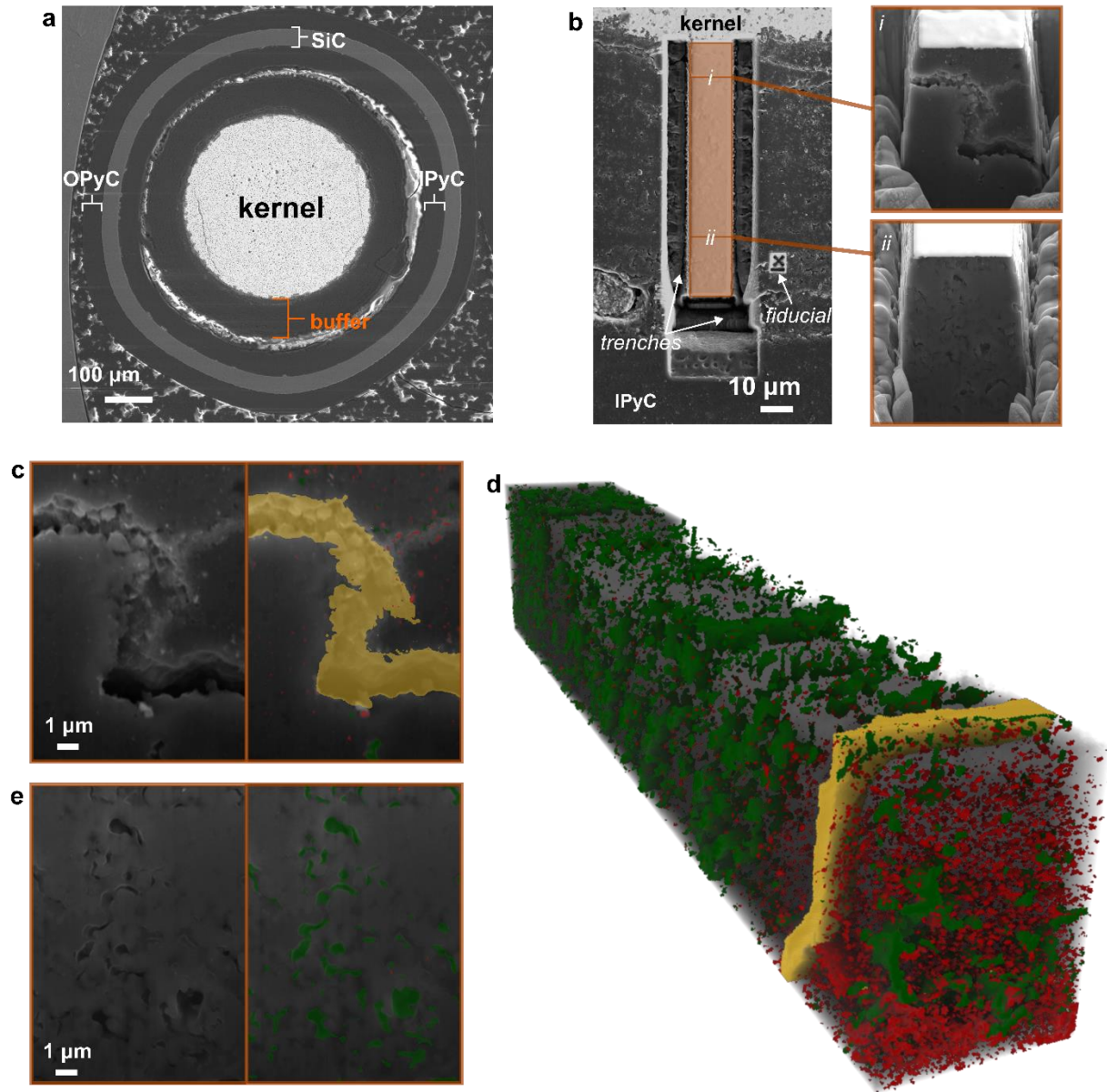


**Figure 4-13: FIB-SEM tomography of irradiated buffer layer** (a) SEM image of TRISO particle with layers identified, (b) SEM image of buffer layer section prepared for FIB-SEM tomography; (i-ii) select SEM images taken during FIB-SEM tomography scan, (c) cropped SEM image and corresponding segmentation results from image (i), (d) virtual 3D microstructure reconstructed from FIB-SEM tomography scan, (e) cropped SEM image and corresponding segmentation results from image (ii).

#### 4.3.2 Porosity and fission product distribution across the buffer layer of particles irradiated at different temperatures and fluences

The FIB-SEM tomography experiments reveal key differences in the porous buffer microstructures depending on the irradiation conditions. Figure 4-14 shows FIB-SEM tomography results from a representative particle exposed to relatively low temperature and low neutron fluence (Capsule 6). Two locations on this particle were identified for microstructural analysis—one near the tip of a crack which appeared to propagate in a mixed radial-tangential direction and second scan spanning a section which includes circumferential cracks near the buffer-kernel and buffer-IPyC interfaces. We notice a few similarities and differences between these two scans within the same particle. The first key observation is that there is a  $\sim 5\text{ }\mu\text{m}$  thick region located between  $10 - 20\text{ }\mu\text{m}$  into the buffer layer where there is no porosity. This is preceded by a crack and a relatively higher concentration of fission products. These observations are consistent between these two scans within the same particle and are also observed in other particles under similar irradiation conditions (low temperature and fluence (Capsule 6) – Appendix B.4). These observations provide key insights into the fracture and densification behavior of these particles. Under these irradiation conditions, densification is accommodated by the closing of micropores near the kernel-buffer interface, facilitated by large thermal and mechanical stresses. Kernel expansion imparts large compressive stresses on the neighboring buffer layer, leading to fracture which propagates in the circumferential direction.

Although both scans on this particle show similarities in their microstructure within the first  $\sim 20\text{ }\mu\text{m}$  from the kernel, the porosity distributions in the remainder of the scans are quite different. For example, in Scan 1 the porosity between  $20 - 50\text{ }\mu\text{m}$  is less than 10% while in Scan 2, the porosity reaches over 30% in this same region. In next  $30\text{ }\mu\text{m}$ , this reverses: maximum porosity is reached in scan 1, while the porosity reduces to  $<20\%$  between  $50 - 70\text{ }\mu\text{m}$  in scan 2. While some of this difference can be attributed to intraparticle heterogeneity in the as-fabricated

buffer, these differences are more extreme than the observed interparticle heterogeneity in the surrogate particles (Section 4.2.3). Therefore, we can conclude that these porosity distribution differences within the same particle are due to non-axisymmetric densification behavior.

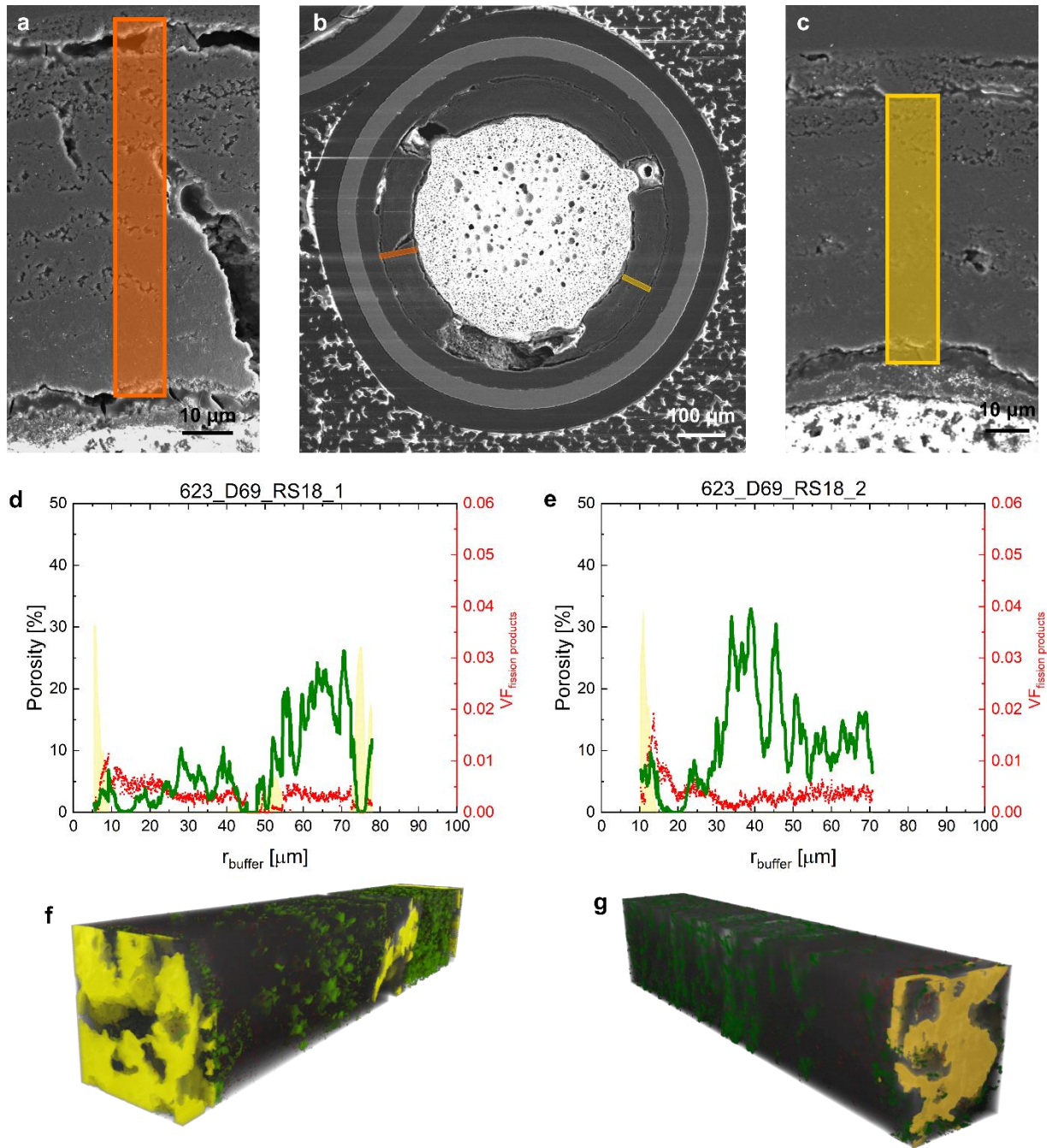


**Figure 4-14: FIB-SEM tomography data from a Capsule 6 particle (low temperature and fluence)** (a) location of scan 1 indicated on SEM image, (b) SEM image of particle cross section, (d) location of scan 2 indicated on SEM image, (d-e) volume fractions of porosity (left axis – green), fission products (right axis – red), and cracks (scale: 0 to 1 – yellow) as a function of radial position within the buffer layer for scan 1 (d) and scan 2 (e), (f-g) 3D reconstructions of microstructures from scan 1 (f) and scan 2 (g) with cracks highlighted in yellow, pores highlighted in green, and fission products highlighted in red.

We can now investigate the effects of increased neutron fluence on the microstructural changes by looking at FIB-SEM tomography results from a representative particle exposed to similarly low temperatures but high neutron fluence (Capsule 5, Figure 4-15). Microstructural features near the kernel are very similar to the Capsule 6 particles: regions of almost zero microporosity accompany circumferential cracks. Since these samples are exposed to similar temperatures but different fluences, this consistency suggests that a thermally dependent mechanism controls the extreme densification and circumferential fracture close to the kernel. In contrast to the Capsule 6 sample, these Capsule 5 scans contain a clear gradient of increased porosity with increasing radial distance. This gradient is more extreme than that observed in the buffer layer of unirradiated TRISO particles. Furthermore, the porosity in this Capsule 5 particle is higher than the particle from Capsule 6 and, in some locations, even higher than the maximum porosity in the as-fabricated particle (~32%). In other regions, the measurable porosity drops to nearly 0%. These dramatic fluctuations in porosity suggest that densification may be accommodated by a combination of nano and microstructural changes. Densification through extreme nanostructural changes may even lead to increased porosity.

Compared to the two scans taken on the Capsule 6 particle, these two scans share more similarities to each other. Both contain a clear gradient of increasing porosity with increasing radial position. The fluctuations and maximum porosity values are similar. And both show extreme densification near the kernel through almost zero porosity in small regions. These similarities suggest that the densification behavior is more symmetric in this particle.



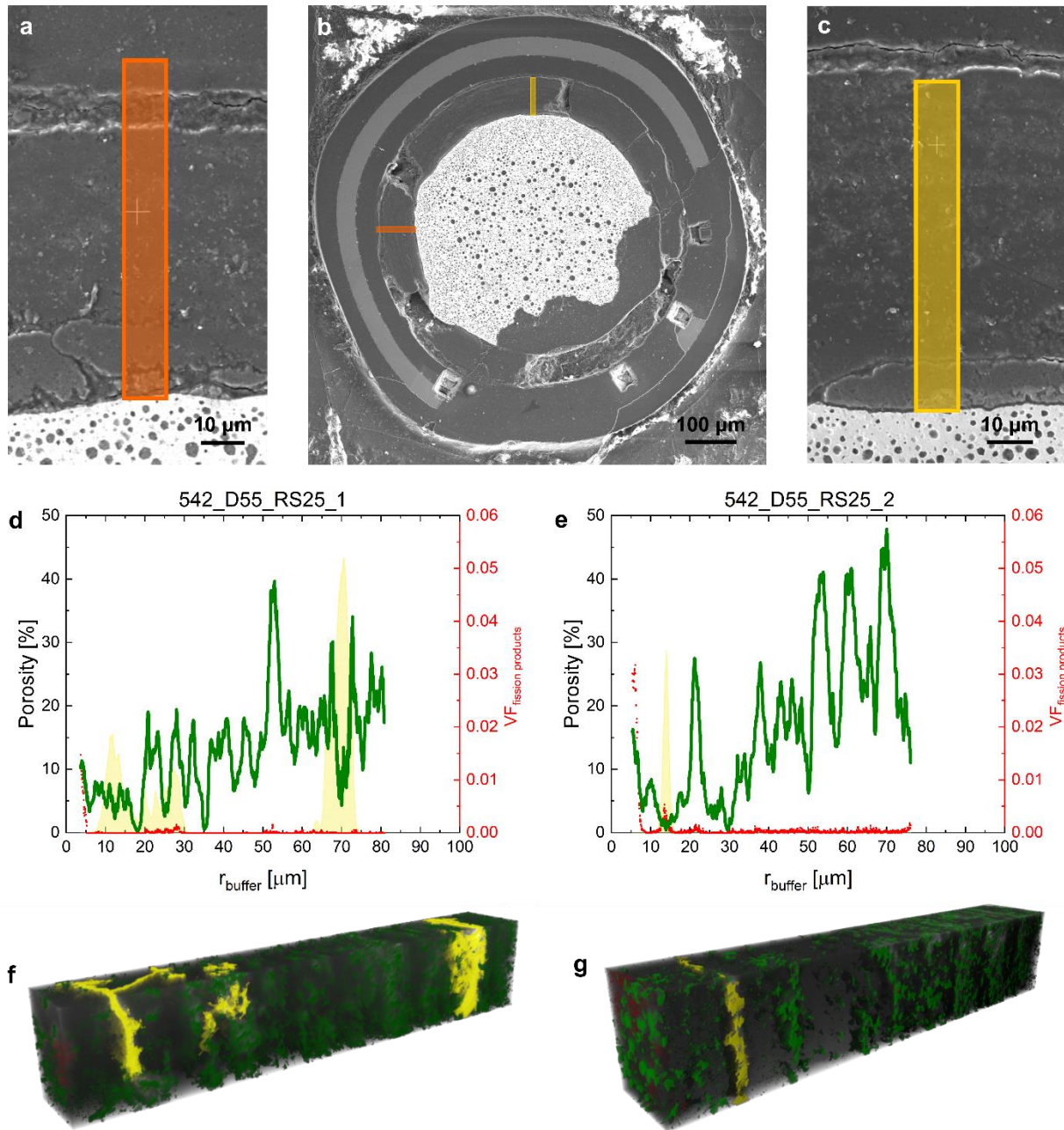


**Figure 4-15: FIB-SEM tomography data from a Capsule 5 particle (low temperature and high fluence)** (a) location of scan 1 indicated on SEM image, (b) SEM image of particle cross section, (d) location of scan 2 indicated on SEM image, (d-e) volume fractions of porosity (left axis – green), fission products (right axis – red), and cracks (scale: 0 to 1 – yellow) as a function of radial position within the buffer layer for scan 1 (d) and scan 2 (e), (f-g) 3D reconstructions of microstructures from scan 1 (f) and scan 2 (g) with cracks highlighted in yellow, pores highlighted in green, and fission products highlighted in red.

Finally, we study the effects of combined high temperature and high fluence on the porous buffer microstructure through FIB-SEM tomography scans of a Capsule 2 particle (Figure 4-16). This particle exhibits the most drastic microstructural changes. With lower average porosity than the Capsule 5 particles and without a clear gradient of increased porosity with increased radial distance like as-fabricated particles (Figure 4-17), a combination of pore expansion and shrinkage combined with extensive nanostructural changes must have occurred. Pore expansion could be facilitated through high pressures exerted by trapped fission gases or through densification within the pyrocarbon nanostructure. Pore shrinkage might be induced through compressive forces exerted through kernel expansion. Additional analysis into the pore sizes, shapes, and connectivity will provide further insight into the irradiation-induced microstructural changes.

Comparing these two scans from the same Capsule 2 particle reveals extreme asymmetry in the densification and fracture behavior under high temperatures and fluences. The peaks and valleys in porosity occur at different locations in these two scans. There is a circumferential crack located  $\sim 20\text{ }\mu\text{m}$  from the kernel and the buffer has completely torn away from the IPyC layer in scan 2. In contrast, the buffer remains intact in scan 1.

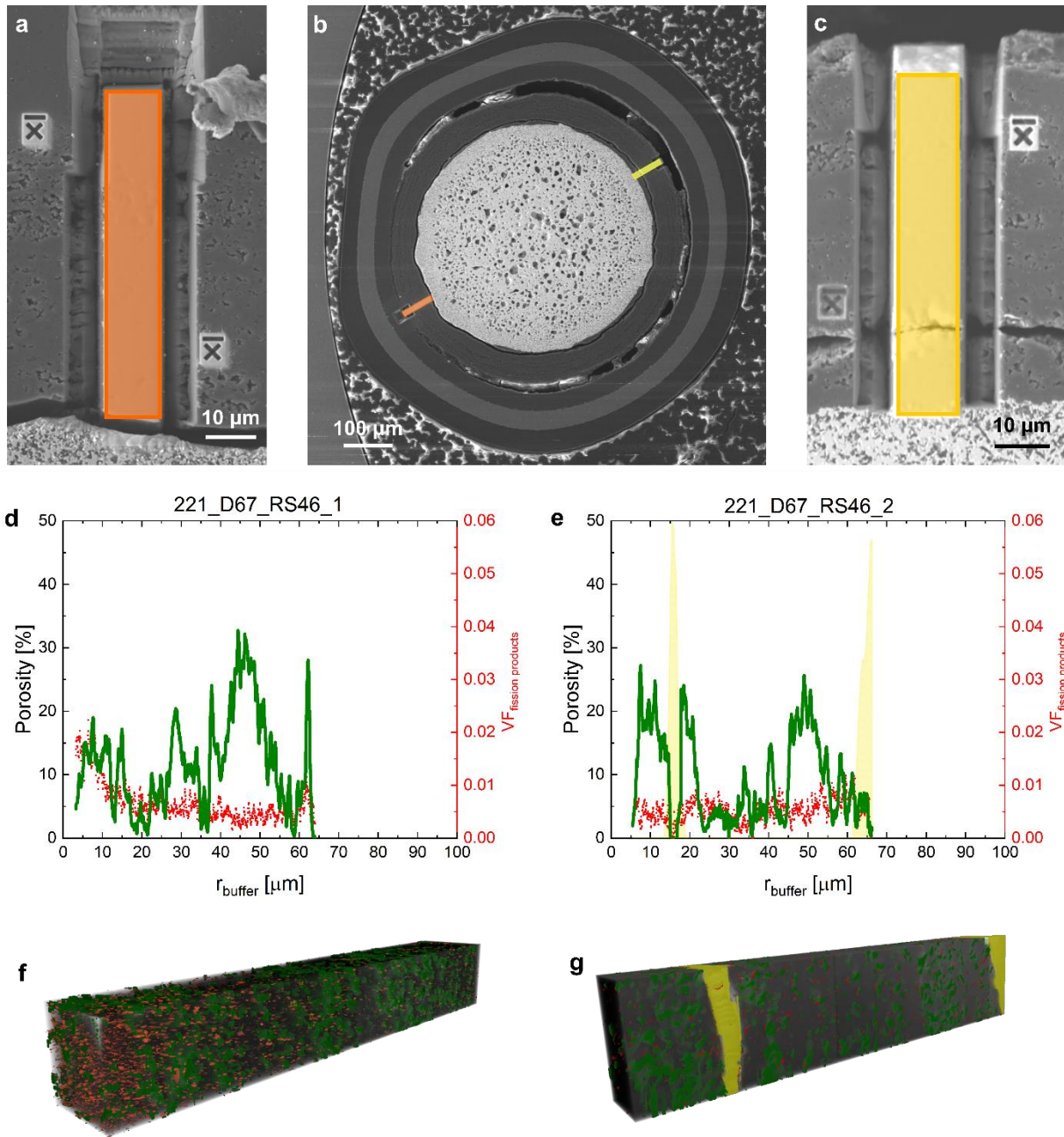


**Figure 4-16: FIB-SEM tomography data from a Capsule 2 particle (high temperature and fluence)** (a) location of scan 1 indicated on SEM image, (b) SEM image of particle cross section, (d) location of scan 2 indicated on SEM image, (d-e) volume fractions of porosity (left axis – green), fission products (right axis – red), and cracks (scale: 0 to 1 – yellow) as a function of radial position within the buffer layer for scan 1 (d) and scan 2 (e), (f-g) 3D reconstructions of microstructures from scan 1 (f) and scan 2 (g) with cracks highlighted in yellow, pores highlighted in green, and fission products highlighted in red.



The observations made through FIB-SEM tomography scans of these three particles have provided a preview into the effects of different irradiation conditions on the fracture and densification behavior. In the next section, we combine all acquired data for each irradiation condition to achieve an overall perspective of consistent behaviors depending on the irradiation conditions.

#### *4.3.3 Implications of irradiation induced microstructural changes to the fracture and densification behavior*

Before drawing conclusions about overall irradiation-induced microstructural changes, we must establish a control representing the unirradiated buffer microstructure. To confirm that the work done on surrogate TRISO particles (Section 4.2) provides an accurate basis for comparison, we performed a full buffer length scan on a TRISO particle from the same batch as particles irradiated in the AGR-2 experiment. This particle was not irradiated, but it does contain a UCO kernel and went through the compact and deconsolidation process. Although the FBCVD conditions used to fabricate the particles are identical, the surrogate particles have a different kernel, which could affect the particle flow within the FBCVD chamber and thus, affect the microstructure of the buffer layer. Additionally, mechanical and thermal stresses are imposed on the particles during the compaction process. Characterization of an unirradiated particle deconsolidated from the compact provides a true initial state of the buffer structure prior to irradiation. Figure 4-17 shows the porosity distributions measured from the surrogate and as-fabricated TRISO particles. While there are some notable differences, they are within the differences seen between surrogate particles (Figure 4-7). Overall, the trend of increasing porosity with increasing radial position is apparent in both samples. Furthermore, the fluctuations follow a similar pattern. These two similarities are indicative of similar FBCVD conditions during

deposition. The largest difference between the two particles occurs within the first 20  $\mu\text{m}$ , where the as-fabricated particle exhibits up to  $\sim 2\times$  higher porosity than the surrogate particle. Since this region is deposited first, large variations in porosity from particle to particle are possible due to variations in particle and gas flow during the initial deposition ramp up time. With this analysis, the surrogate particles are deemed to have statistically equivalent buffer microstructures as the as-fabricated particles. The porosity distributions from these two particles are used as a basis for the unirradiated buffer microstructure for comparison to the irradiated buffer microstructures.

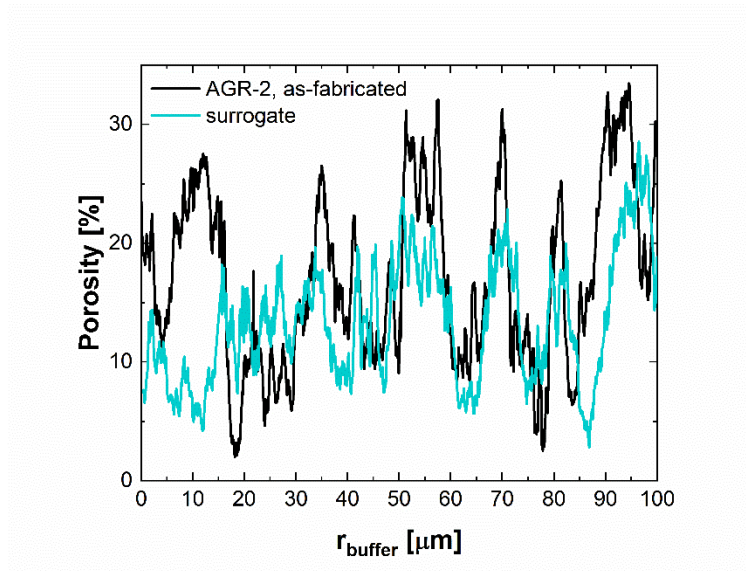


**Figure 4-17: Porosity distribution in the buffer layers of a deconsolidated as-fabricated particle compared to a surrogate TRISO particle**

To investigate consistent microstructural changes within each irradiation condition group, we combine the porosity data from all scans in each irradiation condition group (Table 4-2) and calculate the average and first standard deviation in porosity every 5  $\mu\text{m}$ . Figure 4-18 shows the average porosity (points) and standard deviation (shaded area) distributions for each sample set. We find that several of the observations made from analysis of single particles hold for all particles in that irradiation condition group. For example, both the Capsule 6 (Figure 4-18 (b)) and Capsule

5 (Figure 4-18 (c)) particles exhibit a consistent highly densified region located  $\sim 10\text{-}15\ \mu\text{m}$  from the kernel. This localized minimum in porosity reveals a temperature-dependent mechanism that leads to the closing of micropores close to the kernel. A number of temperature-dependent processes could control this densification—including kernel expansion, fission product transport, and radiation damage. Future detailed analysis and multiscale simulations will provide insight into these observations. The Capsule 5 and Capsule 6 particles also share the similarity of exhibiting gradients of increased porosity with increased radial position. These gradients are even more extreme than the gradient in the unirradiated particles (Figure 4-18 (a)), suggesting a gradient in densification behavior. Clearly, most of the densification accommodated through closing of microporosity is localized near the kernel. This is extreme in the Capsule 5 particles, where at farther distances into the buffer ( $>50\ \mu\text{m}$ ), the porosity dramatically increases to an average of  $\sim 20\text{--}30\%$ . The porosity in this region is even greater than that in the unirradiated particles, revealing that irradiation-induced pore expansion may have occurred. This could be accommodated through pressures exerted by trapped fission product gases or restructuring of the pyrocarbon nanostructure.

In contrast to the Capsule 6 and Capsule 5 particles, Capsule 2 particles do not exhibit a gradient in porosity within the buffer layer (Figure 4-18 (d)). The lack of a gradient reveals that densification through changes in the microstructure is not localized but occurs throughout the buffer layer. A more uniform densification response may be due to the entire buffer being exposed to similar stress, temperature, and radiation damage conditions due to the combined high temperature and fluence. Additionally, note the large standard deviations in porosity, revealing high interparticle heterogeneity in the irradiation-induced microstructural changes. Extensive structural changes occur in these particles due to the extreme irradiation conditions.

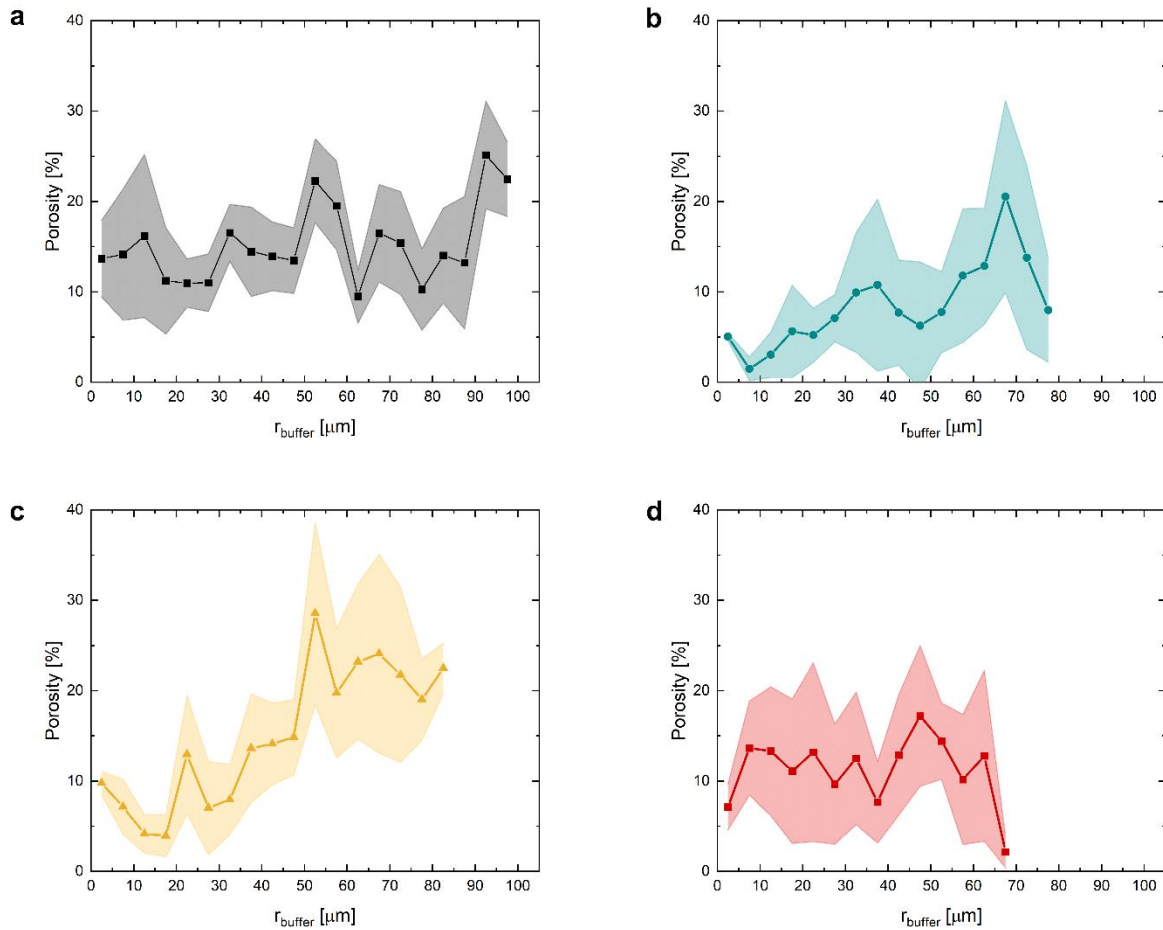


**Figure 4-18: Average and standard deviation in porosity separated by sample set** (a) porosity distribution in unirradiated particles (as-fabricated and surrogate), (b) porosity distribution in Capsule 6 particles (low temperature and fluence), (c) porosity distribution in Capsule 5 particles (low temperature and high fluence), (d) porosity distribution in Capsule 2 particles (high temperature and fluence).

This analysis provides insight into the local densification behavior within the buffer layer depending on the irradiation conditions. We can also draw conclusions about the fracture and densification behavior based on changes in the average porosity. A recently published study reports buffer fraction and densification fractions calculated through x-ray computed tomography measurements [224]. The results obtained for AGR-2 UCO particles are reproduced in Figure 4-19 (a) and Figure 4-20 (a). Figure 4-19 (a) shows that the Capsule 5 particles exhibit consistently

higher radial fracture fractions than the Capsule 2 or Capsule 6 particles. In our study, we found that the Capsule 5 particles have the greatest average microporosity after irradiation compared to particles from the two other capsules. The connection between high porosity and high fracture fraction provides insight into the fracture behavior. Higher porosity is known to decrease the fracture toughness of materials [239,240]. Additionally, nano and microstructural changes in the Capsule 5 particles may be insufficient to alleviate the stress—resulting in the critical stress intensity factor for fracture to be exceeded. Structural changes may be accommodated through radiation creep [241]. In graphite, the radiation creep coefficient has been shown to increase with increasing temperatures [242].

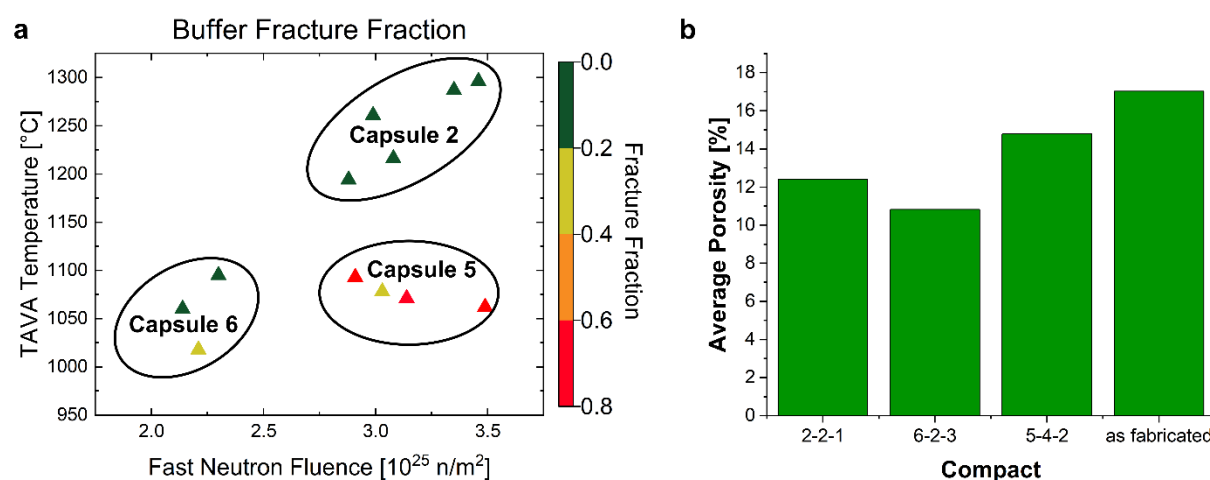


**Figure 4-19: Radial fracture depending on irradiation conditions** (a) radial fracture fractions measured through XCT [224], (b) average porosity measured through FIB-SEM tomography.

The average porosity changes also provide insight into what proportion of buffer densification is accommodated through closing of pores. XCT measurements of buffer densification (Figure 4-20 (a)) shows that particles exposed to high temperatures and fluences (Capsule 2) exhibit the highest densification. From these measured densification values, we can estimate what proportion is due to microstructural changes and what proportion is due to

nanostructural changes from our FIB-SEM tomography average porosity data. The following expression defines these values:

$$df_{total} = \frac{V_{b2}}{V_{b1}} = \frac{V_{P2} + V_{PyC2}}{V_{b1}} = df_P + df_{PyC}$$

where  $V_{b1}$  and  $V_{b2}$  are the volumes of the buffer layer before and after irradiation, respectively (calculated from XCT),  $V_{P2}$  is the total pore volume in the irradiated sample (determined from FIB-SEM tomography), and  $V_{PyC2}$  is the volume of the pyrocarbon matrix (dense/solid phase). Thus, the total densification ( $df_{total}$ ) can be decomposed into a fractions of densification due to microstructural ( $df_P$ ) and nanostructural ( $df_{PyC}$ ) changes. These fractions can be estimated using the average porosity data from FIB-SEM tomography and the total densification fractions from XCT data. The densification fractions for each compact studied are shown in Figure 4-20 (b). Clearly, the average changes in microporosity only account for a small percentage of the total densification. The majority of densification must be accommodated through nanostructural changes.

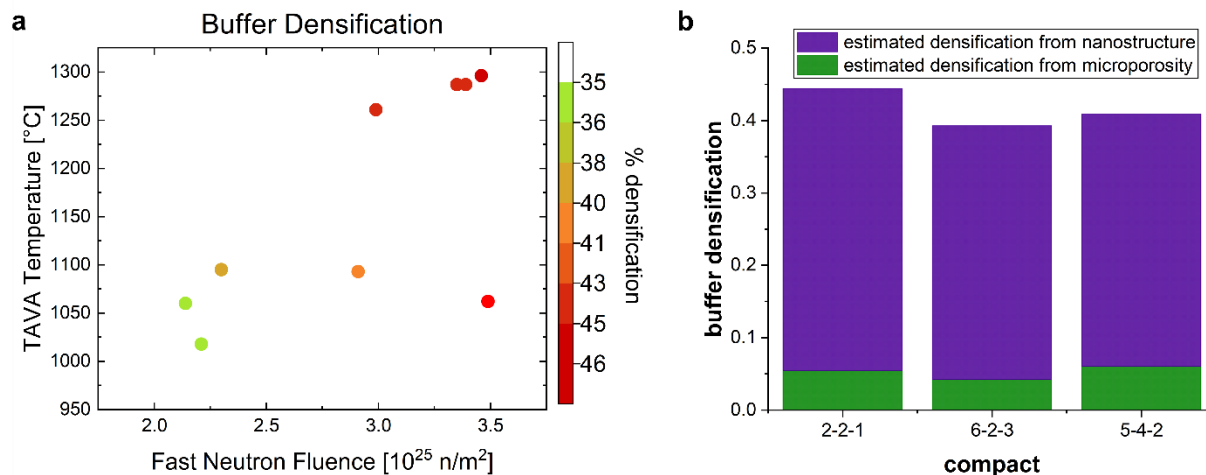


**Figure 4-20: Buffer densification accommodated through changes in microporosity** (a) buffer densification measured through XCT [224], (b) estimated fractions of buffer densification accommodated through changes in the micro and nanostructure.

## 4.4 Irradiation-induced nanostructural changes in pyrocarbon

### 4.4.1 Experimental design

Complementary Raman spectroscopy and transmission electron microscopy (TEM) experiments provide insight into the irradiation-induced changes in the pyrocarbon nanostructure. The particles identified in Table 4-2 were selected for further nanostructural analysis in addition to microstructural analysis. At least one particle from each irradiation condition group, in addition to the as-fabricated particle, was chosen for supplemental nanostructural characterization. Raman spectroscopy and TEM analysis are performed on cross sections extracted from the buffer layer. Sections of the buffer layer spanning the entire thickness, with  $\sim 15$   $\mu\text{m}$  height and  $\sim 2$   $\mu\text{m}$  depth are extracted using the FIB lift-out technique (Figure 4-21 (a-c)). Although this involved sample preparation is not typically needed for Raman spectroscopy, it is used to reduce contamination and exposure risks and allows for correlative TEM analysis on the same sections analyzed with Raman. The lift-outs are attached to FIB grids and the grids placed flat and secured in a sample holder.

Raman maps covering the entire cross-sectional area with a 1  $\mu\text{m}$  step size are performed on each lift out, using a 532 nm laser. A spectrum is acquired at each pixel (Figure 4-21 (d-f)), yielding a total of ~750–1500 spectrum acquisitions for each sample. Peak deconvolution is performed to acquire nanostructural information about the samples. Color maps (Figure 4-21 (d)) are used to visualize spatial variations in quantifiable peak parameters corresponding to nanostructural features—such as peak widths, heights, positions, ratios, etc. More details on data acquisition and processing can be found in Section 2.4.3.

After Raman maps were successfully obtained on the lift-outs, the samples were loaded back into the FIB for subsequent site-specific thinning in preparation for TEM. Windows ~10  $\mu\text{m}$  wide were thinned at select locations which showed interesting spatially dependent nanostructural features in the Raman maps. The TEM analysis is ongoing, in collaboration with a staff scientist at ORNL. Upon completion of the TEM analysis, we will have correlative Raman and TEM nanostructural analysis which will be instrumental in quantifying the nanostructural changes that occur due to irradiation. However, the Raman analysis presented in this section provides key insights into the nanostructural changes, which will be confirmed through TEM analysis.



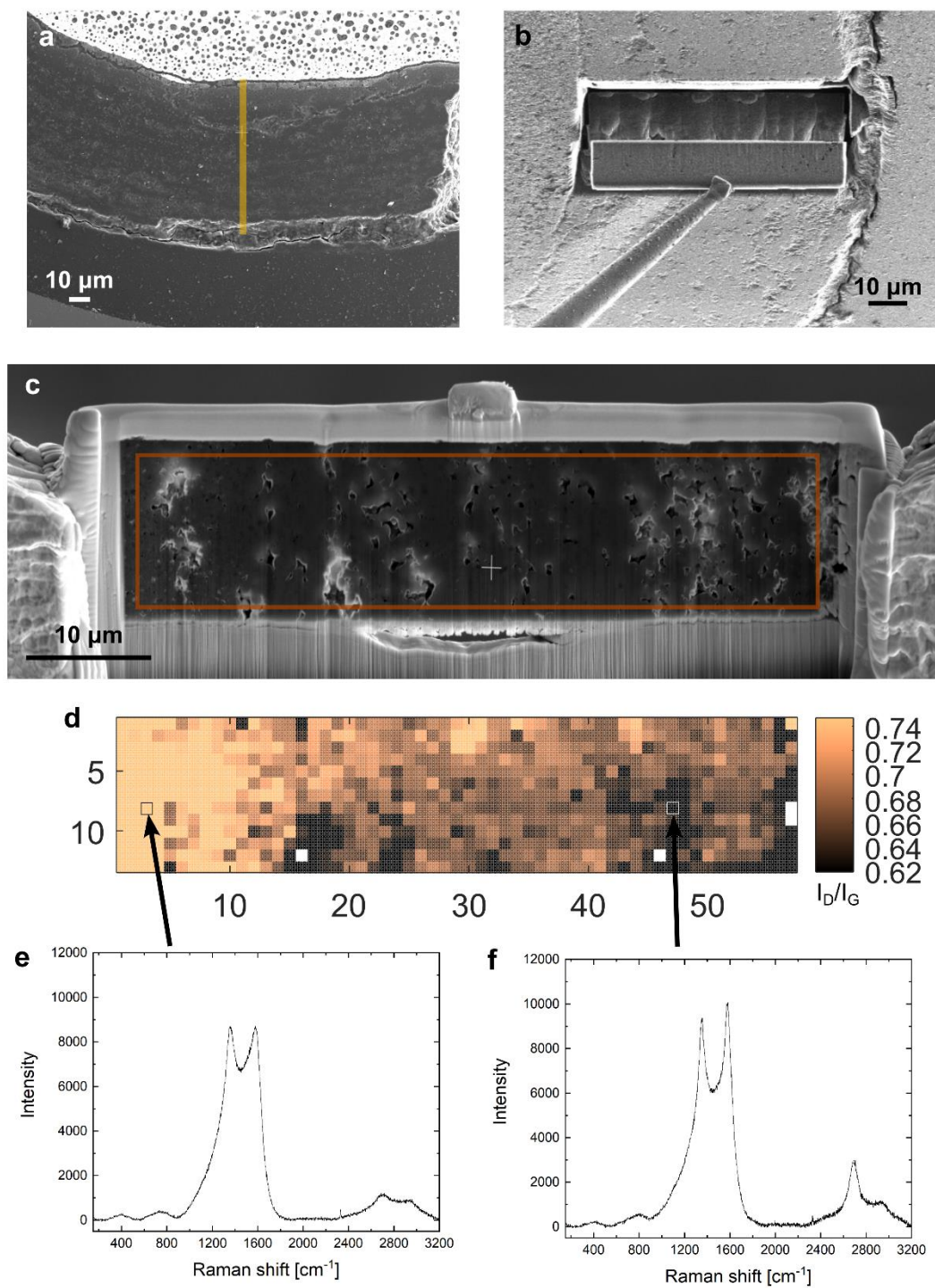


**Figure 4-21: Sample preparation for Raman spectroscopy** (a) SEM image of buffer layer showing location and orientation of lift-out, (b) FIB image showing lift-out process, (c) lift-out attached to FIB-grid; area for Raman map denoted, (d) map of  $I_D/I_G$  values calculated from Raman spectrum at each acquisition point.

#### 4.4.2 Crystallite size changes as a function of irradiation temperature and fluence

By curve fitting the Raman spectra, quantified peak parameters provide information about nanostructural features. For example, information about the crystallite size and defect concentration can be calculated from the intensity ratio of the D and G peaks [243,244]. Through Raman spectroscopy and X-ray diffraction studies of graphene based-systems, the following relationship between the intensity ratio of the D and G peaks and the crystallite size in the basal plane direction ( $L_a$ ) has been established [244]:

$$L_a(nm) = (2.4 \times 10^{-10}) \lambda_l^4 \left( \frac{I_D}{I_G} \right)^{-1},$$

where  $\lambda_l$  is the laser line wavelength (532 nm), and  $I_D$  and  $I_G$  are the peak intensities of the D and G bands. This intensity ratio can also be used to estimate the concentration of one-dimensional defects (border defects with respect to the total crystalline area) through the following established relation [243]:

$$n_D(cm^{-2}) = \frac{(1.8 \times 10^{22})}{\lambda_l^4} \left( \frac{I_D}{I_G} \right).$$

These two equations are used to estimate the average crystallite size and density of point defects from the measured  $I_D/I_G$  ratio. The following four figures show the Raman spectroscopy data yielding information about crystallite size and defect concentration within the unirradiated and irradiated buffer samples.

Figure 4-22 (b) shows the  $I_D/I_G$  ratio map obtained from Raman spectroscopy of a buffer cross section extracted from of an unirradiated particle (Figure 4-22 (a)). The  $I_D/I_G$  ratio ranges from  $\sim 0.6 - 1.5$ , revealing that in some regions, the intensity of the D band is greater than that of the G band, while in other regions, this reverses. Such high  $I_D/I_G$  ratios are common in FBCVD

deposited pyrolytic carbon coatings [245,246]. A higher intensity ratio corresponds to a smaller crystallite size and higher defect concentration. The regions of low  $I_D/I_G$  seem to correspond to the location of pores, when comparing the Raman map (Figure 4-22 (b)) to the optical image of the cross section (Figure 4-22 (a)). This suggests a slightly larger crystallite size and lower defect concentration near pores. The average crystallite size ( $L_a$ ) and defect density ( $n_D$ ) is calculated for each radial position and shown in the plots in Figure 4-22 (c-d). Gradual gradients emerge of increasing crystallite size and decreasing defect concentration with increasing radial position. These gradients are consistent with the porosity gradient along the buffer radial direction which was revealed through FIB-SEM tomography. Previous TEM, SEM, and Raman spectroscopy analysis of porous pyrocarbon produced through FBCVD revealed the presence of globular features, which are composed of clusters of soot particles surrounded by fibrous graphene layers. Large loosely packed globular features were found to surround porous regions [245]. This provides an explanation for the correlation between large crystallite size and higher microporosity.

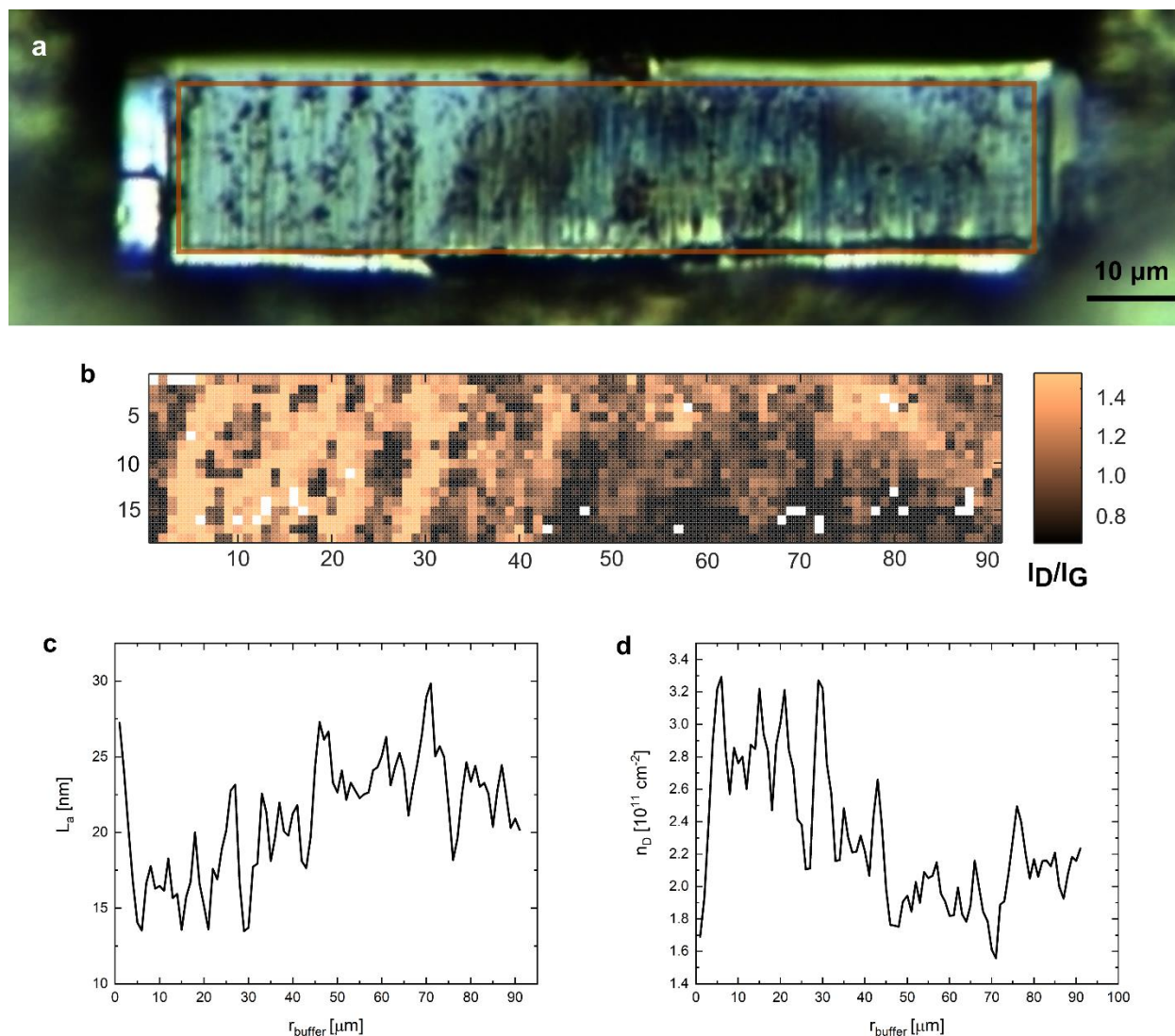


**Figure 4-22: ID/IG ratio analysis of an unirradiated buffer sample** (a) optical microscope image of buffer cross-section with Raman map area identified, (b) color map showing spatial variation of ID/IG ratio, (c) average crystallite size ( $L_a$ ) as a function of radial position in the buffer, (d) average point defect concentration as a function of radial position in the buffer.

Now that we have established a basis for the as-fabricated pyrocarbon crystallite size and defect density, we can investigate the effects of irradiation on these nanostructural features. Figure 4-23, Figure 4-24, and Figure 4-25 show the corresponding crystallite size and defect density data from Capsule 6, Capsule 5, and Capsule 2 particles, respectively. In all three irradiated samples,

the maximum  $I_D/I_G$  ratio is less than that of the unirradiated sample, revealing an overall increase in crystallite size during irradiation. Like the unirradiated sample, the Capsule 6 and Capsule 5 samples (relatively lower TAVA temperatures) exhibit trends of increasing crystallite size with increasing radial position (Figure 4-23 (c), Figure 4-24 (c)). The defect density follows an inverse trend, decreasing with increasing radial position (Figure 4-23 (d), Figure 4-24 (d)). These results also reflect the corresponding porosity gradients revealed through FIB-SEM tomography. As in the unirradiated sample, small  $I_D/I_G$  ratios correspond to regions of high porosity (Figure 4-23 (a-b), Figure 4-24 (a-b), and Figure 4-25 (a-b)). These observations reveal that near the pores, the crystallite size is larger—likely originating from the large globular structures produced during deposition. In all three irradiated samples, the crystallite size is low and the defect density is high near the kernel (Figure 4-23 (b-d), Figure 4-24 (b-d), and Figure 4-25 (b-d)). This suggests that a large amount of radiation damage is concentrated in the pyrocarbon nearest the kernel.

The Capsule 2 sample differs from the other two irradiated samples (Figure 4-25), in that clear gradients in crystallite size and defect density do not exist. The crystallite size generally increases until  $\sim 35 \mu\text{m}$  where it reaches a maximum and then decreases. The defect density follows the opposite trend. The peak in crystallite size at  $\sim 35 \mu\text{m}$  corresponds to a band of high porosity seen in the SEM image of the sample cross section (Figure 4-25(a)). However, the decrease in crystallite size after this point breaks the trend of increasing porosity with increasing radial distance. The absence of a clear gradient follows the microstructural characterization of the Capsule 2 particles (high temperature and fluence, Figure 4-18 (d)). This points to extreme micro- and nanostructural changes due to high temperature and fluence.

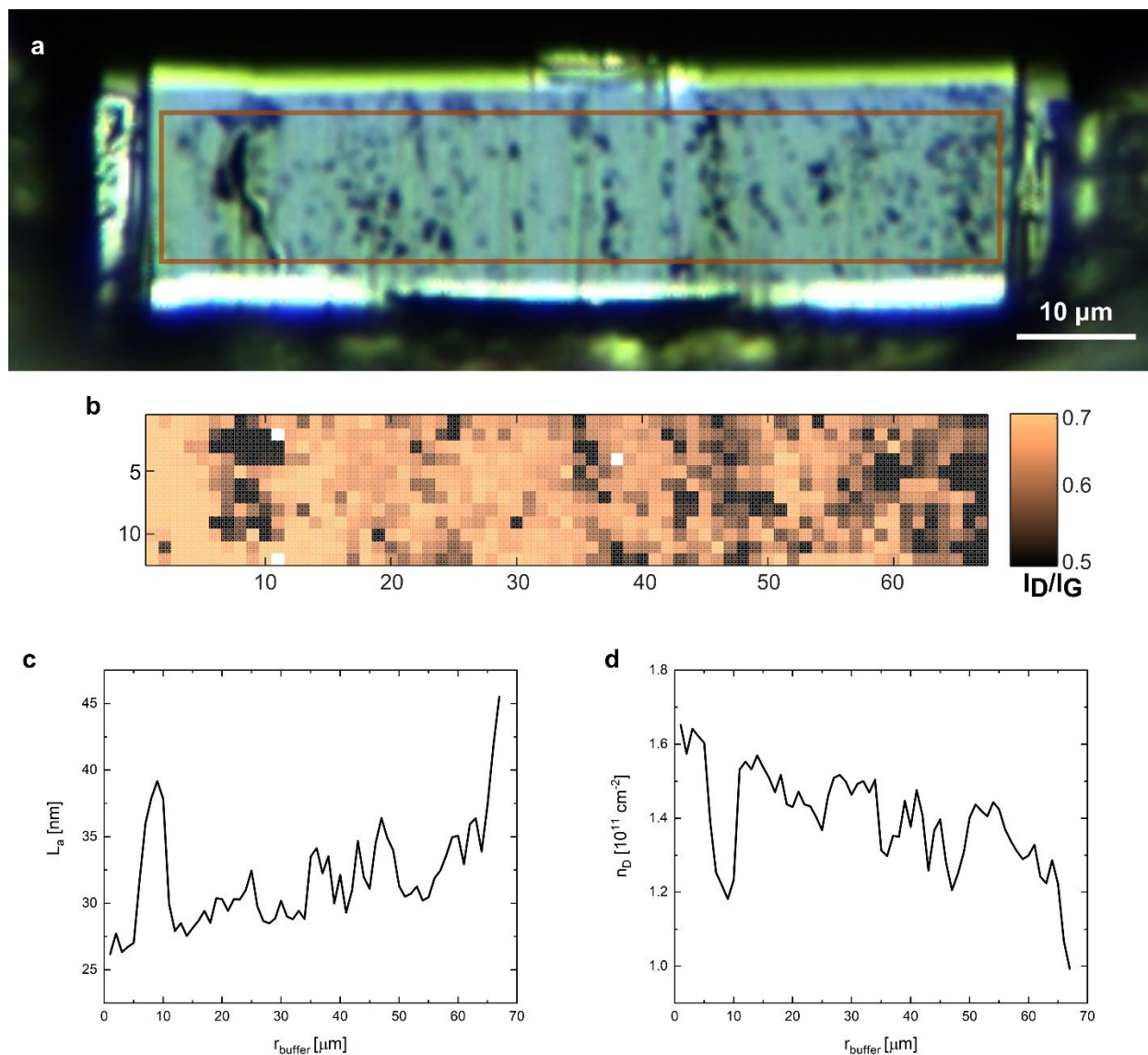


**Figure 4-23: ID/IG ratio analysis of a buffer cross-section from a Capsule 6 particle (low temperature and fluence)** (a) optical microscope image of buffer cross-section with Raman map area identified, (b) color map showing spatial variation of ID/IG ratio, (c) average crystallite size ( $L_a$ ) as a function of radial position in the buffer, (d) average point defect concentration as a function of radial position in the buffer.



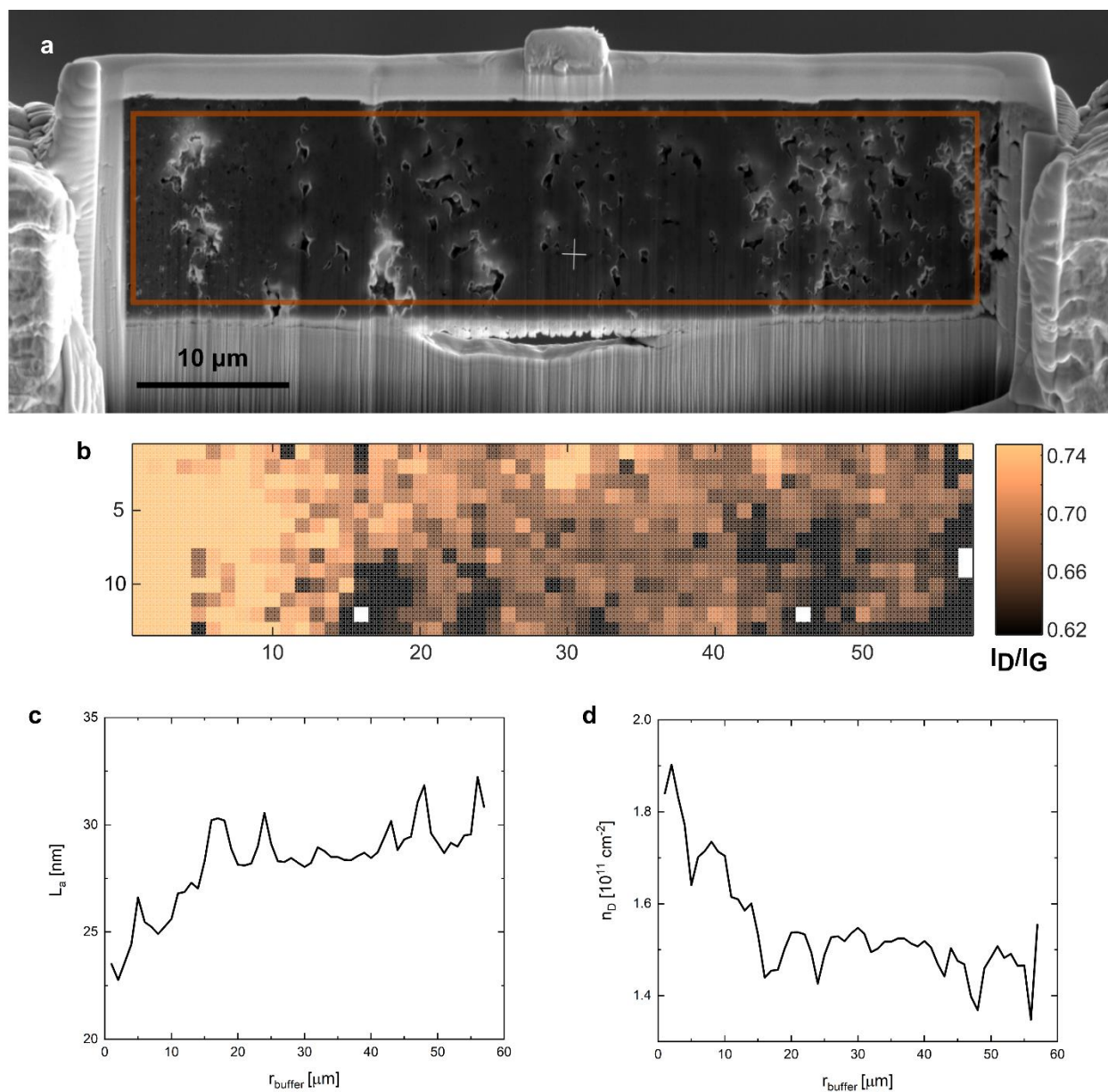


**Figure 4-24: ID/IG ratio analysis of a buffer cross-section from a Capsule 5 particle (low temperature and high fluence)** (a) SEM image of buffer cross-section with Raman map area identified, (b) color map showing spatial variation of ID/IG ratio, (c) average crystallite size ( $L_a$ ) as a function of radial position in the buffer, (d) average point defect concentration as a function of radial position in the buffer.

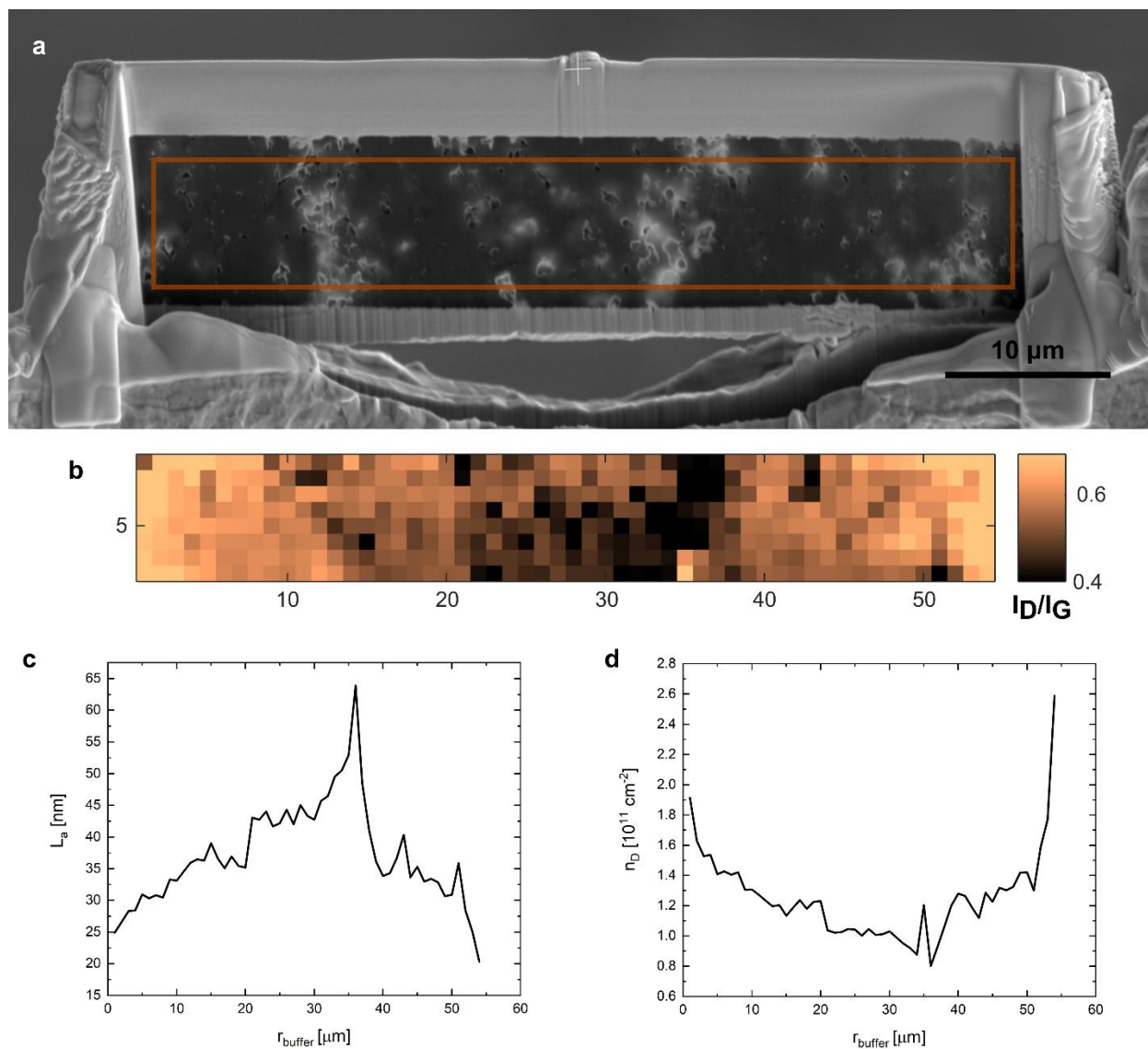


**Figure 4-25: ID/IG ratio analysis of a buffer cross-section from a Capsule 2 particle (high temperature and high fluence)** (a) SEM image of buffer cross-section with Raman map area identified, (b) color map showing spatial variation of ID/IG ratio, (c) average crystallite size ( $L_a$ ) as a function of radial position in the buffer, (d) average point defect concentration as a function of radial position in the buffer.



#### 4.4.3 Changes in the interplanar spacing of graphene sheets due to irradiation

Another feature in the Raman spectrum is the full width at half maximum of the G peak ( $G_{FWHM}$ ), which corresponds to the interplanar spacing of the graphene planes. From x-ray diffraction and Raman spectroscopy measurements, increasing  $G_{FWHM}$  has been associated with increasing interplanar spacing ( $d_{002}$ ) of the graphene layers [247]. We study the distribution of  $G_{FWHM}$  in the unirradiated and irradiated samples to assess the degree of graphitization.

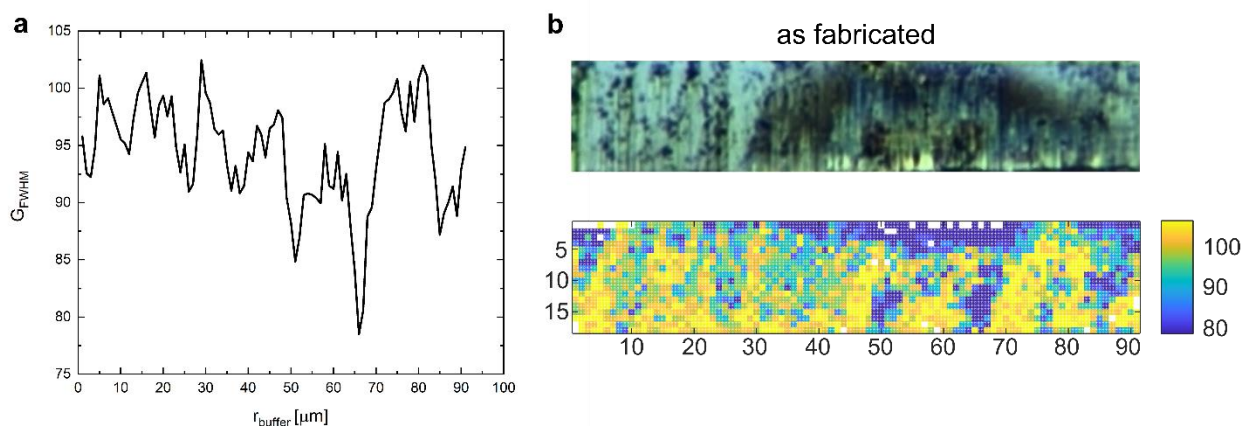


**Figure 4-26:  $G_{FWHM}$  measurements of an unirradiated sample (a) average  $G_{FWHM}$  vs radial position, (b)  $G_{FWHM}$  map.**

There is no clear trend in the  $G_{FWHM}$  data of the unirradiated sample with respect to the radial position (Figure 4-26 (a)), revealing that the interplanar spacing in the deposited pyrocarbon does not consistently increase or decrease with increasing distance from the kernel. A few regions of low  $G_{FWHM}$  on the map can be correlated with regions of high porosity from the optical image (Figure 4-26 (a)). This suggests that the interplanar spacing tends to be smaller near pores. This correlation is even more apparent in the irradiated samples. Low  $G_{FWHM}$  values correspond to regions of high porosity at  $\sim 20 \mu m$  in the Capsule 6 sample (Figure 4-27 (b)),  $\sim 45\text{--}50 \mu m$  in the Capsule 5 sample (Figure 4-28 (b)), and  $\sim 35 \mu m$  in the Capsule 2 sample (Figure 4-29 (b)). In all

three irradiated samples, there is a region of high  $G_{FWHM}$  closest to the kernel. We already know that the defect density is higher in this region and the crystallite size is smaller. These observations, along with the high  $G_{FWHM}$  associated with large interplanar spacing, suggest a very disordered pyrocarbon structure in these neighboring regions to the kernel. Highly disordered pyrocarbon is likely a result of extreme neutron radiation damage. This apparent damage zone extends farther into the buffer layer of the Capsule 5 sample (Figure 4-28 (b)) than the Capsule 6 (Figure 4-27 (b)) or Capsule 2 (Figure 4-29 (b)) samples. Interestingly, despite radiation damage, the  $G_{FWHM}$  values in the irradiated samples are consistently lower than in the unirradiated sample: decreasing  $G_{FWHM}$  suggests irradiation-induced graphitization has occurred.

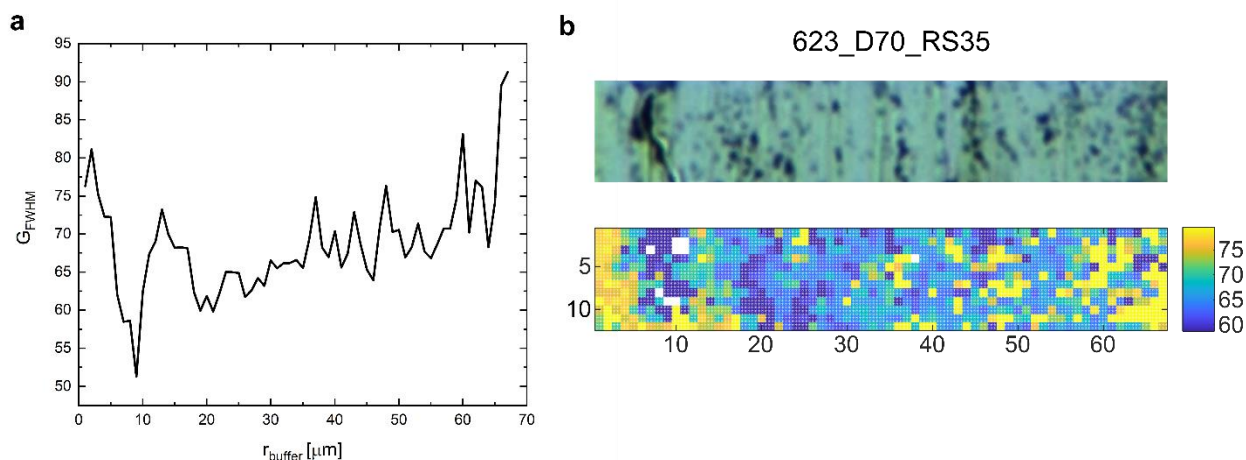


**Figure 4-27: G<sub>FWHM</sub> measurements of a buffer sample from a Capsule 6 particle (a) average G<sub>FWHM</sub> vs radial position, (b) G<sub>FWHM</sub> map.**

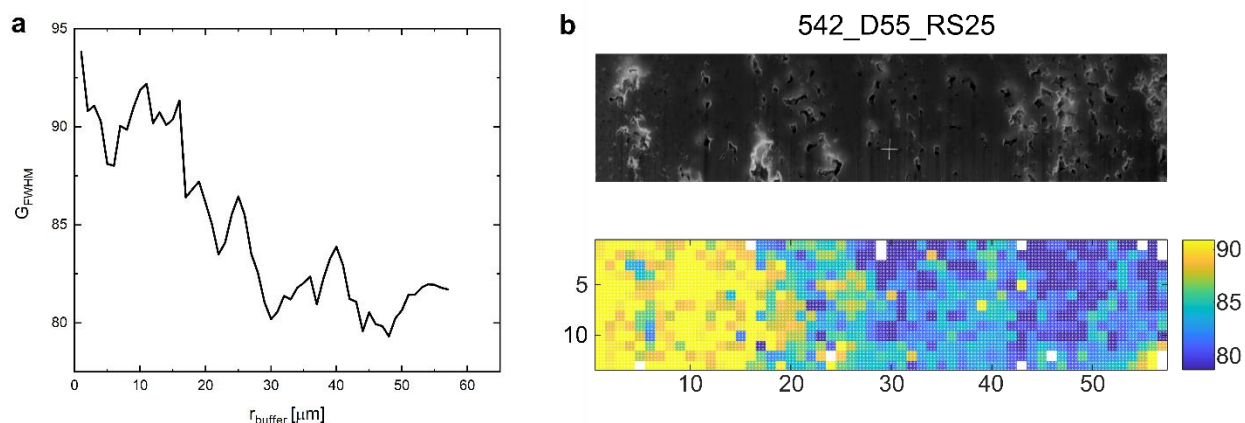


**Figure 4-28: GFWHM measurements of a buffer sample from a Capsule 5 particle (a) average GFWHM vs radial position, (b) GFWHM map.**

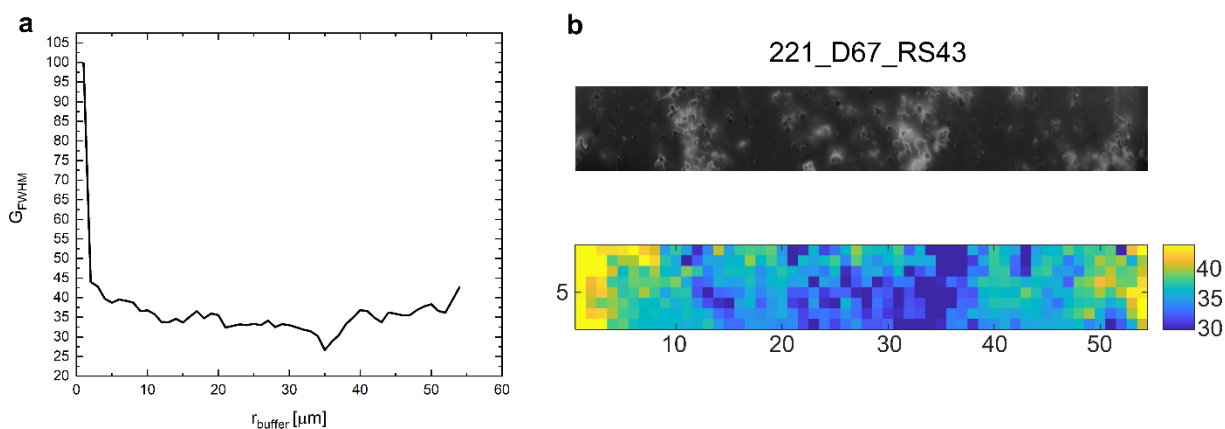


**Figure 4-29: GFWHM measurements of a buffer sample from a Capsule 6 particle (a) average GFWHM vs radial position, (b) GFWHM map.**

#### 4.4.4 Nanostructural changes contributing to densification

The crystallite size and  $G_{\text{FWHM}}$  (interplanar spacing) data provide key insights into the irradiation-induced nanostructural changes which partially accommodate buffer densification. The average crystallite size ( $L_a$ ) and  $G_{\text{FWHM}}$  are plotted for each sample in Figure 4-30. Compared to the as fabricated buffer sample, all irradiated samples have larger average crystallite sizes and

lower  $G_{FWHM}$ , indicating irradiation-induced graphitization occurs. Out of all the irradiated samples the Capsule 2 sample (Compact 2-2-1) has the largest crystallite size and the lowest  $G_{FWHM}$ . The most extensive nanostructural changes occur in the sample exposed to the highest temperature and neutron fluence. Likely driven by high-temperature enhanced irradiation creep, the extreme nanostructural changes in this sample accommodates the high densification reported in Capsule 2 samples (Figure 4-20 (a)). In fact, if the interplanar spacing is assumed to be directly proportional to the  $G_{FWHM}$ , the >50% decrease in the  $G_{FWHM}$  of the Capsule 2 sample compared to the as fabricated sample fully accounts for the densification of the buffer layer.

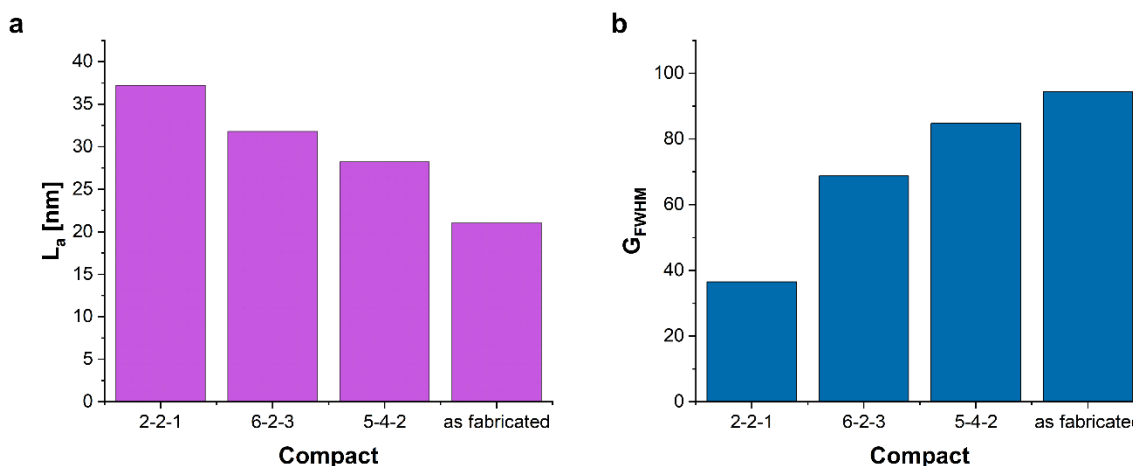


**Figure 4-30: Average crystallite size (a) and  $G_{FWHM}$  (b) for each sample**

The Capsule 5 sample exhibits the least differences in average  $L_a$  and  $G_{FWHM}$  compared to the as-fabricated particle. As hypothesized previously, this shows that fewer nanostructural changes occur within the buffer layer of Capsule 5 particles. Irradiation creep is likely less prevalent in these samples due to the lower TAVA temperatures. Therefore, pronounced nanostructural changes do not occur and radial fracture is more prevalent.

While the Raman data provides key insights into the nanostructural changes which may accommodate densification, TEM analysis provides visual evidence of these changes. Although

the TEM work is ongoing and will be included in future publications, the bright field TEM images in Figure 4-31 provide a preview of the dramatic irradiation-induced structural changes. In Figure 4-31 (a) we can see the formation of long ordered crystallite domains. Bright regions near these large crystallite domains are likely gaps or nano porosity formed because of graphene plane alignment and restructuring. Figure 4-31 (a) shows the formation of large onion structures with highly aligned concentric graphene fringes. These onion structures were likely formed from the as-deposited globular structures. This initial TEM analysis confirms several of the observations made through Raman spectroscopy: irradiation causes graphitization of the pyrocarbon, and this is especially prevalent near the pores because of the arrangement of graphene planes within globular features to form onion structures.

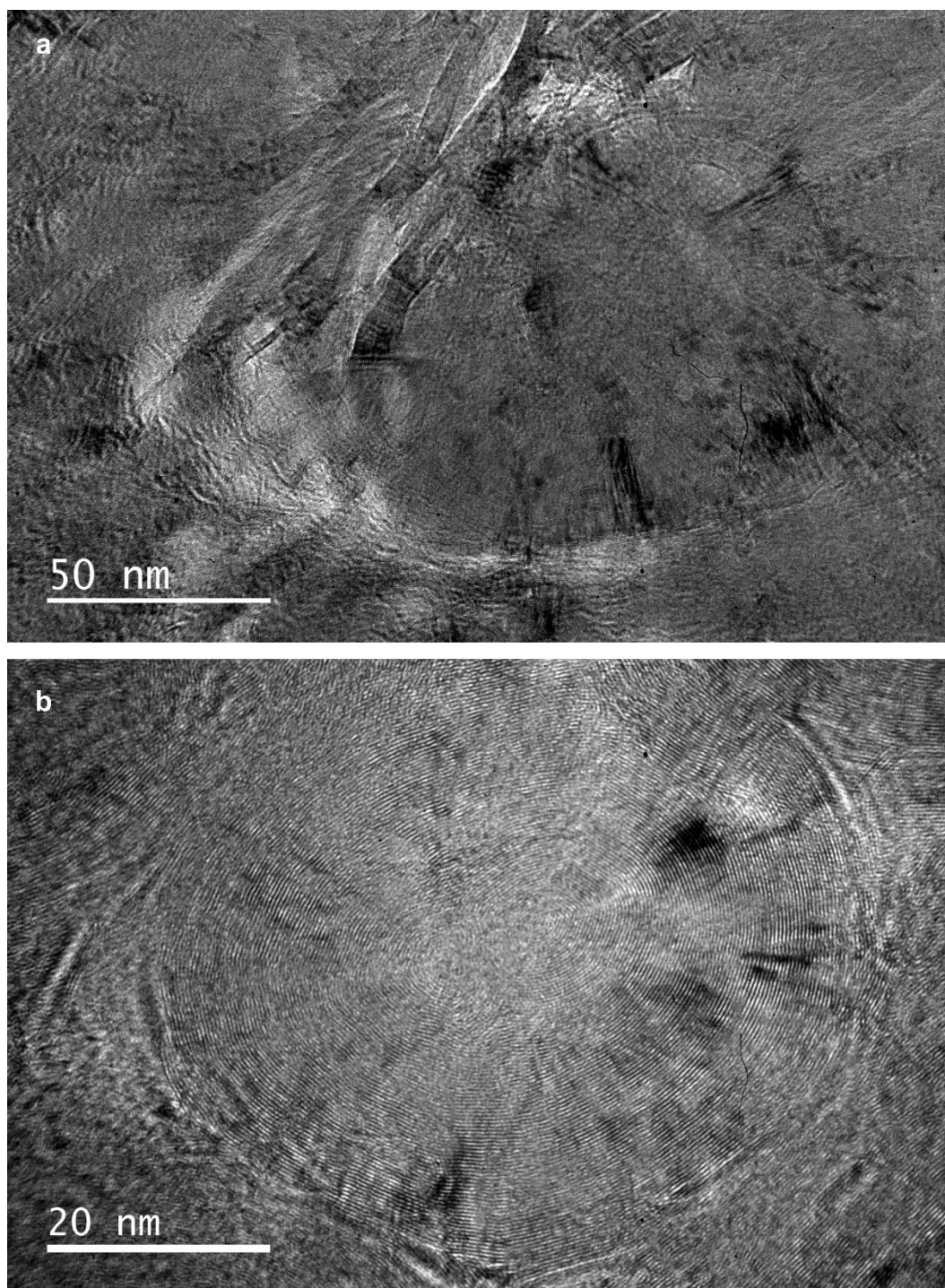


**Figure 4-31: Bright field TEM images of the buffer close to the kernel within a Capsule 6 particle**

## 4.5 Conclusion

The work presented in this chapter provides a fundamental understanding of the process-structure-property relations governing the fracture and densification behavior of the porous pyrocarbon buffer layer in TRISO nuclear fuel particles. Through extensive microstructural characterization of the porous pyrocarbon buffer layer in surrogate TRISO particles, we provide a basis for the initial as-fabricated state. We examine the heterogeneities in the pore structure within the same particle and between particles. In the radial direction, there is a gradient of increasing porosity with increasing radial distance in the buffer layer. This gradient is attributed to the unchanged deposition conditions with increasing particle diameter during the fluidized bed chemical vapor deposition process. The cyclic flow of the particles during the deposition process explains the large and periodic fluctuations in porosity throughout buffer layer in the radial direction. Since the exact deposition conditions (depending on particle and gas flow dynamics) cannot be replicated for each particle, there is some particle-to-particle variability in the porosity distributions. However, all particles show high porosity near the buffer-IPyC interface. Additionally, the average porosity in each particle is consistently around 14.7% (standard deviation of 3.8%). This microporosity does not account for the low density of the buffer (50% theoretical density). With an average microporosity of 14%, the estimated density of the pyrocarbon matrix is 1.31 g/cc or ~58% of the theoretical density of graphite.

The heterogeneous distribution of porosity, pore shape analysis, and mechanical testing provide insights into the potential fracture modes of the buffer layer. Pore shape analysis reveals that pores tend to be elongated along the circumferential directions. This, along with the knowledge that the porosity peaks close to the buffer-IPyC interface, provides strong evidence for the circumferential tearing mode that commonly results in most, if not all, of the buffer being

separated from the IPyC layer during irradiation. The porosity gradient also seems to affect the mechanical properties, as higher yield strengths are attained in both radially and circumferentially compressed pillars positioned at larger radial distances (higher porosity). Although the correlation between higher yield strength and higher porosity is counterintuitive, we expect that the higher porosity allows for enhanced elasticity in the pyrocarbon nanostructure, thereby deferring yielding.

The microstructural characterization of unirradiated buffer provides a firm basis of comparison to determine the irradiation-induced changes in the microstructure. FIB-SEM tomography experiments are conducted on the buffer layer of TRISO particles irradiated under varying temperatures and fast neutron fluences. We find that the most dramatic microstructural changes occur in particles exposed to high temperature and high fluence. The porosity gradient seen in the as-fabricated buffer layer disappears, and large fluctuations in porosity are present throughout the sample. The lack of a gradient reveals that densification through changes in the microstructure is not localized but occurs throughout the buffer layer. In contrast, localized densification occurs in particles under relatively low temperatures (Capsule 5 and Capsule 6 particles). In these particles, localized densification occurs through closing of micropores in the buffer near the kernel. A temperature-dependent process—such as kernel expansion, fission product transport, or radiation damage—could control this localized densification. These particles also show steep gradients of increasing porosity with increasing radial distance. The porosity closer to the IPyC layer is higher in the Capsule 5 particle than the as-fabricated particle, revealing that pore expansion may have occurred. The Capsule 5 (low temperature, high fluence) particles have the largest average porosity, which correlates well to the high radial fracture fraction in these particles.



We find that the average porosity changes only account for a small proportion of the total densification in the buffer layer, revealing that nanostructural changes must accommodate the majority of the densification. Raman spectroscopy analysis reveals that the crystallite size in the basal plane direction ( $L_a$ ) increases and the interplanar spacing of the graphene layers decreases due to irradiation. These two parameters indicate graphitization of the pyrocarbon. This process would result in a net volume reduction, largely contributing to densification. The Capsule 2 samples, which exhibit the highest degree of densification, show the largest crystallite size and smallest  $G_{FWHM}$  (corresponding to interplanar spacing)—pointing to the extreme nanostructural changes which accommodate the high densification in these samples. Preliminary TEM results confirm the Raman results and reveal the formation of highly ordered onion structures. These onion structures are thought to result from graphitization of globular features formed during deposition. These onion structures are expected to be larger and more prevalent near the pores, which explains the increased graphitization near pores as seen in the Raman maps. These key findings from the nano- and microstructural characterization of irradiated particles provide a fundamental understanding of the irradiation condition dependent fracture and densification behavior of the TRISO buffer layer.

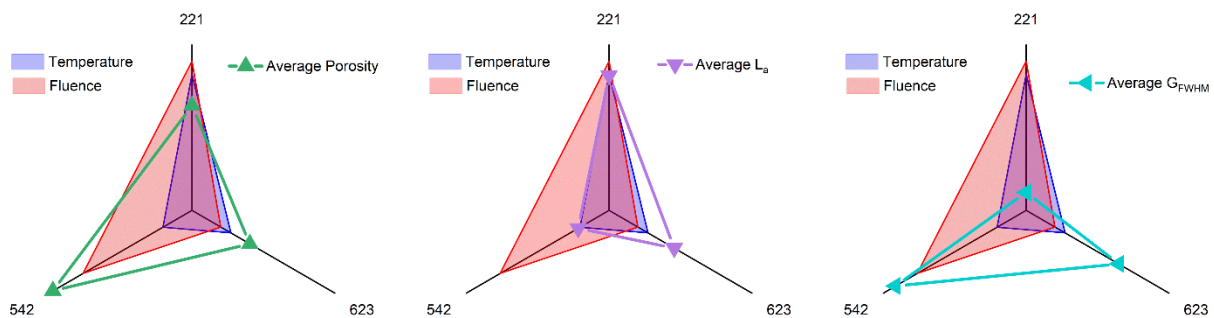


**Figure 4-32: Dependence of micro and nanostructural changes on the irradiation conditions**

# ***Chapter 5. Contributions and future work***

## **5.1 Summary of key findings**

### *5.1.1 Research Thrust I: Improving mechanical properties through impact-induced nanostructural evolution of initially single crystal metals*

The key findings from the work presented in Chapter 3 which complete the research objectives outlined in Section 1.1.1 are summarized below:

**I-1. Determine the rate-dependence on the plasticity of silver single crystals through investigating the two distinct strain-rate regimes of quasi-static compression and high velocity impact.**

- i. Single crystal Ag microcubes remain single crystal when compressed quasi-statically along the  $\langle 100 \rangle$  crystallographic direction but undergo extensive recrystallization and a martensitic phase transformation when impacted along the  $\langle 100 \rangle$  crystallographic direction with a strain rate of  $\sim 10^8 \text{ s}^{-1}$ .
- ii. Dislocations are nucleated simultaneously from all top and bottom corners of the sample when defect-free nanocubes are loaded quasi-statically, while introducing external or internal defects causes heterogeneous dislocation nucleation to occur at lower stresses. The same slip systems are active during high-velocity impact of  $[100]$  oriented microcubes, but dislocation nucleation follows the shock wave propagation and reflection—generating a gradient of dislocation density.

**I-2. Determine the roles that the shock conditions, the free surfaces, and the crystallographic orientations play on the impact-induced nanostructural evolution.**

- i. Through comparison of nanostructures resulting from the impact of single crystal Ag microcubes and spherical microprojectile impact of Ag substrates, we determined that the crystal orientation primarily governs dynamic recrystallization instead of reflective shock dynamics in the presence of free surfaces. Progressive dislocation nucleation on multiple simultaneously activate slip systems leads to extensive dislocation interaction, crystal rotation, and the eventual formation of high angle grain boundaries.
- ii. The crystal orientation has a pronounced effect on the impact-induced nanostructural evolution. [100]-impacted samples undergo extensive recrystallization and a martensitic phase transformation—resulting in smooth and inversely correlated gradients in grain size and GND density. In contrast, limited grain refinement occurs in [110] and [111] oriented samples impacted at similar velocities.

**I-3. Investigate the effects of impact-induced nanostructural evolution on the resultant mechanical properties.**

- i. An average of over 200% improvement in both strength and toughness is achieved through the impact-restructured samples when compared to the original single crystals and bulk polycrystalline silver.
- ii. Samples with a smooth gradient-nano-grained structure exhibit the highest strain hardening rates.

**I-4. Obtain a mechanistic understanding of heterogeneous deformation induced strengthening.**

- i. The impact-induced heterogeneous nanostructures cause stress and strain gradients to form during subsequent quasi-static compression. Sequential yielding along the gradient results in heterogeneous deformation induced stresses that instill higher compressive stresses in nanograin regions and lower compressive stresses (even turning tensile in some samples) in coarser grained regions.
- ii. Heterogeneous deformation causes uncharacteristic but complementary plasticity mechanisms to emerge. Ultra-high strain hardening is achieved through pronounced dislocation accumulation in coarse-grains. Enhanced ductility within typically brittle nanograin domains is achieved through intergranular mechanisms leading to grain coarsening. The extent to which each of these mechanisms is activated can be tuned through distinct impact-orientation dependent heterogeneous nanostructures.

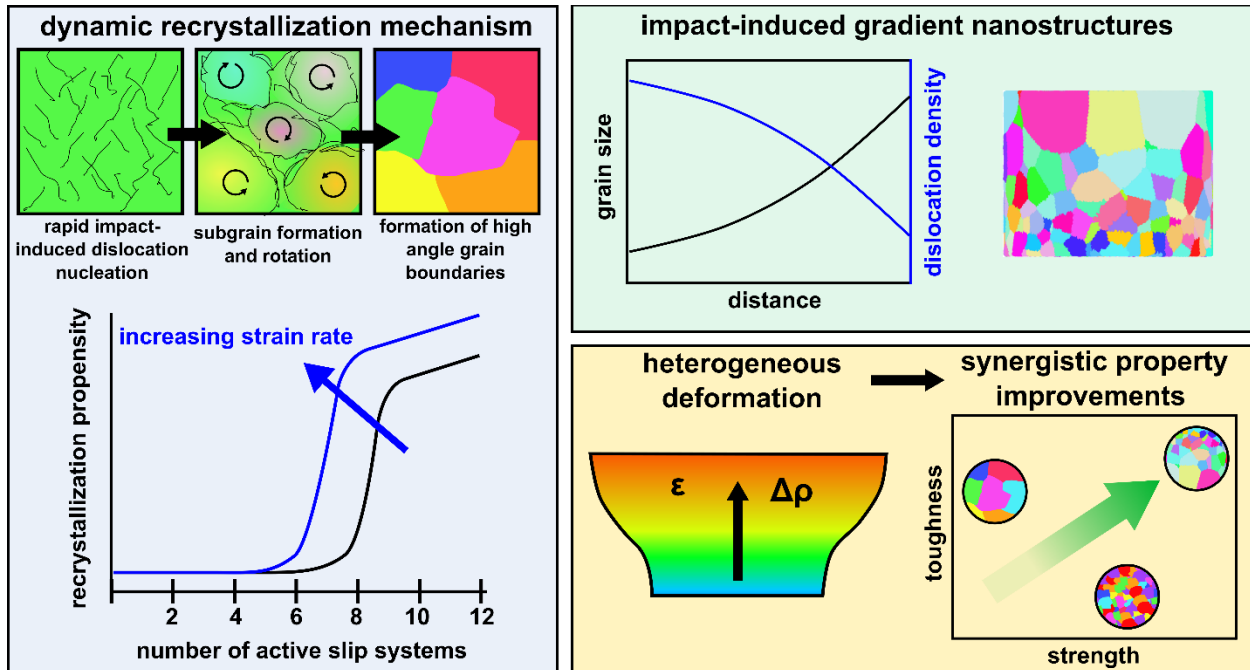


Figure 5-1: Summary of key findings from Research Thrust I

### 5.1.2 Research Thrust II: Investigating the fracture and densification behavior in the pyrocarbon buffer layer of TRISO nuclear fuel particles

The key findings from the work presented in Chapter 4 which complete the research objectives outlined in Section 1.1.2 are summarized below:

#### II-1. Examine the heterogeneity in the synthesized buffer microstructure, and its potential effects on the fracture and densification behavior.

- i. The porosity and heterogeneity in the pore structure increase with increasing distance along the radial direction in the buffer, which is attributed to the deposition process. The increased porosity is mainly driven by the largest pores, which consist of sprawling networks of interconnected voids.

- ii. Characterization of multiple particles shows that the porosity consistently reaches a maximum near the buffer-IPyC interface, which is commonly where circumferential tearing initiates in the buffer layer.

**II-2. Obtain a mechanistic understanding of the anisotropic mechanical behavior, including the effects of structural heterogeneity within the buffer layer.**

- i. The porous pyrocarbon exhibits super-elasticity, as revealed through nanoindentation and microcompression testing. Microcompression tests show that brittle failure is deferred until 10-25% strain. A trend of increasing yield strength with increasing radial position reflects the trend of increasing porosity. We hypothesize that the increased void space allows for enhanced elasticity of the pyrocarbon matrix, thereby deferring yield.
- ii. Pore shape analysis reveals that pores tend to be elongated in the circumferential direction. Pores oriented perpendicular to the loading direction (radial compression) would have higher stress concentration factors, potentially causing yielding at lower applied stresses.

**II-3. Investigate the irradiation-induced micro and nanostructural changes and their contribution to the densification and fracture behavior.**

- i. Densification is partially accommodated through changes in the porous microstructure. However, most of the densification is due to graphitization of the pyrocarbon matrix.
- ii. Circumferential fracture commonly occurs near the kernel-buffer interface, which is correlated to regions of almost zero microporosity and high concentrations of fission products. The high stresses exerted through kernel expansion and radiation

damage likely lead to fracture initiation in this region. Radial fracture is common in particles with high remaining microporosity after irradiation.

#### II-4. Determine the effects of temperature and fast neutron fluence on the structural changes.

- i. Microscale densification located near the kernel is common in particles exposed to relatively lower temperatures, while significant changes in the microporosity occur throughout the buffer layer of particles exposed to high temperature and fluence.
- ii. Particles exposed to high temperatures exhibit the most extensive nanostructural changes. The large increase in crystallite size and decrease in interplanar spacing accommodate the large densification in these samples.

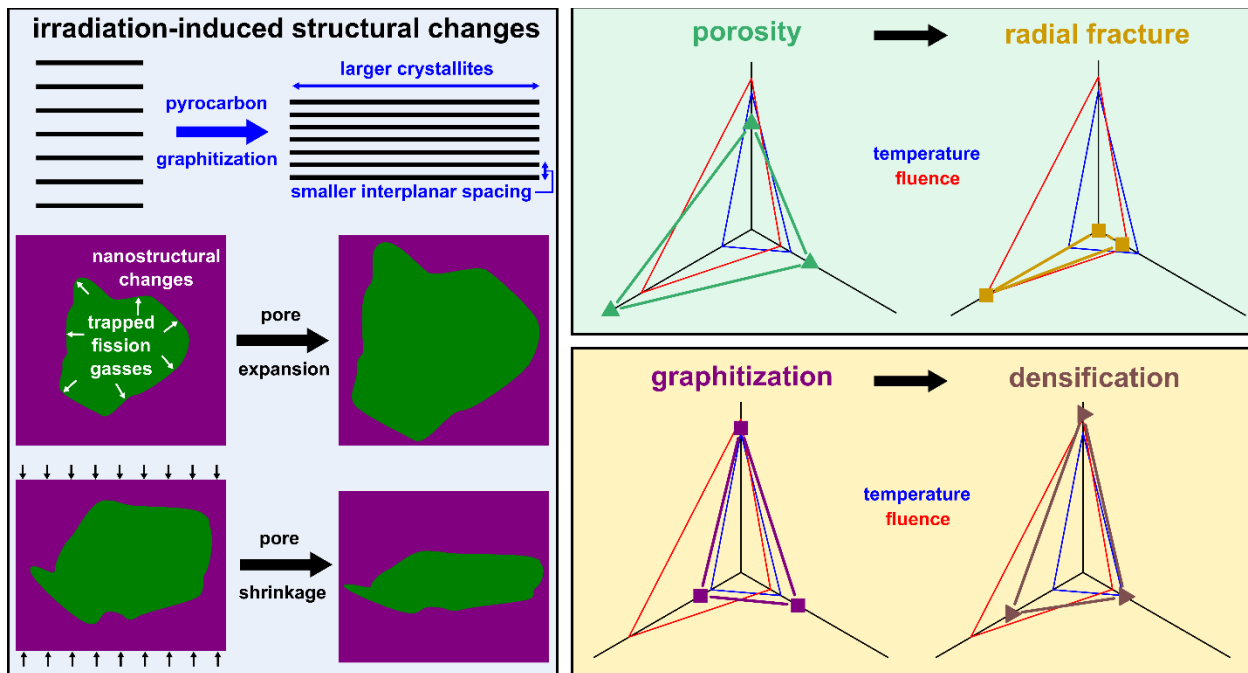


Figure 5-2: Summary of key findings from Research Thrust II

## 5.2 Additional contributions to the fields

In addition to the key research findings presented in the last section, I have made additional contributions to the applicable fields—including developing novel methods and providing valuable new experimental data to inform multi-scale models. A few of these contributions are highlighted here:

1. Development of a robust data analysis workflow incorporating artificial intelligence assisted pore identification and segmentation for porosity characterization of FIB-SEM image stacks where intensity-based grain segmentation is shown to be inaccurate (Section 2.4.5).
2. Application and comparison of novel geometrically necessary dislocation density estimate methods to TKD data of highly deformed nanostructures (Section 2.4.4), and investigation into the accuracy of the calculated magnitudes of GND density through crystal plasticity simulations (Section 2.6.4).
3. Development of a synthetic microstructure generation method capable of producing 3D microstructures with full control over the spatial distribution of grain sizes, grain size extrema, gradient direction, sample shape and dimensions, grain orientations, and dislocation density distribution—which can all be determined through experimental data or specified without experimental input (Section 2.6.3).
4. The large datasets from FIB-SEM tomography of the buffer layer in TRISO nuclear fuel particles (Sections 0 and 4.3) will be made publicly available for other researchers to use. Very little is known about the microstructure of the buffer layer, so such a vast dataset of experimental characterization will be instrumental to future modelling and experimental efforts in the field.



5. Aided in the nanostructural characterization of impacted aluminum substrates, showing the effect of impact-induced dislocation density gradients on the dynamic hardness [169]. These results also reveal that dynamic recrystallization does not occur readily in high stacking fault fcc metals such as aluminum.
6. Aided in the experimental design, data acquisition, and structural characterization for the recently published study investigating the origins of preconditioning in vertically aligned carbon nanotube foams [248].
7. Aided in the experimental quantification of the dynamic performance of nanofiber mats impacted at supersonic speeds [249].

### **5.3 Future work**

Continuation of the research presented in this thesis will provide further insights into the process-structure-property relations of these materials and other material systems. The following work is planned for the immediate future:

1. Investigate the pore shape and orientation changes due to irradiation. Evidence of pore collapse and/or expansion may emerge and could provide further insights into the fracture and densification mechanisms.
2. Complete a deeper analysis of the Raman spectroscopy maps, which may provide information about nanostructural defects—including which types are present and how they are distributed by analyzing the different defect bands in the Raman spectra.
3. Analyze the TEM images, selected area diffraction patterns, and EELS spectra obtained from unirradiated and irradiated buffer samples. Quantify nanostructural features and connect these findings to features in the Raman spectra.

4. Perform crystal plasticity simulations on synthetic microstructures with varied structures to ascertain which gradient nanostructures provide the best mechanical properties. We plan to alter the gradient direction with respect to the loading direction, implement bidirectional gradients, and invert the dislocation density and grain size gradients.

# Appendix A

## A.1 Schmid factor analysis of loading directions in an fcc structure

Schmid factor analysis can be performed to predict which slip planes will be activated first under a given loading direction. The applied normal stress required to initiate slip on a particular set of plane and direction is given by:

$$\sigma = \frac{\tau_{crss}}{m} \quad (\text{A.1-1})$$

where  $m$  is the Schmid factor and is given by:

$$m = \cos \theta \cos \varphi \quad (\text{A.1-2})$$

where  $\varphi$  is the angle between the loading direction and slip plane normal ( $\cos \varphi = \frac{l \cdot n}{|l||n|}$ ), and  $\theta$  is the angle between the loading direction and slip direction ( $\cos \theta = \frac{l \cdot s}{|l||s|}$ ). The lowest required applied stress to initiate slip corresponds to the slip systems with the highest Schmid factors. Therefore, we computed the Schmid factor for each of the 12 fcc slip systems under a [001] loading direction. There are eight slip systems that have the same Schmid factor of ~0.408, which is the maximum value for all 12 slip systems. Thus, these 8 slip systems are equally likely to be activated first under a perfect [001] loading geometry.

The Schmid factors of the slip systems in  $\langle 110 \rangle$  and  $\langle 111 \rangle$  loading of an fcc crystal are also computed. For  $\langle 111 \rangle$  loading, there are 6 slip systems with the maximum Schmid factor of 0.27217. For  $\langle 110 \rangle$  loading, there are 4 slip systems with the maximum Schmid factor of 0.40825.

Next, we investigated what a slight disturbance from perfect  $[001]$  loading geometry would do to the predicted active slip systems. Under a  $[0\ 1\ 100]$  loading direction, which is  $\sim 0.57^\circ$  off from a  $[001]$  loading direction, there are only two slip systems with the same max Schmid factor of  $\sim 0.412$ . There are four slip systems with a slightly lower Schmid factor of  $\sim 0.408$  (same as  $[001]$  loading geometry) and two with a Schmid factor of 0.404. Even this small disturbance from a perfect  $[001]$  loading geometry can result in less slip systems being simultaneously activated, which accommodates the massive strain burst witnessed in some of the quasi-statically compressed cubes.

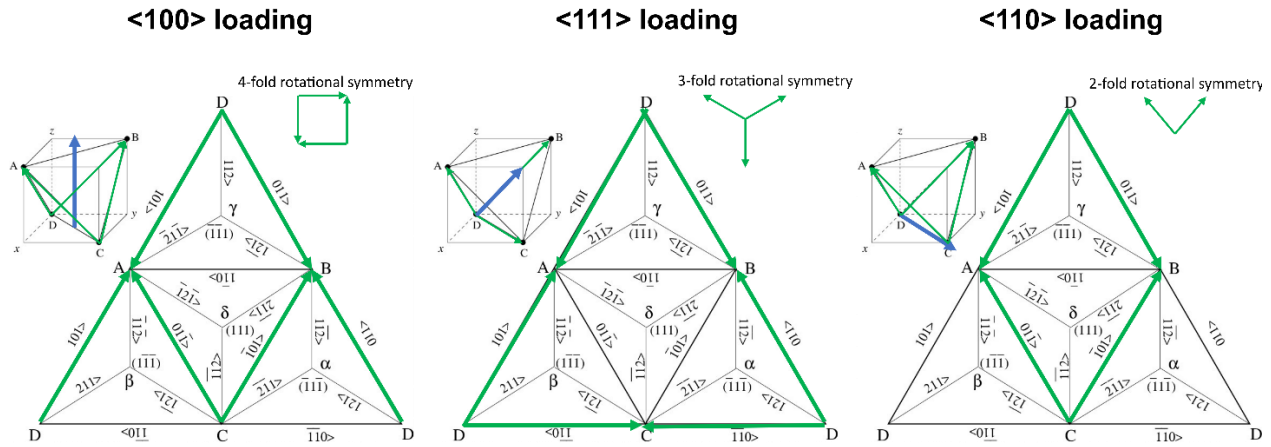


**Figure A - 1: Thompson tetrahedrons of active slip systems for  $\langle 100 \rangle$ ,  $\langle 111 \rangle$  and  $\langle 110 \rangle$  loading in an fcc crystal: active slip systems are shown in green – figure adapted from [250]).**

## A.2 Elastic properties of silver

The elastic constants for silver at room temperature from the Simmons and Wang handbook of Single Crystal Elastic Constants [104] are used for the following calculations. Coordinate transformations can be applied to the compliance tensor to convert from the crystal (reference) configuration to the loading configuration:

$$s'_{ijkl} = a_{im}a_{jn}a_{ko}a_{lp}s_{mnop} \quad (\text{A.2-1})$$

The number of independent elastic constants can be reduced to three in the case of materials with cubic structures and the fourth order tensor can be represented in matrix notation. Thus, the theoretical Young's modulus of a cubic single crystal loaded along the  $[h \ k \ l]$  direction can be determined through the following expression [251]:

$$\frac{1}{E_{[h \ k \ l]}} = s_{12} + \frac{1}{2}s_{44} + \left(s_{11} - s_{12} - \frac{1}{2}s_{44}\right) \left[\frac{h^4 + k^4 + l^4}{(h^2 + k^2 + l^2)^2}\right] \quad (\text{A.2-2})$$

Using the compliance constants for silver at room temperature [104], the Young's modulus in the  $[100]$ ,  $[110]$ , and  $[111]$  directions are calculated to be:

$$E_{[100]} = 43.67 \text{ GPa}, \quad E_{[110]} = 83.61 \text{ GPa}, \quad E_{[111]} = 120.29 \text{ GPa}$$

The shear modulus on the  $\{111\}$  planes in a cubic crystal is given by [252]:

$$G'_4 = \frac{1}{s_{44}} = \left(\frac{3}{1 + 2\left(\frac{2c_{44}}{c_{11} - c_{12}}\right)}\right) c_{44} \quad (\text{A.2-3})$$

which is found to be  $G_{\{111\}} = 19.53 \text{ GPa}$  for silver using the stiffness constants at room temperature [104] for silver.

To compare our data to that found in literature for different sample types and loading directions, we normalized the yield strengths and sample sizes. The yield strengths were normalized by resolving them onto the active slip systems (to find the resolved shear stress) and then dividing them by the shear modulus:

$$\frac{\tau_{res}}{G} = \frac{m\sigma_y}{G} \quad (\text{A.2-4})$$

where  $m$  is the max Schmid factor given by Equation (A.1-2) and determined to be 0.4082 for [001] loading.

To normalize the sample sizes, the effective diameter is divided by the magnitude of the burger's vector:

$$D = \frac{d}{|b|} \quad (\text{A.2-5})$$

where  $|b|$  is computed to be:

$$|b| = \frac{a}{2} |\langle 110 \rangle| = \frac{a}{\sqrt{2}} = \frac{0.4078}{\sqrt{2}} = 0.2884 \text{ nm} \quad (\text{A.2-6})$$

### A.3 Estimates of key parameters of impact deformation [36]

The following are the estimates of the average values of important parameters that describe the high-velocity ( $V = 400 \text{ ms}^{-1}$ ) impact of Ag microcubes (edge length,  $a = 1.4 \times 10^{-6} \text{ m}$ ). Properties of Ag were obtained from the NIST Journal [7]. The approximate impact velocity at which melting would occur is calculated by equating the equations for kinetic energy and melting energy and solving for the impact velocity.

<b>Table B.1: Estimates of the average values of the key parameters of impact deformation</b>		
<b>Parameter</b>		<b>Value</b>
Density, $\rho$ ( $\text{kg m}^{-3}$ )		10490
Mass, $m$ (kg)	$\rho a^3$	$28.78 \times 10^{-15}$
Momentum, $p$ (Ns)	$mV$	$11.5 \times 10^{-12}$
Kinetic energy, $E$ (nJ)	$\frac{1}{2} mV^2$	2.30
Heat capacity, $C_p$ ( $\text{J kg}^{-1} \text{K}^{-1}$ )		240
Latent heat of fusion, $\Delta H_f$ ( $\text{J kg}^{-1}$ )		$111 \times 10^3$
Melting energy of the Ag microcube (nJ)	$\int m C_p dT + m \Delta H_f$	9.65
Average temperature-rise due to impact, $\Delta T$ (K)	$\frac{E}{m C_p}$	333

Average reduction in the height of the sample due to impact, $\Delta h$ (nm)		300
Duration of impact deformation, $t$ (ns)	$\frac{2\Delta h}{V}$	1.5
Nominal strain rate, $\dot{\epsilon}$ (s <sup>-1</sup> )	$\frac{\left(\frac{\Delta h}{a}\right)}{t}$	$1.4 \times 10^8$

#### A.4 Calculation of equilibrium vacancy concentration in silver

We have computed the vacancy formation energy for Ag at 0K using MS. The vacancy formation energy  $V_f$  is given by,

$$V_f = E(N - 1) - \frac{N-1}{N}E(N) \quad (\text{A.4-1})$$

where  $E(N - 1)$  is the energy of the sample containing a vacancy, and  $E(N)$  is the energy of the pristine sample containing  $N$  atoms. Using the interatomic potential, we found that the vacancy formation energy is  $\sim V_f = 1.1$  eV, which agrees well with the monovacancy formation energy of silver stated in literature [253] as  $1.16 \pm 0.02$  eV. Equilibrium vacancy concentration  $c_{eq}$  is then calculated from,

$$c_{eq} = \exp\left(\frac{-V_f}{k_B T}\right), \quad (\text{A.4-2})$$

where  $k_B$  is the Boltzmann constant and  $T$  is the temperature. This leads to an equilibrium vacancy concentration of  $10^{-9}$  at 600 K. However, the concentration of vacancies directly estimated from the MD sample by counting the vacancies in multiple representative volumes is much higher, likely because of the high surface to volume ratio. The estimation gives the number of vacancies in the order of 100-200, which gives a concentration of  $10^{-5}$  at the end of the impact deformation of the sample. It should be noted that even though vacancies are generated, they do not move in the

timescale of the simulation, and therefore, the effect of vacancies during the impact and the dynamic phase transformation is minimal. However, they may have significant effects on the subsequent stress relaxation and recrystallization.



## ***Appendix B***

### **B.1 Stochastic deformation response of quasi-statically compressed single crystal micro- and nano-cubes**

#### ***Strain Burst Magnitudes***

The strain burst can be studied further from the force-time and displacement-time plots (Figure B-1 (b)). The indenter moves at the prescribed constant displacement rate from point (1) to point (2) (corresponding to the linear elastic regime). During the strain burst, the indenter moves quickly with the sample as can be seen from the displacement-time data (points 2-4). We see from the force-time data that the force decreases rapidly during the strain burst (points 2-4) but does not immediately go to zero until point (6). This suggests that the indenter is still doing work on the cube and the entire deformation during the strain burst may not be solely due to the material instability. Ideally, the indenter would not follow the cube and would maintain the prescribed displacement rate. However, since the system is inherently load controlled, a feedback loop is required to run in pseudo-displacement-controlled mode. Consequently, during the dramatic instability of the strain burst, the indenter deviates from the prescribed displacement rate and there is a certain time lag until the feedback loop corrects the indenter position to the subsequent step to where it was before the burst.

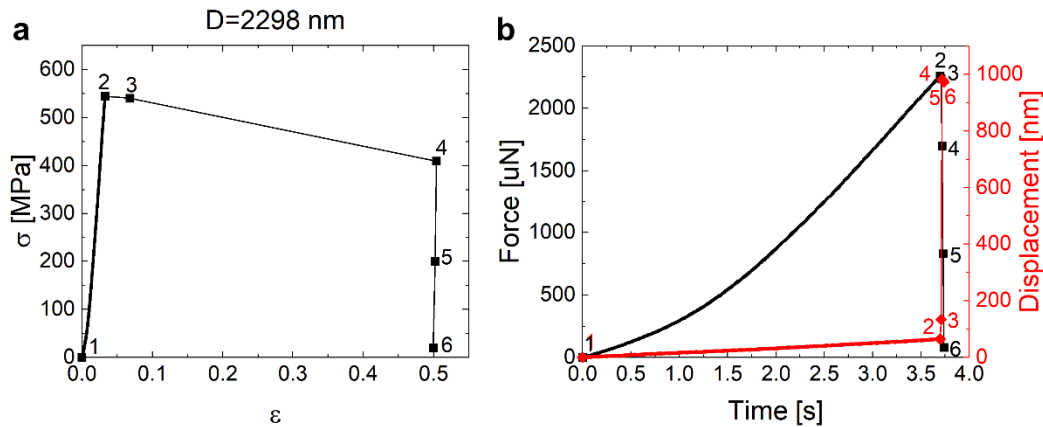


**Figure B-1: Analysis instrument behavior during the strain burst magnitude** (a) stress-strain response of sample in Figure 3-1, (b) corresponding force-time and displacement-time curves

Sample size also appears to play a role in how large the strain burst is. We define the strain burst magnitude as the difference in strain between the on-set of strain burst (yield point) and where the flat punch meets the sample again and begins reloading. As seen in the plot in Figure B-2, as the sample size increases, the strain burst magnitude becomes larger. The stark difference in the strain burst magnitude can also be seen easily with semi-transparent SEM images of the original shape overlaid on the deformed cubes (Figure B-2 (b-c)).

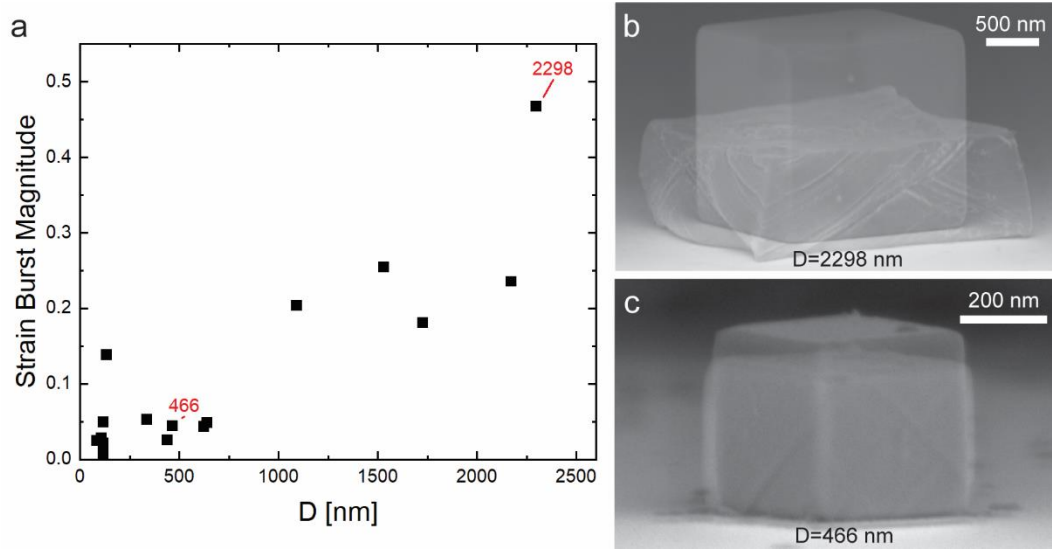
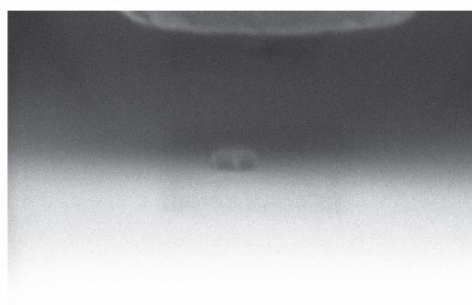
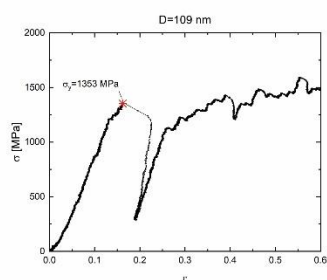
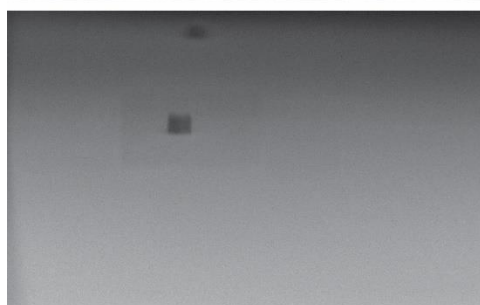
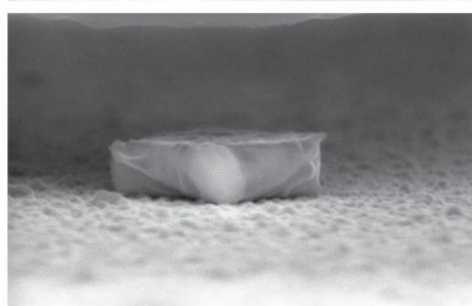
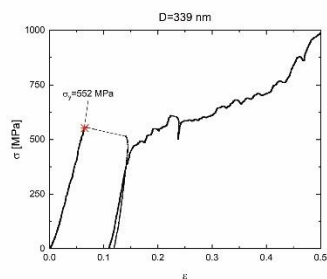
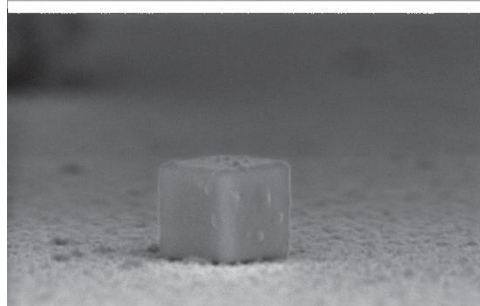
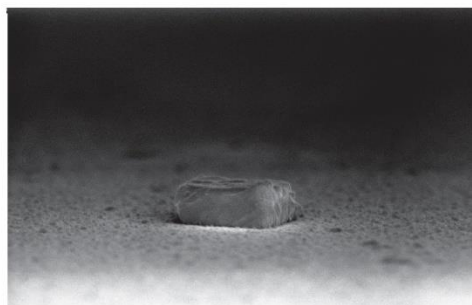
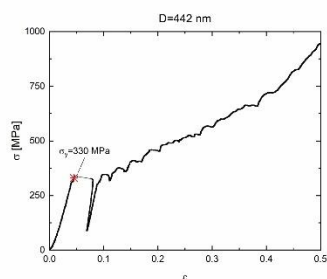
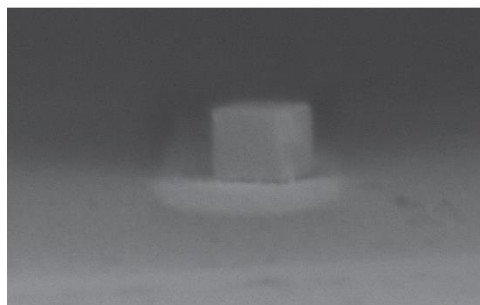
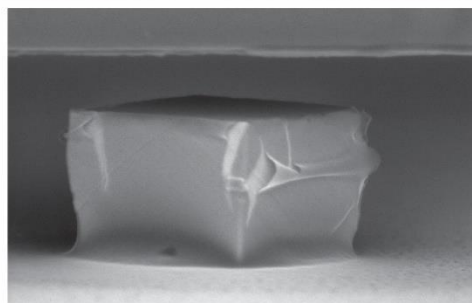
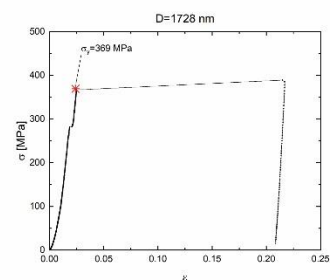
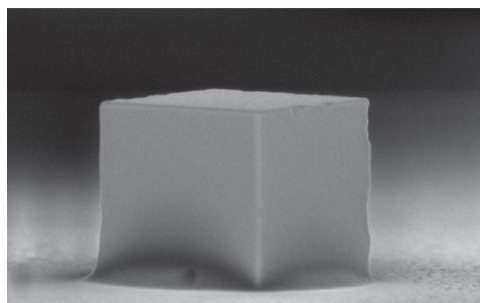
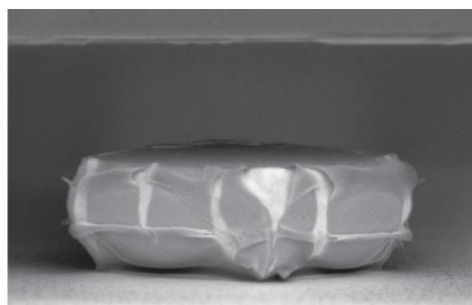
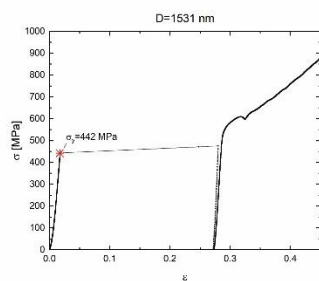
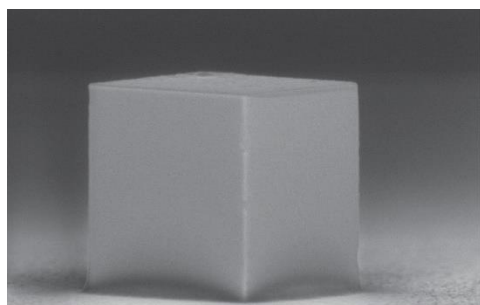


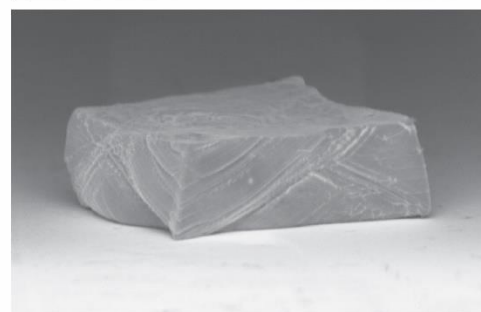
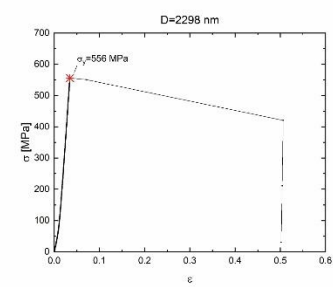
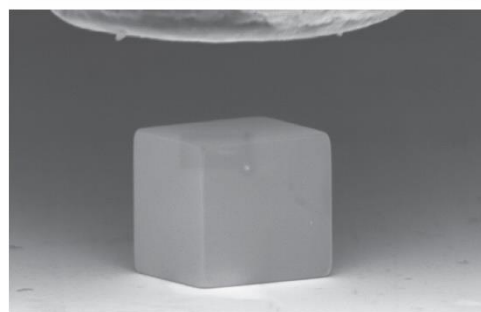
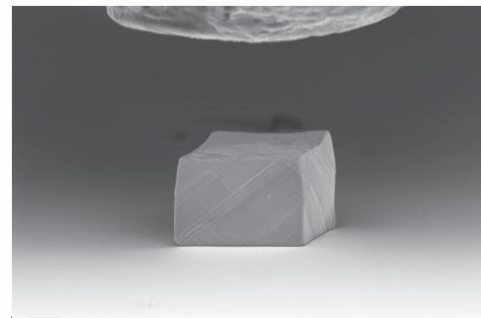
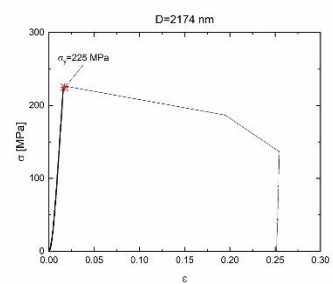
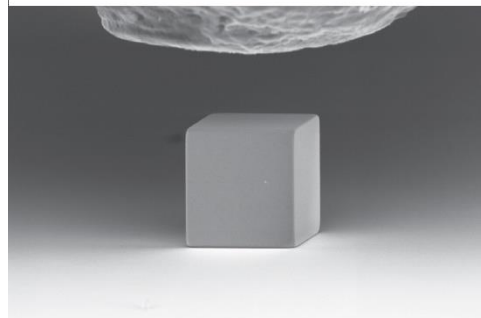
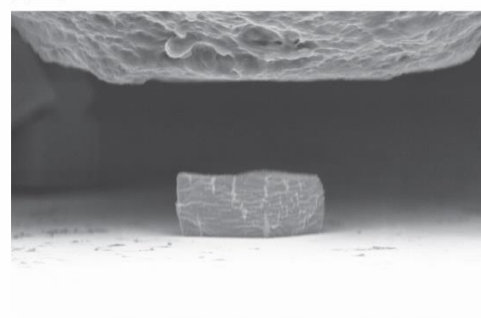
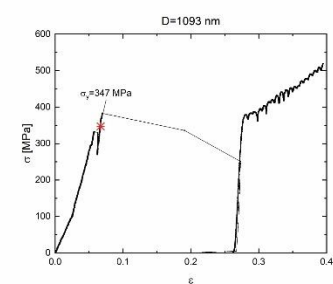
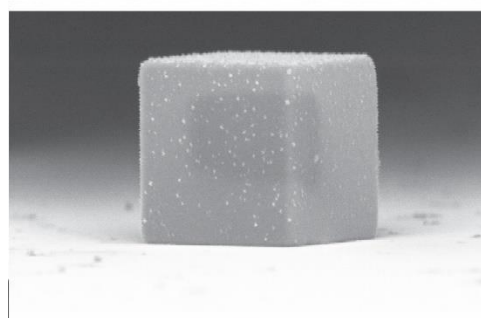
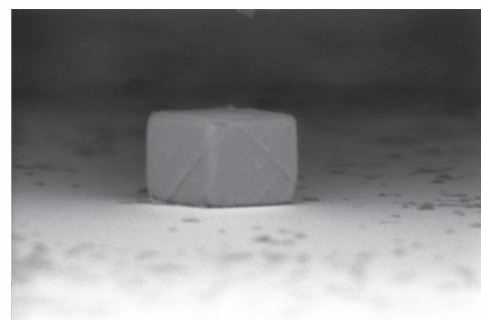
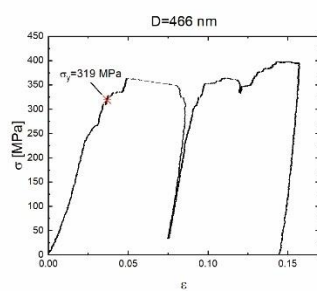
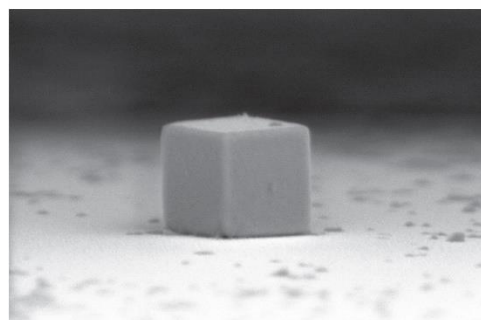
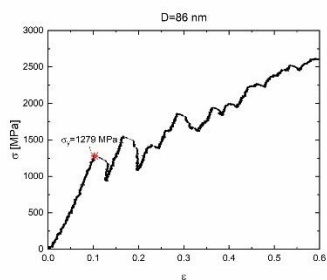
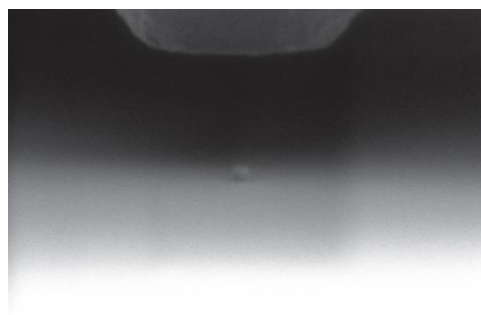
**Figure B-2: Size effect on the strain burst magnitude** (a) strain burst magnitude plotted against sample size, (b) deformed 2298 nm sized sample post strain burst with transparent image of original undeformed sample overlaid—shows much larger strain burst with more slip steps than the smaller sample (c), (c) deformed 466 nm sized sample post strain burst with transparent image of original undeformed sample overlaid.

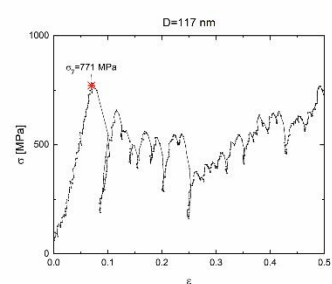
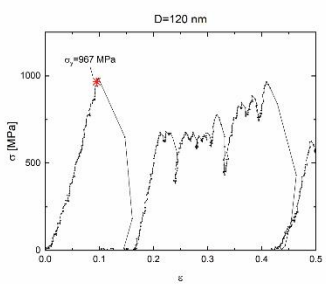
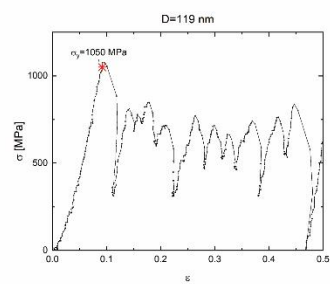
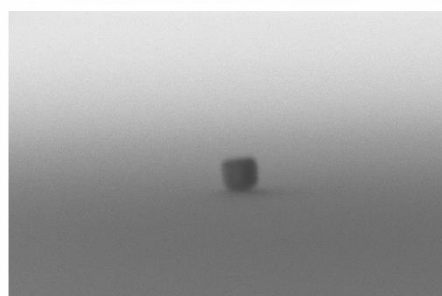
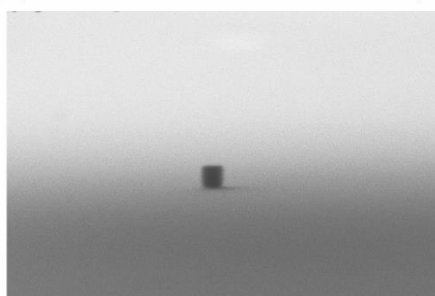
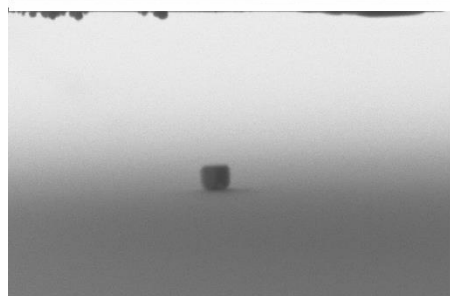
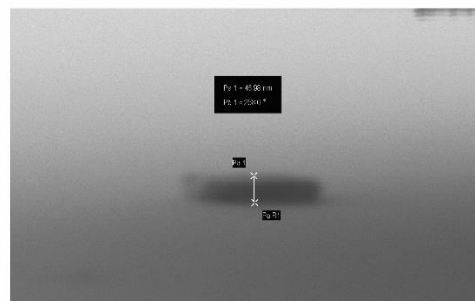
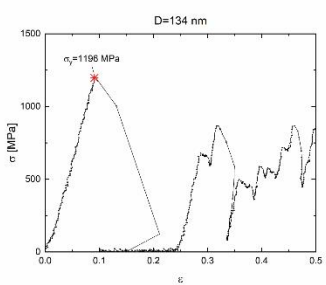
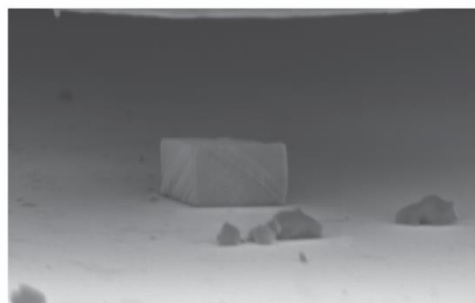
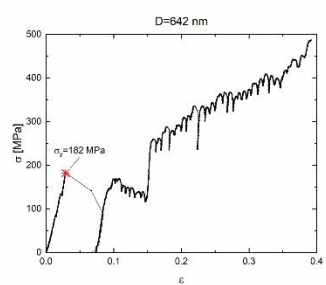
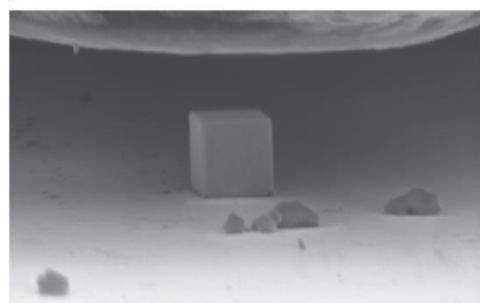
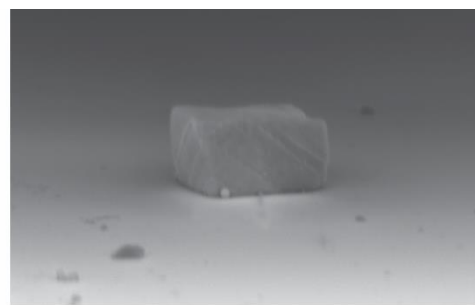
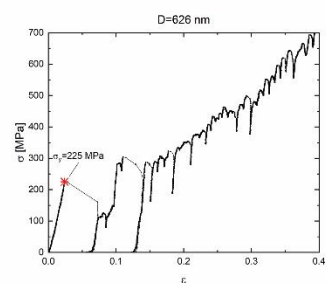
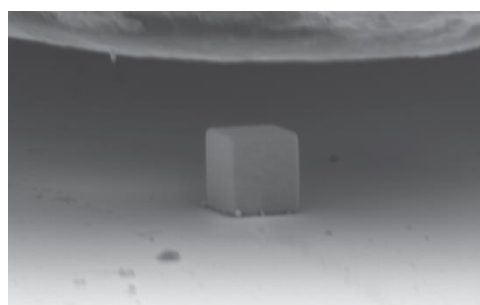
The dislocation nucleation mechanisms described in Section 3.2 could also help to explain this phenomenon. Since larger samples have more sites of high stress concentration—such as surface defects and sharp corners and edges—dislocations are more readily nucleated at lower stress than the smaller samples. A multitude of dislocations are necessary to accommodate slip on multiple planes. An equal strain burst magnitude for larger and smaller samples would already mean that many more dislocations were nucleated in the larger sample since slip would need to occur on more planes. The fact that the largest ( $\sim 2\mu\text{m}$ ) samples exhibit strain burst magnitudes over 10x larger than those of the smallest samples ( $\sim 100\text{nm}$ ) points back to the fact that dislocations are more readily nucleated in larger samples. SEM images taken after the strain burst provide evidence to this hypothesis as the smaller ( $D=466\text{ nm}$ , Figure A-2(c)) sample has fewer slip steps than the larger ( $D=2298\text{ nm}$ , Figure A-2(b)) sample.

However, these observations rely on the strain burst being solely from a dramatic instability in the material, rather than additional work being provided by the indenter during the strain burst. Since the nanoindenter is inherently load controlled, the indenter follows the sample down and appears to exhibit some force on the sample during the strain burst. Therefore, the trend of increasing strain burst magnitude with larger samples could be an artifact of the limitation of the nanoindenter to not have the capability of a truly displacement-controlled mode. It would be interesting to perform similar experiments in a truly displacement-controlled testing device to see if this trend still emerges.

*Details for samples which exhibited a large strain burst*

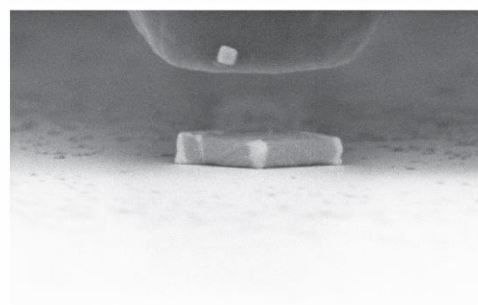
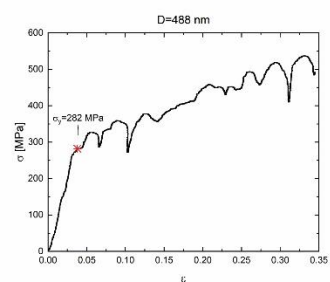
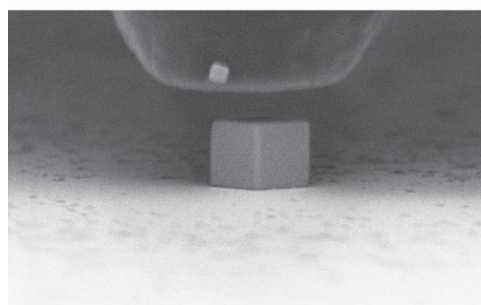
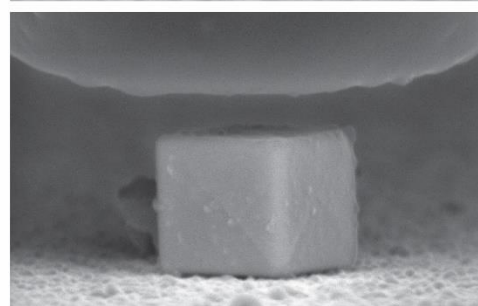
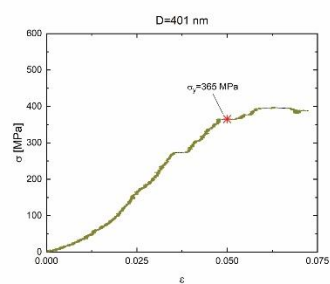
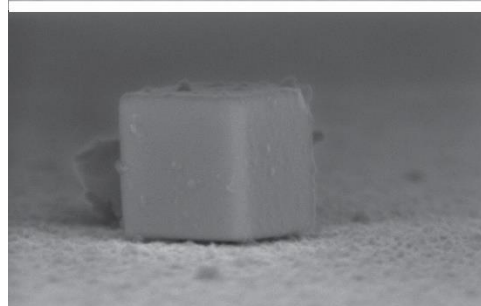
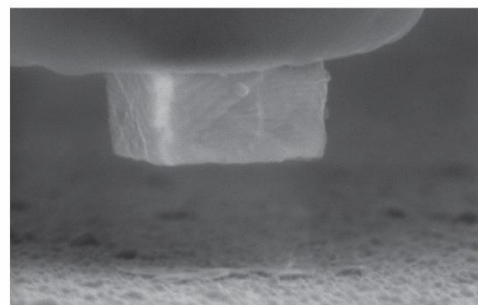
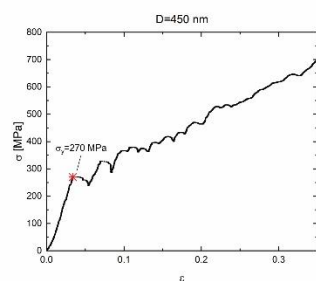
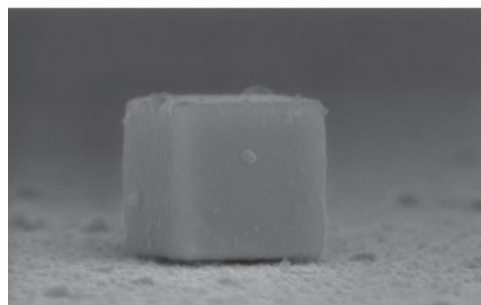
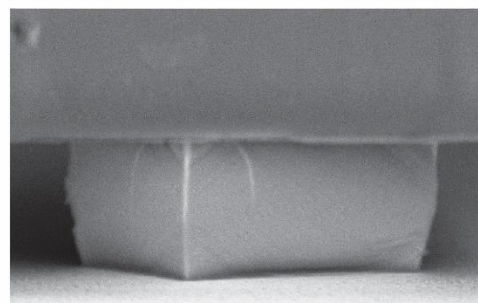
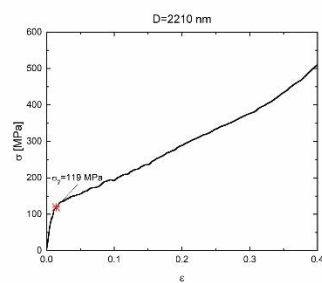
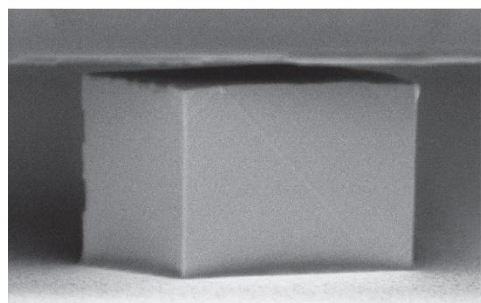
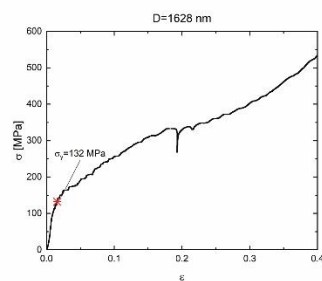
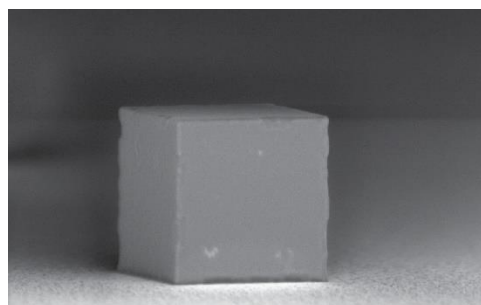




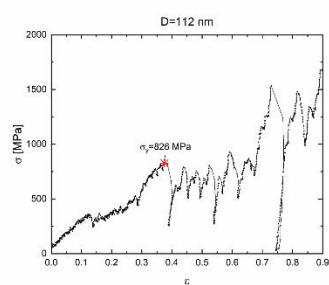
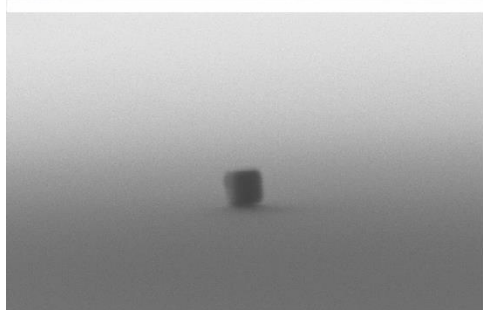
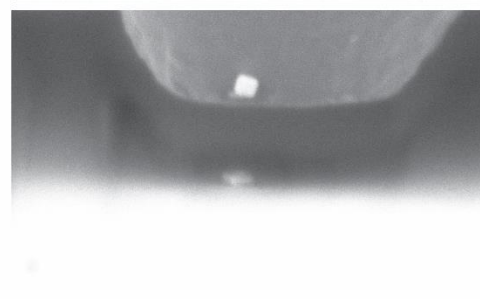
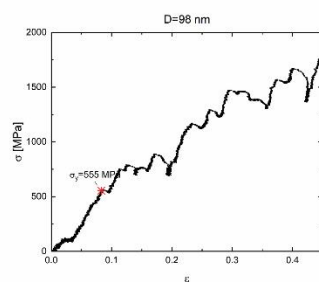
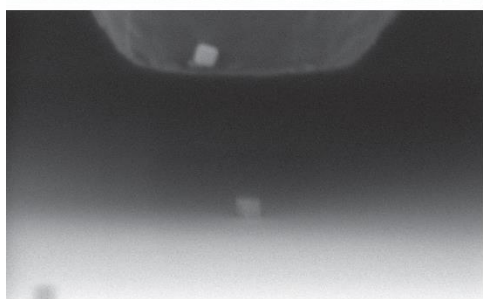
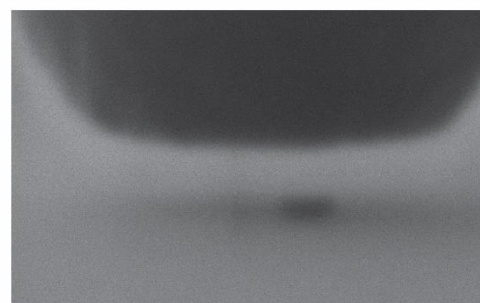
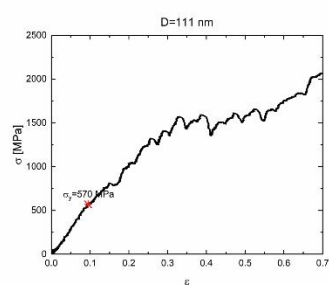
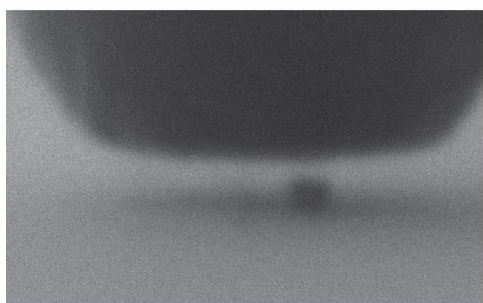
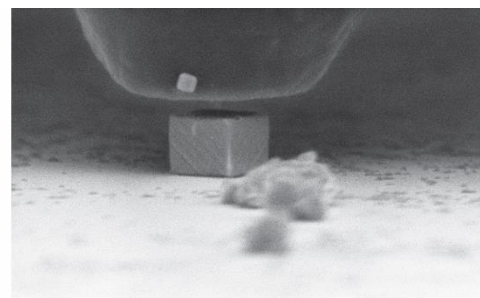
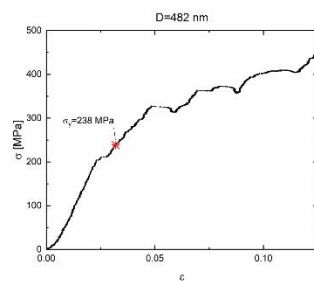
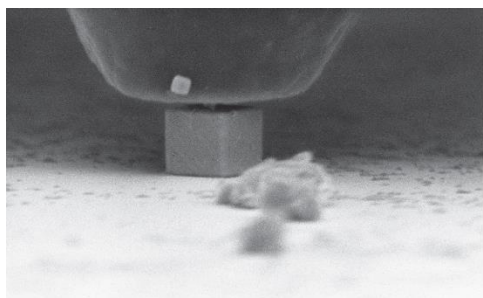




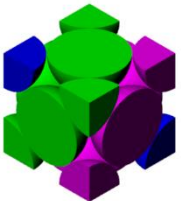
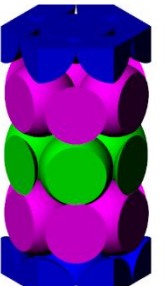
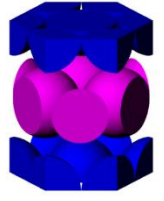
*Details for samples which did not exhibit a large strain burst*







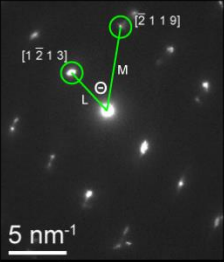
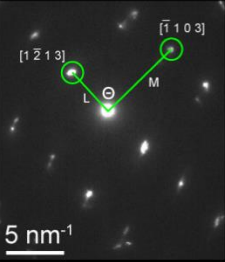
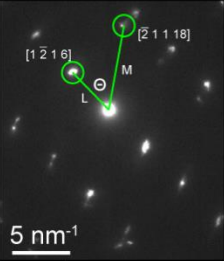
## B.2 Polytypes of Ag – SAD pattern indexing

Table B.1: Physical properties of polytypes of Ag[17]			
Polytype	3C (fcc)	4H (hcp)	2H (hcp)
Unit cell			
Lattice parameter, a (nm)	0.409	0.288	0.283
Lattice parameter, c (nm)	-	1.000	0.638
c/a		3.47	2.25
Density (g cm <sup>-3</sup> )	10.46	9.97	8.09

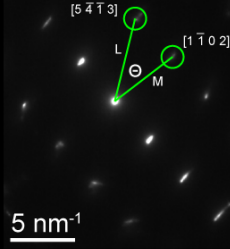
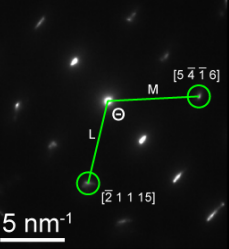
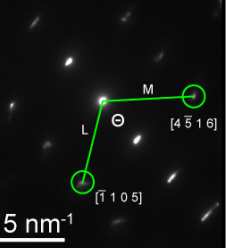
### *Indexing hcp phases in SAD patterns*

Since the hcp grain orientations were not in primary low-order zone axes, after identifying all the possible zone axes, we had to perform detailed error analysis of the error between the theoretical and experimental lattice parameters to identify the most probable zone axes and the associated indexed patterns. Additionally, differentiating between the 4H and 2H phases proved challenging, and the error analysis allowed identifying the 4H pattern to match the experimental SAD patterns consistently at low percent error on lattice distances and angles. These analyses for the three hcp patterns shown in Figure 3-8 (b-d) are given below in Tables B.2-B.4:

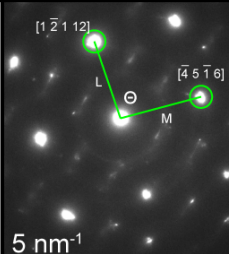
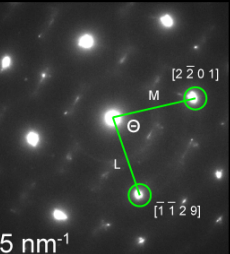
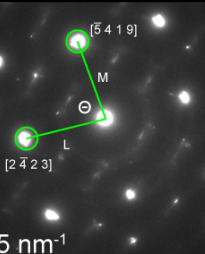
**Table B.2:** Indexing of SAD pattern in Figure 3-8(b). The best fit is 4H  $[10\bar{2}\bar{8}3]$ 

	2H				4H	
Beam Direction	$B=[5\bar{1}\bar{4}3]$		$B=[7\bar{2}\bar{5}3]$		$B=[10\bar{2}\bar{8}3]$	
Indexed Diffraction Pattern						
Experimental	L	4.8 nm <sup>-1</sup>	L	4.7 nm <sup>-1</sup>	L	4.7 nm <sup>-1</sup>
	M	7.3 nm <sup>-1</sup>	M	7.4 nm <sup>-1</sup>	M	7.3 nm <sup>-1</sup>
	Θ	52.4°	Θ	90.1°	Θ	52.4°
Theoretical	L	4.3 nm <sup>-1</sup>	L	4.3 nm <sup>-1</sup>	L	4.5 nm <sup>-1</sup>
	M	6.0 nm <sup>-1</sup>	M	6.0 nm <sup>-1</sup>	M	7.2 nm <sup>-1</sup>
	Θ	55.4°	Θ	94.2°	Θ	51.7°
Error	L	11.6%	L	9.3%	L	4.4%
	M	21.7%	M	23.3%	M	1.4%
	Θ	5.4%	Θ	4.4%	Θ	1.4%

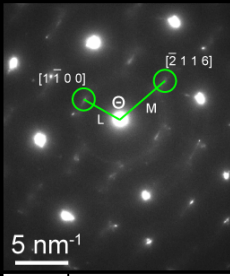
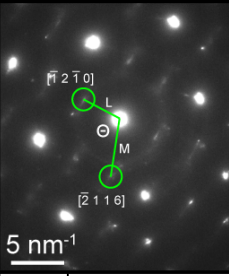
**Table B.3:** Indexing of SAD pattern in Figure 3-8(c). The best fit is 4H  $[\bar{2} \ 19 \ \bar{17} \ 3]$ 

	2H		4H	
Beam Direction	$B=[\bar{1} \ 5 \ \bar{4} \ 3]$		$B=[\bar{2} \ 19 \ \bar{17} \ 3]$	$B=[17 \ 2 \ \bar{19} \ 3]$
Indexed Diffraction Pattern				
Experimental	L	6.7 nm <sup>-1</sup>	L	6.6 nm <sup>-1</sup>
	M	5.8 nm <sup>-1</sup>	M	7.2 nm <sup>-1</sup>
	Θ	37.5°	Θ	106.7°
Theoretical	L	7.2 nm <sup>-1</sup>	L	6.4 nm <sup>-1</sup>
	M	5.0 nm <sup>-1</sup>	M	7.2 nm <sup>-1</sup>
	Θ	36.2°	Θ	107.7°
Error	L	6.9%	L	3.1%
	M	16.0%	M	0%
	Θ	3.6%	Θ	0.9%

**Table B.4a:** Indexing of SAD pattern in Figure 3-8(d); The best fit for grain 1 (indexed in white in Figure 3-8(d)) is 4H  $[1\ 3\ \bar{4}\ 4]$

	2H		4H			
Beam Direction	B=[16 $\bar{2}$ $\bar{14}$ 3]		B=[1 3 $\bar{4}$ 4]		B=[4 $\bar{1}$ $\bar{3}$ 4]	
Indexed Diffraction Pattern						
Experimental	L	7.8 nm <sup>-1</sup>	L	7.8 nm <sup>-1</sup>	L	7.9 nm <sup>-1</sup>
	M	8.0 nm <sup>-1</sup>	M	8.1 nm <sup>-1</sup>	M	7.8 nm <sup>-1</sup>
	Θ	94.2°	Θ	85.7°	Θ	86.1°
Theoretical	L	7.1 nm <sup>-1</sup>	L	7.6 nm <sup>-1</sup>	L	8.1 nm <sup>-1</sup>
	M	7.6 nm <sup>-1</sup>	M	8.1 nm <sup>-1</sup>	M	7.6 nm <sup>-1</sup>
	Θ	98.2°	Θ	87.2°	Θ	87.2°
Error	L	9.9%	L	2.6%	L	2.5%
	M	5.3%	M	0%	M	2.6%
	Θ	4.1%	Θ	1.7%	Θ	1.3%

**Table B.4b:** Indexing of SAD pattern in Figure 3-8(d); the best fit for grain 2 (indexed in yellow in in Figure 3-8(d)) is 4H  $[10 \bar{2} \bar{8} 3]$

	2H		4H	
Beam Direction	$B=[2 \ 2 \ \bar{4} \ 3]$		$B=[4 \ \bar{2} \ \bar{2} \ 3]$	
Indexed Diffraction Pattern				
Experimental	L	3.9 nm <sup>-1</sup>	L	4.0 nm <sup>-1</sup>
	M	5.7 nm <sup>-1</sup>	M	5.4 nm <sup>-1</sup>
	$\Theta$	109.4°	$\Theta$	112.0°
Theoretical	L	4.1 nm <sup>-1</sup>	L	4.1 nm <sup>-1</sup>
	M	5.0 nm <sup>-1</sup>	M	5.0 nm <sup>-1</sup>
	$\Theta$	114.0°	$\Theta$	114.0°
Error	L	4.9%	L	2.4%
	M	14.0%	M	8.0%
	$\Theta$	4.0%	$\Theta$	1.8%

### B.3 Details for impacted samples

Sample details for all impacted cubes are shown in Table B-5. Empty boxes indicate the property for that specific sample could not be determined. For example, some samples do not have impact velocity data because of uncertainty in determining the distance traveled by the particle from the in-flight image.

**Table B.5:** Details for microcompression tests impacted samples

Sample	Orientation	Days after impact	Taper angle [deg]	Impact velocity [m/s]	Effective diameter [nm]	Height [nm]	$\sigma_y$ [MPa]	Toughness [mJ/mm <sup>2</sup> ]	Elastic Modulus (unloading)
Set33_S1	[100]	1	2.7	--	740	704	97.80	77.69	51416.2
Set9_S12	[100]	8	1.8	454	660	783	33.25	107.00	206749.6
Set10_S5	[100]	8	3.2	345	620	958	318.02	176.73	148137.1
Set48_S6	[100]	3	5.2	333	1010	635	276.57	140.31	62117.2
Set48_S9	[100]	3	2.1	389	1033	510	384.07	199.04	47447.1
Set52_S2	[100]	2	2.8	272	972	522	52.89	65.46	56168.2
Set52_S3	[100]	2	2.1	286	966	794	361.95	149.37	81526.0
Set52_S6	[100]	2	2.5	313	949	427	70.01	81.49	39384.1
Set9_S9	[110]	8	2.3	312	642	1484	154.30	101.67	162066.7
Set9_S10	[110]	8	2.8	315	640	1329	199.46	--	72703.3
Set26_S2	[110]	2	3	--	918	983	314.03	133.91	79582.8
Set32_S10	[110]	1	3.2	--	875	1143	129.43	101.58	126452.3
Set0_S10	[110]	4	3.4	--	1435	1410	304.02	--	87631.6
Set9_S14	[110]	8	4	405	594	1072	223.08	--	105682.8
Set12_S7	[110]	3	3.9	--	649	1028	201.72	95.27	181538.0
Set9_S11	[110]	8	1.6	433	653	837	294.72	145.87	97496.4
Set23_S11	[110]	2	2.4	--	918	936	376.03	143.07	33700.8
Set23_S5	[110]	2	2.1	--	981	956	324.51	125.74	42686.8
Set23_S9	[110]	2	1.7	--	930	1216	250.58	132.67	51289.4
Set23_S7	[110]	2	2.2	--	939	926	356.74	--	42560.4

Set23_S8	[111]	2	1.7	--	925	1308	314.06	141.92	60582.0
Set9_S13	[111]	8	2.2	327	620	1502	216.81	--	80270.1
Set23_S10	[111]	2	2	--	935	1162	174.33	115.27	47686.5
Set10_S3	[111]	8	3.2	365	626	983	--	--	141537.4
Set24_S3	[111]	2	2	--	926	1814	310.11	--	72222.5
Set24_S6	[111]	2	2.2	--	968	1274	326.62	142.68	69481.7
Set26_S1	[111]	2	1.9	--	919	1397	286.61	112.88	123424.9
Set4_S10	[111]	1	2.6	343	1496	1465	272.72	133.26	69816.4
Set32_S4	[111]	1	2.3	--	917	1405	157.30	120.30	121395.6
Set32_S6	[111]	1	3.3	--	910	1313	55.64	112.06	102367.1
Set0_S11	[111]	4	4	382.8	919	1926	237.21	--	109577.2
Set23_S6	[111]	2	1	--	939	1316	216.49	126.83	62179.9

Precise control of the impact velocity is challenging, therefore, there is a standard deviation of  $\sim 53$  m/s from the average impact velocity (352 m/s). However, within this short velocity range, we do not observe a velocity-dependent changes in the mechanical properties (Figure B-3).

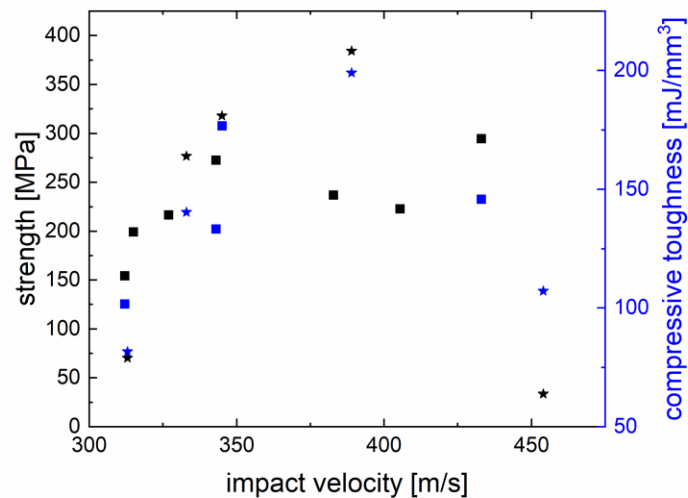
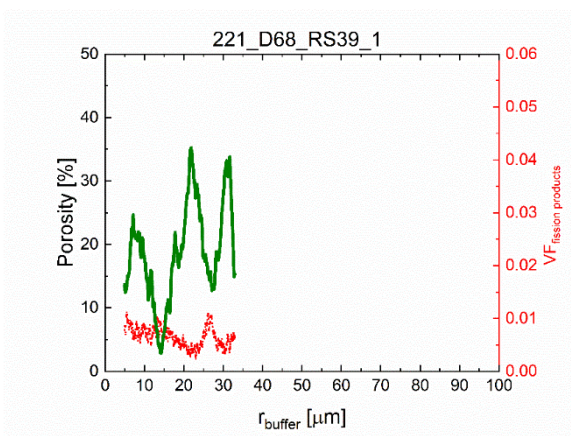
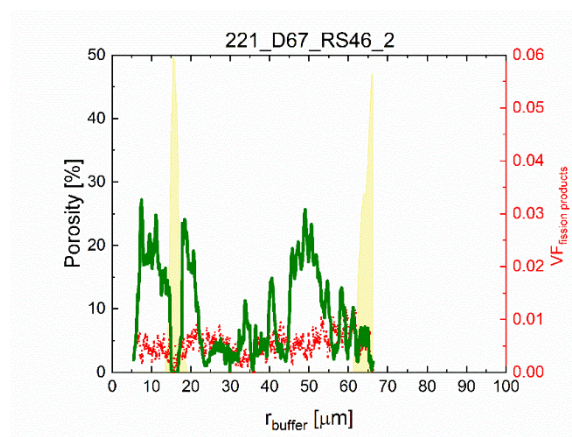
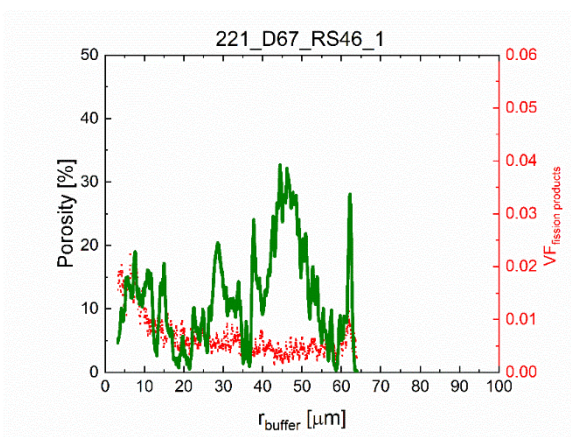
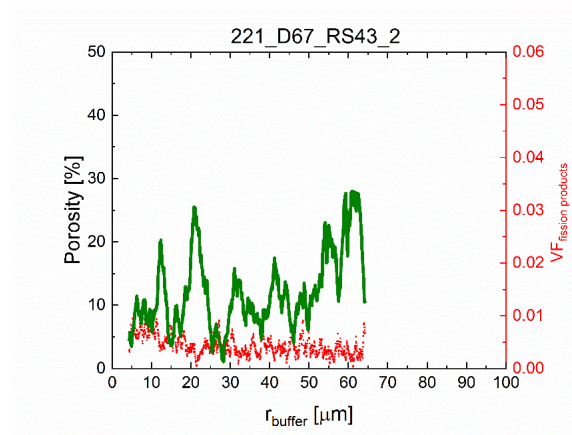
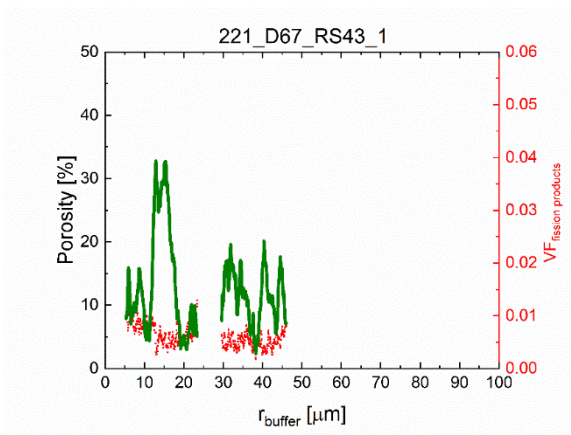
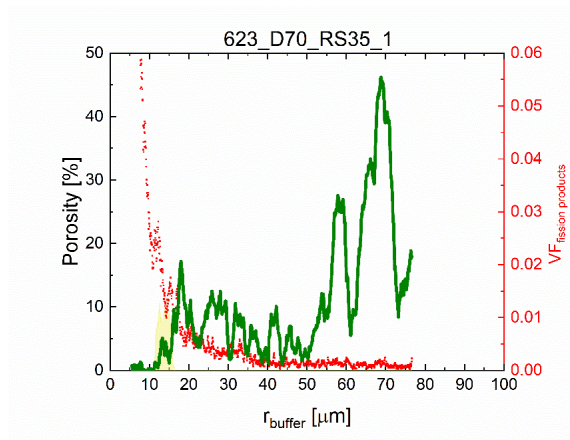
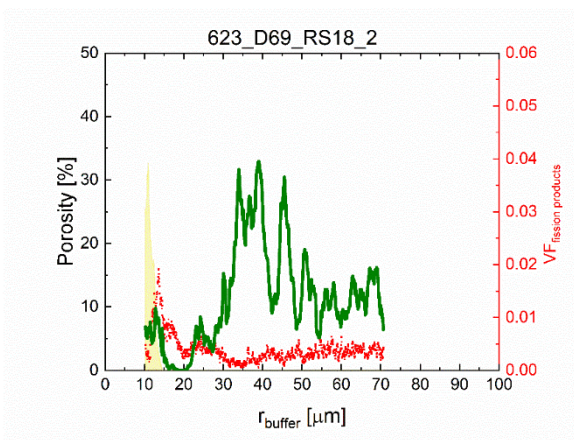
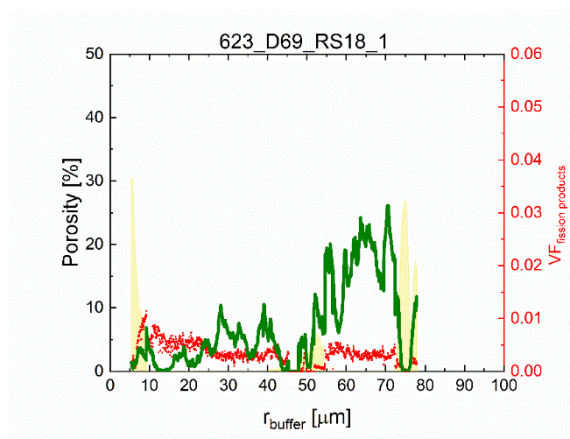
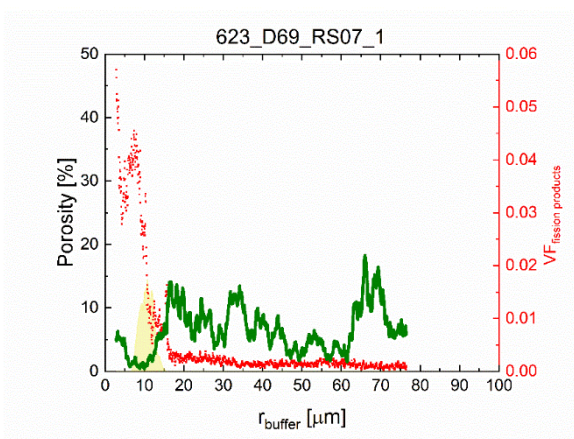
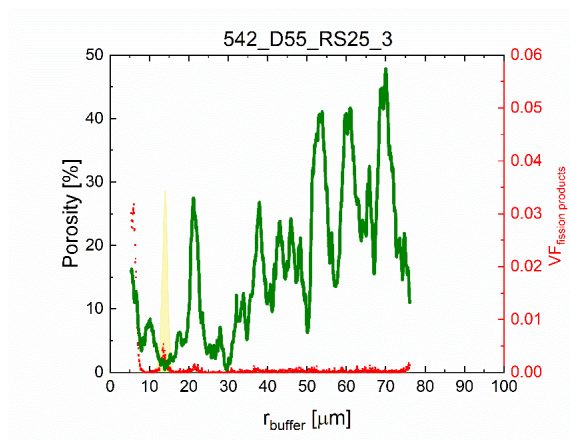
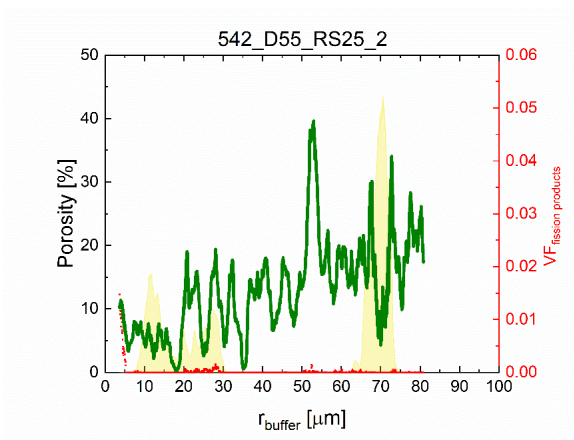


Figure B-3: yield strength and compressive toughness vs impact velocity ([100-impacted samples are denoted with stars)



## B.4 Porosity, fission product, and crack distribution plots from FIB-SEM tomography of irradiated buffer





## *References*

- [1] J. Wadsworth, G.W. Crabtree, R.J. Hemley, R. Falcone, I. Robertson, J. Stringer, P. Tortorelli, G.T. Gray, M. Nicol, J. Lehr, S.W. Tozer, T. Fitzsimmons, J.S. Vetrano, C.L. Ashton, S. Kitts, C. Landson, B. Campbell, G. Gruzalski, D. Stevens, Basic Research Needs for Materials Under Extreme Environments, DOE Rep. 108 (2008) 24. <http://www.osti.gov/servlets/purl/935440-WvJmE8/>.
- [2] H. Yao, M. Dao, D. Carnelli, K. Tai, C. Ortiz, Size-dependent heterogeneity benefits the mechanical performance of bone, *J. Mech. Phys. Solids*. 59 (2011) 64–74. <https://doi.org/10.1016/j.jmps.2010.09.012>.
- [3] U.G.K. Wegst, H. Bai, E. Saiz, A.P. Tomsia, R.O. Ritchie, Bioinspired structural materials, *Nat. Mater.* 14 (2015) 23–36. <https://doi.org/10.1038/nmat4089>.
- [4] Z. Liu, M.A. Meyers, Z. Zhang, R.O. Ritchie, Functional gradients and heterogeneities in biological materials: Design principles, functions, and bioinspired applications, *Prog. Mater. Sci.* 88 (2017) 467–498. <https://doi.org/10.1016/j.pmatsci.2017.04.013>.
- [5] S. Vignolini, N. Bruns, Bioinspiration Across All Length Scales of Materials, *Adv. Mater.* 30 (2018). <https://doi.org/10.1002/adma.201801687>.
- [6] E. Ma, T. Zhu, Towards strength–ductility synergy through the design of heterogeneous nanostructures in metals, *Mater. Today*. 20 (2017) 323–331. <https://doi.org/10.1016/j.mattod.2017.02.003>.
- [7] D.R.D.R. Smith, F.R. Fickett, Low-Temperature Properties of Silver, *J. Res. Natl. Inst. Stand. Technol.* 100 (1995) 119–171. <https://doi.org/10.6028/jres.100.012>.
- [8] N. Narita, J. Takamura, Deformation twinning in silver- and copper-alloy crystals, *Philos. Mag.* 29 (1974) 1001–1028. <https://doi.org/10.1080/14786437408226586>.
- [9] M. Niewczas, Dislocations and twinning in fcc crystals, *Dislocations Solids*. 13. (2007) 264–364.
- [10] M.I. Novgorodovo, A.I. Gorshkov, A. V. Mokhov, Native Silver and Its New Structural



- Modifications, Int. Geol. Rev. 23 (1981) 485–494. <https://doi.org/10.1080/00206818109455083>.
- [11] E. Wetli, M. Hochstrasser, M. Erbudak, Epitaxial growth of Ag in the hexagonal structure, *Surf. Sci.* 377–379 (1997) 876–881. [https://doi.org/10.1016/S0039-6028\(96\)01502-6](https://doi.org/10.1016/S0039-6028(96)01502-6).
- [12] P. Taneja, R. Banerjee, P. Ayyub, G.K. Dey, Observation of a hexagonal (4H) phase in nanocrystalline silver, *Phys. Rev. B.* 64 (2001) 5–8. <https://doi.org/10.1103/PhysRevB.64.033405>.
- [13] X. Liu, J. Luo, J. Zhu, Size effect on the crystal structure of silver nanowires, *Nano Lett.* 6 (2006) 408–412. <https://doi.org/10.1021/nl052219n>.
- [14] A. Singh, A. Ghosh, Stabilizing high-energy crystal structure in silver nanowires with underpotential electrochemistry, *J. Phys. Chem. C.* 112 (2008) 3460–3463. <https://doi.org/10.1021/jp7117967>.
- [15] C. Liang, K. Terabe, T. Hasegawa, M. Aono, Formation of metastable silver nanowires of hexagonal structure and their structural transformation under electron beam irradiation, *Japanese J. Appl. Physics, Part 1 Regul. Pap. Short Notes Rev. Pap.* 45 (2006) 6046–6048. <https://doi.org/10.1143/JJAP.45.6046>.
- [16] Z. Fan, M. Bosman, X. Huang, D. Huang, Y. Yu, K.P. Ong, Y.A. Akimov, L. Wu, B. Li, J. Wu, Y. Huang, Q. Liu, C. Eng Png, C. Lip Gan, P. Yang, H. Zhang, Stabilization of 4H hexagonal phase in gold nanoribbons, *Nat. Commun.* 6 (2015) 7684. <https://doi.org/10.1038/ncomms8684>.
- [17] I. Chakraborty, D. Carvalho, S.N. Shirodkar, S. Lahiri, S. Bhattacharyya, R. Banerjee, U. Waghmare, P. Ayyub, Novel hexagonal polytypes of silver: Growth, characterization and first-principles calculations, *J. Phys. Condens. Matter.* 23 (2011). <https://doi.org/10.1088/0953-8984/23/32/325401>.
- [18] I. Chakraborty, S.N. Shirodkar, S. Gohil, U. V. Waghmare, P. Ayyub, The nature of the structural phase transition from the hexagonal (4H) phase to the cubic (3C) phase of silver, *J. Phys. Condens. Matter.* 26 (2014). <https://doi.org/10.1088/0953-8984/26/11/115405>.
- [19] I. Chakraborty, S.N. Shirodkar, S. Gohil, U. V. Waghmare, P. Ayyub, A stable, quasi-2D

- modification of silver: Optical, electronic, vibrational and mechanical properties, and first principles calculations, *J. Phys. Condens. Matter.* 26 (2014). <https://doi.org/10.1088/0953-8984/26/2/025402>.
- [20] B. Wang, G.T. Fei, Y. Zhou, B. Wu, X. Zhu, L. Zhang, Controlled growth and phase transition of silver nanowires with dense lengthwise twins and stacking faults, *Cryst. Growth Des.* 8 (2008) 3073–3076.
- [21] Ag (Silver) Single Crystal Substrate, MTI Corp. (2021). <https://www.mtixtl.com/Mc-Ag-c-101005S1.aspx>.
- [22] S.-J. Jeon, J.-H. Lee, E.L. Thomas, Polyol synthesis of silver nanocubes via moderate control of the reaction atmosphere, *J. Colloid Interface Sci.* 435 (2014) 105–111. <https://doi.org/10.1016/j.jcis.2014.08.039>.
- [23] S.-J. Jeon, S. Yazdi, R. Thevamaran, E.L. Thomas, Synthesis of Monodisperse Single Crystalline Ag Microcubes via Seed-Mediated Growth, *Cryst. Growth Des.* 17 (2017) 284–289. <https://doi.org/10.1021/acs.cgd.6b01523>.
- [24] D. Petti, J. Maki, J. Hunn, P. Pappano, C. Barnes, J. Saurwein, S. Nagley, J. Kendall, R. Hobbins, The DOE advanced gas reactor fuel development and qualification program, *JOM.* 62 (2010) 62–66. <https://doi.org/10.1007/s11837-010-0140-5>.
- [25] P.A. Demkowicz, J.D. Hunn, R.N. Morris, I. van Rooyen, T.J. Gerczak, J.M. Harp, S.A. Ploger, AGR-1 Post Irradiation Examination Final Report, Idaho Falls, ID (United States), 2015. <https://doi.org/10.2172/1236801>.
- [26] J.D. Stempien, J.D. Hunn, R.N. Morris, T.J. Gerczak, P.A. Demkowicz, AGR-2 TRISO Fuel Post- Irradiation Examination Final Report, Idaho Fall, 2021. <https://www.osti.gov/biblio/1822447>.
- [27] J. Hunn, R. Morris, C. Baldwin, F. Montgomery, G.W. Silva, T. Gerczak, AGR-1 Irradiated Compact 6-1-1 PIE Report: Evaluation of As-Irradiated Fuel Performance Using Leach Burn Leach, IMGA, Materialography, and X-ray Tomography, Oak Ridge, TN (United States), 2012. <https://doi.org/10.2172/1649082>.
- [28] T.J. Gerczak, J.D. Hunn, R.A. Lowden, T.R. Allen, SiC layer microstructure in AGR-1 and

- AGR-2 TRISO fuel particles and the influence of its variation on the effective diffusion of key fission products, *J. Nucl. Mater.* 480 (2016) 257–270. <https://doi.org/10.1016/j.jnucmat.2016.08.011>.
- [29] F. Hofmann, E. Tarleton, R.J. Harder, N.W. Phillips, P. Ma, J.N. Clark, I.K. Robinson, B. Abbey, W. Liu, C.E. Beck, 3D lattice distortions and defect structures in ion-implanted nano-crystals, *Sci. Rep.* 7 (2017) 1–10. <https://doi.org/10.1038/srep45993>.
- [30] Y. Xiao, J. Wehrs, H. Ma, T. Al-samman, S. Korte-kerzel, M. Göken, J. Michler, Investigation of the deformation behavior of aluminum micropillars produced by focused ion beam machining using Ga and Xe ions, 127 (2017) 191–194. <https://doi.org/10.1016/j.scriptamat.2016.08.028>.
- [31] H. Fei, A. Abraham, N. Chawla, H. Jiang, Evaluation of Micro-Pillar Compression Tests for Accurate Determination of Elastic-Plastic Constitutive Relations, *J. Appl. Mech.* 79 (2012) 061011. <https://doi.org/10.1115/1.4006767>.
- [32] H. Zhang, B.E. Schuster, Q. Wei, K.T. Ramesh, The design of accurate micro-compression experiments, *Scr. Mater.* 54 (2006) 181–186. <https://doi.org/10.1016/j.scriptamat.2005.06.043>.
- [33] S. Bals, W. Tirry, R. Geurts, Y. Zhiqing, D. Schryvers, High-quality sample preparation by low kV FIB thinning for analytical TEM measurements, *Microsc. Microanal.* 13 (2007) 80–86. <https://doi.org/10.1017/S1431927607070018>.
- [34] M. Schaffer, B. Schaffer, Q. Ramasse, Sample preparation for atomic-resolution STEM at low voltages by FIB, *Ultramicroscopy.* 114 (2012) 62–71. <https://doi.org/10.1016/j.ultramic.2012.01.005>.
- [35] J.-H. Lee, P.E. Loya, J. Lou, E.L. Thomas, Dynamic mechanical behavior of multilayer graphene via supersonic projectile penetration, *Science* (80-. ). 346 (2014) 1092–1096. <https://doi.org/10.1126/science.1258544>.
- [36] R. Thevamaran, O. Lawal, S. Yazdi, S.-J. Jeon, J.-H. Lee, E.L. Thomas, Dynamic creation and evolution of gradient nanostructure in single-crystal metallic microcubes, *Science* (80-. ). 354 (2016) 312–316. <https://doi.org/10.1126/science.aag1768>.

- [37] W.C. Oliver, G.M. Pharr, An improved technique for determining hardness and elastic modulus using load and displacement sensing indentation experiments, *J. Mater. Res.* 6 (1992).
- [38] A.C. Fischer-Cripps, A review of analysis methods for submicron indentation testing, *Vacuum*. 58 (2000) 569–585.
- [39] S. Pathak, S.R. Kalidindi, Spherical nanoindentation stress-strain curves, *Mater. Sci. Eng. R Reports*. 91 (2015) 1–36. <https://doi.org/10.1016/j.mser.2015.02.001>.
- [40] J.R.J. Greer, J.-Y.J. Kim, M.J.M. Burek, The in-situ mechanical testing of nanoscale single-crystalline nanopillars, *JOM*. 61 (2009) 19–25. <https://doi.org/10.1007/s11837-009-0174-8>.
- [41] I.N. Sneddon, The relation between load and penetration in the axisymmetric boussinesq problem for a punch of arbitrary profile, *Int. J. Eng. Sci.* 3 (1965) 47–57. [https://doi.org/10.1016/0020-7225\(65\)90019-4](https://doi.org/10.1016/0020-7225(65)90019-4).
- [42] R.R. Keller, R.H. Geiss, Transmission EBSD from 10 nm domains in a scanning electron microscope, *J. Microsc.* 245 (2012) 245–251. <https://doi.org/10.1111/j.1365-2818.2011.03566.x>.
- [43] R.H. Geiss, K.P. Rice, R.R. Keller, Transmission EBSD in the Scanning Electron Microscope, *Microsc. Today*. 21 (2013) 16–20. <https://doi.org/10.1017/s1551929513000503>.
- [44] G.C. Sneddon, P.W. Trimby, J.M. Cairney, Transmission Kikuchi diffraction in a scanning electron microscope: A review, *Mater. Sci. Eng. R Reports*. 110 (2016) 1–12. <https://doi.org/10.1016/j.mser.2016.10.001>.
- [45] A.J. Schwartz, M. Kumar, B.L. Adams, *Electron Backscatter Diffraction in Materials Science*, 2001.
- [46] S.I. Wright, M.M. Nowell, R. De Kloe, L. Chan, Orientation precision of electron backscatter diffraction measurements near grain boundaries, *Microsc. Microanal.* 20 (2014) 852–863. <https://doi.org/10.1017/S143192761400035X>.

- [47] Y. Shen, J. Xu, Y. Zhang, Y. Wang, J. Zhang, B. Yu, Y. Zeng, H. Miao, Spatial Resolutions of On-Axis and Off-Axis Transmission Kikuchi Diffraction Methods, *Appl. Sci.* 9 (2019) 4478. <https://doi.org/10.3390/app9214478>.
- [48] R. van Bremen, D. Ribas Gomes, L.T.H. de Jeer, V. Ocelík, J.T.M. De Hosson, On the optimum resolution of transmission-electron backscattered diffraction (t-EBSD), *Ultramicroscopy*. 160 (2016) 256–264. <https://doi.org/10.1016/j.ultramic.2015.10.025>.
- [49] R. Thevamaran, C. Griesbach, S. Yazdi, M. Ponga, H. Alimadadi, O. Lawal, S.-J. Jeon, E.L. Thomas, Dynamic martensitic phase transformation in single-crystal silver microcubes, *Acta Mater.* 182 (2020) 131–143. <https://doi.org/10.1016/j.actamat.2019.10.006>.
- [50] P.W. Trimby, Orientation mapping of nanostructured materials using transmission Kikuchi diffraction in the scanning electron microscope, *Ultramicroscopy*. 120 (2012) 16–24. <https://doi.org/10.1016/j.ultramic.2012.06.004>.
- [51] M. Abbasi, D.-I. Kim, H.-U. Guim, M. Hosseini, H. Danesh-Manesh, M. Abbasi, Application of Transmitted Kikuchi Diffraction in Studying Nano-oxide and Ultrafine Metallic Grains, *ACS Nano*. 9 (2015) 10991–11002. <https://doi.org/10.1021/acs.nano.5b04296>.
- [52] N. Mortazavi, M. Esmaily, M. Halvarsson, The capability of Transmission Kikuchi Diffraction technique for characterizing nano-grained oxide scales formed on a FeCrAl stainless steel, *Mater. Lett.* 147 (2015) 42–45. <https://doi.org/10.1016/j.matlet.2015.02.008>.
- [53] H. Yuan, E. Brodu, C. Chen, E. Bouzy, J.-J. Fundenberger, L.S. Toth, On-axis versus off-axis Transmission Kikuchi Diffraction technique: application to the characterisation of severe plastic deformation-induced ultrafine-grained microstructures, *J. Microsc.* 267 (2017) 70–80. <https://doi.org/10.1111/jmi.12548>.
- [54] G. Proust, P. Trimby, S. Piazzolo, D. Retraint, Characterization of Ultra-fine Grained and Nanocrystalline Materials Using Transmission Kikuchi Diffraction, *J. Vis. Exp.* 122 (2017) 1–11. <https://doi.org/10.3791/55506>.
- [55] S. Suzuki, Features of transmission EBSD and its application, *Jom.* 65 (2013) 1254–1263. <https://doi.org/10.1007/s11837-013-0700-6>.



- [56] S.I. Wright, M.M. Nowell, S.P. Lindeman, P.P. Camus, M. De Graef, M.A. Jackson, Introduction and comparison of new EBSD post-processing methodologies, *Ultramicroscopy*. 159 (2015) 81–94. <https://doi.org/10.1016/j.ultramic.2015.08.001>.
- [57] F. Bachmann, R. Hielscher, H. Schaeben, Texture Analysis with MTEX – Free and Open Source Software Toolbox, *Solid State Phenom.* 160 (2010) 63–68. <https://doi.org/10.4028/www.scientific.net/SSP.160.63>.
- [58] C. McMahon, B. Soe, A. Loeb, A. Vemulkar, M. Ferry, L. Bassman, Boundary identification in EBSD data with a generalization of fast multiscale clustering, *Ultramicroscopy*. 133 (2013) 16–25. <https://doi.org/10.1016/j.ultramic.2013.04.009>.
- [59] B.S. El-Dasher, B.. Adams, A.. Rollett, Viewpoint: experimental recovery of geometrically necessary dislocation density in polycrystals, *Scr. Mater.* 48 (2003) 141–145. [https://doi.org/10.1016/S1359-6462\(02\)00340-8](https://doi.org/10.1016/S1359-6462(02)00340-8).
- [60] W. Pantleon, Resolving the geometrically necessary dislocation content by conventional electron backscattering diffraction, *Scr. Mater.* 58 (2008) 994–997. <https://doi.org/10.1016/j.scriptamat.2008.01.050>.
- [61] M. Kamaya, Assessment of local deformation using EBSD: Quantification of accuracy of measurement and definition of local gradient, *Ultramicroscopy*. 111 (2011) 1189–1199. <https://doi.org/10.1016/j.ultramic.2011.02.004>.
- [62] J. Jiang, T.B. Britton, A.J. Wilkinson, Measurement of geometrically necessary dislocation density with high resolution electron backscatter diffraction: Effects of detector binning and step size, *Ultramicroscopy*. 125 (2013) 1–9. <https://doi.org/10.1016/j.ultramic.2012.11.003>.
- [63] T.J. Ruggles, D.T. Fullwood, Estimations of bulk geometrically necessary dislocation density using high resolution EBSD, *Ultramicroscopy*. 133 (2013) 8–15. <https://doi.org/10.1016/j.ultramic.2013.04.011>.
- [64] C. Moussa, M. Bernacki, R. Besnard, N. Bozzolo, Statistical analysis of dislocations and dislocation boundaries from EBSD data, *Ultramicroscopy*. 179 (2017) 63–72. <https://doi.org/10.1016/j.ultramic.2017.04.005>.
- [65] A. Kundu, D.P. Field, Geometrically Necessary Dislocation Density Evolution in Interstitial

- Free Steel at Small Plastic Strains, *Metall. Mater. Trans. A Phys. Metall. Mater. Sci.* 49 (2018) 3274–3282. <https://doi.org/10.1007/s11661-018-4693-1>.
- [66] A. Vilalta-Clemente, M. Meisnar, S. Lozano-Perez, A.J. Wilkinson, Characterization of Elastic Strain Field and Geometrically Necessary Dislocation Distribution in Stress Corrosion Cracking of 316 Stainless Steels by Transmission Kikuchi Diffraction, *Microsc. Microanal.* 21 (2015) 605–606. <https://doi.org/10.1017/S1431927615003827>.
- [67] S. Naghdy, P. Verleysen, R. Petrov, L. Kestens, Resolving the geometrically necessary dislocation content in severely deformed aluminum by transmission Kikuchi diffraction, *Mater. Charact.* 140 (2018) 225–232. <https://doi.org/10.1016/j.matchar.2018.04.013>.
- [68] X.Z. Liang, M.F. Dodge, J. Jiang, H.B. Dong, Using transmission Kikuchi diffraction in a scanning electron microscope to quantify geometrically necessary dislocation density at the nanoscale, *Ultramicroscopy*. 197 (2019) 39–45. <https://doi.org/10.1016/j.ultramic.2018.11.011>.
- [69] H. Yu, J. Liu, P. Karamched, A.J. Wilkinson, F. Hofmann, Mapping the full lattice strain tensor of a single dislocation by high angular resolution transmission Kikuchi diffraction (HR-TKD), *Scr. Mater.* 164 (2019) 36–41. <https://doi.org/10.1016/j.scriptamat.2018.12.039>.
- [70] N. Saravanan, P.S. Karamched, J. Liu, C. Rainasse, F. Scenini, S. Lozano-Perez, Using local GND density to study SCC initiation, *Ultramicroscopy*. 217 (2020) 113054. <https://doi.org/10.1016/j.ultramic.2020.113054>.
- [71] J.F. Nye, Some geometrical relations in dislocated crystals, *Acta Metall.* 1 (1953) 153–162. [https://doi.org/10.1016/0001-6160\(53\)90054-6](https://doi.org/10.1016/0001-6160(53)90054-6).
- [72] E. Kroner, *Continuum Theory of Dislocations and Self-Stresses*, Springer. 5 (1958).
- [73] T.J. Ruggles, Y.S.J. Yoo, B.E. Dunlap, M.A. Crimp, J. Kacher, Correlating results from high resolution EBSD with TEM- and ECCI-based dislocation microscopy: Approaching single dislocation sensitivity via noise reduction, *Ultramicroscopy*. 210 (2020) 112927. <https://doi.org/10.1016/j.ultramic.2019.112927>.
- [74] H. Gao, Y. Huang, W.D. Nix, J.W. Hutchinson, Mechanism-based strain gradient plasticity

- I. Theory, *J. Mech. Phys. Solids*. 47 (1999) 1239–1263. [https://doi.org/10.1016/S0022-5096\(98\)00103-3](https://doi.org/10.1016/S0022-5096(98)00103-3).
- [75] L.. Kubin, A. Mortensen, Geometrically necessary dislocations and strain-gradient plasticity: a few critical issues, *Scr. Mater.* 48 (2003) 119–125. [https://doi.org/10.1016/S1359-6462\(02\)00335-4](https://doi.org/10.1016/S1359-6462(02)00335-4).
- [76] R. Hielscher, C.B. Silberman, E. Schmidl, J. Ihlemann, Denoising of crystal orientation maps, *J. Appl. Crystallogr.* 52 (2019) 984–996. <https://doi.org/10.1107/S1600576719009075>.
- [77] L. Holzer, M. Cantoni, Review of FIB Tomography, in: *UTKE Nanofabrication Using Focus. Ion Electron Beams*, 2014: pp. 410–435.
- [78] F. Tariq, R. Haswell, P.D. Lee, D.W. McComb, Characterization of hierarchical pore structures in ceramics using multiscale tomography, *Acta Mater.* 59 (2011) 2109–2120. <https://doi.org/10.1016/j.actamat.2010.12.012>.
- [79] J.D. Arregui-Mena, P.D. Edmondson, A.A. Campbell, Y. Katoh, Site specific, high-resolution characterisation of porosity in graphite using FIB-SEM tomography, *J. Nucl. Mater.* 511 (2018) 164–173. <https://doi.org/10.1016/j.jnucmat.2018.08.047>.
- [80] X. Feng, C.J. Burke, M. Zhuo, H. Guo, K. Yang, A. Reddy, I. Prasad, R.-M. Ho, A. Avgeropoulos, G.M. Grason, E.L. Thomas, Seeing mesoatomic distortions in soft-matter crystals of a double-gyroid block copolymer, *Nature*. 575 (2019) 175–179. <https://doi.org/10.1038/s41586-019-1706-1>.
- [81] C.I. Contescu, J.D. Arregui-Mena, A.A. Campbell, P.D. Edmondson, N.C. Gallego, K. Takizawa, Y. Katoh, Development of mesopores in superfine grain graphite neutron-irradiated at high fluence, *Carbon N. Y.* 141 (2019) 663–675. <https://doi.org/10.1016/j.carbon.2018.08.039>.
- [82] T.L. Burnett, R. Kelley, B. Winiarski, L. Contreras, M. Daly, A. Gholinia, M.G. Burke, P.J. Withers, Large volume serial section tomography by Xe Plasma FIB dual beam microscopy, *Ultramicroscopy*. 161 (2016) 119–129. <https://doi.org/10.1016/j.ultramic.2015.11.001>.
- [83] M. Garum, P.W.J. Glover, P. Lorinczi, R. Drummond-Brydson, A. Hassanpour, Micro- and

- Nano-Scale Pore Structure in Gas Shale Using X $\mu$ -CT and FIB-SEM Techniques, *Energy & Fuels*. 34 (2020) 12340–12353. <https://doi.org/10.1021/acs.energyfuels.0c02025>.
- [84] J.D. Arregui-Mena, R.L. Seibert, T.J. Gerczak, Characterization of PyC/SiC Interfaces with FIB-SEM Tomography, *J. Nucl. Mater.* 545 (2021) 152736. <https://doi.org/10.1016/j.jnucmat.2020.152736>.
- [85] W. Weng, X. Zhu, INet: Convolutional Networks for Biomedical Image Segmentation, *IEEE Access*. 9 (2021) 16591–16603. <https://doi.org/10.1109/ACCESS.2021.3053408>.
- [86] S. Plimpton, Fast Parallel Algorithms for Short-Range Molecular Dynamics, *J. Comput. Phys.* 117 (1995) 1–19. <https://doi.org/10.1006/jcph.1995.1039>.
- [87] M.P. Allen, D.J. Tildesley, *Computer Simulation of Liquids*, Clarendon Press, New York, NY, USA, 1989.
- [88] P.L. Williams, Y. Mishin, J.C. Hamilton, An embedded-atom potential for the Cu–Ag system, *Model. Simul. Mater. Sci. Eng.* 14 (2006) 817–833. <https://doi.org/10.1088/0965-0393/14/5/002>.
- [89] W.H. Press, B.P. Flannery, S.A. Teukolsky, W.T. Vetterling, *Numerical Recipes in Fortran 77: The Art of Scientific Computing*, Cambridge University Press, 1992.
- [90] A. Stukowski, V. V. Bulatov, A. Arsenlis, Automated identification and indexing of dislocations in crystal interfaces, *Model. Simul. Mater. Sci. Eng.* 20 (2012) 085007. <https://doi.org/10.1088/0965-0393/20/8/085007>.
- [91] A. Stukowski, Visualization and analysis of atomistic simulation data with OVITO—the Open Visualization Tool, *Model. Simul. Mater. Sci. Eng.* 18 (2010) 015012. <https://doi.org/10.1088/0965-0393/18/1/015012>.
- [92] C.A. Bronkhorst, J.R. Mayeur, V. Livescu, R. Pokharel, D.W. Brown, G.T. Gray, Structural representation of additively manufactured 316L austenitic stainless steel, *Int. J. Plast.* 118 (2019) 70–86. <https://doi.org/10.1016/j.ijplas.2019.01.012>.
- [93] J.R. Rice, INELASTIC CONSTITUTIVE RELATIONS FOR SOLIDS : THEORY AND ITS APPLICATION, *J. Mech. Phys. Solids*. 19 (1971) 433–455.

- [94] R. Hill, J.R. Rice, Constitutive analysis of elastic-plastic crystals at arbitrary strain, *J. Mech. Phys. Solids*. 20 (1972) 401–413. [https://doi.org/10.1016/0022-5096\(72\)90017-8](https://doi.org/10.1016/0022-5096(72)90017-8).
- [95] R.. Asaro, J.R. Rice, Strain Localization in Ductile Single Crystals, *J. Mech. Phys. Solids*. 25 (1977) 309–338.
- [96] R.. Asaro, Crystal plasticity, *J. Appl. Mech.* 50 (1983) 921–934. <https://doi.org/10.3390/cryst11010044>.
- [97] R.J. Asaro, Micromechanics of Crystals and Polycrystals, *Adv. Appl. Mech.* 23 (1983) 1–115. [https://doi.org/10.1016/S0065-2156\(08\)70242-4](https://doi.org/10.1016/S0065-2156(08)70242-4).
- [98] C.A. Bronkhorst, S.R. Kalidindi, L. Anand, Polycrystalline plasticity and the evolution of crystallographic texture in FCC metals, *Philos. Trans. R. Soc. London. Ser. A Phys. Eng. Sci.* 341 (1992) 443–477. <https://doi.org/10.1098/rsta.1992.0111>.
- [99] C.A. Bronkhorst, B.L. Hansen, E.K. Cerreta, J.F. Bingert, Modeling the microstructural evolution of metallic polycrystalline materials under localization conditions, *J. Mech. Phys. Solids*. 55 (2007) 2351–2383. <https://doi.org/10.1016/j.jmps.2007.03.019>.
- [100] C. Alleman, D.J. Luscher, C. Bronkhorst, S. Ghosh, Distribution-enhanced homogenization framework and model for heterogeneous elasto-plastic problems, *J. Mech. Phys. Solids*. 85 (2015) 176–202. <https://doi.org/10.1016/j.jmps.2015.09.012>.
- [101] U.F. Kocks, A.S. Argon, M.F. Ashby, Thermodynamics and Kinetics of Slip, *Prog. Mater. Sci.* 19 (1975).
- [102] L. Anand, Single-crystal elasto-viscoplasticity: Application to texture evolution in polycrystalline metals at large strains, *Comput. Methods Appl. Mech. Eng.* 193 (2004) 5359–5383. <https://doi.org/10.1016/j.cma.2003.12.068>.
- [103] S.R. Kalidindi, C.A. Bronkhorst, L. Anand, Crystallographic texture evolution in bulk deformation processing of fcc metals, *J. Mech. Phys. Solids*. 40 (1992) 537–569.
- [104] G. Simmons, H. Wang, *Single Crystal Elastic Constants and Calculated Aggregate Properties*, 1965.
- [105] A.J. Beaudoin, A. Acharya, S.R. Chen, D.A. Korzekwa, M.G. Stout, Consideration of grain-

- size effect and kinetics in the plastic deformation of metal polycrystals, *Acta Mater.* 48 (2000) 3409–3423. [https://doi.org/10.1016/S1359-6454\(00\)00136-1](https://doi.org/10.1016/S1359-6454(00)00136-1).
- [106] J.W. Aldrich, R.W. Armstrong, The grain size dependence of the yield, flow and fracture stress of commercial purity silver, *Metall. Trans.* 1 (1970) 2547–2550. <https://doi.org/10.1007/BF03038382>.
- [107] R.P. Carreker, Tensile Deformation of Silver as a Function of Temperature, Strain Rate, and Grain Size, *J. Met.* (1957) 112–115.
- [108] M.A. Groeber, M.A. Jackson, DREAM.3D: A Digital Representation Environment for the Analysis of Microstructure in 3D, *Integr. Mater. Manuf. Innov.* 3 (2014) 56–72. <https://doi.org/10.1186/2193-9772-3-5>.
- [109] R. Quey, P.R. Dawson, F. Barbe, Large-scale 3D random polycrystals for the finite element method: Generation, meshing and remeshing, *Comput. Methods Appl. Mech. Eng.* 200 (2011) 1729–1745. <https://doi.org/10.1016/j.cma.2011.01.002>.
- [110] M. Henrich, F. Pütz, S. Münstermann, A Novel Approach to Discrete Representative Volume Element Automation and Generation-DRAGen, *Materials (Basel)*. 13 (2020) 1887. <https://doi.org/10.3390/ma13081887>.
- [111] S.P. Donegan, A.D. Rollett, Simulation of residual stress and elastic energy density in thermal barrier coatings using fast Fourier transforms, *Acta Mater.* 96 (2015) 212–228. <https://doi.org/10.1016/j.actamat.2015.06.019>.
- [112] M. Miodownik, Monte Carlo Potts Model, in: *Comput. Mater. Eng.*, 2007: pp. 47–108. <https://doi.org/10.1016/B978-0-12-369468-3.50003-4>.
- [113] A. Lyckegaard, E.M. Lauridsen, W. Ludwig, R.W. Fonda, H.F. Poulsen, On the use of laguerre tessellations for representations of 3D grain structures, *Adv. Eng. Mater.* 13 (2011) 165–170. <https://doi.org/10.1002/adem.201000258>.
- [114] S. Falco, J. Jiang, F. De Cola, N. Petrinic, Generation of 3D polycrystalline microstructures with a conditioned Laguerre-Voronoi tessellation technique, *Comput. Mater. Sci.* 136 (2017) 20–28. <https://doi.org/10.1016/j.commatsci.2017.04.018>.

- [115] B. Flipon, C. Keller, R. Quey, F. Barbe, A full-field crystal-plasticity analysis of bimodal polycrystals, *Int. J. Solids Struct.* 184 (2020) 178–192. <https://doi.org/10.1016/j.ijsolstr.2019.02.005>.
- [116] Y. Li, A.J. Bushby, D.J. Dunstan, The Hall-Petch effect as a manifestation of the general size effect, *Proc. R. Soc. A Math. Phys. Eng. Sci.* 472 (2016). <https://doi.org/10.1098/rspa.2015.0890>.
- [117] M.D. Uchic, D.M. Dimiduk, J.N. Florando, W.D. Nix, Sample Dimensions Influence Strength and Crystal Plasticity, *Science* (80-. ). 305 (2004) 986–989. <https://doi.org/10.1126/science.1098993>.
- [118] Z.-J. Wang, Q.-J. Li, Z.-W. Shan, J. Li, J. Sun, E. Ma, Sample size effects on the large strain bursts in submicron aluminum pillars, *Appl. Phys. Lett.* 100 (2012). <https://doi.org/10.1063/1.3681582>.
- [119] R. Maaß, L. Meza, B. Gan, S. Tin, J.R. Greer, Ultrahigh Strength of Dislocation-Free Ni<sub>3</sub>Al Nanocubes, *Small*. 8 (2012) 1869–1875. <https://doi.org/10.1002/sml.201102603>.
- [120] H. Xie, T. Yu, F. Yin, A Tension – compression asymmetry in homogeneous dislocation nucleation stress of single crystals Cu , Au , Ni and Ni<sub>3</sub>Al, *Mater. Sci. Eng. A*. 604 (2014) 142–147. <https://doi.org/10.1016/j.msea.2014.03.018>.
- [121] I. Issa, J. Amodeo, J. Réthoré, L. Joly-Pottuz, C. Esnouf, J. Morthomas, M. Perez, J. Chevalier, K. Masenelli-Varlot, In situ investigation of MgO nanocube deformation at room temperature, *Acta Mater.* 86 (2015) 295–304. <https://doi.org/10.1016/j.actamat.2014.12.001>.
- [122] A. Sharma, J. Hickman, N. Gazit, E. Rabkin, Y. Mishin, Nickel nanoparticles set a new record of strength, *Nat. Commun.* 9 (2018) 1–9. <https://doi.org/10.1038/s41467-018-06575-6>.
- [123] A. Sharma, R. Kositski, O. Kovalenko, D. Mordehai, E. Rabkin, Giant shape- and size-dependent compressive strength of molybdenum nano- and microparticles, *Acta Mater.* 198 (2020) 72–84. <https://doi.org/10.1016/j.actamat.2020.07.054>.
- [124] M.T. Kiani, R.P. Patil, X.W. Gu, Dislocation surface nucleation in surfactant-passivated

- metallic nanocubes, *MRS Commun.* 9 (2019) 1029–1033.  
<https://doi.org/10.1557/mrc.2019.84>.
- [125] C. Griesbach, S.-J. Jeon, D.F. Rojas, M. Ponga, S. Yazdi, S. Pathak, N. Mara, E.L. Thomas, R. Thevamaran, Origins of size effects in initially dislocation-free single-crystal silver micro- and nanocubes, *Acta Mater.* 214 (2021) 117020.  
<https://doi.org/10.1016/j.actamat.2021.117020>.
- [126] J.R. Greer, W.D. Nix, Nanoscale gold pillars strengthened through dislocation starvation, *Phys. Rev. B - Condens. Matter Phys.* 73 (2006) 1–6.  
<https://doi.org/10.1103/PhysRevB.73.245410>.
- [127] H. Bei, S. Shim, M.K. Miller, G.M. Pharr, E.P. George, Effects of focused ion beam milling on the nanomechanical behavior of a molybdenum-alloy single crystal, *Appl. Phys. Lett.* 91 (2007) 1–4. <https://doi.org/10.1063/1.2784948>.
- [128] C.P. Frick, B.G. Clark, S. Orso, A.S. Schneider, E. Arzt, Size effect on strength and strain hardening of small-scale [1 1 1] nickel compression pillars, *Mater. Sci. Eng. A.* 489 (2008) 319–329. <https://doi.org/10.1016/j.msea.2007.12.038>.
- [129] S. Buzzi, M. Dietiker, K. Kunze, R. Spolenak, J.F. Löffler, Deformation behavior of silver submicrometer-pillars prepared by nanoimprinting, *Philos. Mag.* 89 (2009) 869–884.  
<https://doi.org/10.1080/14786430902791748>.
- [130] S. Shim, H. Bei, M.K. Miller, G.M. Pharr, E.P. George, Effects of focused ion beam milling on the compressive behavior of directionally solidified micropillars and the nanoindentation response of an electropolished surface, *Acta Mater.* 57 (2009) 503–510.  
<https://doi.org/10.1016/j.actamat.2008.09.033>.
- [131] A.T. Jennings, M.J. Burek, J.R. Greer, Microstructure versus Size: Mechanical properties of electroplated single crystalline Cu nanopillars, *Phys. Rev. Lett.* 104 (2010) 1–4.  
<https://doi.org/10.1103/PhysRevLett.104.135503>.
- [132] D. Jang, J.R. Greer, Size-induced weakening and grain boundary-assisted deformation in 60 nm grained Ni nanopillars, *Scr. Mater.* 64 (2011) 77–80.  
<https://doi.org/10.1016/j.scriptamat.2010.09.010>.



- [133] D. Mordehai, S.W. Lee, B. Backes, D.J. Srolovitz, W.D. Nix, E. Rabkin, Size effect in compression of single-crystal gold microparticles, *Acta Mater.* 59 (2011) 5202–5215. <https://doi.org/10.1016/j.actamat.2011.04.057>.
- [134] S. Basu, M.W. Barsoum, Deformation micromechanisms of ZnO single crystals as determined from spherical nanoindentation stress-strain curves, *J. Mater. Res.* 22 (2007) 2470–2477. <https://doi.org/10.1557/jmr.2007.0305>.
- [135] S. Basu, O.A. Elshrief, R. Coward, B. Anasori, M.W. Barsoum, Microscale deformation of (001) and (100) rutile single crystals under spherical nanoindentation, *J. Mater. Res.* 27 (2012) 53–63. <https://doi.org/10.1557/jmr.2011.337>.
- [136] S. Pathak, J.L. Riesterer, S.R. Kalidindi, J. Michler, Understanding pop-ins in spherical nanoindentation, *Appl. Phys. Lett.* 105 (2014). <https://doi.org/10.1063/1.4898698>.
- [137] H.D. Patel, S.W. Lee, Spherical nanoindentation on tungsten single crystal: The transition from source-controlled plasticity to bulk plasticity, *Scr. Mater.* 175 (2020) 16–19. <https://doi.org/10.1016/j.scriptamat.2019.08.038>.
- [138] Y. Feruz, D. Mordehai, Towards a universal size-dependent strength of face-centered cubic nanoparticles, *Acta Mater.* 103 (2016) 433–441. <https://doi.org/10.1016/j.actamat.2015.10.027>.
- [139] K. Shreiber, D. Mordehai, Dislocation-nucleation-controlled deformation of Ni<sub>3</sub>Al nanocubes in molecular dynamics simulations, *Model. Simul. Mater. Sci. Eng.* 23 (2015) 17. <https://doi.org/10.1088/0965-0393/23/8/085004>.
- [140] J.R. Greer, J.T.M. De Hosson, Plasticity in small-sized metallic systems: Intrinsic versus extrinsic size effect, *Prog. Mater. Sci.* 56 (2011) 654–724. <https://doi.org/10.1016/j.pmatsci.2011.01.005>.
- [141] S.H. Oh, M. Legros, D. Kiener, G. Dehm, In situ observation of dislocation nucleation and escape in a submicrometre aluminium single crystal, *Nat. Mater.* 8 (2009) 95–100. <https://doi.org/10.1038/nmat2370>.
- [142] O. Kraft, P.A. Gruber, M. Reiner, D. Weygand, Plasticity in Confined Dimensions, *Annu. Rev. Mater. Res.* 40 (2010) 293–317. <https://doi.org/10.1146/annurev-matsci-082908->

145409.

- [143] J. Senger, D. Weygand, C. Motz, P. Gumbsch, O. Kraft, Aspect ratio and stochastic effects in the plasticity of uniformly loaded micrometer-sized specimens, *Acta Mater.* 59 (2011) 2937–2947. <https://doi.org/10.1016/j.actamat.2011.01.034>.
- [144] E.O. Hall, The Deformation and Ageing of Mild Steel: II Characteristics of the L ders Deformation, *Proc. Phys. Soc. Sect. B.* 64 (1951) 742–747. <https://doi.org/10.1088/0370-1301/64/9/302>.
- [145] N. Petch, The Cleavage Strength of Polycrystals, *J. Iron Steel Inst.* 173 (1953) 25–28.
- [146] A.H. Chokshi, A. Rosen, J. Karch, H. Gleiter, On the validity of the Hall-Petch relationship in nanocrystalline materials, *Scr. Metall.* 23 (1989) 1679–1684.
- [147] C. Sawangrat, S. Kato, D. Orlov, K. Ameyama, Harmonic-structured copper: performance and proof of fabrication concept based on severe plastic deformation of powders, *J. Mater. Sci.* 49 (2014) 6579–6585. <https://doi.org/10.1007/s10853-014-8258-4>.
- [148] A.Y. Chen, H.H. Ruan, J.B. Zhang, X.R. Liu, J. Lu, Introducing a hierarchical structure for fabrication of a high performance steel, *Mater. Chem. Phys.* 129 (2011) 1096–1103. <https://doi.org/10.1016/j.matchemphys.2011.05.068>.
- [149] A. Chen, D. Li, J. Zhang, H. Song, J. Lu, Make nanostructured metal exceptionally tough by introducing non-localized fracture behaviors, *Scr. Mater.* 59 (2008) 579–582. <https://doi.org/10.1016/j.scriptamat.2008.04.048>.
- [150] R.O. Ritchie, The conflicts between strength and toughness, *Nat. Mater.* 10 (2011) 817–822. <https://doi.org/10.1038/nmat3115>.
- [151] Y. Wei, Y. Li, L. Zhu, Y. Liu, X. Lei, G. Wang, Y. Wu, Z. Mi, J. Liu, H. Wang, H. Gao, Evading the strength–ductility trade-off dilemma in steel through gradient hierarchical nanotwins, *Nat. Commun.* 5 (2014) 3580. <https://doi.org/10.1038/ncomms4580>.
- [152] Z. Zhang, H. Sheng, Z. Wang, B. Gludovatz, Z. Zhang, E.P. George, Q. Yu, S.X. Mao, R.O. Ritchie, Dislocation mechanisms and 3D twin architectures generate exceptional strength–ductility–toughness combination in CrCoNi medium-entropy alloy, *Nat. Commun.* 8 (2017)

14390. <https://doi.org/10.1038/ncomms14390>.
- [153] K. Lu, Making strong nanomaterials ductile with gradients, *Science* (80-. ). 345 (2014) 1455–1456. <https://doi.org/10.1126/science.1255940>.
- [154] X. Wu, P. Jiang, L. Chen, F. Yuan, Y.T. Zhu, Extraordinary strain hardening by gradient structure, *Proc. Natl. Acad. Sci.* 111 (2014) 7197–7201. <https://doi.org/10.1073/pnas.1324069111>.
- [155] F. Yuan, P. Chen, Y. Feng, P. Jiang, X. Wu, Strain hardening behaviors and strain rate sensitivity of gradient-grained Fe under compression over a wide range of strain rates, *Mech. Mater.* 95 (2016) 71–82. <https://doi.org/10.1016/j.mechmat.2016.01.002>.
- [156] Z. Yin, L. Le Sun, Y. Shen, Y.Z. Pang, J. Yang, Y.L. Gong, J.M. Tao, X.K. Zhu, Gradient Nano-Grained Cu and Cu-Zn Alloys Processed by Surface Mechanical Attrition Treatment, *Mater. Sci. Forum.* 848 (2016) 580–587. <https://doi.org/10.4028/www.scientific.net/msf.848.580>.
- [157] C.W. Shao, P. Zhang, Y.K. Zhu, Z.J. Zhang, Y.Z. Tian, Z.F. Zhang, Simultaneous improvement of strength and plasticity: Additional work-hardening from gradient microstructure, *Acta Mater.* 145 (2018) 413–428. <https://doi.org/10.1016/j.actamat.2017.12.028>.
- [158] Y. Lin, J. Pan, H.F. Zhou, H.J. Gao, Y. Li, Mechanical properties and optimal grain size distribution profile of gradient grained nickel, *Acta Mater.* 153 (2018) 279–289. <https://doi.org/10.1016/j.actamat.2018.04.065>.
- [159] L. Wang, B. Li, Y. Shi, G. Huang, W. Song, S. Li, Optimizing mechanical properties of gradient-structured low-carbon steel by manipulating grain size distribution, *Mater. Sci. Eng. A.* (2019). <https://doi.org/10.1016/j.msea.2018.11.042>.
- [160] M.-X. Yang, R.-G. Li, P. Jiang, F.-P. Yuan, Y.-D. Wang, Y.-T. Zhu, X.-L. Wu, Residual stress provides significant strengthening and ductility in gradient structured materials, *Mater. Res. Lett.* 7 (2019) 433–438. <https://doi.org/10.1080/21663831.2019.1635537>.
- [161] H.H. Lee, J.I. Yoon, H.K. Park, H.S. Kim, Unique microstructure and simultaneous enhancements of strength and ductility in gradient-microstructured Cu sheet produced by

- single-roll angular-rolling, *Acta Mater.* 166 (2019) 638–649. <https://www.sciencedirect.com/science/article/pii/S1359645419300357?via%3Dihub> (accessed January 27, 2020).
- [162] T.H. Fang, W.L. Li, N.R. Tao, K. Lu, Revealing Extraordinary Intrinsic Tensile Plasticity in Gradient Nano-Grained Copper, *Science* (80-. ). 331 (2011) 1587–1590. <https://doi.org/10.1126/science.1200177>.
- [163] X. Zhou, X.Y. Li, K. Lu, Strain hardening in gradient nano-grained Cu at 77 K, *Scr. Mater.* 153 (2018) 6–9. <https://doi.org/10.1016/j.scriptamat.2018.04.039>.
- [164] M.N. Hasan, Y.F. Liu, X.H. An, J. Gu, M. Song, Y. Cao, Y.S. Li, Y.T. Zhu, X.Z. Liao, Simultaneously enhancing strength and ductility of a high-entropy alloy via gradient hierarchical microstructures, *Int. J. Plast.* 123 (2019) 178–195. <https://doi.org/10.1016/j.ijplas.2019.07.017>.
- [165] Y. Wang, F. Guo, Q. He, L. Song, M. Wang, A. Huang, Y. Li, C. Huang, Synergetic deformation-induced extraordinary softening and hardening in gradient copper, *Mater. Sci. Eng. A* 752 (2019) 217–222. <https://doi.org/10.1016/j.msea.2019.03.020>.
- [166] K. Larkin, A. Hunter, M. Buechler, Simulation of dislocation evolution in microparticle impacts over a wide range of impact velocities, *Int. J. Plast.* 158 (2022) 103408. <https://doi.org/10.1016/j.ijplas.2022.103408>.
- [167] G. Agarwal, R.R. Valisetty, A.M. Dongare, Shock wave compression behavior and dislocation density evolution in Al microstructures at the atomic scales and the mesoscales, *Int. J. Plast.* 128 (2020) 102678. <https://doi.org/10.1016/j.ijplas.2020.102678>.
- [168] D.F. Rojas, O.K. Orhan, M. Ponga, Dynamic recrystallization of Silver nanocubes during high-velocity impacts, *Acta Mater.* 212 (2021) 116892. <https://doi.org/10.1016/j.actamat.2021.116892>.
- [169] J. Cai, C. Griesbach, S.G. Ahnen, R. Thevamaran, Dynamic Hardness Evolution in Metals from Impact Induced Gradient Dislocation Density, *Acta Mater.* (2023) 118807. <https://doi.org/10.1016/j.actamat.2023.118807>.
- [170] J.A. Hines, K.S. Vecchio, S. Ahzi, A Model for Microstructure Evolution in Adiabatic Shear

- Bands, *Metall. Mater. Trans. A*. 29A (1998) 191–203.
- [171] T.J. Jackson, J. Rolph, R.C. Buckingham, M.C. Hardy, *The Effect of Shot Peening on the Ductility and Tensile Strength of Nickel-Based Superalloy Alloy 720Li*, Springer International Publishing, 2020. [https://doi.org/10.1007/978-3-030-51834-9\\_52](https://doi.org/10.1007/978-3-030-51834-9_52).
- [172] Y. Zhu, X. Wu, Perspective on hetero-deformation induced (HDI) hardening and back stress, *Mater. Res. Lett.* 7 (2019) 393–398. <https://doi.org/10.1080/21663831.2019.1616331>.
- [173] S. Lu, J. Zhao, M. Huang, Z. Li, G. Kang, X. Zhang, Multiscale discrete dislocation dynamics study of gradient nano-grained materials, *Int. J. Plast.* 156 (2022) 103356. <https://doi.org/10.1016/j.ijplas.2022.103356>.
- [174] C. Liu, W. Lu, G.J. Weng, J. Li, A cooperative nano-grain rotation and grain-boundary migration mechanism for enhanced dislocation emission and tensile ductility in nanocrystalline materials, *Mater. Sci. Eng. A*. 756 (2019) 284–290. <https://doi.org/10.1016/j.msea.2019.04.055>.
- [175] J.P. Liebig, M. Mačković, E. Spiecker, M. Göken, B. Merle, Grain boundary mediated plasticity: A blessing for the ductility of metallic thin films?, *Acta Mater.* 215 (2021) 117079. <https://doi.org/10.1016/j.actamat.2021.117079>.
- [176] P. Cao, The Strongest Size in Gradient Nanograined Metals, *Nano Lett.* 20 (2020) 1440–1446. <https://doi.org/10.1021/acs.nanolett.9b05202>.
- [177] X. Wang, L. Zhong, S.X. Mao, Advances in understanding atomic-scale deformation of small-sized face-centered cubic metals with in situ transmission electron microscopy, *Mater. Today Nano*. 2 (2018) 58–69. <https://doi.org/10.1016/j.mtnano.2018.09.002>.
- [178] Y. Gao, H. Bei, Strength statistics of single crystals and metallic glasses under small stressed volumes, *Prog. Mater. Sci.* 82 (2016) 118–150. <https://doi.org/10.1016/j.pmatsci.2016.05.002>.
- [179] S. Lee, J. Jeong, Y. Kim, S.M. Han, D. Kiener, S.H. Oh, FIB-induced dislocations in Al submicron pillars: Annihilation by thermal annealing and effects on deformation behavior, *Acta Mater.* 110 (2016) 283–294. <https://doi.org/10.1016/j.actamat.2016.03.017>.

- [180] R. Dou, B. Derby, A universal scaling law for the strength of metal micropillars and nanowires, *Scr. Mater.* 61 (2009) 524–527. <https://doi.org/10.1016/j.scriptamat.2009.05.012>.
- [181] D. Hull, D. Bacon, *Introduction to Dislocations*, 4th ed., Butterworth-Heinemann, Oxford, UK, 2001.
- [182] L. Clément, R. Pantel, L.F.T. Kwakman, J.L. Rouvière, Strain measurements by convergent-beam electron diffraction: The importance of stress relaxation in lamella preparations, *Appl. Phys. Lett.* 85 (2004) 651–653. <https://doi.org/10.1063/1.1774275>.
- [183] A. Stukowski, Structure identification methods for atomistic simulations of crystalline materials, *Model. Simul. Mater. Sci. Eng.* 20 (2012) 45021.
- [184] D.F. Rojas, M. Isiet, M. Ponga, Dynamic recrystallization in face-centered cubic particles during high-velocity impacts, *Mech. Mater.* 168 (2022) 104268. <https://doi.org/10.1016/j.mechmat.2022.104268>.
- [185] J.A. Hines, K.S. Vecchio, S. Ahzi, A model for microstructure evolution in adiabatic shear bands, *Metall. Mater. Trans. A Phys. Metall. Mater. Sci.* 29 (1998) 191–203. <https://doi.org/10.1007/s11661-998-0172-4>.
- [186] N. Zaafarani, D. Raabe, R.N. Singh, F. Roters, S. Zaefferer, Three-dimensional investigation of the texture and microstructure below a nanoindent in a Cu single crystal using 3D EBSD and crystal plasticity finite element simulations, *Acta Mater.* 54 (2006) 1863–1876. <https://doi.org/10.1016/j.actamat.2005.12.014>.
- [187] C. Zambaldi, F. Roters, D. Raabe, U. Glatzel, Modeling and experiments on the indentation deformation and recrystallization of a single-crystal nickel-base superalloy, *Mater. Sci. Eng. A* 454–455 (2007) 433–440. <https://doi.org/10.1016/j.msea.2006.11.068>.
- [188] N. Zaafarani, D. Raabe, F. Roters, S. Zaefferer, On the origin of deformation-induced rotation patterns below nanoindents, *Acta Mater.* 56 (2008) 31–42. <https://doi.org/10.1016/j.actamat.2007.09.001>.
- [189] E. Demir, D. Raabe, N. Zaafarani, S. Zaefferer, Investigation of the indentation size effect through the measurement of the geometrically necessary dislocations beneath small indents

- of different depths using EBSD tomography, *Acta Mater.* 57 (2009) 559–569. <https://doi.org/10.1016/j.actamat.2008.09.039>.
- [190] Y. Liu, S. Varghese, J. Ma, M. Yoshino, H. Lu, R. Komanduri, Orientation effects in nanoindentation of single crystal copper, *Int. J. Plast.* 24 (2008) 1990–2015. <https://doi.org/10.1016/j.ijplas.2008.02.009>.
- [191] S.M. Han, M.A. Phillips, W.D. Nix, Study of strain softening behavior of Al–Al<sub>3</sub>Sc multilayers using microcompression testing, *Acta Mater.* 57 (2009) 4473–4490. <https://doi.org/10.1016/j.actamat.2009.06.007>.
- [192] Y. Zhang, G.J. Tucker, J.R. Trelewicz, Stress-assisted grain growth in nanocrystalline metals: Grain boundary mediated mechanisms and stabilization through alloying, *Acta Mater.* 131 (2017) 39–47. <https://doi.org/10.1016/j.actamat.2017.03.060>.
- [193] Advances in High Temperature Gas Cooled Reactor Fuel Technology, in: Int. At. Energy Agency, Vienna, 2012: p. 711. IAEA-TECDOC-CD-1674.
- [194] M. Fisher, Nuclear High Temperature Heat Could Replace Fossil Fuels in Industry, Mitigate Climate Change, Int. At. Energy Agency. (2017). <https://www.iaea.org/newscenter/news/nuclear-high-temperature-heat-could-replace-fossil-fuels-in-industry-mitigate-climate-change>.
- [195] P.A. Demkowicz, B. Liu, J.D. Hunn, Coated particle fuel: Historical perspectives and current progress, *J. Nucl. Mater.* 515 (2019) 434–450. <https://doi.org/10.1016/j.jnucmat.2018.09.044>.
- [196] R. Hecker, W. Rausch, R. Schulten, Development of High Temperature Thermal Reactors in Germany, in: Nucl. Energy Meet., Julich, Germany, 1967: p. 38.
- [197] D.A. Petti, J. Buongiorno, J.T. Maki, R.R. Hobbins, G.K. Miller, Key differences in the fabrication, irradiation and high temperature accident testing of US and German TRISO-coated particle fuel, and their implications on fuel performance, *Nucl. Eng. Des.* 222 (2003) 281–297. [https://doi.org/10.1016/S0029-5493\(03\)00033-5](https://doi.org/10.1016/S0029-5493(03)00033-5).
- [198] J.A. Phillips, C.M. Barnes, J.D. Hunn, Fabrication and Comparison of Fuels for Advanced Gas Reactor Irradiation Tests, in: HTR 2010, Prague, Czech Republic, 2010: p. 11.

- [199] B.P. Collin, AGR-1 Irradiation Test Final As-Run Report, Rev. 3, Idaho Falls, ID (United States), 2015. <https://doi.org/10.2172/1173081>.
- [200] B.P. Collin, AGR-2 Irradiation Test Final As-Run Report (Revision 4), Idaho Falls, ID (United States), 2018. <https://doi.org/10.2172/1514716>.
- [201] J.D. Hunn, C.A. Baldwin, T.J. Gerczak, F.C. Montgomery, R.N. Morris, C.M. Silva, P.A. Demkowicz, J.M. Harp, S.A. Ploger, Detection and analysis of particles with failed SiC in AGR-1 fuel compacts, *Nucl. Eng. Des.* 306 (2016) 36–46. <https://doi.org/10.1016/j.nucengdes.2015.12.011>.
- [202] J.D. Hunn, C.A. Baldwin, F.C. Montgomery, T.J. Gerczak, R.N. Morris, G.W. Helmreich, P.A. Demkowicz, J.M. Harp, J.D. Stempien, Initial examination of fuel compacts and TRISO particles from the US AGR-2 irradiation test, *Nucl. Eng. Des.* 329 (2018) 89–101. <https://doi.org/10.1016/j.nucengdes.2017.09.017>.
- [203] R.N. Morris, J.D. Hunn, C.A. Baldwin, F.C. Montgomery, T.J. Gerczak, P.A. Demkowicz, Initial results from safety testing of US AGR-2 irradiation test fuel, *Nucl. Eng. Des.* 329 (2018) 124–133. <https://doi.org/10.1016/j.nucengdes.2017.08.006>.
- [204] R.N. Morris, C.A. Baldwin, P.A. Demkowicz, J.D. Hunn, E.L. Reber, Performance of AGR-1 high-temperature reactor fuel during post-irradiation heating tests, *Nucl. Eng. Des.* 306 (2016) 24–35. <https://doi.org/10.1016/j.nucengdes.2016.04.031>.
- [205] T.J. Gerczak, R. Seibert, J.D. Hunn, Role of microstructure on CO corrosion of SiC layer in UO<sub>2</sub>-TRISO fuel, *J. Nucl. Mater.* 537 (2020) 152185. <https://doi.org/10.1016/j.jnucmat.2020.152185>.
- [206] J. Stempien, M. Plummer, J. Schulthess, P. Demkowicz, Measurement of kernel swelling and buffer densification in irradiated UCO and UO<sub>2</sub> TRISO fuel particles from AGR-2, Idaho Falls, ID (United States), 2019. <https://doi.org/10.2172/1599772>.
- [207] S.A. Ploger, P.A. Demkowicz, J.D. Hunn, J.S. Kehn, Microscopic analysis of irradiated AGR-1 coated particle fuel compacts, *Nucl. Eng. Des.* 271 (2014) 221–230. <https://doi.org/10.1016/j.nucengdes.2013.11.036>.
- [208] F.J. Rice, J.D. Stempien, P.A. Demkowicz, Ceramography of irradiated TRISO fuel from



- the AGR-2 experiment, *Nucl. Eng. Des.* 329 (2018) 73–81. <https://doi.org/10.1016/j.nucengdes.2017.10.010>.
- [209] G.W. Helmreich, D. Richardson, S. Venkatakrishnan, A. Ziabari, Method for measurement of TRISO kernel and layer volumes by X-ray computed tomography, *J. Nucl. Mater.* 539 (2020) 152255. <https://doi.org/10.1016/j.jnucmat.2020.152255>.
- [210] J.J. Powers, B.D. Wirth, A review of TRISO fuel performance models, *J. Nucl. Mater.* 405 (2010) 74–82. <https://doi.org/10.1016/j.jnucmat.2010.07.030>.
- [211] J.D. Hales, R.L. Williamson, S.R. Novascone, D.M. Perez, B.W. Spencer, G. Pastore, Multidimensional multiphysics simulation of TRISO particle fuel, *J. Nucl. Mater.* 443 (2013) 531–543. <https://doi.org/10.1016/j.jnucmat.2013.07.070>.
- [212] H. Wei, J. Zhang, X. Jian, Y. Zhang, L. Li, S. Ding, Q. Ren, Effects of the key parameters of TRISO particle buffer layer on in-pile thermo-mechanical behavior in FCM fuel pellets, *J. Nucl. Mater.* 551 (2021) 152977. <https://doi.org/10.1016/j.jnucmat.2021.152977>.
- [213] J.D. Hunn, G.E. Jellison, R.A. Lowden, Increase in pyrolytic carbon optical anisotropy and density during processing of coated particle fuel due to heat treatment, *J. Nucl. Mater.* 374 (2008) 445–452. <https://doi.org/10.1016/j.jnucmat.2007.10.003>.
- [214] R. Kirchhofer, J.D. Hunn, P.A. Demkowicz, J.I. Cole, B.P. Gorman, Microstructure of TRISO coated particles from the AGR-1 experiment: SiC grain size and grain boundary character, *J. Nucl. Mater.* 432 (2013) 127–134. <https://doi.org/10.1016/j.jnucmat.2012.08.052>.
- [215] R.L. Seibert, B.C. Jolly, M. Balooch, D.P. Schappel, K.A. Terrani, Production and characterization of TRISO fuel particles with multilayered SiC, *J. Nucl. Mater.* 515 (2019) 215–226. <https://doi.org/10.1016/j.jnucmat.2018.12.024>.
- [216] T. Lowe, R.S. Bradley, S. Yue, K. Bari, J. Gelb, N. Rohbeck, J. Turner, P.J. Withers, Microstructural analysis of TRISO particles using multi-scale X-ray computed tomography, *J. Nucl. Mater.* 461 (2015) 29–36. <https://doi.org/10.1016/j.jnucmat.2015.02.034>.
- [217] L. Tan, T.R. Allen, J.D. Hunn, J.H. Miller, EBSD for microstructure and property characterization of the SiC-coating in TRISO fuel particles, *J. Nucl. Mater.* 372 (2008) 400–

404. <https://doi.org/10.1016/j.jnucmat.2007.04.048>.
- [218] D. H  lary, O. Dugne, X. Bourrat, Advanced characterization techniques for SiC and PyC coatings on high-temperature reactor fuel particles, *J. Nucl. Mater.* 373 (2008) 150–156. <https://doi.org/10.1016/j.jnucmat.2007.05.041>.
- [219] K. Bari, C. Osarinmwian, E. L  pez-Honorato, T.J. Abram, Characterization of the porosity in TRISO coated fuel particles and its effect on the relative thermal diffusivity, *Nucl. Eng. Des.* 265 (2013) 668–674. <https://doi.org/10.1016/j.nucengdes.2013.08.067>.
- [220] J.C. Bokros, G.L. Guthrie, A.S. Schwartz, The influence of crystallite size on the dimensional changes induced in carbonaceous materials by high-temperature irradiation, *Carbon N. Y.* 6 (1968) 55–63. [https://doi.org/10.1016/0008-6223\(68\)90050-X](https://doi.org/10.1016/0008-6223(68)90050-X).
- [221] J.C. Bokros, R.J. Price, Dimensional changes induced in pyrolytic carbon by high-temperature fast-neutron irradiation, *Carbon N. Y.* 5 (1967) 301–312. [https://doi.org/10.1016/0008-6223\(67\)90012-7](https://doi.org/10.1016/0008-6223(67)90012-7).
- [222] J.E. Brocklehurst, B.T. Kelly, The dimensional changes of highly-oriented pyrolytic graphite irradiated with fast neutrons at 430  C and 600  C, *Carbon N. Y.* 31 (1993) 179–183. [https://doi.org/10.1016/0008-6223\(93\)90170-F](https://doi.org/10.1016/0008-6223(93)90170-F).
- [223] F. Cancino-Trejo, M. S  enz Padilla, E. L  pez-Honorato, U. Carvajal-Nunez, J. Boshoven, J. Somers, The effect of heat treatment on the microstructure and diffusion of silver in pyrolytic carbon coatings, *Carbon N. Y.* 109 (2016) 542–551. <https://doi.org/10.1016/j.carbon.2016.08.010>.
- [224] G.W. Helmreich, A.K. Kercher, T.J. Gerczak, D. Richardson, F.C. Montgomery, D.J. Skitt, J.D. Hunn, Microstructure of irradiated AGR TRISO particle buffer layers as measured by X-ray computed tomography, *J. Nucl. Mater.* 572 (2022) 154061. <https://doi.org/10.1016/j.jnucmat.2022.154061>.
- [225] H.B. Mann, Non-parametric test against trend, *Econometrica.* 13 (1945) 163–171.
- [226] M. Kendall, Rank Correlation Methods, 4th ed., Charles Griffin, London, 1975.
- [227] C.M. Barnes, D.W. Marshall, J.T. Keeley, J.D. Hunn, Results of tests to demonstrate a 6-

- in.-diameter coater for production of TRISO-coated particles for advanced gas reactor experiments, *J. Eng. Gas Turbines Power.* 131 (2009) 1–6. <https://doi.org/10.1115/1.3098424>.
- [228] P.A. Demkowicz, B. Liu, J.D. Hunn, Coated particle fuel: Historical perspectives and current progress, *J. Nucl. Mater.* 515 (2019) 434–450. <https://doi.org/10.1016/j.jnucmat.2018.09.044>.
- [229] J.D. Hunn, R.A. Lowden, Data Compilation for AGR-1 Baseline Coated Particle Composite LEU01-46T, Oak Ridge National Lab, Oak Ridge, TN (United States), 2006. <https://doi.org/10.2172/974594>.
- [230] C. de Tomas, A. Aghajamali, J.L. Jones, D.J. Lim, M.J. López, I. Suarez-Martinez, N.A. Marks, Transferability in interatomic potentials for carbon, *Carbon N. Y.* 155 (2019) 624–634. <https://doi.org/10.1016/j.carbon.2019.07.074>.
- [231] S.J. BLOTT, K. PYE, Particle shape: a review and new methods of characterization and classification, *Sedimentology.* 55 (2007) 070921092734002-???. <https://doi.org/10.1111/j.1365-3091.2007.00892.x>.
- [232] D.S. Harding, W.C. Oliver, G.M. Pharr, Cracking during nanoindentation and its use in the measurement of fracture toughness, *Mater. Res. Soc. Symp. - Proc.* 356 (1995) 663–668. <https://doi.org/10.1557/proc-356-663>.
- [233] K.E. Wright, J. Stempien, W. Jiang, I.J. van Rooyen, Fission product distribution in irradiated safety-tested and as-irradiated AGR-2 TRISO particles, *J. Nucl. Mater.* 559 (2022) 153468. <https://doi.org/10.1016/j.jnucmat.2021.153468>.
- [234] T. Davis, D. Healy, A. Bubeck, R. Walker, Stress concentrations around voids in three dimensions: The roots of failure, *J. Struct. Geol.* 102 (2017) 193–207. <https://doi.org/10.1016/j.jsg.2017.07.013>.
- [235] A. Bubeck, R.J. Walker, D. Healy, M. Dobbs, D.A. Holwell, Pore geometry as a control on rock strength, *Earth Planet. Sci. Lett.* 457 (2017) 38–48. <https://doi.org/10.1016/j.epsl.2016.09.050>.
- [236] S. Tammas-Williams, P.J. Withers, I. Todd, P.B. Prangnell, The Influence of Porosity on

- Fatigue Crack Initiation in Additively Manufactured Titanium Components, *Sci. Rep.* 7 (2017) 7308. <https://doi.org/10.1038/s41598-017-06504-5>.
- [237] S.Y. Wang, L. Sun, C. Yang, S.Q. Yang, C.A. Tang, Numerical study on static and dynamic fracture evolution around rock cavities, *J. Rock Mech. Geotech. Eng.* 5 (2013) 262–276. <https://doi.org/10.1016/j.jrmge.2012.10.003>.
- [238] G.R. Bower, S.A. Ploger, P.A. Demkowicz, J.D. Hunn, Measurement of kernel swelling and buffer densification in irradiated UCO-TRISO particles, *J. Nucl. Mater.* 486 (2017) 339–349. <https://doi.org/10.1016/j.jnucmat.2017.01.006>.
- [239] M. Liu, C. Chen, A micromechanical analysis of the fracture properties of saturated porous media, *Int. J. Solids Struct.* 63 (2015) 32–38. <https://doi.org/10.1016/j.ijsolstr.2015.02.031>.
- [240] Z. Chen, X. Wang, F. Giuliani, A. Atkinson, Fracture Toughness of Porous Material of LSCF in Bulk and Film Forms, *J. Am. Ceram. Soc.* 98 (2015) 2183–2190. <https://doi.org/10.1111/jace.13507>.
- [241] E. Voice, Radiation-induced Creep in Pyrocarbon, *Nature*. 230 (1971) 47–48.
- [242] R.J. Price, Irradiation-induced creep in graphite: A review, Department of Energy, 1981.
- [243] L.G. Cançado, A. Jorio, E.H.M. Ferreira, F. Stavale, C.A. Achete, R.B. Capaz, M.V.O. Moutinho, A. Lombardo, T.S. Kulmala, A.C. Ferrari, Quantifying Defects in Graphene via Raman Spectroscopy at Different Excitation Energies, *Nano Lett.* 11 (2011) 3190–3196. <https://doi.org/10.1021/nl201432g>.
- [244] L.G. Cançado, K. Takai, T. Enoki, M. Endo, Y.A. Kim, H. Mizusaki, A. Jorio, L.N. Coelho, R. Magalhães-Paniago, M.A. Pimenta, General equation for the determination of the crystallite size  $L_a$  of nanographite by Raman spectroscopy, *Appl. Phys. Lett.* 88 (2006) 163106. <https://doi.org/10.1063/1.2196057>.
- [245] E. López-Honorato, P.J. Meadows, P. Xiao, Fluidized bed chemical vapor deposition of pyrolytic carbon – I. Effect of deposition conditions on microstructure, *Carbon N. Y.* 47 (2009) 396–410. <https://doi.org/10.1016/j.carbon.2008.10.023>.
- [246] E. López-Honorato, P.J. Meadows, R.A. Shatwell, P. Xiao, Characterization of the

- anisotropy of pyrolytic carbon by Raman spectroscopy, *Carbon* N. Y. 48 (2010) 881–890. <https://doi.org/10.1016/j.carbon.2009.11.010>.
- [247] A. Yoshida, Y. Kaburagi, Y. Hishiyama, Full width at half maximum intensity of the G band in the first order Raman spectrum of carbon material as a parameter for graphitization, *Carbon* N. Y. 44 (2006) 2333–2335. <https://doi.org/10.1016/j.carbon.2006.05.020>.
- [248] A. Gupta, C. Griesbach, J. Cai, S. Weigand, E.R. Meshot, R. Thevamaran, Origins of mechanical preconditioning in hierarchical nanofibrous materials, *Extrem. Mech. Lett.* 50 (2021) 101576. <https://doi.org/10.1016/j.eml.2021.101576>.
- [249] J. Cai, C. Griesbach, R. Thevamaran, Extreme Dynamic Performance of Nanofiber Mats under Supersonic Impacts Mediated by Interfacial Hydrogen Bonds, *ACS Nano*. 15 (2021) 19945–19955. <https://doi.org/10.1021/acsnano.1c07465>.
- [250] W. Cai, V. V. Bulatov, J. Chang, J. Li, S. Yip, Dislocation core effects on mobility, in: *Dislocations in Solids*, 2004: pp. 1–80. [https://doi.org/10.1016/S1572-4859\(05\)80003-8](https://doi.org/10.1016/S1572-4859(05)80003-8).
- [251] J.M. Zhang, Y. Zhang, K.W. Xu, V. Ji, Young's modulus surface and Poisson's ratio curve for cubic metals, *J. Phys. Chem. Solids*. 68 (2007) 503–510. <https://doi.org/10.1016/j.jpcs.2007.01.025>.
- [252] K.M. Knowles, P.R. Howie, The Directional Dependence of Elastic Stiffness and Compliance Shear Coefficients and Shear Moduli in Cubic Materials, *J. Elast.* 120 (2015) 87–108. <https://doi.org/10.1007/s10659-014-9506-1>.
- [253] W. Triftshäuser, J.D. McGervey, Monovacancy formation energy in copper, silver, and gold by positron annihilation, *Appl. Phys.* 6 (1975) 177–180. <https://doi.org/10.1007/BF00883748>.